Interaction of Structured Femtosecond Light Pulses with Matter

by

Mitra Rahimiangolkhandani

Thesis submitted to the
University of Ottawa
In partial fulfillment of the requirements for the
Doctor of Philosophy in
Physics

Department of Physics
Faculty of Science
University of Ottawa

Abstract

Physics and potential applications of femtosecond laser pulses interacting with matter have captured interest in various fields, such as nonlinear optics, laser micromachining, integrated optics, and solar cell technologies. On the one hand, such ultrashort intense pulses make them practical elegant tools to be utilized for direct structuring of materials with high accuracy and numerous potential applications. On the other hand, studying the fundamental aspects and nonlinear nature of such interactions opens new remarkable venues for various unique investigations.

In recent years, the emerging topic of structured light (also known as twisted or optical vortex light), i.e., a beam of light with a twisted wave-front that can carry orbital angular momentum (OAM), has attracted the attention of many researchers working in the field of light-matter interaction. Such beams offer various applications from classical and quantum communication to imaging, micro/nano-manipulation, and modification of fundamental processes involved in light-matter interactions, e.g., absorption and emission. Nevertheless, the fabrication of complex structures, controlled modification, and achieving a high spatial resolution in material processing still remain in the spotlight. Moreover, the fundamental role of orbital angular momentum in the nonlinear absorption of materials, particularly in solids, has yet remained a subject of debate. Addressing these points was the main motive behind this dissertation. To accomplish this objective and investigate new aspects of structured light-matter interaction, I conducted various experiments, the results of which are presented in this work.

The general idea was to study the interaction of femtosecond laser radiation, having a structured phase and polarization, with the matter in two aspects: (i) surface morphology modification and (ii) nonlinear absorption of solids.

In this regard, I studied surface processing of crystalline silicon and CVD diamond with femtosecond laser vortex pulses generated by a birefringent phase-plate, known as q-plate, in single and multiple pulse irradiation regimes, respectively. The characterization of the modified region was performed using optical microscopy, scanning electron microscopy (SEM), and atomic force microscopy (AFM). I demonstrated that upon irradiation of a single vortex pulse on silicon, a nano-cone structure is formed within the ablated crater, whose height was independent of the helicity of the twisted light. However, for a linearly polarized vortex pulse, the height of the nano-cone decreases at higher pulse energies. The dynamics of nano-cone formation and the role of polarization were also investigated by simulating the mass transport function in this process.

Moreover, using superimposed vortex beams, we fabricated complex patterns containing several nano-cones, by single-shot irradiation on the silicon surface. My experimental results offer an ability to actively control and manipulate material, in terms of the nano-cones position, in two dimensions with an ultra-high resolution.

I further proceeded with our experiments in the multiple pulse regime on a diamond target. By irradiation of a high number of superimposed vortex pulses, I was able to imprint complex polarization states of structured light on the target surface in the form

of periodic nano-ripples. This procedure enabled us to not only generate spatially varying nano-gratings but also directly visualize and study very complex states of polarization.

Besides these surface structuring, I carried out experimental studies to investigate the response of bulk material to an incident circularly polarized vortex beam that carries orbital angular momentum. The experimental results reveal, for the first time, that such an interaction can produce a differential absorption that gives rise to helical dichroism. We demonstrate that this response is sensitive to the handedness and degree of the twist in the incident vortex beam. Such a dichroism effect may be attributed to the excitation of dipole-forbidden atomic transitions, e.g., electric quadrupole transitions. However, this explanation is not absolute and remains open to further research and investigations.

Acknowledgements

First of all, I would like to thank my PhD supervisor, professor Ravi Bhardwaj for all of his great and helpful scientific discussions, which assisted me in choosing my thesis topic. Undoubtedly, his professional guidance along with the immense time and effort he put, paved the way for me to complete my studies and led to the publication of this thesis. Professor Bhardwaj, I have learned a lot from you, and it was a privilege for me to work under your supervision.

My Special thanks to professor Ebrahim Karimi for all of his brilliant scientific ideas and discussions he put forward. No doubt that my PhD thesis has been highly influenced by collaborating with him and his group members, including Dr. Frédérich Bouchard and Mr. Hugo Larocque. Professor Karimis personality, along with his excellent physics intuition, has highly inspired me in my research.

I would also like to thank professors Paul Corkum and Thomas Brabec. In many stages of my PhD work, I had the honour to have several scientific discussions with these great scientists. These meetings have greatly influenced the quality of my work and inspired me in many directions. I would like to thank you all for your great and novel ideas. It has always been a pleasure for me to learn from you.

Many thanks to Dr. Anthony Olivieri for kindly taking the time to train me and teaching me how to access and use the various equipment in the cleanroom. Specifically, I would like to mention how patient and helpful he was while I was learning.

I would also like to thank my great friends and colleagues, Mr. Ashish Jain, Ms. Maryam Alameer, Ms. Hajar Al-khazraji, and Dr. Ali Alshehri. All of us, as members of the extreme ultrafast photonics group, have spent many hours together talking about science and working on shared projects. I am always thankful for having such brilliant and bright colleagues. No doubt, high-quality scientific work in our group would have never been possible without the friendly and cooperative environment that you all created. I should mention that many of my friends and colleagues whom I have not named here have all played some role at some point during my PhD journey. I obviously will not forget them, and I would like to acknowledge every one of them.

I would also like to specifically thank my loving parents, my mother Effat and my father Ebrahim, for their endless support and love, and my dear siblings, Rahele and Mohammadreza, for always encouraging me during my PhD journey. Although they all live halfway around the world, their emotional care has motivated me greatly towards successfully completing my PhD studies.

I would like to thank my late father-in-law, Dr. Taher Nejadsattari, for his kind support and for motivating me to pursue my PhD. Furthermore, I should mention my dear aunt, Soraya, and her husband for their supportive help. They all played a significant role in my application process for studying here in Canada.

Last but definitely not least, I would like to thank my dear husband and colleague, Dr. Farshad Nejadsattari for his love and care. From the very first day I started my PhD studies, he was always there for me, whether it was about science or simply emotional

support. I would never forget the countless hours we spent together reading papers, talking about science, and attending conferences. Farshad, I would not have reached this far if it were not for you. I am greatly thankful for having you as my husband, best friend, and colleague.

Dedicated to

My love, Farshad

and

My dear parents, Effat and Ebrahim

List of publications included in this thesis

The research in this thesis has resulted in several publications in peer reviewed scientific journals. The content in chapter 7 is currently in the form of a draft manuscript and is being improved to be ready for submission.

- Chapter 4:

  M. G. Rahimian, F. Bouchard, H. Al-Khazraji, E. Karimi, P. B. Corkum, V. R. Bhardwaj

  Polarization dependent nanostructuring of silicon with femtosecond vortex pulse

  APL PHOTONICS **2**, 086104 (2017)

- Chapter 5:

  M. G. Rahimian, A. Jain, H. Larocque, P. B. Corkum, E. Karimi, V. R. Bhardwaj

  Spatially controlled nano-structuring of silicon with femtosecond vortex pulses

  Scientific Reports **10**, 12643 (2020)

- Chapter 6:

  M. Alameer, A. Jain, **M. G. Rahimian**, H. Larocque, P. B. Corkum, E. Karimi, V. R. Bhardwaj

  Mapping Complex Polarization States of Light on a Solid

  Optics Letters **43**, No.23, 5757(2018)

- Chapter 7:

  M. G. Rahimian, A. Jain, A. Parks, H. Larocque, P. B. Corkum, E. Karimi, T. Brabec, V. R. Bhardwaj

  Helical Dichroism induced by orbital angular momentum of light in bulk materials

  In preparation (2020)

Table of Contents

List of Tables

List of Figures

Chapter 1

Introduction

This chapter provides a brief overview of the importance of studying the interaction of light endowing structured intensity, polarization, and phase with matter. A comprehensive study of such interactions open new horizons in this field, from the fundamental phenomena involved in the process to the application prospects such as novel laser structuring techniques. Moreover, a short section enumerates the contents presented in the next chapters of this thesis and experiments that I have carried out in the field of femtosecond structured light-matter interaction.

1.1 Overview

There are generally two approaches to study the interaction between femtosecond pulses and matter. The first approach is the characterization of light-matter interactions, where we examine the femtosecond pulse as it interacts with materials. The outcomes of this methodology highlight the physical mechanisms involved in these processes. In comparison, the second approach is a post-interaction analysis in the form of studying the surface morphology and material structuring in a controlled fashion.

Investigating the underlined physics of the interaction with intense fs pulses, particularly when the interaction takes place inside a solid, is difficult and not yet fully understood. The reason is that:

(a) Theoretical studies are challenging due to high intensities involved in this process, perturbation theory is not valid. In addition, many-body quantum calculations are required to account for a large number of atoms present in the interaction volume. The interaction occurs on different time scale (fs-ms) and length scale (nm-mm). Moreover, to have a proper interpretation, nonlinear optical and plasma effects and several other physical processes describing the light propagation and ionization need to be considered.

(b) From the experimental point of view, there is no direct access to the electrons and ions created in the bulk by ionization, unlike on surfaces or in isolated atoms and

molecules. In fact, most of the experimental tools developed for such studies, e. g., ion and electron imaging, high harmonic generation spectroscopy [1], and attosecond extreme ultra-violet (XUV) streaking [2], are mostly used for the case of atoms and molecules. Although nowadays they are applicable even in bulk materials, more beneficial and practical approaches and techniques are still required in order to investigate the interaction of solids with fs-laser radiation.

Post-interaction analysis and material structuring: the ultra-high intensity of ultrashort pulses combined with their spatial intensity distribution and polarization states produce many novel effects and applications. Such studies promote science and technology in nano-fabrication and material manipulation techniques in two and three dimensions. Due to material modification/removal, several types of features, either on the surface or inside the bulk, can be generated once the sample is irradiated by fs laser pulses. Such material structuring was typically achieved using Gaussian beam by employing their properties such as intensity profile, pulse duration, and polarization. As an example, one can find various surface structures from a single microring [3] to randomly-formed nanocone forests [4–6], and nanograting that was first observed by Birnbaum *et al.* [7]. Nevertheless, there is still a demand to structuring materials in more complex shapes and a well-controlled manner by altering beam parameters and physical properties of the specimen.

Nowadays, the interest is to discover whether the physics of the light-matter interaction and its outcome is different if the intensity profile, polarization state, and phase are altered. In 1992, Allen *et al.* [8] proposed that light carries orbital angular momentum (OAM) as a consequence of its helical wavefront and on-axis phase singularity. Since then, such modifications in the laser beam and their influences in the field of laser beam interaction with matter has extensively expanded in two directions. First from the fundamental perspective and second from the application aspect.

During the past decade, light possessing OAM (also known as structured light) has intrigued many scientists to explore new fundamental concepts of light-matter interactions that remains a subject of debate to this day. Investigations of structured light has led to various applications including optical trapping and manipulation [9–11], optical telecommunications [12, 13], quantum physics [14], and super-resolution microscopy with a spatial resolution beyond the diffraction limit [15–17]. A multidisciplinary breakthrough showing the influence of structured light has led to a Nobel prize in Chemistry in 2014 [18]. In this research, super-resolution fluorescence microscopy was developed based on the stimulated emission depletion (STED) effect that uses a superposition of Gaussian and OAM beams.

Explorations of structured light have increased during the past decades leading to understanding new fundamental concepts of light-matter interactions and advancing laser machining techniques.

The early studies in the field of structured light/optical vortices (OVs) mainly focused on establishing fundamental theories and exploring basic physical phenomena. Indeed, they opened doors into further investigations of the light-matter interaction, topological structures, and quantum nature of light. For instance, studies that focused on the characteristic intensity structure of OAM beams demonstrated that such beams could confine atoms to

regions of maximal or minimal light intensity [19]. Furthermore, studies that focused on the physics of the interaction of OVs with particles discovered fundamental phenomena in action. For example, a torque exertion (including a mechanical rotation) on the atomic clouds, an OAM transfer to the internal state of an atom resulting in an improvement in the selection rules, and an OAM beam differentiation by molecules (dichroism effect) originated from its phase handedness [20–22].

Some research also showed how irradiation by OAM beam could mechanically twist a variety of materials, from silicon to polymers [23–25]. Over time, due to the development of OAM manipulation, new vortex and OAM applications rapidly emerged and were extended to various fields and are still enabling incredible novelties and many breakthroughs in advanced optics [26–32]. These developments and technological advancements are intimately connected with the progress in studying OAM phenomena in solid-state physics, quantum electrodynamics, chemistry, and several other disciplines [33–35].

The primary objective of my research was to (1) open up new territories through the application-based capacity of structured light interaction with matter and (2) investigate whether OAM can drive a dichroism effect in a bulk material. Doing so, I tried to obtain a firm understanding of the structured light-matter interaction.

Here I briefly discuss the primary outline of this dissertation.

1.1.1 Nanostructring with Structured Light

The major part of my thesis focuses on the nano/micro fabrication with femtosecond structured light (also known as vortex beam). An optical vortex beam, e. g., the LaguerreGaussian (LG) beam, is characterized by a phase factor, $exp(i\ell\varphi)$, and can carry OAM equivalent to $\ell\hbar$ per photon (where ℓ is an integer number) [36]. To form nano- and microstructures on the target's surface, I have taken advantage of the unique properties of vortex beams. For instance, their intensity profiles result from the phase singularities and their complex polarization states that indicate the relative phase relations between the polarization vectors' components. The significant novel fabrication aspects presented in this thesis are:

(a) formation of individual nanocones, for the first time, using a single femtosecond laser vortex pulse on the surface of a silicon wafer. This was further improved by utilizing unconventional beams, e.g., superpositions of vortex beams, to fabricate several nanocones positioned in a single complex-patterned feature. The experiment was performed in the single-pulse regime.

(b) demonstrating a method to spatially control the position of individual nanocones with nanoscale precision. This was achieved by altering the relative phase between superimposed vortex beams.

(c) creation of periodic structures in the multiple-pulse regime on a diamond surface by exploiting vortex beams possessing various polarization states. The resultant ripple structures are precisely decorated parallel to the local electric field's direction (laser polarization).

Notably, a peak laser fluence slightly above the ablation/modification threshold value was used to obtain all these well-defined structures. As a result, only the maximum intensity region of the beam could modify the materials.

The overall aim of this part of my work is to present a simple, rapid, and accurate fabrication technique based on the direct laser writing method to form two- and three-dimensional nano/micro-structures with many potential applications in photonics, for example, fabrication of optical devices, optical data storage, and displays.

1.1.2 Dichroism Effect Introduced by OAM

I present, for the first time, a dichroism effect when laser pulses endowing OAM with opposite helicities interact with bulk transparent materials. Understanding the processes involved in such chiral interactions has been of interest for more than a decade and across many areas of atomic and molecular physics, and quantum electrodynamics. Although the actual underlying mechanism is not yet revealed and fully understood, there have been several attempts, experimentally and theoretically, to obtain an intuition on how materials respond to a beam of light carrying OAM.

Conventionally, a Gaussian beam with circular polarization (spin angular momentum or SAM) is used to study the chiral interactions between light and chiral materials. The resultant phenomenon is known as Circular Dichroism (CD), where a chiral molecule realizes the handedness of the circular polarization state (sign of spin angular momentum) of a light beam. This phenomenon causes a chiral molecule to absorb the incident left and right circularly polarized light at different rates. One may anticipate a similar chiroptical effect when a beam of light with chirality in its phase interacts with matter.

In fact, one of the early ideas in the field of structured light-matter interaction was to observe a chiral response of the material with respect to the handedness of the beams wavefront. At first, scientists failed to observe such an effect [37] or to produce any feasible applications because the experiments were conducted in linear absorption regime. However, further studies investigated different mechanisms involved in OAM beam interaction with atoms and molecules. They have predicted and discovered surprising effects, from selection rules modification to the chiral response of molecules. Indeed, current studies on the chiroptical response of molecules [20–22] have been developed by a renewed consideration in selection rules based on quantum electrodynamics [38] and may be soon well-understood and brought to applications.

Although, in recent years, atoms and molecules interacting with OAM beams have been explored, there has been no research investigating the role of OAM in the response of bulk material. The reason might be the difficulties and limitations in both theoretical and experimental studies of bulk material, mentioned in Sec.1.1. One of the most beneficial and practical ways to cope with those difficulties and explore such interactions is to analyze the light transmitted through bulk material [39]. Any internal changes and post-interaction properties due to ionization, absorption, momentum exchange, and other optical processes can be then investigated and analyzed utilizing other well-known techniques such as imaging microscopy [40].

Looking into all these novelties and tackling the open problems were a motivation towards the second part of my research. The idea was to explore any possible influences that the number of twists and the direction of the twists may have in the light-matter interactions when an OAM beam passes through a bulk of transparent material. To experimentally investigate such effects, a transmission measurement technique was applied that allowed us to analyze the **nonlinear response** of transparent materials under irradiation of OAM beams with different topological charges and opposite helicities. The analysis of the transmitted vortex beam seems to be the only readily available tool to explore whether the target can distinguish between OAM beams carrying phase vortices with opposite signs. I proceeded with my research by focusing the OAM laser beam inside the target using an aspheric lens with a sufficiently high numerical aperture. This way, all the surface effects were eliminated, and the interaction was confined to a 3D. My experiment was carried forward by collecting the transmitted radiation while several laser beam parameters, such as pulse energy, duration of the pulse, polarization state, and the OAM value carried by the beam, were precisely controlled. The outcome indeed shows that a dichroism-like effect takes place when an OAM beam interacts with transparent bulk material. In other words, the handedness of an optical vortex, i.e., the direction of the twisted phase front of the beam, could produce chiroptical interactions. My experimental results indicate that using an OAM beam with a higher topological charge, i.e., more twists in the phase front, could enhance the chiroptical effect.

I hope these findings open new horizons in this field of research.

1.2 Organization of the Dissertation

Chapter 2: This chapter provides a brief review of the physical mechanisms behind the interaction of ultrashort laser pulses with material, particularly relevant to the experiments presented in this work. It highlights the benefits of ablation with femtosecond lasers over the lasers with longer pulse duration. This chapter also introduces the details of the femtosecond laser system used in the presented experiments, the experimental setup consisting of machining systems, and the analytical techniques used to evaluate the experimental data. Various crucial parameters that need to be controlled during experiments are also discussed.

Chapter 3: This chapter briefly introduces vortex beams and presents an overview of LaguerreGaussian (LG) beams having structured intensity, polarization, and phase, with a doughnut-shaped intensity profile that carry orbital angular momentum (OAM). It also discusses various methods to generate such beams are presented; the focus, however, is mainly on one of the most applied devices in vortex generation, called q-plate.

Chapter 4 presents experimental investigations of the ablation of silicon surface and, for the first time, the formation of individual nanocone features upon irradiation of single femtosecond laser vortex pulse. Under irradiation, the intensity distribution of the structured light is mapped onto the silicon surface, causing localized melting. Subsequent fluid dynamics lead to the formation of a nanocone at the null intensity region. Experimental

results also reveal the evolution of the crater formation as a function of pulse energy and the number of pulses on the surface. Moreover, the role of both spin and orbital angular momenta on the height of the formed nanocones was explored.

Chapter 5 addresses how light can be used to actively manipulate material in two dimensions with nanoscale precision. It demonstrates a technique to fabricate individual nanocones in a complex-patterned structure on the surface of silicon and control their position with nanometer resolution. This technique exploits the phase and polarization singularities of the vortex beam that allow us to control the null intensity regions in the beam profile. It is shown that varying the phase retardation of the two orthogonal polarization states of the incident structured light can control the position of the fabricated nanocones.

Chapter 6 discusses the characterization of complex polarization states of light. The standard approach to determine the light's polarization state involves measuring Stokes parameters. Extending this technique to characterize very complex polarization states requires polarization tomography, where the output polarization state is reconstructed from the measured spatially dependent intensity profiles of six different zero-order polarization states. In comparison, our method lies in the direct visualization of complex polarization states by imprinting them onto a solid surface in the form of laser-induced periodic nanogratings oriented parallel to the local structure of the electric field of light. In this chapter, it is demonstrated that this technique can be extended to even more complex polarization states produced by the coherent superposition of vortex beams.

Chapter 7 reviews some of the recent studies on the interactions of structured light with atoms and molecules. This chapter will then continue by presenting my experimental investigations on the role of OAM in producing helical dichroism in solids. Results reveal, for the first time, that a bulk of transparent material irradiated by OAM beam shows a chiroptical response. This significant chiroptical influence in light-matter interactions seems to be associated with the OAM of the beam and depends on the direction in which the vortex beam twists (considered as the OAM's sign) and is enhanced by increasing the magnitude of the OAM.

Chapter 8 summarizes the key results presented in this thesis and provides a broader outlook by proposing future research to address several potential applications as well as unanswered questions regarding the interaction of femtosecond vortex pulses with material.

Bibliography

[1] J. Itatani, J. Levesque, D. Zeidler, H. Niikura, H. Pépin, J. C. Kieffer, P. B. Corkum, and D. M. Villeneuve, "Tomographic imaging of molecular orbitals", Nature, 432, 867 (2004).

[2] P. Corkum and F. Krausz, "Attosecond science", Nature Phys., 3, 381 (2007).

[3] H. Al-Khazraji, V. R. Bhardwaj, "Polarization dependent micro-structuring of silicon with a femtosecond laser", Applied Surface Science, 353, 600-607 (2015).

[4] E. Fadeeva, S. Schlie, J. Koch, A. Ngezahayo, B.N. Chichkov, "The hydrophobic properties of femtosecond laser fabricated spike structures and their effects on cell proliferation", Phys. Status Solidi A, 206(6) 13481351 (2009).

[5] B. Raillard, L. Gouton, E. Ramos Moore, S. Grandthyll, F. Müller, F. Mücklich, "Ablation effects of femtosecond laser functionalization on steel surfaces", Surf. Coat. Technol., 207, 102109 (2012).

[6] B. R. Tull, J.E. Carey, E. Mazur, J. P. McDonald, S. M. Yalisove, "Silicon surface morphologies after femtosecond laser irradiation", MRS Bull., 31, (08) 626633 (2006).

[7] M. Birnbaum, "Semiconductor Surface Damage Produced by Ruby Lasers", J. Appl. Phys, 35, no. 11, 3688 (1965).

[8] L. Allen, M. W. Beijersbergen, R. J. C. Spreeuw, and J. P. Woerdman, "Orbital angular momentum of light and the transformation of Laguerre-Gaussian laser modes", Physical Review A, 45, 8189 (1992).

[9] T. Kuga, Y. Torii, N. Shiokawa, T. Hirano, Y. Shimizu, H. Sasada, "Novel Optical Trap of Atoms with a Doughnut Beam", Phys. Rev. Lett., 78, 4713 (1997).

[10] M. Padgett, R. Bowman, "Tweezers with a twist", Nat. Photonics, 5, 343 (2011).

[11] K. Dholakia, T. Čižmár, "Shaping the future of manipulation", Nat. Photonics, 5, 335 (2011).

[12] J. Wang, J. Y. Yang, I. M. Fazal, N. Ahmed, Y. Yan, H. Huang, Y. Ren, Y. Yue, S. Dolinar, M. Tur, A. E. Willner, "Terabit free-space data transmission employing orbital angular momentum multiplexing", Nat. Photonics, 6, 488 (2012).

[13] N. Bozinovic, Y. Yue, Y. Ren, M. Tur, P. Kristensen, H. Huang, A. E. Willner, S. Ramachandran, "Terabit-scale orbital angular momentum mode division multiplexing in fibers", Science, 340, 1545 (2013).

[14] G. Molina-Terriza, J. P. Torres, L. Torner, "Twisted photons", Nat. Phys., 3, 305 (2007).

[15] I. Heller, G. Sitters, O. D. Broekmans, G. Farge, C. Menges, W. Wende, S. W. Hell, E. J. G. Peterman, G. J. L. Wuite, "STED nanoscopy combined with optical tweezers reveals protein dynamics on densely covered DNA", Nat. Methods, 10, 910 (2013).

[16] T. Watanabe, Y. Iketaki, T. Omatsu, K. Yamamoto, M. Sakai, M. Fujii, "Two-point-separation in super-resolution fluorescence microscope based on up-conversion fluorescence depletion technique", Opt. Express, 11, 3271 (2003).

[17] M. Kamper, H. Ta, N. A. Jensen, S. W. Hell, S. Jakobs, "Near-infrared STED nanoscopy with an engineered bacterial phytochrome", Nat. Commun., 9, 4762 (2018).

[18] https://www.nobelprize.org/uploads/2018/06/advanced-chemistryprize2014.pdf

[19] N. B. Simpson, L. Allen, and M. J. Padgett, "Optical tweezers and optical spanners with LaguerreGaussian modes", J. Mod. Opt. 43, 24852491 (1996).

[20] R. M. Kerber, J. M. Fitzgerald, S. S. Oh, D. E. Reiter, and O. Hess, "Orbital angular momentum dichroism in nanoantennas", COMMUNICATIONS PHYSICS 1, 87(2018).

[21] L. C. Dávila Romero, A. R. Carter, M. Babiker, and D. L. Andrews, "Interaction of Laguerre-Gaussian light with liquid crystals", Proceedings of SPIE - The International Society for Optical Engineering. 5736. 10.1117/12.585295 (2005).

[22] L. A. Sordillo, S. Mamani, M. Sharonov, and R. R. Alfano, "The interaction of twisted Laguerre-Gaussian light with a GaAs photocathode to investigate photogenerated polarized electrons", Appl. Phys. Lett. 114, 041104 (2019).

[23] C. Hnatovsky, V. G. Shvedov, W. Krolikowski, and A. V. Rode, "Materials processing with a tightly focused femtosecond laser vortex pulse", Optics Letters Vol. 35, Issue 20, 3417-3419 (2010).

[24] K. Toyoda, K. Miyamoto, N. Aoki, R. Morita, and T. Omatsu, "Using Optical Vortex To Control the Chirality of Twisted Metal Nanostructures", Nano Lett., 12, 3645 (2012).

[25] S. Syubaev, A. Zhizhchenko, A. Kuchmizhak, A. Porfirev, E. Pustovalov, O. Vitrik, Y. Kulchin, S. Khonina, S. Kudryashov, "Direct laser printing of chiral plasmonic nanojets by vortex beams", OPTICS EXPRESS, 25, No. 9 10214 (2017).

[26] K. Lou, S.X. Qian, X. Wang, Y. Li, B. Gu, C. Tu, H. Wang, "Two-dimensional microstructures induced by femtosecond vector light fields on silicon", Opt. Express 20, 120 (2012).

[27] K.K. Anoop, R. Fittipaldi, A. Rubano, X. Wang, D. Paparo, A. Vecchione, L. Marrucci, R. Bruzzese and S. Amoruso, "Direct femtosecond laser ablation of copper with an optical vortex beam", J. App. Phys. 116, 113102 (2014).

[28] J. J. J. Nivas, H. Shutong, K. K. Anoop, A. Rubano, R. Fittipaldi, A. Vecchione, D. Paparo, L. Marrucci, R. Bruzzese, AND S. Amoruso, "Laser ablation of silicon induced by a femtosecond optical vortex beam", Optics Letters Vol. 40, No. 20 (2015).

[29] J. J. J Nivas, Sh. He, A. Rubano, A. Vecchione, D. Paparo, L. Marrucci, R. Bruzzese, and S. Amoruso, "Direct Femtosecond Laser Surface Structuring with Optical Vortex Beams Generated by a q-plate", Scientific Reports, vol. 5, 17929 (2015).

[30] M. G. Rahimian, F. Bouchard, H. Al-Khazraji, E. Karimi, P. B. Corkum, and V. R. Bhardwaj, "Polarization dependent nanostructuring of silicon with femtosecond vortex pulse" APL Photonics 2 (8) 086104 (2017).

[31] J.J.J. Nivas, H. Shutong, A. Rubano, A. Vecchione, D. Paparo, L. Marrucci, R. Bruzzese and S. Amoruso, "Surface Structuring with Polarization-Singular Femtosecond Laser Beams Generated by a q-plate", Sci. Rep. 7, 42142 (2017).

[32] M. Alameer, A. Jain, M. G. Rahimian, H. Larocque, P. B. Corkum, E. Karimi, and V. R. Bhardwaj, "Mapping complex polarization states of light on a solid", Optics Letters Vol. 43, 23, 5757-5760 (2018).

[33] A. Babazadeh, M. Erhard, F. Wang, M. Malik, R. Nouroozi, M. Krenn, and A. Zeilinger, "High-dimensional single-photon quantum gates: Concepts and experiments", Phys. Rev. Lett., 119(18):180510 (2017).

[34] M. Erhard, M. Malik, and A. Zeilinger, "A quantum router for high-dimensional entanglement", Quantum Sci. Technol., 2(1):014001 (2017).

[35] K. A. Forbes and D. L. Andrews, "Spin-orbit interactions and chiroptical effects engaging orbital angular momentum of twisted light in chiral and achiral media", PHYSICAL REVIEW A 99, 023837 (2019).

[36] V. Y. Bazhenov, M. S. Soskin, and M. V. Vasnetsov, "Screw dislocations in light wavefronts", J. Mod. Opt. 39, 985990 (1992).

[37] D.L. Andrews, L.C. Dávila Romero, M. Babiker, "On optical vortex interactions with chiral matter", Optics Communications, 237, 133139 (2004).

[38] P. Woźniak, I. De Leon, K. Höflich, G. Leuchs, AND P. Banzer, "Interaction of light carrying orbital angular momentum with a chiral dipolar scatterer", Optica, Vol. 6, No. 8 (2019).

[39] D. M. Rayner, A. Naumov, and P. B. Corkum, "Ultrashort pulse nonlinear optical absorption in transparent media", Opt. Exp., vol. 13, pp. 3208-3217, 2005.

[40] R. S. Taylor, C. Hnatovsky, E. Simova, D. M. Rayner, M. Mehandale, V. Bhardwaj, and P. B. Corkum, "Ultra-high resolution index of refraction profiles of femtosecond laser modified silica structures", Opt. Express, 11, 7, 775-781 (2003).

Chapter 2

Basics of Femtosecond Laser Interaction with Matter

Femtosecond laser pulses with moderate energies can have an extremely high peak power, and intensity that makes them effective candidates in material processing and precise laser structuring [1–4]. Understanding the basic physics of the interaction of such ultrashort laser pulses with matter enables one to develop new and more precise techniques to study and manipulate material properties for various applications.

This chapter presents the importance of femtosecond laser pulses in the field of laser-matter interaction as they overcome some limitations of a long-pulsed laser system for micro/nanoscale fabrication. It also introduces different mechanisms for energy absorption and deposition (resulting in a rapid build-up of free carriers and coupling with the lattice subsystem) in laser-irradiated material. An overview of Ti:Sapphire laser system that was used in our experiments along with my experimental setup used for micro/nano fabrication by structured femtosecond laser pulses is provided. Moreover, a brief review of the key experimental parameters in femtosecond laser structuring is presented.

2.1 Why Femtosecond Lasers?

Among all types of lasers used in laser material processing, femtosecond lasers have been widely used for micro and/or nanoscale fabrication as they overcome some limitations of long pulse laser systems.

Extremely high laser intensities ($10^{13} - 10^{14}$ W/cm^2) can be readily produced with fs pulses at moderate pulse energies. For instance, a laser pulse with a duration of 100 fs and pulse energy of 0.33 mJ, when focused to a diameter of 20 μm, yields a peak intensity of $10^{15} W/cm^2$. While a 100 J pulse would be required to acquire the same intensity from a 10 nanosecond laser pulse [5]. At high enough intensities, electrons absorb the light through nonlinear ionization processes (avalanche and multiphoton absorption) which leads to plasma formation. Then a considerable amount of laser energy is absorbed in the ablated plasma plume. Such a nonlinearity along with the ultrashort duration of fs

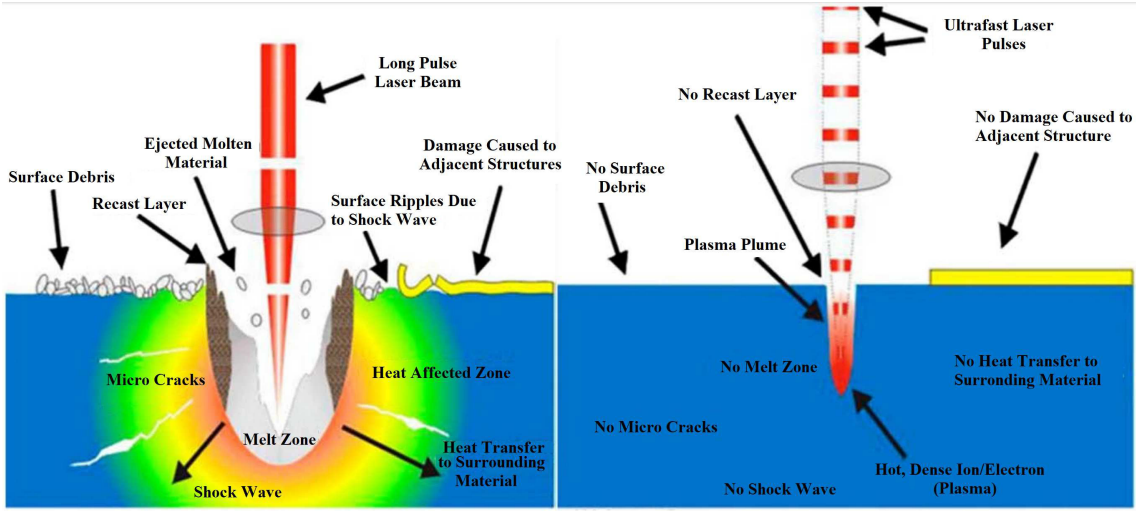

Figure 2.1: Long-pulse (ns) and ultrafast-pulse (fs) laser interaction with material [6] (the graphic is used with permission from Clark-MXR, Inc). The absence of thermal effects in fs ablation can lead to a less heat-affected zone, collateral damage, shockwaves, cracks, surface debris and unwanted ripple formation. This makes fs laser ablation a precise machining technique [7].

laser pulses lead to a localized interaction, i.e., confined in the focal volume of the laser with submicron precision. For long laser pulses, in contrast, the pulse intensity is not enough to substantially ionize the material. Therefore, the absorbed energy is used to break the bonds during the pulse not to generate a high density plasma. This will result in sputtering of the target surface, as shown in Fig. 2.1.

Moreover, the pulse duration of femtosecond lasers is shorter than the electron relaxation time (which is of the order of 1 ps) and also the duration of heat conduction (micro- to nanoseconds). Therefore, the energy deposition in the light-matter interaction process occurs within the pulse [8], i.e., faster than the speed at which atoms move in the air or vibrate within molecules, and before initiating any relaxation or thermalization processes [9]. It means any heat transfer from highly excited electrons to ions begins long after the pulse has left the material, from several hundred femtoseconds to a few picoseconds, depending on the material. Due to these non-equilibrium conditions, the situation is often described by a two-temperature model, where electron and lattice temperatures can be treated independently [10, 11].

In contrast, for long (pico- and nanosecond) pulses , the electron-lattice energy transfer takes place in the pico- and nanosecond timescale. Therefore, the electron and ion will be in thermal equilibrium and the lattice temperature increases during the pulse. This eventually leads to a thermal expansion and the formation of a large heat-affected zone (HAZ). This heat flow to regions outside the processing area leads to collateral damage, a large amount of molten material, vaporization, and micro cracks creation that causes permanent damage to the material. As material evaporates, plasma absorption may also occur resulting in shockwaves and may produce unwanted surface ripples or even damage

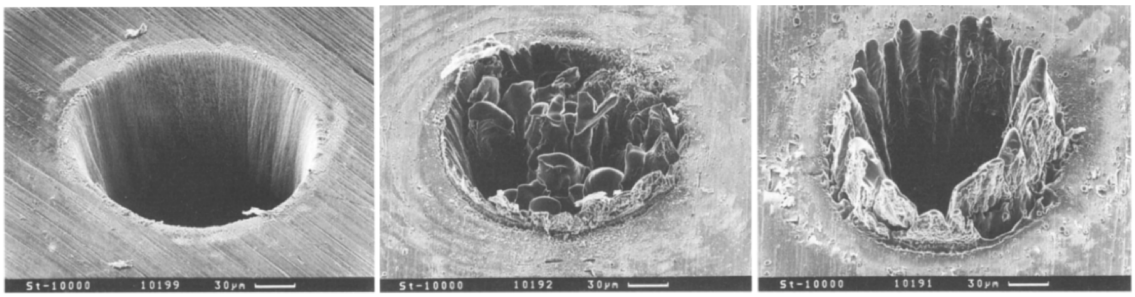

Figure 2.2: SEM images of a hole drilled in 100 μm thick steel foil at 780 nm with (left) 200 fs, 120 μJ, F=0.5 J/cm^2 laser pulses, (middle) 80 ps, 900 pJ, F=3.7 J/cm^2, and (right) 3.3 ns, 1 mJ, and F=4.2 J/cm^2 laser pulses [12].

to the nearby structures and an improper structuring.

Another key advantage of material processing with fs pulses is that the energy deposition in the material is relatively small [1] and also temporally separated from the material removal. Therefore, there is no interaction between the ejected material and the laser pulse. As a result, an improvement in the localization of energy deposition, a reduced HAZ with no shockwaves, and a precise ablation and/or modification is achieved. It is also notable that material processing with fs laser pulses does not require defect electrons to initiate the absorption process, i. e., it is considered a deterministic process.

All these unique features of femtosecond laser pulses enable minimal mechanical and thermal collateral damages resulting in a clean and highly precise patterning, and ablation process [1, 5]. As a result, the fabrication of geometrically complex structures in three dimensions is possible. Figure 2.2 shows advantages of femtosecond laser pulses over nano- and picosecond pulses for precise material processing [12]. It demonstrates that due to the absence of thermal losses in the femtosecond regime, holes in metal targets can be drilled with much lower laser fluences.

2.2 Physical Processes Involved in Femtosecond Laser-Matter Interaction

As I briefly discussed earlier, femtosecond laser pulses have shown significant impact on basic research, e. g., fundamental physical processes that occur in solids in ultrashort time scales, as well as industrial applications through material modification/ablation in terms of spatial precision. In general, the basic phenomena during these processes are excitations that take place in femtosecond timescales (during the presence of the laser pulse), melting in the picosecond regime, and material removal that takes up to several nanoseconds. Here a brief review of the main mechanisms during the femtosecond light-matter interaction is

[1] This is because they require less energy to produce any optical breakdown in the material.

presented. Figure 2.3 [13, 14] also shows detailed-processes that occur after irradiation of the laser pulse on material.

The laser beam energy, irradiated on the surface of a solid, can be absorbed by free carriers and/or electrons in the valance band, depending on the material. In metals, for example, free carriers (i.e. electrons in the conduction band) absorb photons and acquire energy while in semiconductors and dielectrics electrons are excited from the valence bands to the conduction bands. This energy absorption occurs in the timescale of the laser pulse duration. The energy absorption will be followed by energy transfer from electrons to phonon. This is when lattice heating takes place. When the excitation is weak, the energy distribution of the laser-excited electrons is nonthermal (it is explained below), and the energy transfer from the electrons to the lattice is delayed [13]. In contrast, a strong excitation causes a rapid thermalization, and consequently, melting and ablation will occur.

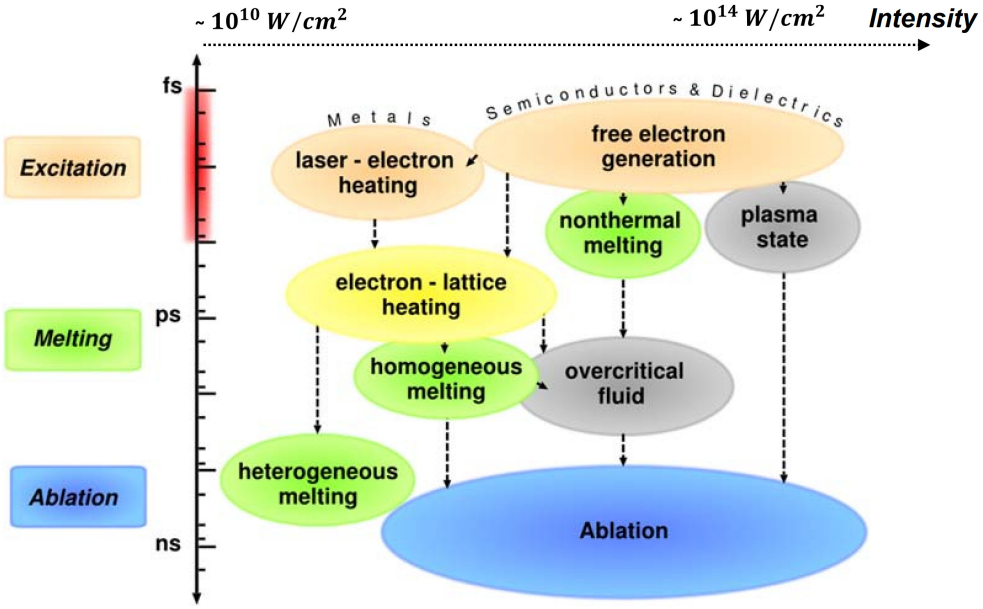

Figure 2.3: Typical timescales and intensity ranges of the processes involved in the femtosecond pulses (about 100 fs) interaction with solid [13, 14]. Excitation takes place duration of the laser pulse (in the range of femtoseconds). The timescale of melting in the picosecond regime, however, it may vary for different processes. Material removal (ablation) lasts up to the nanosecond regime.

Sufficiently high laser intensities (10^{14} W/cm^2 or higher) can fully ionize the solid material and produce a hot plasma. In this case, a direct transition from the solid to the plasma state takes place. In the case of covalent semiconductors, excitation by femtosecond pulses with intensities around 10^{12} W/cm^2 leads to a rapid transition to the liquid state. The excited electron-hole plasma makes the lattice unstable and disordered, on a time scale faster than the lattice heating time($\sim$ 100 fs) [15]. In fact, irradiation of high-fluence femtosecond laser pulses causes an extreme non-equilibrium state that lasts for a few picoseconds and can be characterized by the existence of extremely hot electrons. Such

high temperature is a result of absorbing a large number of photons from the laser pulse and thermalizing through electron-electron collisions. The lattice, on the other hand, remains at the room temperature. This is because the time scale needed for laser excitation and electron thermalization are considerably shorter than lattice heating via electron-phonon interaction. However, due to rapid variations in the effective potential acting on the ions at room temperature, they are still subjected to tremendous forces. As a result of such rapid change in the potential, the ions begin to move. For high enough forces, material become disordered or in other words molten in an ultrafast time scale. This process is often known as nonthermal melting. In fact, nonthermal melting happens when atoms are still at room temperature or considerably below the melting point. Ultrafast melting within less than one picosecond was demonstrated by Shank *et al.* [16].

At low energy densities, the heating rate in ions is slow allowing a slow melting process. which is limited by the speed of sound on a timescale in the range of $\sim$ 100 ps. In this case, lattice temperature reaches the material's melting point (T_m), and the heterogeneous melting process begins. The process is initiated on defects on the material's surface, liquid nucleation sites, and grain boundaries [17], where the energy threshold for melting can be overcome. A melt front during heterogeneous melting propagates from the surface into the substance, with speed limited by the speed of sound. It indicates that irradiation of large laser intensities with heating rates of several tens or hundreds of Kelvin per picosecond leads to large superheating. However, upon irradiation of ultrashort pulse laser at large laser fluences, extremely high heating rates (10^{14} K/s and higher) are achievable. Such strong superheating (temperatures T $> 1.5\ T_m$) is sufficient to initiate rapid homogeneous nucleation [18] of the liquid phase inside the superheated crystal. In this situation, the melting threshold fluence exceeds, and the crystal stability and structure break in the whole overheated region within a few picoseconds. This time scale is determined by the time required for electron-lattice equilibration, making this process significantly faster than heterogeneous melting. In fact, the contributions of homogeneous and heterogeneous melting in the thermal melting process depend on the laser fluence, pulse duration, and electron-phonon coupling strength. Homogeneous nucleation at a high rate will eventually lead to a rapid transition to a vapor phase similar to an explosion. This process is known as phase explosion or explosive boiling. At very high heating rates, when the material is in a non-equilibrium state of high pressure and high temperature, rapid melting and transition to an overcritical fluid is possible. The final state will be the hydrodynamic expansion of the heated material and ablation (material removal). Material expansion of the complete heated layer occurs on a timescale $\sim$100 ps. This means, although femtosecond laser pulses interact with the material on a fs timescale, the actual ablation process is much slower. Expansion and ablation of the laser-excited material are in a timescale within the nanosecond regime [19].

2.2.1 Excitation

The first step in material modification under laser irradiation is laser energy absorption. The energy absorption involves excitation of (a) free carriers in metals (electrons in the conduction band absorb photons and obtain higher energy) or (b) electrons from valance

bands in semiconductors and dielectrics (resulting in transitions to the conduction band). In all cases, the energy deposition takes place within the laser pulse duration. When the electrons absorb the photon's energy, they undergo a transition either through a linear absorption, if photon energy exceeds the bandgap, or a nonlinear absorption, when the band gap is larger than the photon energy.

Several parameters, such as wavelength and laser intensity, play a crucial role in energy absorption mechanisms. For example, non-UV wavelengths cause different absorption mechanisms in absorbing materials such as metals and semiconductors than transparent dielectric materials such as glasses and plastics. In addition to the pulse energy and the wavelength, the absorption mechanism is also governed by the material bandgap. For instance, in transparent materials, with large bangaps, the absorption is a nonlinear process and causes laser-induced optical breakdown [5]. The reason is that the ionisation occurs at intensities in the range of 10^{13}-10^{14} W/cm^2, with a strong nonlinear dependence on intensity. In this case, a significant amount of the laser energy is transferred to the material and produces a large number of ionized electrons ($\sim 10^{21}$ cm^{-3} for femtosecond laser pulses of wavelengths in the visible and near IR), and consequently, a permanent material modification by transferring the energy to the lattice. In fact, in this process, a strong tightly-focused fs laser pulse transforms a transparent material into an absorbing plasma. Further energy absorption by the generated plasma causes heating and subsequent irreversible damage to the material. The nonlinear processes that may cause breakdown are multiphoton absorption and formation of an electron cascade or avalanche ionization.

In case of the interaction of fs-laser pulses with semiconductors, the peak of the electric fields are orders of magnitude larger than the Coulomb fields ($10^9 V/m$) that bind electrons to atoms [20]. As a result, the nonlinear absorption in the form of two-photon or higher-order multiphoton electronic transitions is dominant. For example, the interaction of 800 nm laser pulses with silicon (bandgap of 1.1 eV) will be primarily a linear absorption process. However, femtosecond pulses (intensity of 10^{13}-10^{14}W/cm^2) have energies high enough to make the two-photon absorption significantly probable.

Multiphoton Ionization (MPI) is a nonlinear absorption process in which the valance electrons can be lifted across the bandgap to the conduction band by the simultaneous absorption of two or more photons. This nonlinear absorption occurs when fs laser pulses at high laser intensities (greater than 10^9 W/cm^2) and high laser frequencies (but not high enough for single photon absorption) interact with the target. In other words, MPI is probable if the energy of the absorbed photons exceeds the bandgap energy (E_g) of the material, $n\hbar\omega \geq E_g$, where ω is the frequency of the laser photons and $\hbar$ is Planck's constant. Therefore, in dielectric materials, multiphoton absorption is dominant because, generally, their bandgap is much larger than the photon energy. For example, the photon energy of 800 nm femtosecond laser pulses is calculated to be 1.55 eV. Therefore, a material with an ionization potential of 5.47 eV (e.g., diamond) requires to absorb at least 4 photons. The probability of multiphoton absorption is proportional to the laser intensity,

$$P^{(n)} = \sigma_n \, I^n \tag{2.1}$$

where n is the number of photons, σ_n is the absorption/ionization cross-section for n photons and I is the laser intensity.

For strong laser fields and comparatively low laser frequencies, this process transfers to tunneling ionization. In the tunneling ionization, the strong electric field of the incident laser beam is sufficient to lower the Coulomb potential barrier of the bound electrons. The electron can then escape or tunnel through this reduced potential well and ionize the atom.

The two different ionization regimes are differentiated by a parameter, known as the Keldysh parameter [21], defined as

$$\gamma = \frac{\omega}{e}\sqrt{\frac{m\ c\ \varepsilon_0\ E_g}{I}} \tag{2.2}$$

here ω is the laser frequency, e and m are the charge and mass of an electron, respectively, I is the laser intensity, E_g is the bandgap energy of the material, ε_0 is the permittivity of the free space, and c is the speed of light in vacuum. Although, under some conditions, this parameter is not suitable and does not properly predict the ionization mechanism [22].

- For $\gamma \ll 1$, tunneling ionization takes place.
- In the case of $\gamma \gg 1$, the electron is ionized from atoms by multiphoton ionization.
- There is always an intermediate regime ($\gamma \approx 1$) in which both mechanisms are probable.

Avalanche Ionization is another important photoionization mechanism that occurs when high intensity laser pulses interact with matter. The two key mechanisms that explains the avalanche ionization are "inverse bremsstrahlung"and "impact ionization".When laser pulse irradiates into solid materials, the quasi-free electron oscillates with the electromagnetic field generated by the laser light and collides with nearby atoms/molecules, absorbing or losing energy (inverse bremsstrahlung effect).

At high intensities, the energy absorbed by the electron during the collisions is more than what it loses. By acquiring more energy, the ionization threshold of the material is surpassed, and second-generation quasi-free electron is created (impact ionization). In other words, the avalanche ionization is considered a secondary ionization process as it requires a population of free carriers to be present in the conduction band and seed the exponential growth of free carriers. These seed electrons can be produced by thermally excited impurities or defect states or directly from multiphoton and/or tunneling ionization [5]. When electrons become excited, their energy is transferred to phonons (lattice vibrations) and bound electrons by collisions and thermalization[2]. In fact, electron-electron collisions lead to thermalization (on a timescale of up to several hundreds of femtoseconds),

[2]The energy transfer from electrons to the lattice is often described by a two-temperature model. The two-temperature model assumes that both electrons and phonons energy distributions are thermal distributions characterized by the electron temperature and the lattice temperature, respectively.However, the two-temperature model is not valid when the timescale is shorter than the electronic thermalization time

whereas electron-phonon collisions cause relaxation between electrons and phonons (on a timescale from several hundred femtoseconds to a few picoseconds depending on the material) [23]. The maximum collision rate occurs when the electrons are at Fermi temperature, during which the electron energy reaches the ionization potential and the solid turns into a plasma. At this point, the collision rate is equal to the plasma frequency (ω_p). This process promotes more electrons to the conduction band as long as the seed electrons gain at least twice the bandgap energy from the laser field [24]. A newly freed electron (seed electron) collides with another valance electron and elevates it to the conduction band. Both electrons gain sufficiently high kinetic energy to force other bound electrons to overcome the ionization potential. This process, known as electron impact ionization, can double the number of free electrons and will be repeated for other excited electrons. Therefore, the energy of valence electrons increases and eventually exceeds the minimum of the conduction band energy. When a chain of impact ionization occurs, the resultant phenomenon is referred to as an electron avalanche ionization.

Plasma Formation occurs when an intense laser pulse is focused onto a solid such that the energy density surpasses the ablation threshold of the material. The leading edge of the pulse ionizes the material and forms a plasma, while the trailing edge of the pulse interacts with the generated plasma. As the electron equilibration time for a plasma density of $10^{23}\mathrm{cm}^{-3}$ is shorter than the pulse duration, an equilibrium is reached by the plasma. Therefore, the electron energy distribution follows the laser intensity profile for the remainder of the pulse [24]. The plasma oscillates at the frequency of the electrons that form it. Once the frequency of the plasma reaches the frequency of the incident pulse, i.e., a critical plasma ($N_c \sim 10^{21} cm^{-3}$) condition is satisfied, and a significant amount of the laser beam will be absorbed by the plasma. Above the critical plasma frequency, the laser pulse is mostly reflected and slightly absorbed. However, below the critical plasma frequency, the laser beam propagates through the plasma with a minor attenuation.

As shown in equation 2.3, the plasma frequency depends on the electron density (N), the charge of the electron (e), the electric permittivity (ε), and the effective mass of the electron (m).

$$\omega_p = \sqrt{\frac{Ne^2}{\varepsilon\, m}} \tag{2.3}$$

This equation states that overdense plasmas (N greater than N_c) oscillate at frequencies higher than the critical frequency while underdense plasmas (N lower than the N_c) oscillate below the critical value.

(as the electron temperature looses its meaning [10].Since the electrons and lattice are not in equilibrium, they can be studied in two separate but coupled heat transport equations. This process depends on the material and happens in a timescale from several hundred femtoseconds to a few picoseconds. For most metals, thermalization time is on the order of $10^{-12} - 10^{-10} s$, whereas in non-metals it can be as long as $10^{-6} s$ [25], and in polymers and dielectric materials, it is on the slower end of this range.

2.2.2 Melting and Resolidification

For low laser fluences (below the melting threshold), localized laser heating can cause large temperature gradients and rapid self-quenching of the material, leading to a highly non-equilibrium situation [26]. The result would induce thermal stresses accompanied by acoustic waves, warping or cracking [27]. However, for fluences above the melting threshold, energy transfer from highly excited electrons to the lattice occurs that results in melting process.

As mentioned earlier, there are two types of melting, thermal and nonthermal. When the pulse energy is large enough to excite electrons in a way they can exceed 10%15% of valence electrons and achieve a critical density of conduction band electrons ($10^{22} cm^{-3}$), an atomic disordering is induced [16]. This situation results in an ultrafast phase transition to a liquid state. This process is known as nonthermal melting because it is originated from the interaction of hot electrons with cold (initially room-temperature) atomic nuclei that are not in thermal equilibrium [28]. In thermal melting, in the absence of any sudden disordering of the lattice, electron-phonon coupling leads to a heat flow from excited electrons to the lattice. Over several picosecond [3], therefore, they both reach the same temperature that is sufficient for melting. Afterwards, a thin layer near the material surface faces a transition to a liquid phase.

After thermalization, the spatial distribution of the laser energy is identified by the temperature profile; *vis-a-vis* profile of the optical absorption. Therefore, one anticipates a high temperature gradient in highly absorbing material. Such a thermal gradient causes a thermal diffusion into the solid bulk; therefore, heat is pushed away from the molten layer. This results in cooling and solidification of the molten material that takes place on a timescale of 10^{-11}-10^{-10} s [29]. When energy is deposited into the material on a time scale much faster than the thermal diffusion time, ablation of the material surface occurs resulting in permanent changes to the bulk structure. In the following, we review the ablation process.

2.2.3 Ablation

Laser ablation is the removal of material from a target's surface. In this process, absorption of the laser energy by the material eventually causes boiling of the molten surface. Ablation takes place in timescales of the order of hundreds of nanoseconds. There are several physical mechanisms involved in the ablation process, such as spallation [30], phase expansion (explosive boiling) [32], Coulomb explosion [33], material ejection, and evaporation [34]. Material properties and defects, surface morphology, as well as laser parameters such as wavelength, fluence, and pulse duration are essential to determine which ablation mechanism is dominant. For instance, in single pulse regime, typical threshold fluences required to ablate metals are between 1 and 10 J/cm^2 and to ablate insulators are between 0.5 and 2 J/cm^2 [25]. Ablation thresholds may decrease in the multiple-pulse regime.

[3] This process takes place over several picoseconds [31]. However, it has been shown that depending on the laser fluence, thermal melting can occur in a timescale shorter than 1 ps [18].

Spallation is the mechanism of material ejection that occurs when the laser fluence is just above the ablation threshold. For example, Fang *et al.* [35] reported a fluence of 0.1-0.25 J/cm^2 required for a metal ablation to occur. When the laser heating takes place in a time interval shorter than the time needed for the material expansion, laser ablation occurs under mechanical stress confinement. The laser heating in constant volume conditions leads to the generation of strong compressive stresses. The resultant mechanical action ejects a molten layer/droplets from the material. This material ejection mechanism is known as spallation [36]. The final shape of the surface structure generated in this process is governed by two factors: the resistance of the colder periphery of the laser irradiated spot to the ejection of spalled layers, and the rapid solidification of the transient molten material [37]. In laser fluences above the spallation threshold, the spalled layer gradually decreases until it vanishes, which leads to the phase explosion [38].

Phase Explosion and Thermal Evaporation happens when the laser fluence increases (0.35-1.0 J/cm^2) [35]. In this condition, the thickness of the spalled layer decreases and eventually vanishes [39]. For example, the central part of a laser pulse with a Gaussian intensity profile may cause the phase explosion mechanism while its outer region can simultaneously induce spallation. In the phase explosion, the molten material changes its phase to a liquid-gas metastable state. Subsequently, homogeneous nucleation of gas bubbles occurs that will lead to the formation of a heterogeneous phase of gas and liquid droplets. At a high enough excitation fluence, the surface layer of the material can become atomized entirely, and material removal proceeds by the vaporization process. Condensation of vaporized atoms as well as decomposition of ejected liquid layers or a porous foam generated by the phase explosion can eventually form nanoparticles.

Coulomb Explosion is an ion emission process that may occur during the ablation. This process typically takes place at high intensities where plasma formation and ablation occurs.

In this process, after the material absorbs the laser pulse energy, the excited electrons are ejected from the target surface. The electron ejection forms positive charges on the surface. The resultant charge separation between the ejected electrons and the ionized atoms generates a strong electric field resulting in repulsive forces between the ions. Once the repulsive force passes the binding forces of the ions in the lattice, a strong ion emission pulls them out of the target. It, in fact, leads to the removal of the first few monolayers (several nanometers) of the lattice within the skin depth of the material [40].

2.3 Laser System

Among all types of femtosecond lasers, Ti:Sapphire regenerative amplifier laser system is one of the most widely-used ones because of its broad continuous wavelength tuning range. This allows the production and amplification of optical pulses with extremely short duration. This chapter presents a brief introduction to the operating principle of a Ti:Sapphire

femtosecond laser, including its oscillator and amplifier. Besides, the autocorrelation technique to measure ultrashort pulses is explained.

2.3.1 Ti:Sapphire Crystal

The gain medium is a Ti:Sapphire crystal produced by introducing Ti_2O_3 into a melt of Al_2O_3, where Ti^{3+} (titanium) ions replace a small percentage of the Al^{3+} (aluminum) ions [41]. Absorption transitions occur over a wide range of wavelengths from 400 nm to 600 nm, and fluorescence transitions occur from wavelengths as short as 600 nm to wavelengths greater than 1000 nm, as shown in Fig 2.4. However, lasing is only possible at wavelengths longer than 670 nm because of the overlap between the long wavelengths of the absorption band and the short wavelengths of the fluorescence spectrum. Ti:Sapphire crystal has an emission spectrum that can support pulses down to $\sim 6fs$ [5]. A Ti:Sapphire laser is pumped with a frequency-doubled Nd:YAG laser (530 nm) to excite the crystal and initiate the lasing process.

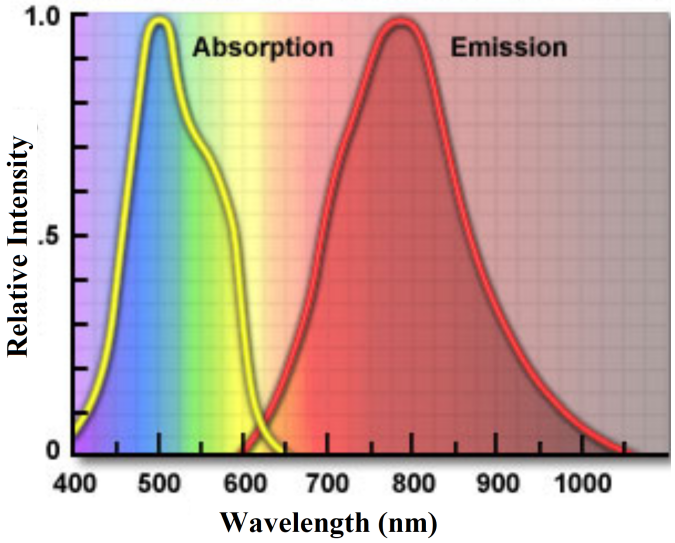

Figure 2.4: Absorption and emission spectra of Ti:Sapphire crystal [42].

2.3.2 Oscillator

A typical laser oscillator system contains the Ti:Sapphire rod and several optics, including pump beam mirrors, focusing mirrors, an output coupler, dispersion control prisms, a slit for wavelength selection, and tuning elements, as shown in Fig 2.5.

The presence of several optical elements inside the laser cavity produces a positive group velocity dispersion (GVD), i.e., shorter wavelengths propagate slower than longer wavelengths. This phenomenon causes an unwanted pulse broadening. Several techniques have been developed, employing dispersive materials, to compensate for such broadening.

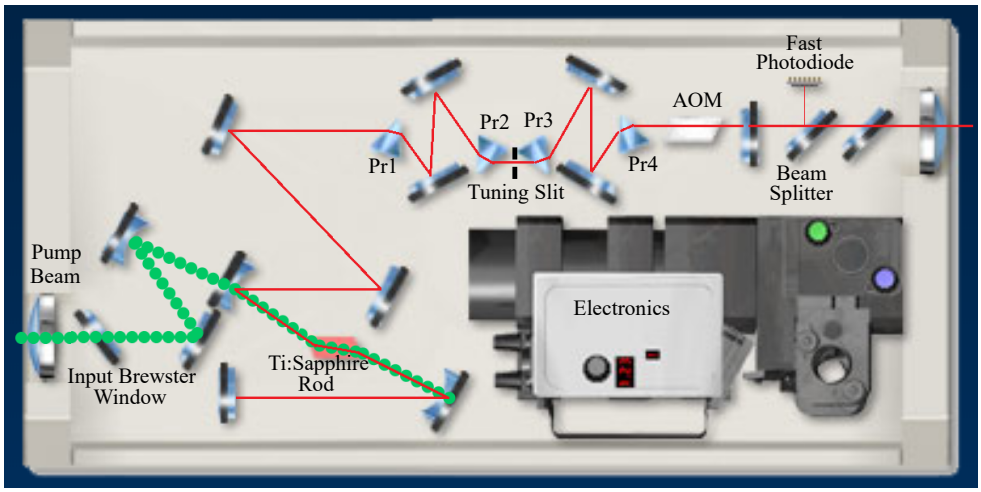

Figure 2.5: Basic layout of Ti:Sapphire mode-locked oscillator [43].

Studies of the dispersion properties of optical elements such as prisms and gratings in the 1970s 1980s introduced a valuable approach to shorten the laser pulses and develop femtosecond lasers. Using a prism sequence [44] is one way to obtain stable short output pulses. This sequence spatially expands the wavelengths and produces a negative group velocity dispersion (GVD) inside the laser cavity. In fact, the first prism spatially disperses the pulse such that the red components of the pulse travel through more material in the second prism than the blue components. Consequently, shorter wavelengths travel in a shorter time. By placing the second prism, the spatial offset is compensated, and the pulse retraces its path through the prism [45]. Changing the position of prisms varies the amount of the prism material in the beam path, consequently changing the GVD and the pulse width. Several prism arrangements could be considered. Figure 2.6 demonstrates one of the most well-known arrangements, which exploits two prism sets with an incident Brewster angle at each surface [46].

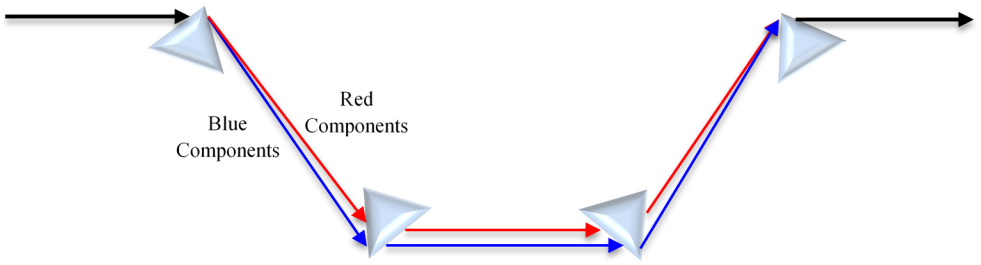

Figure 2.6: A schematic showing a prism arrangement with an incident Brewster angle at each surface. This combination is used to compensate the dispersion inside the laser cavity.

Another essential element inside the cavity is a variable slit located in the path of the dispersed beam, as shown in Fig 2.5. By changing the position of the slit in the vertical

plane, it is possible to tune the output wavelength. The bandwidth of the output pulse can also be varied by changing the width of the slit.

Using prism and grating arrays allow us to control the pulse duration and mode-locking status of the femtosecond laser. However, other techniques are also required to improve the laser power.

Mode-locking

In general, laser emission has a finite spectral bandwidth of $\Delta\nu$ due to the finite linewidth of the laser transition. When the gain bandwidth ($\Delta\nu$) is larger than the mode spacing of $c/2L$ (where c is the speed of light and L is the optical length of the laser cavity), then laser oscillations can take place at several longitudinal modes, ν_m. These modes are separated by a mode-spacing of $\delta\nu$, as presented in Fig 2.7.

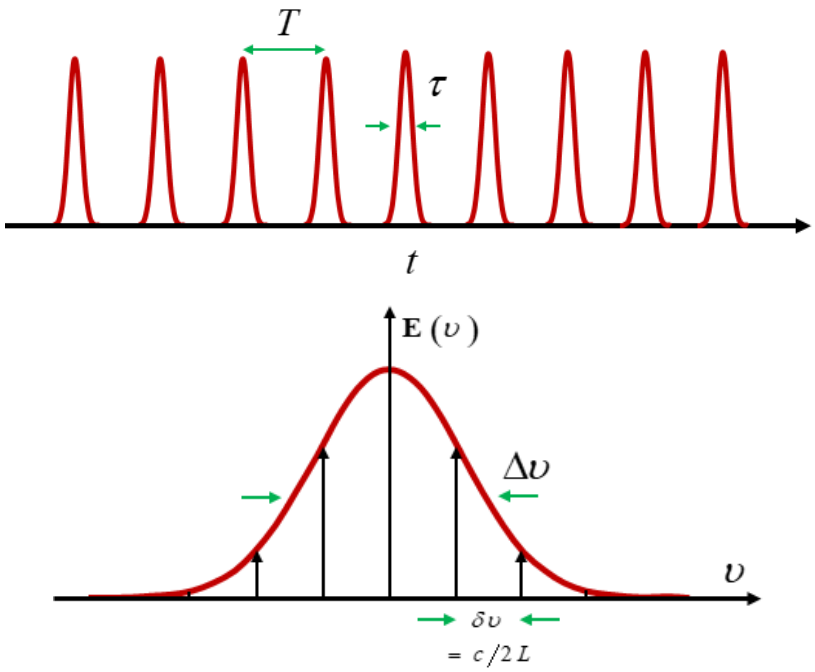

Figure 2.7: Basics of mode-locking. (Upper panel) the laser output representing the modes that are forced to have an equal phase. (Lower panel) longitudinal cavity modes separated by the frequency spacing $\delta\nu = c/2L$. $\Delta\nu$, τ, and T are referred to as the bandwidth of the output, duration of the pulse, and pulse repetition rate, respectively.

With no control on the laser spectrum, each mode oscillates independently, and their amplitudes and phases vary randomly with time. The resultant interference between the modes causes an incoherent laser output and fluctuations in the output intensity. However, it is possible to manipulate phases of the modes to obtain well-defined, perfect ultrashort pulses. To achieve this goal, an active medium with a broad gain bandwidth, and hence a multimode lasing regime is required. The multimode lasing is achievable by exploiting

a mode-locking technique [47]. A laser is said to be mode-locked when the phases of electromagnetic waves of all oscillating modes (longitudinal modes) are forced to maintain equal frequency spacing with a fixed phase relationship to each other. As a result, there will be constructive interference between the modes at a specific moment and destructive interference at any other time. The resultant output will appear as a pulse with a duration of τ, determined by the entire spectral bandwidth. The output pulse propagates at the group velocity corresponding to the central frequency of the pulse. Due to the interference, emitted energy from the modes is concentrated in a single pulse with a period of $T = c/2L$. The temporal profile is then the Fourier transform of the spectral profile.

A train of mode-locked ultrashort pulses can be generated using a variety of approaches. The most common techniques are categorized into two regimes; active [48] and passive mode-locking [49], as schematically shown in Fig 2.8.

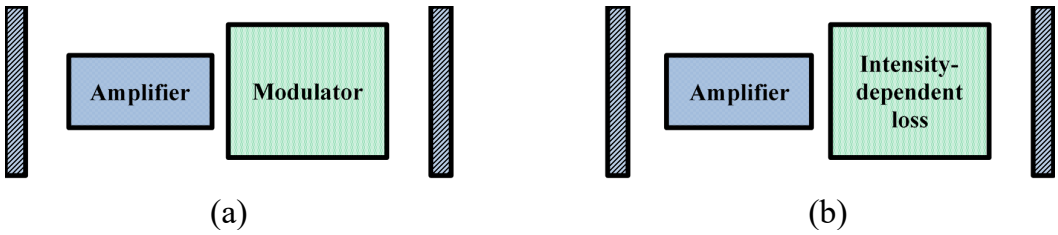

Figure 2.8: Schematic of (a) active and (b) passive mode-locking techniques [50].

- **Active mode-locking**: In this approach, an externally driven signal matching the cavity round trip time modulates the radiation in the laser cavity. The modulator is often either an electro-optic modulator (EOM) or acousto-optic modulator (AOM). In AOM, a time-varying amplitude (loss) modulation, referred to as AM mode-locking, takes place while EOM produces a time-varying phase change, often referred to as FM mode-locking.

- **Passive mode-locking**: In this technique, a nonlinear medium such as a saturable absorber is inserted into the cavity. Due to the nonlinear effect in the medium, intense pulses are transmitted while weak pulses are absorbed by the medium. Therefore, laser radiation itself generates a modulation. This modulation is thus automatically synchronized to the cavity round-trip frequency and requires no external signal.

  Kerr lens mode-locking (KLM) [51], also referred to as self-mode-locking, is one of the most important passive mode-locking methods. This technique is the most used method where femtosecond laser pulses shorter than 100 fs is required [52]. In the Kerr effect, the pulse intensity causes a refractive index change along the optical path. Due to the spatial intensity distribution of the laser pulse, this effect is more significant in the center of the beam than the side. It causes the nonlinear crystal to behave as a lens that leads to a strong self-focusing effect. The high intensity region of the beam incident onto the Kerr lens is then focused through an aperture, placed after the Kerr lens, and results in an ultra-short intense pulse.

The Ti:Sapphire oscillator (Tsunami) that I worked with to perform my experiments was an AOM mode-locked oscillator. In the following, a brief introduction to the acousto-optic modulation is presented.

Acousto-optic Modulation

As mentioned, acousto-optic modulation is the most employed approach to achieve active mode-locking. An acousto-optic modulator consists of a crystalline medium such as quartz with polished surfaces and a piezoelectric transducer attached to one surface. A radio frequency (RF) signal source drives the transducer to oscillate. The transducer's vibration is then transferred to the optical medium and creates acoustic waves. The frequency of acoustic waves correspond to half the cavity round-trip frequency $c/2L$ [50] (the laser repetition rate) or twice the RF frequency. The sound wave generation can also be explained as a result of moving periodic planes of expansion and compression in the material which is accompanied by local changes in the material refractive index . This periodic change of the refractive index, traveling at the sound velocity in the medium, acts as a phase grating with a periodicity equal to the acoustic wavelength and an amplitude proportional to the sound amplitude [53]. A beam of light passes through the material (refractive index grating), interacts with the traveling acoustic waves and experiences Bragg diffraction.

Once the incoming light beam interacts with this grating, a portion of it is diffracted and phase shifted and an interference pattern similar to that in Bragg diffraction occurs. Some properties of the light exiting the AOM can be listed as:

(a) The acoustic wave resonance of the transducer can be controlled by the thickness of the transducer crystal. The transducer can be made very thin if it is used to launch an acoustic wave into a Bragg cell to have the three lowest diffraction orders (such as a quartz block).

(b) The frequency of the diffracted beam will be Doppler-shifted by an amount equal to the acoustic frequency [54].

(c) For acoustic waves of sufficiently high power, most of the light incident on the acousto-optic modulator can be diffracted and therefore deflected from its incident direction.

(d) The diffracted beam experiences a frequency shift by an amount equal to the frequency of the sound wave.

2.3.3 Chirped-Pulse and Regenerative Amplification

One key advantage of the sapphire crystal is its resistivity to thermally induced damage. This capability makes it a preferred option to be optically pumped at very high average powers. However, due to the self-focusing effect, high peak powers coming directly from amplified femtosecond pulses cause permanent damage to the crystal. This issue can be

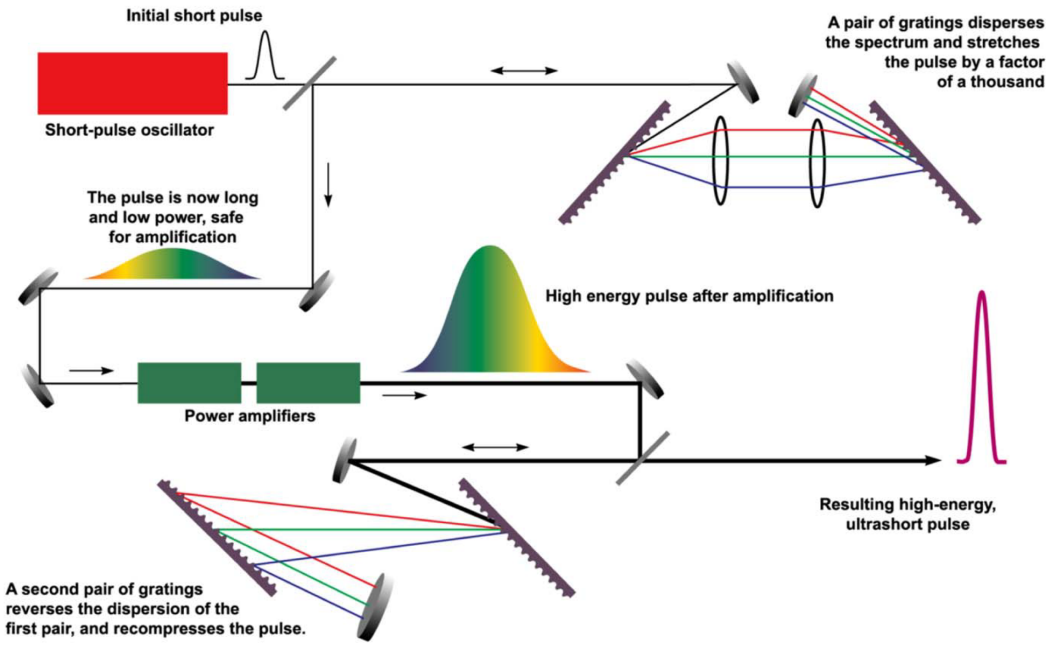

Figure 2.9: Schematic of chirped pulse amplification. This process enables generation of ultrafast laser pulse and consists of beam stretching, amplifying, and compressing [56].

resolved using a technique known as chirped-pulse amplification (CPA) [55] that consists of three steps: pulse spreading, amplification, and pulse compression (Fig. 2.9).

In CPA, laser pulses coming from Ti:Sapphire oscillator operating in a mode-locked regime are temporally stretched. Frequencies in the pulse disperse (chirped), i.e., they become extended from low to high values for a positively chirped pulse and from high to low frequencies for a negatively chirped pulse. The stretching process reduces the peak power while the fluence remains unchanged. This prevents the optics inside the amplifier from being damaged. In the next step, stretched pulses are amplified using a pump laser that excites the crystal before the stretched pulse arrives. The amplified pulse is then compressed. Through the CPA process, higher repetition rates, higher powers, and shorter pulse lengths are achievable. As shown in Fig. 2.9, such a femtosecond laser system consists of an oscillator operating in a mode-locked regime that provides the seed pulse, a stretcher, an amplifier, and a compressor.

In order to produce pulses as short as $\sim 50fs$ with high energy (up to joules), a widely-used technique known as "regenerative amplification" [57] is used. In this technique, the pulse is trapped in the laser cavity to be amplified. Trapping the pulse and releasing it is achieved by exploiting a Pockels cell (as a pulse picker) and a polarizer. The Pockels cell consists of a birefringent crystal that can change the polarization of a traveling laser field by applying a high voltage on it. In general, a regenerative amplification can be explained by three operating phases [45]:

(a) pump phase when the voltage applied to Pockels cell is zero, and the laser action is

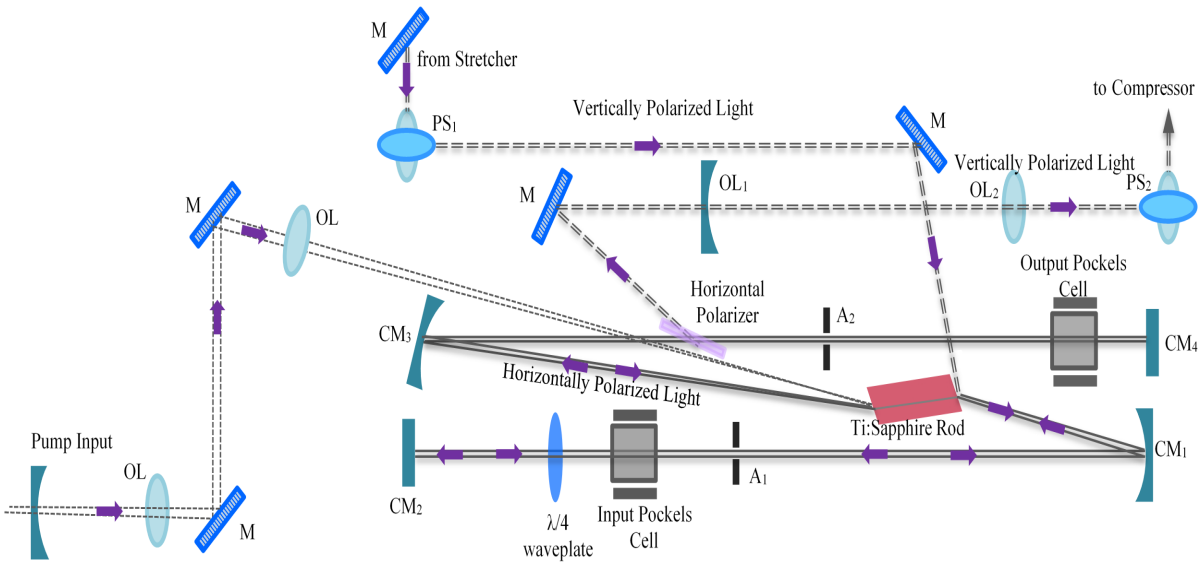

Figure 2.10: Regenerative amplifier optical components. The element are as follows, PS1 and PS2: polarization rotating periscope, OL1 and OL2: negative and positive lenses combination to make an expanding telescope (to reduce the beam intensity in the compressor), CM: cavity mirror (CM1, for example, directs the pulses to the input Pockels cell), A1 and A2: apertures, $\lambda/4$: quarter wave plate, and M: mirror.

prevented by the quarter-wave plate.

(b) amplification phase, when Pockels cell is switched to $\lambda/4$ retardation.

(c) cavity dump phase, when the applied voltage to the Pockels cell is zero (or is switched to $\lambda/2$ retardation).

Figure 2.10 shows a schematic of a typical regenerative amplifier.

2.4 Experimental Setup

Laser structuring using a femtosecond laser has become a widely-used technique for micro/nanostructuring of materials. In contrast to other techniques such as lithography and replica molding, it does not require multiple sample preparation steps and can modify material properties in 3D.

The laser system that I worked with to perform my experiments includes a mode-locked Ti:sapphire oscillator (Tsunami, Spectra-Physics) capable of producing $\sim$ 30 fs pulses with the pulse energy of 5 nJ at a central wavelength of 800 nm and repetition rate of 76 MHz. A 5 W Nd:YVO4 diode solid-state laser (Millenia, Spectra-Physics, 532 nm) was used to

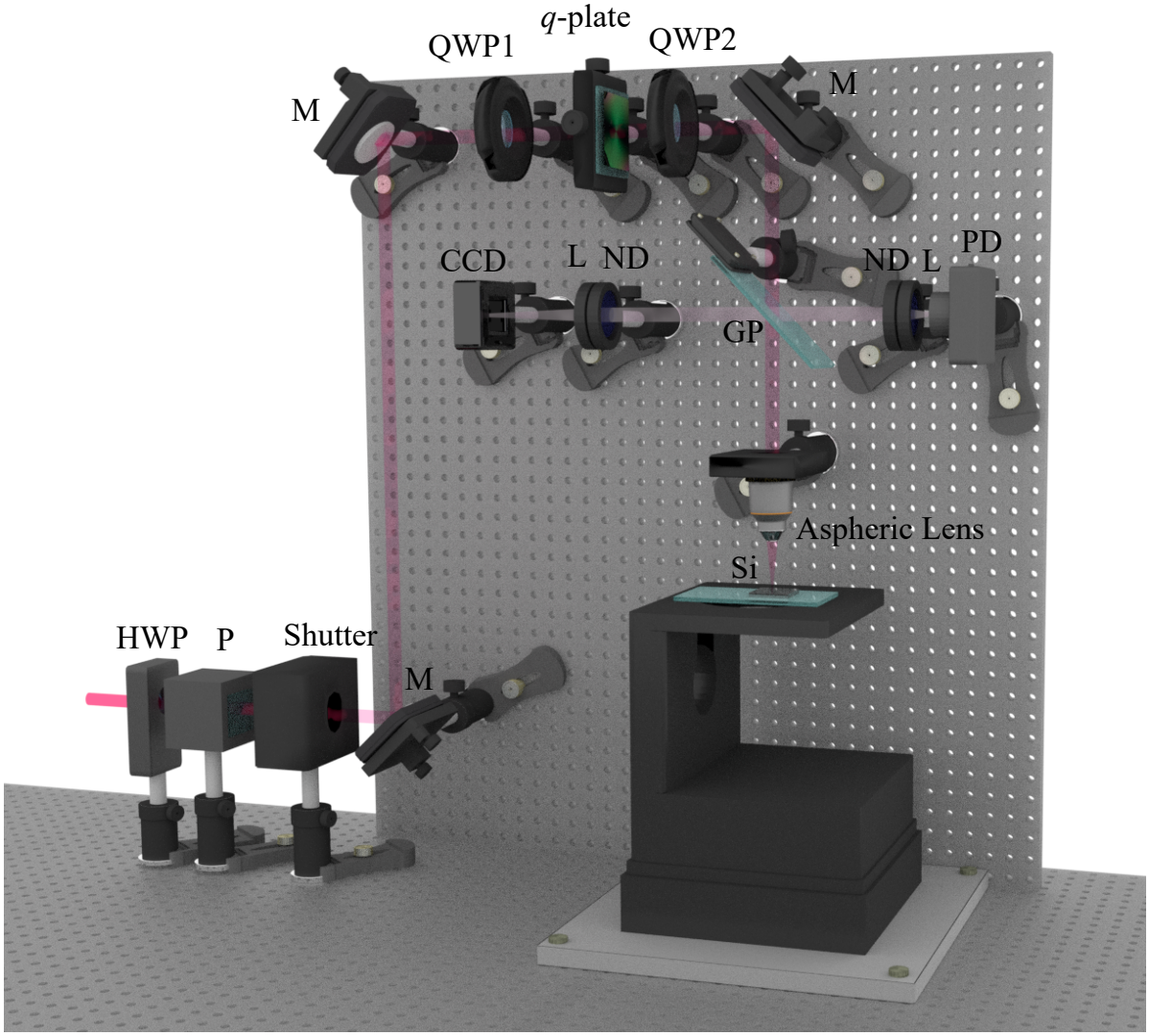

Figure 2.11: Micro/nanomachining setup. The optical elements shown here are: mirrors (M), a combination of a polarizer (P) and a half-wave plate (HWP) to control the laser power, a quarter-wave plate (QWP1) to obtain a circularly polarized beam, a q-plate (q=1/2) to convert the Gaussian beam to a doughnut-shaped vortex beam, second quarter-wave plate (QWP2) to convert the polarization state to circular polarization, computerized translation stages (XYZ), a glass plate (GP) to direct the reflected beam from the sample towards the camera, a CCD camera to accurately monitor the sample surface, fast Photodiode (PD) to monitor any fluctuations in the laser power incident on the sample, lenses (L) to focus the light into the camera and PD, and an aspheric lens.

pump the oscillator. Femtosecond pulses from the oscillator are sent into a regenerative amplifier (Spitfirepro, Spectra-Physics) to be amplified. The amplifier was pumped by a 30 W frequency-doubled Nd:YLF (Empower, Spectra-physics, 527 nm) laser. The amplifier operates at a repetition rate of 1 kHz and produces pulses of 40 fs with a maximum pulse

energy of 2.5 mJ.

In my experiment, as shown in the schematic representation of Fig. 2.11, linearly polarized Gaussian laser beam coming from the regenerative amplifier is directed towards the experimental setup via highly reflective mirrors. Prior to my setup, a small portion of the beam ($\sim 4\%$) was selected to enter the autocorrelator via a beam dumper to continuously monitor the pulse duration. The transmitted beam was then divided in two using a beam splitter such that 20% of the beam entered the setup. In this way, I managed not to damage the optics but keep the energy that is required in my experiments.

A combination of a motorized rotating half-wave plate (HWP) mounted on a rotation stage (PR50CC, Newport) with a resolution of 0.02° and calcite-based cubed polarizer (with high distinction ratio) was employed to control/attenuate the laser power. The polarization of the input beam rotates about the optical axis of HWP in a plane perpendicular to the propagation direction. Therefore, rotating the optical axis of the HWP relative to the incidence polarization (electric field direction) can vary the electric field's amplitude when it passes through the polarizer. In the next steps, a combination of neutral density (ND) filters was used to obtain a different combination of optical densities (OD) to dissipate the beam's power even more. Optical densities are described as:

$$P_{out} = P_{in} \times 10^{-(OD)} \tag{2.4}$$

where P_{out} and P_{in} are the power of the beam before and after the ND filter, respectively. A combination of quarter-wave plates and a q-plate was used to acquire circularly polarized vortex beams owing orbital angular momentum of $\ell = \pm 1$. To generate a linearly polarized beam, a cube polarizer (CM1-PBS252, 620-1000 nm, Thorlabs) was introduced in the beam path.

The generated optical vortex beam was then focused either on the surface or inside the bulk using a 0.25 NA (Newport, 16×, 11.0 mm EFL) aspheric objective lens. Just before the lens, a glass plate at 45° was mounted. A small percentage (4%) of the input beam is reflected from the glass towards a photodiode to precisely monitor any power fluctuations. Transmitted light through the glass plate was focused on the sample and reflected back towards the glass plate and then directed and focused (Thorlabs, f = 100 mm, plano-convex lens) onto a CCD camera (MCE-B013-US, Mightex). A series of ND filters were placed before the camera to avoid any damage to the camera due to the intensity of the focused light. This technique was applied to accurately determine the position of the laser focus relative to the sample's surface. For a normal incident beam, by adjusting the sample position in Z direction, two nicely-round and sharp spots (coming from both top and bottom surface of the glass plate), with the smallest size, appeared on a software operating the camera.

In all experiments, samples were mounted on three-axis translation stages (XMS50, XMS50, and VP-25XA, Newport) with a resolution of 100 nm along the axial direction (Z) and 50 nm along the lateral dimensions (X, Y). The stages were controlled by a motion controller (XPS-C8, Newport) via LabVIEW interface. All the experiments were performed with the laser in a gated mode. Triggering the laser and data acquisition were performed by

a data acquisition card (USB-6251, National Instrument) and the timing delay generator (TDG) box. The control software was written in LabVIEW.

In gated mode, when the laser output could be a single or multiple-pulse, a signal from the laser was delivered to the TDG box and the input of the data acquisition card. This signal was then used as a reference to send the triggering signal from the data acquisition card to the laser. The triggering signal was then sent back to the enable-delay channel on the TDG box. The time duration of the triggering signal was exploited to choose the number of pulses required for the experiment and was controlled by the LABVIEW software.

2.5 Characterization of the Laser Beam

Several laser parameters, including laser fluence, beam intensity profile, spot size, and pulse duration, are crucial in the laser processing of materials. Therefore, a precise structuring requires proper knowledge of them. These parameters are discussed in the following subsections.

2.5.1 Laser Power and Laser Fluence

Characterization of the laser beam requires precise measurements of the power. The power measurements for most of the experiments presented in this thesis were performed with a power meter with a thermal detector (UP12E-10S-H5-D0, Gentec-eo), capable of measuring powers between 1 mW to 10 W with the power calibration uncertainty quoted as ± 2.5 %. The rise time of the power meter was 0.3 seconds. Therefore, by dividing the measured average power by the repetition rate of the laser (1 kHz), the energy of individual pulses can be determined.

In the experiments presented in this thesis, the incident pulses' energies were measured after the microscope objective. This way, we considered all the losses caused by the transmission and reflection of the optics. Once the power is measured, we can determine other crucial parameters in laser-solid interactions, such as laser intensity at the focus and laser fluence.

The laser fluence (J/cm^2) is defined as energy per pulse delivered per unit area (surface of the beam), and is written as,

$$F = \frac{E}{A} = \frac{P_{ave}}{fA} \tag{2.5}$$

where E is the energy per pulse (J), A the area of the beam(cm^2), P_{ave} is the average laser output power (W) measured by the power meter, and f is the repetition rate (Hz). Another key parameter is the laser peak power that can be used to calculate the peak laser intensity delivered to the sample. The laser peak power is given by

$$P_{peak} = \frac{E}{\tau} = \frac{P_{ave}}{f\tau} = \frac{F\ A}{\tau} \tag{2.6}$$

where τ is the pulse duration. Therefore, intensity at the focus will be

$$I = \frac{P_{peak}}{A} = \frac{F}{\tau} \tag{2.7}$$

In this work, the pulse energy used in different experiments varied from 50 nJ to 2 μJ.

2.5.2 Pulse Duration Measurement

A single shot autocorrelator measured the pulse duration of the laser at the output of the laser system used in my experiment. This autocorrelator is capable of measuring durations within the range of 30-150 fs. In a single-shot autocorrelation, the amplifier output beam is split into two separate beams using a beam splitter. These two separated beams are then focused on a BBO crystal after a time delay. A second harmonic (SH) signal is generated in the crystal whose intensity changes if the time delay between the pulses varies. The maximum signal intensity is achieved when there is a temporal overlap. In the case of intensity autocorrelation, an autocorrelation in time is transformed into a spatial intensity distribution. Therefore, the intensity of the SH signal (A) is expressed by

$$A(\tau) = \int_{-\infty}^{\infty} I_s(t)\, I_r(t-\tau)\, dt \tag{2.8}$$

where I_s is the intensity of a beam with no delay and $I_r(t-\tau)$ is the intensity of the delayed beam. The autocorrelation signal is detected by a CCD camera and measured using a LABVIEW program.

To measure the pulse duration coming from the regenerative amplifier, a beam sampler (BSF10-B1, Thorlabs, 650-1050 nm) was used to direct a 4% of the beam towards the autocorrelator. The pulse duration measured using this technique was 45 fs. Notably, this value shows the duration of the pulse right after the laser amplifier. However, after passing through every optics, the pulse duration is stretched due to the group velocity dispersion. Therefore, to find the duration of the pulse that enters the experimental setup, all the dispersive media in the beam path need to be considered. The pulse duration can be calculated along with all optics (5 mm beam sampler, 5 mm beam splitter, 6.35 mm HWP, 25.4 mm polarizer, and 1 mm filter) using the following relation [58]

$$\tau = \tau_0 \sqrt{1 + \left(\frac{GDD}{\tau_0^2}\, 4\, ln2\right)^2} \tag{2.9}$$

where τ_0 is the pulse duration before entering the dispersive medium and GDD is the group delay dispersion. Considering the thickness and GVD (silica quartz:36.16 fs^2/mm and BK7:44.65 fs^2/mm) of each optical component and calculating the GDD for each element, the pulse duration before the microscope objective was calculated to be $\sim$81 fs. Through direct measurement, the pulse duration at the back aperture of the aspheric lens, with all the optics in the beam path, was 72 fs.

2.5.3 Laser Spot Size and Threshold Fluence

There are several techniques to determine the laser spot size. One of the most practical techniques is known as the knife edge technique. In this method, the laser beam's spatial distribution is interrupted along the x- or y-axis by a knife-edged device moving at a uniform speed. The transmitted power is then collected using a photodiode.

The spatial intensity distribution of a Gaussian beam of radius w as a function of the Cartesian coordinates x and y, measured from the beam centre perpendicular to the axis of propagation, is given by [59]

$$I(x,y) = \frac{2P_0}{\pi w^2}\, exp\left(-\frac{2x^2+2y^2}{w^2}\right) \tag{2.10}$$

where P_0 is the total power. When the knife edge blocks the beam, the transmitted power can be determined by

$$P(x,y) = \int_{-\infty}^{\infty}\int_{-\infty}^{\infty} I(x,y)\, dx\, dy \tag{2.11}$$

Therefore, the normalized transmitted power at the knife's position is calculated to be as

$$\frac{P(x)}{P_0} = erfc\left(\frac{\sqrt{2}x}{w}\right) \tag{2.12}$$

where $erfc$ is the complimentary error function. We also know that, for a Gaussian beam, the beam radius is determined by

$$w(z) = w_0\sqrt{1+\left(\frac{z}{z_R}\right)^2} \tag{2.13}$$

where w_0 is the spot size and z_R is the Rayleigh range ($z_0 = \pi w_0^2/\lambda$), the location where the beam radius increases by a factor of $\sqrt{2}$. By fitting equations 2.12 and 2.13 to the photodiode output data, a value of the radius of the Gaussian beam (w) can be obtained, as shown in Fig. 2.12. Using this technique, the spot size for an aspheric lens with a numerical aperture of 0.25 and 16× magnification was determined to be 1.8±0.1 μm.

Another way to measure the spot size of a tightly focused laser beam with a Gaussian intensity profile is to measure the dimensions of the ablation crater. This will also enable us to find the ablation/modification threshold fluence, F_{th}, that depends on the material and on the number of laser pulses delivered to the target. The spatial distribution of fluence for a Gaussian beam, F(r), is given by

$$F(r) = F\, e^{-2\, r^2/w_0^2} \tag{2.14}$$

where

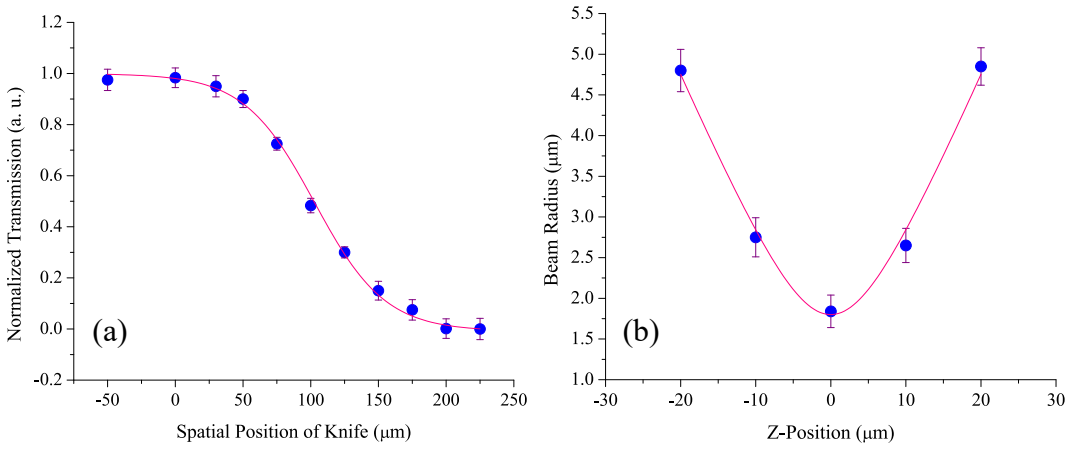

Figure 2.12: Spot size measurement using knife edge technique for a Gaussian beam. (a) The transmitted power is plotted as a function of the edge position (x). (b) The spot size is plotted as a function of the edge position along the beam's propagation direction.

$$F = \frac{2E_0}{\pi w_0^2} \tag{2.15}$$

is the peak fluence of a Gaussian beam, E_0 is the pulse energy, w_0 is the spot size (beam radius at $1/e^2$ of the intensity profile), and r is the distance from the beam center. Therefore, the diameter of the modified region (D) can be found using the relations below [60].

$$\begin{aligned} \frac{F_{th}}{F} &= e^{-2\,(D/2)^2/w_0^2} \\ &= e^{-D^2/2w_0^2} \\ D^2 &= 2w_0^2\; ln\frac{F}{F_{th}} \end{aligned} \tag{2.16}$$

This method is usually used for a laser beam with a Gaussian intensity profile. However, it can also provide approximately accurate values for a beam of light with a doughnut-shaped intensity profile (e. g., Hyper-Geometric Gaussian modes, a Laguerre-Gauss modes subclass). Therefore, we used this method to estimate the spot size and threshold fluence of the laser beam for single and multiple pulse irradiation.

Single Pulse: To experimentally find the spot size at the target surface, several ablation craters were produced upon single pulse irradiation on the silicon surface. Beam was focused using a 16× aspheric lens with NA=0.25. Pulse energy was varied over a range of values. There is a linear relationship between the pulse energy (E_{pulse}) and its fluence (F), therefore, a semi-logarithmic plot of D^2 versus $ln(E_{pulse})$ was plotted. A linear fit can be extrapolated from the graph, where its slope (m) approximately determines a value for a w_0 of the laser spot at the focus [60].

$$w_0 = \sqrt{\frac{m}{2}} \tag{2.17}$$

Different D^2 values were determined using the software "ImageJ" and measuring the dimensions of all the ablation craters on a silicon target, captured by scanning electron microscope(SEM). Employing this method, as shown in Fig. 2.13, the beam diameter and the laser threshold fluence are determined to be 2.8 $\pm$0.2 μm and 0.41 J/cm^2, respectively.

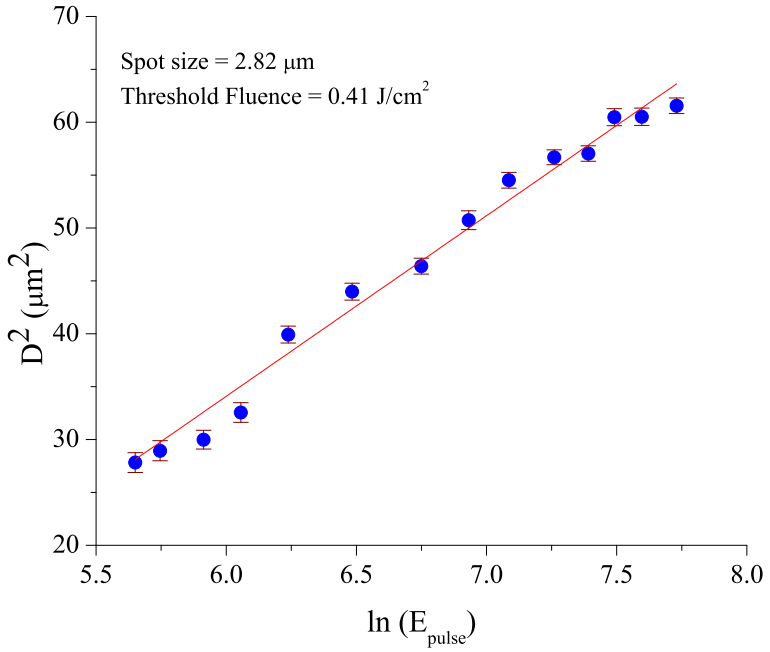

Figure 2.13: Graphs of D^2 versus $ln(E_{pulse})$ for single pulse irradiation. Measurement were performed when a Hyper-Geometric Gaussian modes laser beam was irradiated on silicon surface, i. e., beam had a doughnut intensity profile. The beam diameter and the laser threshold fluence are determined to be 2.8 $\pm$0.2 μm and 0.41 J/cm^2, respectively.

There is also a theoretical way to determine the spot size of a Hyper-Geometric Gaussian laser beam, given by [61]

$$w_{max} = w(z)\,(|\ell|\ \ (|\ell|+1))^{1/4} \tag{2.18}$$

where w_{max} is the radius of maximum intensity, $w(z)$ is the Gaussian beam radius, and ℓ is the azimuthal index (integer) in the amplitude of a Laguerre-Gauss beam representing its order (more information is provided in the next chapter). According to this equation, the diameter of the maximum intensity was 2.3μm, which is in good agreement with our experimental data.

Multiple Pulses: As the surface morphology in this regime is different, another method is required to determine the laser spot size and threshold fluence. The annular

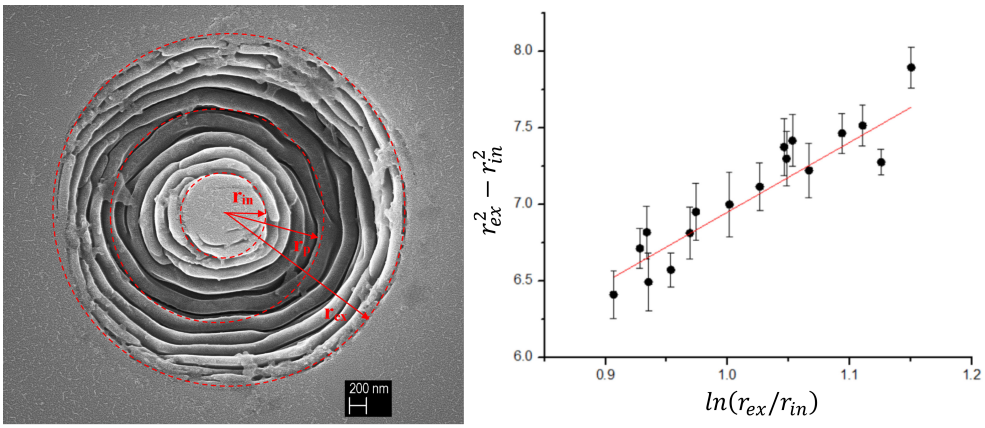

Figure 2.14: Determination of spot size in multiple pulse regime. Measurement were performed when a Hyper-Geometric Gaussian modes laser pulses were irradiated on a CVD single crystal diamond. The beam spot size is determined to be 2.13 ±0.51 μm.

ablation crater in this regime is limited by the internal, r_{in}, and external, r_{ex}, radii, at which the pulse fluence equals the ablation threshold fluence [62]. The theoretical profiles of the fluence spatial distribution (F_ℓ) and the peak fluence ($F_{\ell,peak}$) are [62]

$$\begin{aligned} F_\ell(r) &= F_{\ell,peak} c_\ell \left(\frac{\sqrt{2}r}{w_0}\right)^{2\ell} e^{\left(\frac{-2r^2}{w_0^2}\right)} \\ F_{\ell,peak} &= F_\ell(r_p) = \frac{2e^{-\ell}\ell^\ell}{\ell!}\frac{E}{\pi w_0^2} \end{aligned} \tag{2.19}$$

The peak value of the fluence profile is at r_p that is given by [62]

$$r_p = \sqrt{\frac{\ell}{2}} w_0 \tag{2.20}$$

In this case, the spot size is determined by

$$w_0 = \sqrt{\frac{(r_{ex}^2 - r_{in}^2)}{\ell\, ln\left(\frac{r_{ex}}{r_{in}}\right)}} \tag{2.21}$$

Using these equations, for irradiation of 100 pulses on a CVD single crystal diamond target, spot size was calculated to be 2.13±0.51 μm, as shown in Fig. 2.14. The single pulse threshold fluence was also determined to be 0.61 J/cm^2.

Bibliography

[1] S. Preuss, A. Demchuk, and M. Stuke, "Sub-picosecond UV laser ablation of metals", Applied Physics A, 61, 3337(1995).

[2] X. Zhu, D. M. Villeneuve, A. Y. Naumov, S. Nikumb, and P. B. Corkum, "Experimental study of drilling sub-10 μm holes in thin metal foils with femtosecond laser pulses", Appl. Surf. Sci., 152 13848 (1999).

[3] H. Varel, D. Ashkenasi, A. Rosenfeld, M. Wähmer, and E. E. B. Campbell, "Micromachining of quartz with ultrashort laser pulses", Appl Phys A 65, 367373 (1997).

[4] T. V. Kononenko, S. V. Garnov, S. M. Klimentov, V. I. Konov, E. N. Loubnin, F. Dausinger, A. Raiber, and C. Taut, "Laser ablation of metals and ceramics in picosecondnanosecond pulsewidth in the presence of different ambient atmospheres", Appl. Surf. Sci. 109110 4851 (1997).

[5] X. Liu, D. Du, and G. Mourou, "Laser ablation and micromachining with ultrashort laser pulses", IEEE JOURNAL OF QUANTUM ELECTRONICS, 33, NO. 10 (1997).

[6] P. Bado, W. Clark, A. Said, "Ultrafast Laser Micromachining Handbook", https://www.cmxr.com/resources/

[7] K. C. Phillips, H. H. Gandhi, E. Mazur, and S. K. Sundaram, "Ultrafast laser processing of materials: a review", Advances in Optics and Photonics, 7, No. 4 (2015).

[8] K. Richardson A. Zoubir, L. Shah and M. Richardson, "Practical uses of femtosecond laser micro-materials processing", Appl. Phys. A, 77, 311, (2003).

[9] D. S. Correa, J. M. P. Almeida, G. F. B. Almeida, M. R. Cardoso, L. De Boni and C. R. Mendonç, "Ultrafast Laser Pulses for Structuring Materials at Micro/Nano Scale: From Waveguides to Superhydrophobic Surfaces", Photonics, 4, 8 (2017).

[10] S. I.Anisimov, B.L.Kapeliov, T. L. Perelman, "Electron-emission from surface of metals induced by ultrashort laser pulses", Sov. Phys.-JETP 39 3757 (1974).

[11] C. Momma, S. Nolte, B. N. Chichkov, F. von Alvensleben, A. Tunnermann, "Precise laser ablation with ultrashort pulses", Appl. Surf. Sci., 109, 1519 (1997).

[12] B. N. Chichkov, C. Momma, S. Nolte, F. Alvensleben, A. Tünnermann, "Femtosecond, picosecond and nanosecond laser ablation of solids", Appl. Phys. A, 63, 109115 (1996).

[13] B. Rethfeld, K. Sokolowski-Tinten, D. Von der linde, S. I. Anisimov, "Timescales in the response of materials to femtosecond laser excitation", Appl. Phys. A, 79, 767 (2004).

[14] B. Rethfeld, D. S. Ivanov, M. E. Garcia, and S. I. Anisimov, "Modelling ultrafast laser ablation", J. Phys. D: Appl. Phys., 50, 193001 (2017).

[15] P. Stampfli, K. H. Bennemann, "Time dependence of the laser-induced femtosecond lattice instability of Si and GaAs: Role of longitudinal optical distortions", Phys. Rev. B 49, 7299 (1994).

[16] C. V. Shank, R. Yen, C. Hirlimann, "Femtosecond-time-resolved surface structural dynamics of optically excited silicon", Phys. Rev. Lett. 50, 454 (1983).

[17] M. Z. Mo, Z. Chen, R. K. Li, M. Dunning, B. B. L. Witte1, J. K. Baldwin, L. B. Fletcher, J. B. Kim, A. Ng, R. Redmer, A. H. Reid, P. Shekhar, X. Z. Shen, M. Shen, K. Sokolowski-Tinten, Y. Y. Tsui, Y. Q. Wang, Q. Zheng, X. J. Wang, S. H. Glenzer, "Heterogeneous to homogeneous melting transition visualized with ultrafast electron diffraction", Science 360, 14511455 (2018).

[18] B. Rethfeld, K. Sokolowski-Tinten, S.I. Anisimov, D. von der Linde, "Ultrafast thermal melting of laser-excited solids by homogeneous nucleation", Phys. Rev. B 65, 092 103 (2002).

[19] B. Rethfeld, A. Kaiser, M. Vicanek, G. Simon, "Femtosecond laser-induced heating of electron gas in aluminium", Appl. Phys. A 69 [Suppl.], 109 (1999).

[20] M. T. Winkler, "Non-equilibrium chalcogen concentrations in silicon: physical structure, electronic transport, and photovoltaic potential", Ph.D. thesis, Harvard University (2009).

[21] L. V. Keldysh, "Ionization in the field of a strong electromagnetic wave", Sov. Phys.-JETP, 20, 130714 (1965).

[22] K. Yamanouchi, "Lectures on Ultrafast Intense Laser Science 1", Volume 1 (Springer Berlin Heidelberg (2011).

[23] R. H. M. Groeneveld, R. Sprik, and A. Lagendijk, "Effect of a nonthermal electron distribution on the electron-phonon energy relaxation process in noble metals", Phys. Rev. B, 45, 5079 (1992).

[24] B. Luther-Davies, E.G. Gamaly, A.V. Rode and V.T. Tikhonchuk, "Ablation of solids by femtosecond lasers; ablation mechanism and ablation thresholds for metals and dielectrics", Physics of Plasmas, 9, 949 (2004).

[25] D. Bäuerle, "Laser Processing and Chemistry", Springer, Berlin (2000).

[26] K. Sugioka, M. Meunier, A. Piqué, "Laser Precision Microfabrication", Chaper 4, Springer Berlin Heidelberg (2010).

[27] X. Wang, X. Xu, "Thermoelastic wave induced by pulsed laser heating", Appl. Phys. A. 73, 107 (2001).

[28] T. Zier, E. S. Zijlstra, A. Kalitsov, I. Theodonis, and M. E. Garcia, "Signatures of nonthermal melting", STRUCTURAL DYNAMICS 2, 054101 (2015).

[29] P. Lorazo, L. J. Lewis, and M. Meunier, "Thermodynamic pathways to melting, ablation, and solidification in absorbing solids under pulsed laser irradiation", PHYSICAL REVIEW B 73, 134108 (2006).

[30] L. V. Zhigilei, B. J. Garrison, "Microscopic mechanisms of laser ablation of organic solids in the thermal and stress confinement irradiation regimes", Appl. Phys. 88, 1281 (2000).

[31] S. K. Sundaram and E. Mazur, "Inducing and probing non-thermal transitions in semiconductors using femtosecond laser pulses", Nat. Mater. 1, 217224 (2002).

[32] D. Perez, L. J. Lewis, "Ablation of solids under femtosecond laser pulses", Phys. Rev. Lett. 89, 255504 (2002).

[33] E. G. Gamaly, S. Juodkazis, K. Nishimura, H. Misawa, B. Luther-Davies, "Laser-matter interaction in the bulk of a transparent solid: Confined microexplosion and void formation", Phys. Rev. B, 73, 214101 (2006).

[34] N. M. Bulgakova, A. V. Bulgakov, "Pulsed laser ablation of solids: Transition from normal vaporization to phase explosion", Appl. Phys. A Mater. Sci. Process., 73, 199208 (2001).

[35] R. Fang, A. Vorobyev, and C. Guo, "Direct visualization of the complete evolution of femtosecond laser-induced surface structural dynamics of metals", Light: Science and Applications, 6, e16256 (2017).

[36] E. Leveugle, D. S. Ivanov, L. V. Zhigilei, "Photomechanical spallation of molecular and metal targets: molecular dynamics study", Appl. Phys. A , 79, 1643-1655 (2004).

[37] A. Naghilou, M. He, J. S. Schubert, L. V. Zhigilei, and W. Kautek, "Femtosecond laser generation of microbumps and nanojets on single and bilayer Cu/Ag thin films", Phys. Chem. Chem. Phys., 21, 11846 (2019).

[38] K.W. Kolasinski, M.C. Gupta, L.V. Zhigilei, "Encyclopedia of Interfacial Chemistry Surface Science and Electrochemistry- Chapter: Plume and Nanoparticle Formation During Laser Ablation", Elsivier, Pages 594-603 (2018).

[39] C. P. Wu, L. V. Zhigilei, "Microscopic mechanisms of laser spallation and ablation of metal targets from large-scale molecular dynamics simulations", Appl. Phys. A, 114, 11-32 (2014).

[40] S. Musazzi and U. Perini (eds.), "Laser-Induced Breakdown Spectroscopy", Springer Series in Optical Sciences, 182, Springer-Verlag Berlin Heidelberg (2014).

[41] P. F. Moulton, "Spectroscopic and laser characteristics of $Ti : A1_2O_3$", Opt. Soc. Am. B, 3, 1 (1986).

[42] https://www.olympus-lifescience.com/en/microscope-resource/primer/java/lasers/tsunami/

[43] https://www.olympus-lifescience.com/en/microscope-resource/primer/java/lasers/tsunami/

[44] W. Dietel, J. J. Fontaine, and J. C. Diels, "Intracavity pulse compression with glass: a new method of generating pulses shorter than 60 fs", Opt. Lett. 8, 4-6 (1983).

[45] W. Koechner, "Solid-State Laser Engineering", New York: Springer New York (2006).

[46] R. L. Fork, 0. E. Martinez, and J. P. Gordon, "Negative dispersion using pairs of prisms", OPTICS LETTERS, 9, No. 5 (1984).

[47] P.W. Smith, "Mode-locking of lasers", IEEE, 58, NO. 9 (1970).

[48] L. E. Hargrove, R. L. Fork, and M. A. Pollack, "Locking of HeNe laser modes induced by synchronous intracavity modulation", Appl. Phys. Lett. 5, 4 (1964).

[49] E. P. Ippen, C. V. Shank, and A. Dienes, "Passive mode locking of the cw dye laser", Appl. Phys. Lett. 21, 348 (1972).

[50] P.M.W.French, "The generation of ultrashort laser pulses", Rep. Prog. Phys. 58, 169-267 (1995).

[51] T. Brabec, Ch. Spielmann, P. F. Curley, and F. Krausz, "Kerr lens mode locking", OPTICS LETTERS, 17, No. 18 (1992).

[52] D. E. Spence, P. N. Kean, and W. Sibbett, "60-fsec pulse generation from a self-mode-locked Ti:sapphire laser", Opt. Lett., 16, 424 (1991).

[53] O. Svelto, "Principles of Lasers", Fifth ed. Springer, Chap. 8 (2010).

[54] A. Yariv, "Optical Electronics", fourth ed. (Saunders College Publ., Fort Worth, Chap. 12 (1991).

[55] T. Norris, T. Sizer, and I. N. Duling, "Kilohertz synchronous amplification of 85-femtosecond optical pulses", J. Opt. Soc. Amer. B, 2, pp. 616618 (1985).

[56] M. Perry, "Multilayer dielectric gratings: increasing the power of light", Sci. Technol. Rev. 2433 (1995).

[57] G. Vaillancourt, "Operation of a 1-kHz pulse-pumped Ti:sapphire regenerative amplifier", OPTICS LETTERS, 15, No. 6 (1990).

[58] J. C. Diels, and W. Rudolph, "Ultrashort laser pulse phenomena", Academic Press, 36 (2006).

[59] D. R. Skinner and R. E. Whitcher, "Measurement of the radius of a high-power laser beam near the focus of a lens", Journal of Physics E: Scientific Instruments, 5 (1972).

[60] H. D. Hoffmann, H. G. Treusch, J. Jandeleit, G. Urbasch, and E. W. Kreutz, "Picosecond laser ablation of thin copper films", Appl. Phys. A, 63(2), 117 (1996).

[61] F. Bouchard, J. Harris, H. Mand, R. W. Boyd, and E. Karimi, "Observation of subluminal twisted light in vacuum: supplementary material", Optica, 3, Issue 4, 351-354 (2016).

[62] E. Allahyari, J. JJ Nivas, F. Cardano, R. Bruzzese, R. Fittipaldi, L. Marrucci, D. Paparo, A. Rubano, A. Vecchione, and S. Amoruso, "Simple method for the characterization of intense Laguerre-Gauss vector vortex beams", Appl. Phys. Lett., 112, 211103 (2018).

Chapter 3

Structured Light

3.1 Introduction

In this chapter, we discuss some of the physical principles governing structured light, e.g., light carrying orbital angular momentum (OAM), and spin angular momentum (SAM). We introduce these physical properties of light in both classical and quantum mechanical frameworks.

It is well known that electromagnetic radiation and in particular light beams consist of photons that carry energy and momentum. Whenever light interacts with matter, the energy and momentum of photons can be transferred to matter. For example, the tail of a comet approaching the sun and pointing opposite to it is, in fact, the result of the linear momentum transfer of photons to the ice material of the comet's core. The rising temperature of a swimming pool full of water during summer also indicates that the photons coming from the sun transfer energy to the water in the pool and raise its temperature. With the advance in optical technology, we have been able to generate electromagnetic radiation so that upon interaction with material particles, it can cause them to rotate about an axis aligned with the direction of the propagation of light. In other words, the same as the rotation of Earth about the sun, these particles carry OAM, which is transferred to them by light. Moreover, the interaction of photons with free particles can also result in the spin of the particle about its own axis, indicating the transfer of SAM to the particle. Both transfers of OAM and SAM of light has been demonstrated and verified experimentally [1]. In Fig. 3.1 a schematic of lights OAM and SAM features is shown.

3.2 Solutions to Maxwell's Equations

Here we start with a classical treatment of structured light. As we know, electromagnetic radiation consists of oscillations of the electric filed, **E** and magnetic field, **B** in space and time. Propagating electromagnetic radiation are mathematically described as the solutions to Maxwell's equations. In free space with no charge and current density sources, these equations take the simple form (in SI units) of:

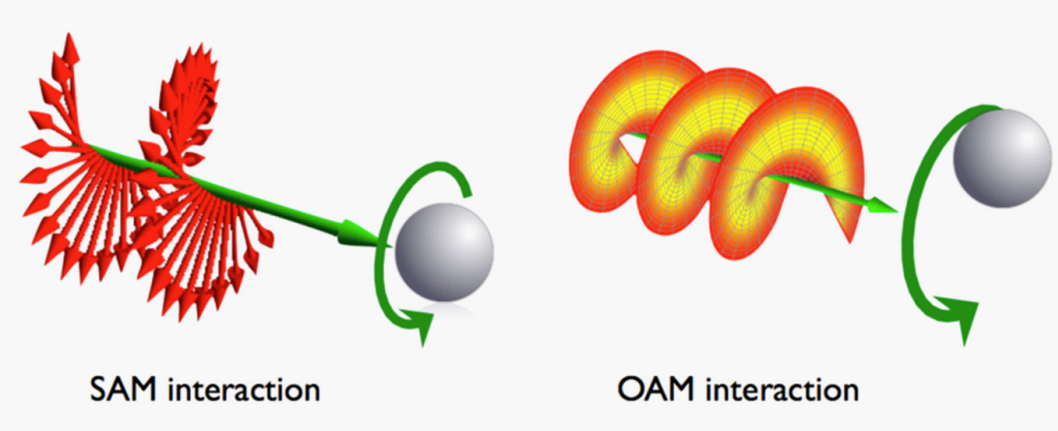

Figure 3.1: SAM interaction with a particle induces spin about its axis. OAM interaction with a particle causes an orbital motion about the axis of the beam [2].

$$\begin{aligned} \nabla \cdot \mathbf{E} &= 0 \\ \nabla \cdot \mathbf{B} &= 0 \\ \nabla \times \mathbf{E} + \frac{\partial \mathbf{B}}{\partial t} &= 0 \\ \nabla \times \mathbf{B} - \frac{1}{c^2}\frac{\partial \mathbf{B}}{\partial t} &= 0 \end{aligned} \tag{3.1}$$

Here c is the speed of light in a medium with no electric and magnetic properties otherwise known as vacuum ($c = (\varepsilon_0 \mu_0)^{-1/2}$, where ε_0 and μ_0 are the permittivity and permeability of free space, respectively). The 4 first order equations above are equivalent to the two 2^{nd} order wave equations given by the wave equation

$$\begin{aligned} \nabla^2 \mathbf{E} - \frac{1}{c^2}\frac{\partial^2 \mathbf{E}}{\partial t^2} &= 0 \\ \nabla^2 \mathbf{B} - \frac{1}{c^2}\frac{\partial^2 \mathbf{B}}{\partial t^2} &= 0 \end{aligned} \tag{3.2}$$

One notes that $\nabla \cdot \mathbf{B}=0$ indicates the existence of a vector potential function $\mathbf{A}$ such that $\mathbf{B}=\nabla \times \mathbf{A}$. As a result the 3rd Maxwell equation can be rewritten as $\nabla \times (\mathbf{E} + \partial \mathbf{A}/\partial t)=0$ making it possible to define a scalar potential function Φ such that $\mathbf{E}=-\nabla \Phi - \partial \mathbf{A}/\partial t$. The vector and scalar potentials satisfy the following equation (see appendix for details):

$$\nabla^2 \mathbf{A} - \frac{1}{c^2}\frac{\partial^2 \mathbf{A}}{\partial t^2} = \nabla \left(\nabla \cdot \mathbf{A} + \frac{1}{c^2}\frac{\partial \Phi}{\partial t} \right) \tag{3.3}$$

In the Lorentz gauge, the electromagnetic potentials are chosen such that $\nabla \cdot \mathbf{A} + \frac{1}{c^2}\frac{\partial \Phi}{\partial t}$ and hence the vector potential satisfies a wave equation similar to that of the fields:

$$\nabla^2 \mathbf{A} - \frac{1}{c^2}\frac{\partial^2 \mathbf{A}}{\partial t^2} = 0 \tag{3.4}$$

In order to simply the wave equation, we consider solutions in the form of harmonic oscillations in time. In this way we can separate the time dependence from the spatial dependence; $\mathbf{A}(\mathbf{r}, t) = \mathbf{A}(\mathbf{r})exp(i\omega t)$. Here ω is the angular frequency of the oscillating temporal field. With this separation, the wave equation transforms into the Helmholtz equation for the spatial part,

$$(\nabla^2 + k^2)\mathbf{A}(\mathbf{r}) = 0 \tag{3.5}$$

Here k represents the wave number and satisfies the dispersion relation ω=kc. A standard set of solutions to the Helmholtz equation are "plane" waves. They can be represented by $\mathbf{A}(\mathbf{r}) = \hat{n}Ae^{-i\mathbf{k}\cdot\mathbf{r}}$. Here $\hat{n}$ is the unit vector which indicates the direction of the polarization of the field, and $\mathbf{k}$ is the wavevector indicating the direction of the propagation of the plane wave. From Maxwell's 1^{st} equation in a source-less medium, $\nabla \cdot \mathbf{E}$=0, it can be verified that $\nabla \cdot \mathbf{A}(\mathbf{r})$=0 and this indicates that $\hat{n} \cdot \mathbf{k}$=0 . This indicates that the polarization always oscillates in a plane perpendicular to the direction of propagation. Plane waves have a well- defined wavevector, and through Heisenberg's uncertainty relation, they extend to infinity and thus cannot be physically realizable. However, there exists an approximation known as the paraxial wave approximation in which one can modulate the plane wave with a slowly varying envelope along the direction of propagation. It is convenient to take the z direction as the propagation direction of the wave, $\mathbf{k}$=k$\hat{z}$. As a result, we have

$$\mathbf{A}(\mathbf{r}, t) = \hat{n}Ae^{-i(kz-\omega t)} \tag{3.6}$$

In general, A can be a complex function of position, in other words, it can be represented as an envelope to the field and thus modulating it in space; A=A($\mathbf{r}$). The Helmholtz equation thus reads as:

$$(\nabla^2 + k^2)\hat{n}\, A\, e^{-i(kz-\omega t)} = 0 \tag{3.7}$$

The above equation can be simplified as:

$$\nabla^2 A - 2ik\frac{\partial A}{\partial z} = 0 \tag{3.8}$$

At this stage we apply the paraxial approximation. That is, we assume the field to be slowly varying along the z direction such that one can neglect the $\partial^2 A/\partial z^2$ term in the Laplacian above:

$$\frac{\partial^2 A}{\partial x^2} + \frac{\partial^2 A}{\partial y^2} - 2ik\frac{\partial A}{\partial z} = 0 \tag{3.9}$$

As we consider the field to slowly vary along the z direction we can use the cylindrical coordinate system to describe the vector potential:

$$\mathbf{A}(\mathbf{r},t) = (\hat{x}c_x + \hat{y}c_y)A(\rho,z)e^{i\ell\varphi}e^{-i(kz-\omega t)} \tag{3.10}$$

Here ρ is the radial distance from the z axis, not to be confused with the charge density. c_x and c_y are complex quantities and satisfy the normalization relation $|c_x|^2+|c_y|^2$=1. ℓ is the azimuthal quantum number (an integer) to satisfy the single valued property of the field and φ is the azimuthal coordinate. $(\hat{x}c_x+\hat{y}c_y)$ determines the polarization plane of the filed. Considering the paraxial approximation, the electric field is approximately perpendicular to the field propagation direction, i.e. $\mathbf{E}\cdot\mathbf{k}\cong$0 since: $\nabla\cdot\mathbf{E} = -\nabla^2\Phi - \frac{\partial}{\partial t}\nabla\cdot\mathbf{A}$ in a source free medium ρ=0 and hence the vector potential is almost perfectly perpendicular to the propagation direction ($\mathbf{k}\cdot\mathbf{A}\cong$0).

3.2.1 Polarization Degree of Freedom

Here we consider the polarization of the fields; in particular, we will focus on the electric field. In general, the complex electric field can be represented in polar coordinates by $\mathbf{E}$=$|\mathbf{E}|\,e^{i\chi}$ where $|\mathbf{E}|$ is the modulus and χ is the phase angle. The two-dimensional field in the transverse plane representing an electric field which is perpendicular to the propagation direction can be represented by $\mathbf{E}$=$E_h\hat{h} + E_v\hat{v}$. Here, $\hat{h}$ and $\hat{v}$ are unit vectors representing the horizontal and vertical polarizations, respectively. E_h and E_v are the (complex) components, or in other words, the field amplitude components in the horizontal and vertical directions, their modulus's squares are proportional to the intensity of the fields in those directions and satisfy the relation E^2=$|E_h|^2+|E_v|^2$. In terms of polarization one can normalize the components such that, $|e_h|^2+|e_v|^2$=1. The horizontal ($\hat{h}$)and vertical ($\hat{v}$) unit vectors together span a two-dimensional vector space which represents the polarization of the electric field. These unit vectors constitute one of the infinite possible bases of polarization representation.

Two other useful bases are the circular and diagonal bases defined as $\hat{l} \equiv \frac{1}{\sqrt{2}}(\hat{h}+i\hat{v})$ (left circular polarization vector) $\hat{r} \equiv \frac{1}{\sqrt{2}}(\hat{h}-i\hat{v})$ (right circular polarization vector) $\hat{d} \equiv \frac{1}{\sqrt{2}}(\hat{h}+\hat{v})$ (diagonal polarization vector) $\hat{a} \equiv \frac{1}{\sqrt{2}}(\hat{h}-\hat{v})$ (anti-diagonal polarization vector). The unit vectors are replaced by eigenkets Diracs's notation of quantum mechanical state vectors: $|h\rangle$ (horizontal polarization eigenket) $|v\rangle$ (vertical polarization eigenket) Similarly, the eigenkets in the other two representations are given by: $|l\rangle = \frac{1}{\sqrt{2}}(|h\rangle + i\,|v\rangle)$ (left circular polarization eigenket) $|r\rangle = \frac{1}{\sqrt{2}}(|h\rangle - i\,|v\rangle)$ (right circular polarization eigenket) $|d\rangle = \frac{1}{\sqrt{2}}(|h\rangle + |v\rangle)$ (diagonal polarization eigenket) $|a\rangle = \frac{1}{\sqrt{2}}(|h\rangle - |v\rangle)$ (anti-diagonal polarization eigenket). The spin eigenvalues of photons (which are bosons of total spin 1) can take two values, σ_+=1 and σ_-=-1. Thus the above eigen kets can be represented by spinors in a two dimensional Hilbert space. Working in the linear bases in which the polarization matrix is diagonalized, one can show these states as: $|h\rangle=\binom{1}{0}$, $|v\rangle=\binom{0}{1}$, $|l\rangle=\frac{1}{\sqrt{2}}\binom{1}{i}$, $|r\rangle=\frac{1}{\sqrt{2}}\binom{1}{-i}$, $|d\rangle=\frac{1}{\sqrt{2}}\binom{1}{1}$, $|a\rangle=\frac{1}{\sqrt{2}}\binom{1}{-1}$.

The state of polarization of light can be described in different ways, one way is via examining the polarization ellipse. This ellipse is formed by the trace that the tip of the polarization vector traverses as the field propagates, and the orientation of this ellipse is given by an angle. However, there are more efficient ways to represent the polarization state of light, as described in the following section.

3.3 Energy, Momentum, and Angular Momentum of the Electromagnetic Field

The energy, momentum, and angular momentum of an electromagnetic field in a vacuum inside a volume τ are defined as

$$\begin{aligned} W &= \frac{\varepsilon_0}{2} \int |\mathbf{E}|^2 \, d\tau + \frac{1}{2\mu_0} \int |\mathbf{B}|^2 \, d\tau \\ \mathbf{P} &= \varepsilon_0 \int \mathbf{E} \times \mathbf{B} \, d\tau \\ \mathbf{J} &= \varepsilon_0 \int \mathbf{r} \times (\mathbf{E} \times \mathbf{B}) \, d\tau \end{aligned} \tag{3.11}$$

It can be shown that the angular momentum can be separated into two portions, spin angular momentum ($\mathbf{S}$) and orbital angular momentum ($\mathbf{L}$),

$$\mathbf{J} \; = \; \mathbf{S} \; + \; \mathbf{L} \tag{3.12}$$

where,

$$\begin{aligned} \mathbf{S} &= \varepsilon_0 \int \mathbf{E} \times \mathbf{A} \, d\tau \\ \mathbf{L} &= \varepsilon_0 \sum_{i=x,y,z} \int E_i \, (\mathbf{r} \times \nabla) \, A_i \, d\tau \end{aligned} \tag{3.13}$$

3.4 Structured Waves and Vortices

Generally, plane waves are nothing more than an abstract construction that cannot occur naturally, whereas, in the physical world generic wave fields can exhibit features that are substantially different from planar phase fronts propagating in the normal direction. These wave fields which are essentially different from plane waves (or smooth Gaussian waves) are often called structured waves. On the other hand, and from a mathematical viewpoint, structured waves appear as solutions to the wave equation when an "external potential" is

applied. The Schrödinger Equation with an external potential has a counterpart in wave optics; the paraxial wave equation. Moreover, free space electromagnetic waves are also generally structured waves since they can be represented as superpositions of plane waves. Plane waves form a complete set of orthonormal basis, therefore, any arbitrary wave can be represented by a Fourier transform of plane waves: $\mathbf{E}(\mathbf{r},t) = \int \mathcal{E}(\mathbf{k},\omega)e^{i(\mathbf{k}\cdot\mathbf{r}-\omega t)}d\mathbf{k}d\omega$. Even the interference of two plane waves can already be considered as a structured wave field. The most interesting and generic forms of structured waves start from three-wave interference [3]. Phase singularities are considered dislocations of phase fronts or vortices [4,5] which naturally occur as a result of three or more interfering plane waves. These phase singularities are a result of the destructive interference of waves. Let's assume $\mathbf{r} = \mathbf{r}_s$ is such as singularity. The (complex) amplitude of the electromagnetic wave vanishes at this point, $\mathbf{E}_0(\mathbf{r}_s,t)$=0, and thus leaves the phase, φ, undefined. Since the amplitude is, in general, a complex quantity, at points of singularity, both the imaginary and real parts of it must vanish. Therefore, these points of singularity appear as points in 2D planes and lines in 3D planes. Outside the singularity, the phase is well-defined where its integral over a closed-loop containing the singularity can be calculated as:

$$\oint \nabla\varphi \cdot d\mathbf{r} = 2\pi\ell \tag{3.14}$$

where $\ell = 0, \pm1, \pm2, \cdots$ is the topological charge.

As vortices are generic wave forms, in many earlier studies of different types of waves, they frequently appeared in the literature [6, 7].

3.5 Spin Angular Momentum (SAM)

Here we specifically focus on the spin angular momentum of light (SAM). SAM is the component of angular momentum of light associated with the photon's spin or, in classical electrodynamics, the electromagnetic wave's circular or, in general, elliptical polarization.

For electromagnetic radiation, if the electric and magnetic field vectors rotate continuously about the axis of the beam upon propagation, then the polarization of the beam is considered to be circular. If the polarization vector traverses a circle in the clockwise (counter-clockwise) direction from a viewer's perspective that is observing the beam on a plane perpendicular to the beam direction, the beam is considered to be Left (Right) circular. However, the convention is ambiguous; in some literature, it is the opposite.

Circularly polarized light, as with any other type of electromagnetic wave consists of countless photons. Photons, which are bosons with a total spin of 1, can possess two values with respect to the quantization axis. Left circular photons carry a spin angular momentum of $\hbar$, and right circular photons carry a spin angular momentum of -$\hbar$.

This spin angular momentum is directed along the beam axis, or other words, the quantization axis. It is in the same direction of the propagation direction if positive, and it is in the opposite direction to it if negative). Figure 3.2 shows the instantaneous

structure of the electric field of left (L) and right (R) circularly polarized light in space. The propagation direction is considered to be along the z-axis. The field components of the circularly polarized plane waves are given for each polarization. It can be shown that for a monochromatic electromagnetic wave, the spin angular momentum can be expressed as

$$\mathbf{S} = \frac{\varepsilon_0}{2i\omega} \int \mathbf{E}^* \times \mathbf{E}\, d\tau \tag{3.15}$$

From the expression above, one can verify that the spin angular momentum of light vanishes for linear polarization. For example, consider the case in which the filed oscillates with a diagonal polarization in the xy plane; $\mathbf{E} = \frac{1}{\sqrt{2}}(\hat{x}+\hat{y})|\mathbf{E}|, \mathbf{E}^* = \frac{1}{\sqrt{2}}(\hat{x}+\hat{y})|\mathbf{E}|$, therefore, $\mathbf{E} = \mathbf{E}^*$ and $\mathbf{E}^* \times \mathbf{E}$=0 leading to $\mathbf{S}$=0.

On the other hand, for circular or elliptically polarized light, the spin angular momentum will take a non-zero value as seen in the following example for left circular light; $\mathbf{E} = \frac{1}{\sqrt{2}}(\hat{x} + i\hat{y})|\mathbf{E}|, \mathbf{E}^* = \frac{1}{\sqrt{2}}(\hat{x} - i\hat{y})|\mathbf{E}|$, therefore, $\mathbf{E}^* \times \mathbf{E}$=$i|\mathbf{E}|^2\hat{z}$ leading to

$$S_z = \frac{\varepsilon_0}{2\omega} \int |\mathbf{E}|^2\, d\tau \tag{3.16}$$

The electric field energy in the expression above is given by $\frac{\varepsilon_0}{2}\int |\mathbf{E}|^2\, d\tau$, therefore in the language of photons, one can replace this term with the energy of n photons: n$\hbar\omega$. For a single left circular photon, this energy is $\hbar\omega$ and thus $S_z = \hbar$. Likewise, it can be shown that for a single photon with right circular polarization $S_z = -\hbar$.

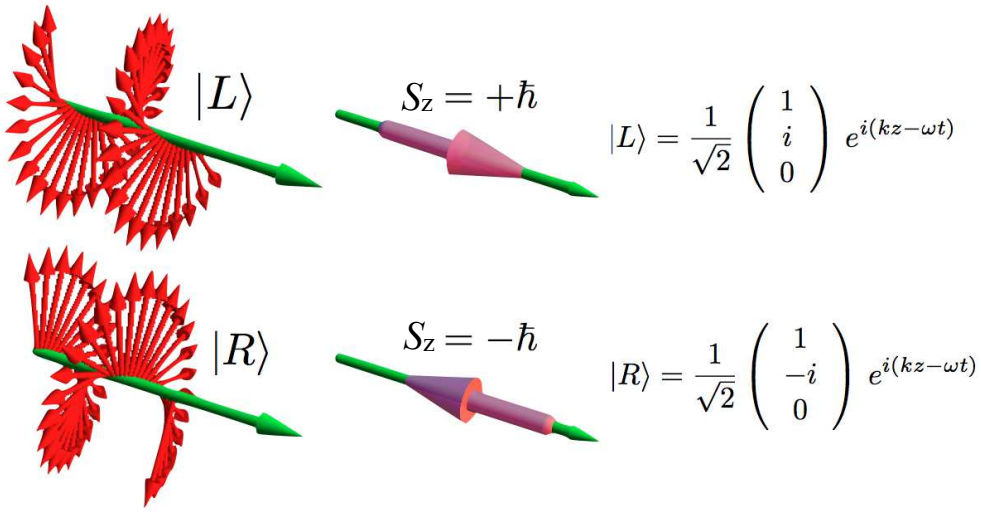

Figure 3.2: Left- and right-handed circular polarization, and their associate angular momentum [8].

3.6 Orbital Angular Momentum (OAM)

We now turn to orbital angular momentum (OAM) of light. Besides the polarization degree of light, an electromagnetic wave can also have a structure associated with it. In other words, the orbital angular momentum of light is an additional degree of freedom that light possesses and is related to the spatial profile of the electromagnetic wave. The orbital angular momentum of light can be considered to be a combination of two parts. First, an origin-independent term which is called the internal orbital angular momentum and is associated with the helicity of the wavefront of light. Second, an external orbital angular momentum which is origin dependent and can be expressed as a vector product of the beam position and its linear momentum. The external angular momentum vanishes if the beam has cylindrical symmetry and the origin is chosen on the axis of the beam.

In the paraxial regime, light can be in certain modes called helical modes. These modes are examples of the internal orbital angular momentum of light, shown in Fig. 3.3 . Each such mode is quantified by an integral number, m, known as the topological charge of the optical vortex. If ℓ=0, then light does not have an interesting structure, but its spatial distribution is merely composed of a sequence of disconnected plane waves. Light with $|\ell| \geq 1$ is what is known as twisted light, as the light propagates, the helical wavefronts twist like a corkscrew, the handedness is determined by the sign of the topological charge, for $\ell=\pm 1$ a full twist of the wavefront happens after one wavelength of propagation, for higher (lower) values of topological charge, a full twist comes in integral fractions of a wavelength. Points on the axis of the beam are known as phase singularities. A brief description of phase singularities will be introduced later. It can be shown that for a monochromatic electromagnetic wave, the orbital angular momentum can be expressed as

$$L = \frac{\varepsilon_0}{2i\omega} \sum_{i=x,y,z} \int E_i^* (\mathbf{r} \times \nabla) E_i \, d\tau \tag{3.17}$$

In the language of quantum mechanics, every single photon may acquire $L_z = \ell\hbar$ as its possible values for orbital angular momentum.

To look into OAM beams more technically, let us consider the mathematical structure of a paraxial wave in cylindrical coordinates: $\mathbf{A}(\mathbf{r}, t) = (\hat{x}c_x + \hat{y}c_y)A(\rho, z)e^{i\ell\varphi}e^{-i(kz-\omega t)}$.

The topological charge ℓ appears in the phase factor $e^{i\ell\varphi}$. There are many possible solutions to the paraxial wave equation. The most important are Bessel beams, Laguerre-Gauss (LG) beams, and Hyper Geometric (HYGG) beams [9]. The helical modes of light form a complete orthonormal basis, such that any structured light can be expanded in terms of a superposition of these modes. In order to see this, note that these modes (denoted by $|\ell\rangle$ are eigenmodes (of the z component) of orbital angular momentum; $\hat{L}_z|\ell\rangle = \ell\hbar|\ell\rangle$, solving this equation for the azimuthal wave function, $\psi_\ell(\varphi) = \langle\varphi|\ell\rangle$ leads to:

$$\begin{aligned} &-i\hbar\partial_\varphi\psi_\ell(\varphi) = \ell\hbar\psi_\ell(\varphi) \\ &\frac{d\psi_\ell(\varphi)}{\psi_\ell(\varphi)} = i\ell d\varphi \quad \rightarrow \quad \psi_\ell(\varphi) = \frac{1}{\sqrt{2}}e^{i\ell\varphi} \end{aligned} \tag{3.18}$$

Here $1/\sqrt{2}\pi$ is the normalization factor. The orthonormality relation between different helical modes immediately follows,

$$\langle \ell' | \ell \rangle = \frac{1}{2\pi} \int_0^{2\pi} d\varphi \, e^{-i\ell'\varphi} e^{i\ell\varphi} = \delta_{\ell,\ell'} \tag{3.19}$$

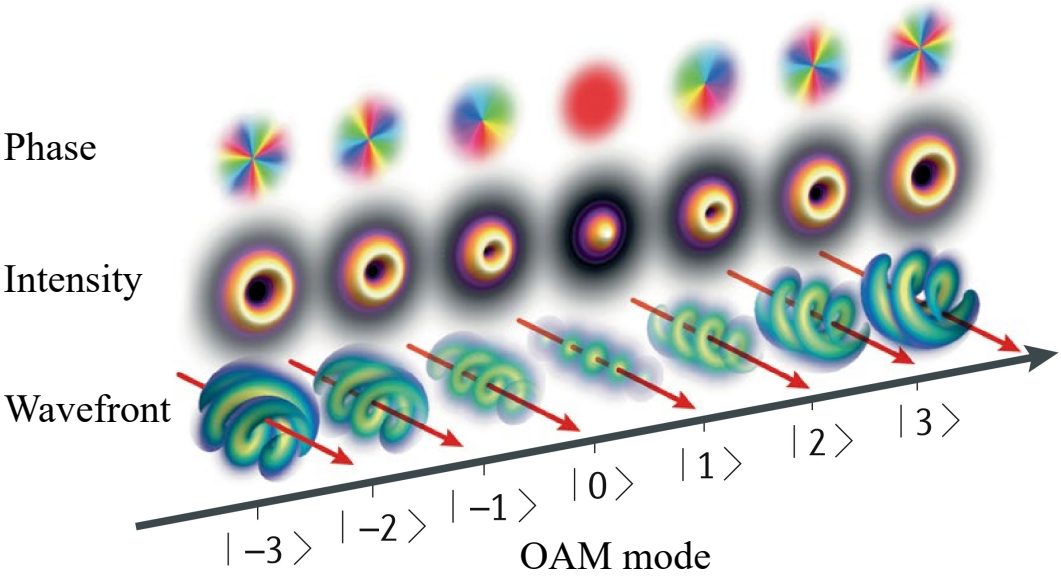

Figure 3.3: The phase, intensity, and wavefront of the structured light. The orbital angular momentum states spanning from ℓ=-3 to ℓ=+3 [10].

So far, we have discussed the azimuthal structure of a paraxial beam via a complete set of helical modes. The radial structure must also be determined in order to complete our description of a structured light beam. In the following, we examine three such solutions to the paraxial wave equation, which are of most interest.

3.6.1 Bessel Beams

The simplest family of solutions to the paraxial wave equation in cylindrical coordinates are the so-called Bessel functions. The general profile of these beams has a mathematical structure of

$$E(\rho, \varphi, z) = E_0 J_\ell(k_\rho \rho) e^{i(\ell\varphi + k_z z)} \tag{3.20}$$

where J_ℓ is the ℓth order Bessel function of first kind, ℓ=0,$\pm$1,$\pm$2,$\cdots$ being the topological charge, k_ρ and k_z are the radial and longitudinal wave vectors, with the wave vector $k = \sqrt{k_\rho^2 + K_z^2} = 2\pi/\lambda$. These cylindrically symmetric modes, known as Bessel modes, have a cylindrical intensity distribution independent of z. In other words, they propagate without diffraction, which makes them un-physical to generate in a laboratory environment. They are the simplest theoretical examples of vortex beams.

3.6.2 Laguerre-Gauss Beams

A family of solutions to the paraxial wave equation are the Laguerre-Gauss (LG) modes [11, 12].

The field of an LG beam with a topological charge ℓ and with p radial nodes (p=0,1,2,$\cdots$)is

$$E_{\ell,p}(\rho,\varphi,z) = \frac{E_0}{w(z)}\left(\frac{\sqrt{2}r}{w(z)}\right)^{|\ell|} e^{-r^2/w^2(z)} L_p^{|\ell|}\left(\frac{2r^2}{w^2(z)}\right) e^{-ikr^2/2R(z)} e^{-i\varphi\ell + i(2p+|\ell|+1)tan^{-1}(\frac{z}{z_R})} \tag{3.21}$$

here E_0 is a constant. $w(z)$ is the beam radius at z, given by $w(z) = w_0\sqrt{(1+z/z_R)}$ that slowly varies with z due to diffraction. w_0 is the beam radius at z=0 and $z_R = \pi w_0^2/\lambda$ is the Rayleigh range of the beam. The radius of curvature of the wavefronts is given by $R(z) = z(1+(z_R/z)^2)$. $L_p^{|\ell|}$ are the associated Laguerre polynomials which satisfy the orthonormality condition, $\int\int r\,dr\,d\varphi\, L_p^{\ell *} L_{p'}^{\ell'} = \delta_{p,p'}\delta_{\ell,\ell'}$. The term given by $\tan^{-1} z/z_R$ is the Gouy phase [13]. The Gouy phase yields an additional phase difference of (2p+|ℓ|+1) upon the beam propagation through its focal point from $z/z_R \ll$-1 to $z/z_R \gg$1. The Gouy phase is closely related to the transverse confinement of the modes [13, 14]. The index p characterizes the radial structure of the mode. In addition to the central dark spot, the transverse profile has p dark nodal rings. The first few LG modes are shown in the Fig. 3.4.

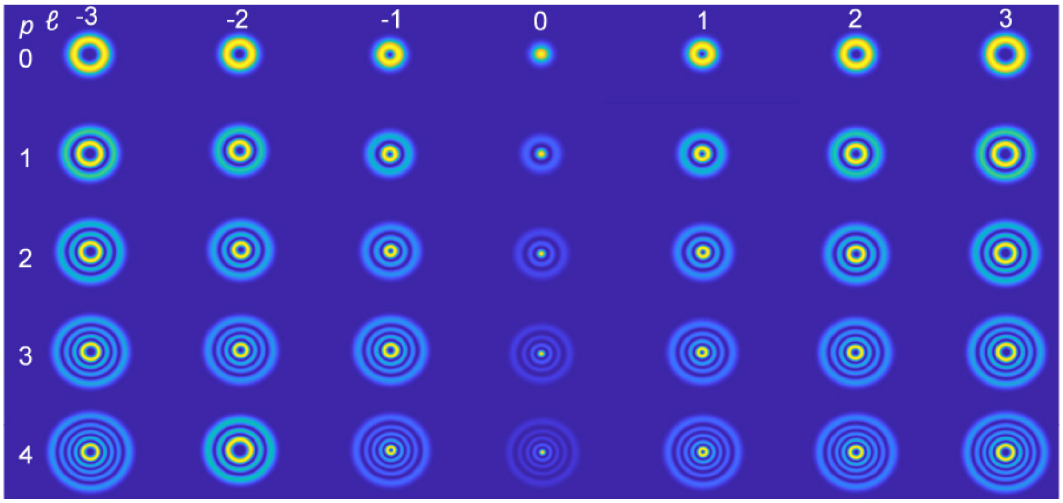

Figure 3.4: Intensity profiles of a set of LG modes with different radial and azimuthal components [15].

3.6.3 Hyper Geometric Gaussian Beams

Finally, it is worth mentioning that another class of solutions to the paraxial wave equation are the so-called hyper geometric gaussian modes, denoted by $|HyGG\rangle_{p\ell}$. The amplitude of these novel modes is proportional to the confluent hypergeometric function, and hence their name. Though these modes do not form an orthonormal set, they do carry a finite power and are physically realizable. It is known that any hypergeometric Gaussian mode with a fixed topological charge can be expanded in terms of an infinite series of Laguerre Gauss modes [16]

$$|HyGG\rangle_{p\ell} = \sum_{q=0}^{\infty} A_{pq} |HyGG\rangle_{q\ell} \tag{3.22}$$

Two types of these beams have been recently introduced and studied. The first type of Hypergeometric Gauss modes is not shape invariant under free propagation. While these beams propagate, a dramatic change of the intensity profile can be seen. The second type, though, suffers very low diffraction upon propagation [16].

3.7 How to obtain light with desired structure?

In this section, we briefly introduce some common methods used for structuring light. The case with q-plates is discussed in detail.

3.7.1 Spiral Phase Plates

Spiral phase plates are used for photons in different frequency ranges [17–19] in order to produce a delay between the components of the polarization vector. When light propagates through a dielectric plate, it acquires an additional phase as compared with free-space propagation. This phase is proportional to the plate thickness $\Phi{=}\xi d$. Therefore, a plate with spiral thickness varying with the azimuthal angle, $d = \zeta\varphi$, will create the corresponding spiral phase in the transmitted wave, $\Phi = \xi\zeta\varphi$. Thus, if the incident wave was a plane wave, the transmitted wave will carry a vortex $e^{i\xi\zeta\varphi}$ with topological charge $\ell = \xi\zeta$, as shown in Fig 3.5.

3.7.2 Diffraction Grating with a Fork Dislocation

The second way of generating vortex beams is through diffraction from a grating with a fork dislocation. The vortex structure in a wave field represents a screw dislocation of the phase front [4, 5, 20]. As shown in Fig. 3.6, a Gaussian beam incident on a diffraction grating with a pitch-fork pattern leads to multiple orders of diffraction, each carrying extra phases which translates into twists in their profile upon propagation [21, 22].

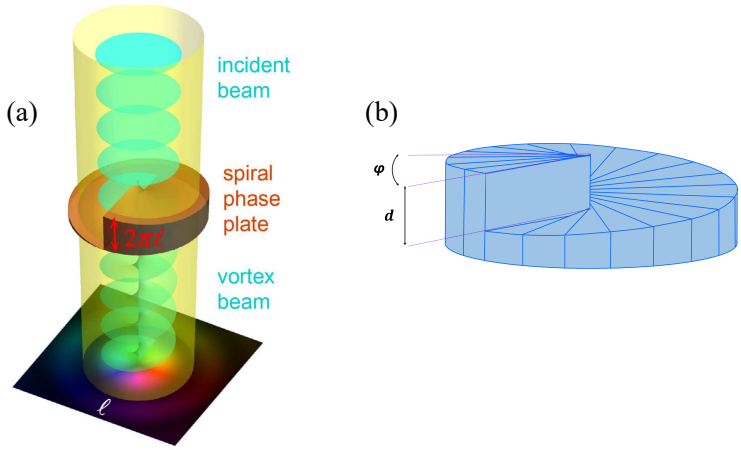

Figure 3.5: (a) Schematic for the generation of vortex beams using a spiral phase plate with a $2\pi\ell$ phase-shift increment around its center (here ℓ=1) [23]. (b) Shows the top surface of the phase plate spirals upward.

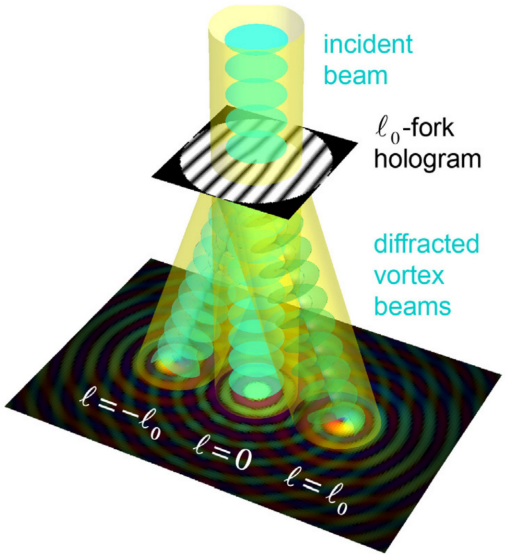

Figure 3.6: Schematic for the generation of vortex beams using a diffraction grating (hologram) with a fork-like edge dislocation of order ℓ_0 (here ℓ_0=1) [23].

If the dislocation in the grating is of order ℓ_0, then the N^{th} order of diffraction transforms the incident Gaussian-like beam (ℓ=0) into a vortex beam with ($\ell=N\ell_0$). Thus, this technique allows the generation of states with an intrinsic orbital angular momentum of any order which is impossible with spin angular momentum.

A computer-programmable device can produce a hologram diffraction grating via manipulating the orientations of liquid crystal molecules in specific patterns using an external

voltage. These devices which are widely used in optics laboratories worldwide, are known as spatial light modulators [24].

3.7.3 q-Plates

q-plates were introduced to the scientific community back in 2006 [25]. Nowadays, q-plates play an essential role in diverse areas and fields, from fundamental research on structured light to applications in innovations and novel devices. To this day, new emerging topics, such as quantum information, have found their protocols through the use of q-plates on the angular momentum of light.

General Features of a q-plate

A typical q-plate is a thin nematic liquid crystal (LC) medium confined to two indium-tin oxide (ITO)-coated plane glasses. Liquid crystals are generally non-homogeneous and non-isotropic media. They are birefringent fluids in which the constituent molecules locally possess a specific orientation. This direction is specified by a unit vector $\hat{n}(r) = (sin\theta\, cos\alpha, sin\theta\, sin\alpha, cos\theta)$, known as the molecular director, where θ=$\theta(r)$ and α=$\alpha(r)$ are the polar angles. What differentiates a q-plate from conventional liquid crystal cells is that in the latter, there is a uniform director over the entire liquid crystal medium, whereas, in the former, the director shows an azimuthal profile or pattern with respect to a point at the centre of the q-plate. Let us consider the horizontal direction (x-axis) as a reference, then the angle between $\hat{n}$ and the reference line is given by a simple linear relation

$$\alpha(\varphi) = q\varphi + \alpha_0 \tag{3.23}$$

Here, φ is the azimuthal angle in the liquid crystal plane, α_0 is the angle of the liquid crystal director on the reference line, and q is the topological charge of the liquid crystal which characterizes the central pattern singularity. In other words, in any circular counter-clockwise path around the origin, the liquid crystal director makes exactly q turns around itself. If the liquid crystal director's rotation is clockwise, then q may as well be negative. Since the director indicates an orientation in the liquid crystal, from a physical point of view $\hat{n}$ and -$\hat{n}$ are equivalent, thus the topological charge q may also acquire half integer values. The orbital angular momentum quantum number which a q-plate generates is given by $2q$. Apart from q, there is a phase retardation parameter δ indicating the total birefringent phase retardation, which is naturally a function of the liquid crystal thickness. The δ parameter can be modified by applying an external electric field to the liquid crystal medium, hence manipulating the orientation of the liquid crystal molecules and the director resulting in a change in the optical retardation of the light beam that passes through the q-plate [26]. Thus one can effectively control the phase retardation by turning the external field on and off.

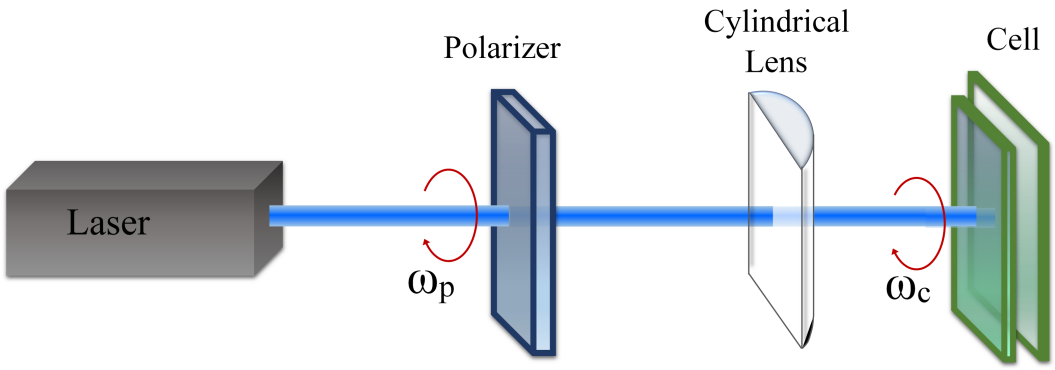

Figure 3.7: Schematic of simplified photo-alignment technique to fabricate a q-plate. Both the polarizer and the cell are placed in motorized rotational stages, with angular speeds of ω_p and ω_c, respectively.

Fabricating q-plates

Here, we briefly introduce a method that is used to fabricate q-plates without mentioning the technical details. A light source, a polarizer, a cylindrical lens, and a glass cell are the main elements required in q-plate fabrication setup, as shown in Fig. 3.7. Two indium-tin oxide (ITO)-coated glass are used as substrates to form the LC cell. Each glass is spin-coated with a photosensitive solution (sulphonic azo-dye). The next step is the most-applied method used in fabricating a q-plate in a laboratory environment, a so-called photo-alignment method [26–28]. In these methods, one applies a blue or ultraviolet light in the crystal medium and slowly scans the entire plate in the process of writing the pattern on the azo-dye layer. The molecules tend to orient themselves in a direction perpendicular to the polarization of the light beam. The polarization of the incident light is controlled by a polarizer. This photo-alignment process is quite critical, and the result depends on the light intensity, wavelength, exposure time, and many other parameters [29]. Using this method, one can obtain any integer, half-integer, a positive or negative value for the topological charge, q. This high degree of freedom is guaranteed by the photo alignment procedure making one capable of writing any pattern on the plate, given it has azimuthal cylindrical symmetry. The polarized beam passes through a cylindrical lens, which allows an illumination only on a narrow angular sector of the cell. Both the polarizer and the cell are placed in motorized rotational stages, with angular velocities of ω_p and ω_c, respectively. The ratio between the angular rotations of these two elements, determines the q value, q=1$\pm\,\omega_p/\omega_c$. The "+" and the "−" signs are used when the two elements rotate in the same and opposite directions, respectively.

It is worth mentioning that masks and other more refined techniques allow one to obtain a generic pattern and thus opening a window to investigate the space of complex beams that can be produced with this method. More details of q-plate fabrication can be bound in [29].

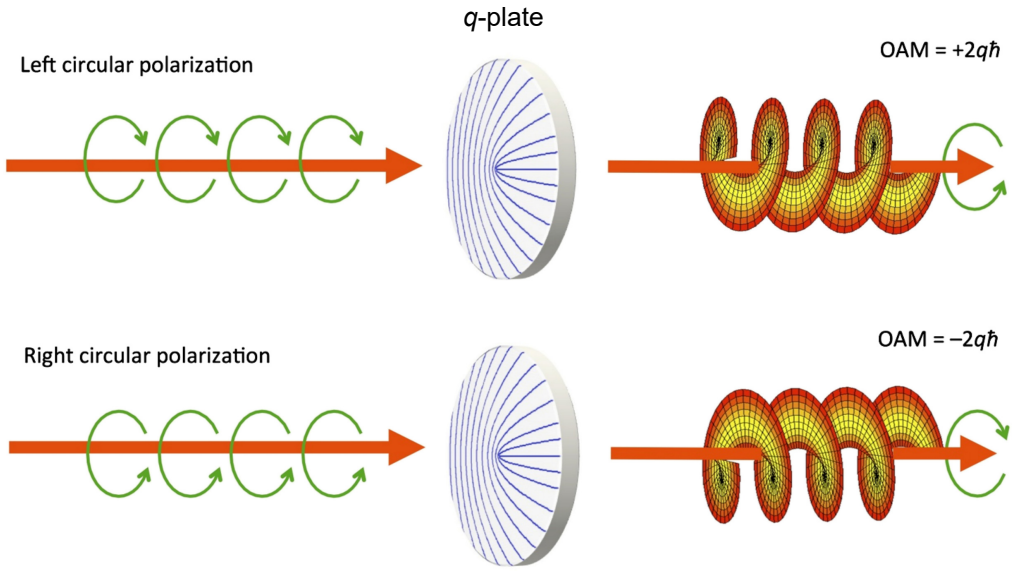

Figure 3.8: q-plate working principle in the optimal case $\delta = \pi$. Incident left (right) circularly polarized light with no OAM is converted into a right (left) circularly polarized light possessing an OAM of $+2q\hbar$ (-$2q\hbar$) per photon [30].

Operating Principle of q-plates

By applying an AC voltage to the electrodes of a q-plate, one can control the birefringent phase retardation δ for a given operation wavelength and temperature. When a beam traverses a q-plate with topological charge q and phase retardation δ, a fraction $\sin^2(\delta/2)$ of the photons in the beam has its spin angular momentum reversed and changes its orbital angular momentum by an amount $2q$. The remaining fraction of photons, $\cos^2(\delta/2)$ remains in its initial spin angular momentum and orbital angular momentum states [25]. Theoretically, as with any optical elements such as beam splitters, wave plates, and etc., the operation of q-plates can be represented by unitary operators

$$\begin{aligned} U|L\rangle &= \cos\left(\frac{\delta}{2}\right)|L\rangle + i\sin\left(\frac{\delta}{2}\right)|R\rangle \\ U|R\rangle &= \cos\left(\frac{\delta}{2}\right)|R\rangle + i\sin\left(\frac{\delta}{2}\right)e^{-2i\alpha(\varphi)}|L\rangle \end{aligned} \tag{3.24}$$

These relations show that a phase retardation of π changes all the photons from left polarization to right polarization and vice versa. In this process, photons also gain a helical phase of $\pm 2\alpha(\varphi) = \pm 2(q\varphi + \alpha_0)$. q-plates with a topological charge of q=1 are particularly interesting as they completely transfer the spin angular momentum to orbital angular momentum [31]. Thus, these q-plates can be considered devices that couple the spin and orbital angular momentum degrees of freedom. A schematic representation of the operation of a q-plate for a phase retardation of π is seen in Fig. 3.8.

The most straightforward applications of the q-plate are for generating optical beams carrying OAM starting from ordinary Gaussian beams or for modifying the input OAM according to prescribed laws. In this, q-plates are similar to ordinary spiral phase plates, but with several advantages, such as polarization control of the OAM variation, electrical switching and tuning, and multiple wavelength operation, etc.

Key Advantages of Using a q-plate

Compared to other technologies to produce structured light beams (such as spiral phase plates and holographic elements), the q-plates have some practical advantages. These devices are thin, compact, and stable elements working in high efficiency (85%) transmission geometry; therefore, aligning them is not challenging. The q-plate does not induce any light deflection, and hence, astigmatism in the transmitted beam. The q-plates can be electrically controlled. It allows us to turn them on/off or tune them for partial OAM conversion that enables us to shift the phase singularities (corresponds to the null intensity regions) in the beam. Moreover, the OAM sign (the direction of the twist in the phase front) is easily controlled by the input polarization. Exploiting this significant feature alongside several q-plates arranged in cascade enables one to generate superpositions of SAM/OAM states (vector vortex beams and polarization-singular beams).

Bibliography

[1] A. O'Neil, I. MacVicar, L. Allen, and M. Padgett, "Intrinsic and extrinsic nature of the orbital angular momentum of a light beam", Phys. Rev. Lett. 88, 053601 (2002).

[2] E. Karimi, achieved at: https://en.wikipedia.org/wiki/Angular_ momentum_ of_ light

[3] J. Masajada, B. Dubik, "Optical vortex generation by three plane wave interference", Opt. Commun. 198, 21-27 (2001).

[4] J. F. Nye, M. V. Berry, "Dislocations in wave trains", Proc. Roy. Soc. A 336, 165-190 (1974).

[5] M. R. Dennis, K. O'Holleran, M. J. Padgett, Singular optics: Optical vortices and polarization singularities, Prog. Opt.53 (2009) 293-363

[6] H. Wolter, Zur frage des lichtweges bei totalreexion, Z. Naturf. 5 (1950) 276-283. translated to English and reprinted as H. Wolter, "Concerning the path of light upon total reection", J. Opt. A: Pure Appl. Opt. 11, 090401 (2009).

[7] M. Born, E. Wolf, "Principles of Optics", Cambridge University Press, 1999, W. Braunbek, G. Laukien, Einzelheiten zur halbebenen-beugung, Optik 9 174-179 (1952).

[8] E. Karimi, available on: https://en.wikipedia.org/wiki/Spin_ angular_ momentum_ of_ light

[9] E. Karimi, "Generation and manipulation of laser beams carrying orbital angular momentum for classical and quantum information applications", PhD thesis (2009).

[10] E. Cohen, H. Larocque, F. Bouchard, F. Nejadsattari, Y. Gefen, and E. Karimi, "Geometric phase from AharonovBohm to PancharatnamBerry and beyond", Nature Reviews Physics, 1, pages 437449 (2019).

[11] A. E. Siegman, "Lasers", Mill Valley, California, (1986).

[12] L. Allen, M. W. Beijersbergen, R. J. C. Spreeuw, and J. P. Woerdman, "Orbital angular momentum of light and the transformation of laguerre-gaussian laser modes", Physical Review A, 110(11), 8185 (1992).

[13] S. Feng, H. G. Winful, "Physical origin of the Gouy phase shift", Opt. Lett. 26 485-487 (2001).

[14] R. L. Phillips, L. C. Andrews, "Spot size and divergence for Laguerre Gaussian beams of any order", Appl. Opt. 22 643-644 (1983.)

[15] A. Trichili, K.Park, M. Zghal, B. S. Ooi, and M. Alouini, "Communicating Using Spatial Mode Multiplexing: Potentials, Challenges, and Perspectives", IEEE COMMUNICATIONS SURVEYS and TUTORIALS, VOL. 21, NO. 4, FOURTH QUARTER (2019).

[16] E. Karimi, G. Zito, B. Piccirillo, L. Marrucci, and E. Santamato, "Hypergeometric-Gaussian modes", OPTICS LETTERS, Vol. 32, No. 21 (2007).

[17] M. W. Beijersbergen, R. P. C. Coerwinkel, M. Kristensen, J. P. Woerdman, "Helical-wavefront laser beams produced with a spiral phaseplate", Opt. Commun. 112 321-327 (1994).

[18] G. A. Turnbull, D. A. Robertson, G. M. Smith, L. Allen, M. J. Padgett, "The generation of free-space Laguerre-Gaussian modes at millimetre-wave frequencies by use of a spiral phaseplate", Opt. Commun. 127 183-188 (1996).

[19] A. G. Peele, P. J. McMahon, D. Paterson, C. Q. Tran, A. P. Mancuso, K. A. Nugent, J. P. Hayes, E. Harvey, B. Lai, I. McNulty, "Observation of an x-ray vortex", Opt. Lett. 27 1752-1754 (2002).

[20] M. S. Soskin, M. V. Vasnetsov, Singular optics, Prog. Opt. 42 (2001) 219-276

[21] V. Y. Bazhenov, M. Vasnetsov, M. Soskin, "Laser beams with screw dislocations in their wavefronts", JETP Lett. 52 429-431 (1990).

[22] N. R. Heckenberg, R. McDu, C. P. Smith, H. Rubinsztein-Dunlop, M. J. Wegener, "Laser beams with phase singularities", Opt. Quant. Electron. 24, S951-S962 (1992).

[23] K.Y. Bliokh, I.P. Ivanov, G. Guzzinati, L. Clark, R. Van Boxem, A. Béché, R. Juchtmans, M. A. Alonso, P. Schattschneider, F. Nori, J. Verbeeck, "Theory and applications of free-electron vortex states", Physics Reports 690, 170 (2017).

[24] Jack, B., Yao, A. M., Leach, J., Romero, J., Franke-Arnold, S., Ireland, D. G., Barnett, S. M., Padgett, M. J., "Entanglement of arbitrary superpositions of modes within two-dimensional orbital angular momentum state spaces", Physical Review A. 81 (4): 043844 (2010).

[25] L. Marrucci, C. Manzo, and D. Paparo, "Optical spin-to-orbital angular momentum conversion in inhomogeneous anisotropic media", Phys. Rev. Lett. 96(16), 163905 (2006).

[26] B. Piccirillo, V. D'Ambrosio, S. Slussarenko, L. Marrucci, and E. Santamato, "Photon spin-to-orbital angular momentum conversion via an electrically tunable q-plate", Appl. Phys. Lett. 97, 241104 (2010).

[27] S. Slussarenko, A. Murauski, T. Du, V. Chigrinov, L. Marrucci, and E. Santamato, "Tunable liquid crystal q-plates with arbitrary topological charge", Opt. Express 19, 40854090 (2011).

[28] S. Slussarenko, B. Piccirillo, V. Chigrinov, L. Marrucci, and E. Santamato, "Liquid crystal spatial-mode converters for the orbital angular momentum of light", J. Opt. 15, 025406 (2013).

[29] A. Rubano, F. Cardano, B. Piccirillo, and L. Marrucci, "Q-plate technology: a progress review", Journal of the Optical Society of America B, Vol. 36, No. 5 (2019).

[30] L. Marrucci, "The q-plate and its future", Journal of Nanophotonics, 7, 078598-2 (2013).

[31] L. Marrucci, C. Manzo, and D. Paparo, "Pancharatnam-Berry phase optical elements for wavefront shaping in the visible domain: switch able helical modes generation", Appl. Phys. Lett. 88, 221102 (2006).

Chapter 4

Nanostructuring with Femtosecond Structured-Light

In conventional laser processing of materials, Gaussian beams are often used. Recently, there has been significant interest in material processing with non-Gaussian beams both from a fundamental perspective as it enables to manipulate light-matter interaction and from an applied perspective as it enables to fabricate complex structures. Specifically, optical vortices in the form of helical beams carrying an orbital angular momentum have been shown to produce micro-needles that exhibited spiral conical structures with the handedness of the optical vortex pulse imprinted on them. However, these chiral structures could be produced only with nano- and picosecond pulses and not with femtosecond pulses. Moreover, the role of laser polarization on the formation of these features remained unclear, although periodic patterns were fabricated in a multi-pulse irradiation regime that preserved the laser polarization.

In this chapter, the formation of polarization dependent nano-cone on silicon with a single femtosecond vortex pulse is demonstrated, in contrast to previous reports. We showed that a $\sim$ 1 μm high nano-cone with a tip dimension of $\sim$ 70 nm is formed in the middle of the ablation crater. We also simulated the action of the laser pulse on the dynamics of the molten silicon and demonstrated that the nano-cone is formed due to the radial inward motion of the molten silicon. We showed the nano-cone height to decrease for linearly polarized OV beam compared to circular polarization due to an asymmetry in the fluid motion arising from transient light-plasma interaction.

We believe our findings have a broad appeal in two aspects: fundamentally, it could shed new light on intense vortex light-matter interaction, and technologically, it opens potential applications in material manufacturing industries such as solar cell technology, microelectronic devices, and high harmonic generation in solids.

4.1 Introduction

Cone structures, also called pillars, needles, spikes or peaks, are a typical structure created by the femtosecond Gaussian laser pulse irradiation on materials. They are produced in the form of randomly positioned dense forests whose formation can be controlled by the laser parameters, ambient conditions, or chemical composition of the irradiated sample. For example, Fadeeva *et al.* [1] has demonstrated that the laser fluence has a significant effect in the formation phenomena of the spikes. By increasing the laser energy density from 0.36 to 3.6 J/cm^2, 100 pulses, the aspect and height of the spikes formed on the surface of Si samples drastically changed.

The effect of the number of pulses, at a constant fluence above the ablation threshold, was also studied by Raillard *et al.* [2]. Cone structures have been shown to appear when the number of pulses exceeds a certain value. In this study, it is shown that cones are generated randomly, disordered, and with various sizes in the middle of the ablated region. There have also been several studies performed by Tull *et al.* [3] on silicon that revealed by increasing the number of pulses creation of highly ordered and sharp conical structures is possible. Laser polarization also has an impact on spikes formation. In the case of a linearly polarized laser, Tull *et al.* also reported that the orientation of the major diameter of the cones elliptical basis is aligned perpendicular to the laser polarization.

However, in all these experiments, the conical structures are generated upon irradiation of a high number of pulses. Moreover, cones are randomly distributed, and their shape, aspect, thickness, size, and repartition are not regular and cannot be individually controlled.

Dealing with this randomness was our motivation to employ optical vortex beams to fabricate individual nano-cones under single pulse irradiation, with an ability to control their dimensions. The generated structures can be nicely placed in a precise array.

4.2 Mechanism of the Nano-cone Formation

From the fluid dynamics model, the formation of a nanocone at the center of the ablated region irradiated by an annular beam was anticipated.

The interaction of femtosecond pulses (with either Gaussian or vortex intensity profile) at 800 nm (photon energy of 1.55 eV) with silicon (bandgap of 1.1 eV) is dominated by linear and two-photon absorption. During the energy absorption process, free carriers are generated. Later on, the doughnut-shaped intensity distribution of the laser pulse translates to the spatial profile of the carrier density and hence into a lattice temperature distribution that is zero at the center and high in a ring-shaped band in the mid-region and falls off to the edges. The temperature distribution creates a thin molten layer in silicon (a few hundred nanometers, determined by the penetration depth). Molten silicon then flows in two opposite directions: (1) radially outward to the peripheral region and (2) radially inwards to the central region of the crater. Two main forces can be considered to affect

the flow of molten layer: (a) thermocapillary forces (also known as Marangoni flow), or (b) hydrodynamic forces exerted by the plasma pressure on the surface.

Femtosecond pulse irradiation on the silicon surface forms a molten layer and strong radial temperature gradients at the liquid surface. These temperature gradients produce radial gradients in the surface tension, which, in turn, generate radial convective liquid flows (Thermocapillary or Marangoni effect) [4]. In fact, in thermocapillary flow, the intensity profile of the vortex laser beam induces a temperature gradient on the surface that causes a surface tension gradient. This surface tension decreases with growing melt temperature and drives the molten material from the hot regions to the cold regions. The required time attributed to this process is defined as [5]

$$\tau_M \approx \frac{\mu L^2}{\gamma_T T_m \langle h_m \rangle} \tag{4.1}$$

where $\langle h_m \rangle$ is an average melt depth, L is a typical radial dimension of the crater, γ_T is a constant defined as the temperature coefficient of the surface tension, T_m is the melting temperature, and μ is the viscosity of the molten material.

Thermocapillary effect most likely occurs in materials where the surface tension decreases as the fluid gets hotter [5], as what we observed in our experiments performed on silicon. However, in the case of a glass irradiated by laser pulses, the fluid motion would be from the cold region to the hot region. The reason is that a glass target has a high viscosity and a flow timescale much longer than the typical melt timescale; therefore, the thermocapillary effect in the glass is not significant.

Hydrodynamics forces, on the other hand, are induced by pressure gradients that are exerted by the plasma onto the molten silicon. In fact, these forces induce a gradient of ablation pressure on the surface that drives the melt flow to the cold regions. This effect is key in the rim formation: a gradient of ablation pressure on the molten surface induce a lateral melt flow to the periphery [6]. These pressure gradients are large at the plasma/air interface, i. e., near the edges of the molten layer that results in a melt flow to the periphery and gives rise to a thin rim at the edge. This effect, when accompanied by high pulse energy, can cause the peripheral rim to look much like a splash of a liquid.

It has been shown that a rim with the height of 150 nm can be formed within the first nanoseconds of the ablation process [5]. As the generated plasma expands, its pressure drops quickly, from millions of atm in the first tens of picosecond to several tens of atm within a few tens of nanoseconds [7]. During this time, the plasma pressure gradient, which is high at the periphery, pushes the molten layer underneath the plasma and forms an elevated rim surrounding the ablation crater. The created rim will eventually tilt outwards because of the pressure difference between the high pressure plasma inside and the atmospheric air pressure outside.

Moreover, the gradient of plasma pressure induces melt flow from the high-pressure middle region at the spot center towards the low-pressure central region of the molten pool. It makes this effect to be significantly involved in the nanocone formation. The characteristic time associated with the pressure-driven flow is [5]

$$\tau_p \approx \frac{\mu L^2}{\langle P_{pl} \rangle \langle h_m \rangle^2} \tag{4.2}$$

where $\langle P_{pl} \rangle$ is an average plasma pressure. In the case of silicon, both characteristic times are in the same order, meaning that both types of forces are involved in the fluid motion and nanocone formation.

4.3 Polarization Dependent Nanostructuring of Silicon with Femtosecond Vortex Pulse

Author Contribution

In the following, my paper published in APL PHOTONICS journal is presented. The experiments using vortex beams and Gaussian beams were performed by M. G. Rahimian and H. Al-Khazraji, respectively, at Ultrafast Photonics lab, University of Ottawa, ON, under the supervision of V. R. Bhardwaj. M. G. Rahimian conducted data analysis, SEM and AFM measurments, and figure preparation. Theoretical simulation and q-plate fabrication had been performed by F. Bouchard and E. Karimi. P. B. Corkum, E. Karimi, and V. R. Bhardwaj designed the experiment and analysed the data. M. G. Rahimian wrote the first draft of the manuscript. All authors contributed to the final manuscript.

APL PHOTONICS **2**, 086104 (2017)

Polarization dependent nanostructuring of silicon with femtosecond vortex pulse

M.G. Rahimian, F. Bouchard, H. Al-Khazraji, E. Karimi, P.B. Corkum, V.R. Bhardwaj

Department of Physics, Advanced Research Complex, University of Ottawa, 25 Templeton Street, Ottawa, ON, K1N 6N5, Canada

We fabricated conical nanostructures on silicon with a tip dimension of ~ 70 nm using a single twisted femtosecond light pulse carrying orbital angular momentum ($\ell = \pm 1$). The height of the nano-cone, encircled by a smooth rim, increased from ~ 350 nm to ~ 1 μm with the pulse energy and number of pulses whereas the apex angle remained constant. The nano-cone height was independent of the helicity of the twisted light, however, it reduced for linear polarization compared to circular at higher pulse energies. Fluid dynamics simulations show nano-cones are formed when compressive forces arising from the radial inward motion of the molten material pushes it perpendicular to the surface and undergoes re-solidification. Simultaneously, the radial outward motion of the molten material re-solidifies after reaching the cold boundary to form a rim. Overlapping of two irradiated spots conforms to the fluid dynamics model. [http://dx.doi.org/10.1063/1.4999219]

Light-matter interaction can be controlled by manipulating the beam polarization, spatial intensity and phase profile. Structured light in the form of non-conventional beam shapes, such as Bessel, Airy, Laguerre-Gaussian or optical vortex (OV) beams have been used in optical trapping and manipulation [8, 9], atom guiding [10, 11] and super resolution microscopy [12, 13]. Recently, structured light has been extended to material processing [14–16], specifically OV beams [17,18,20–26]. Optical vortices in the form of helical beams have an annular intensity profile with an orbital angular momentum $\ell\hbar$ per photon, where ℓ indicates the number of twists in the helical wavefront in one wavelength and its sign determines the chirality of the helix. They can also possess spin angular momentum $s\hbar$ per photon associated with polarization helicity with values of $s = \pm 1$ corresponding to the left and right circular polarizations. OV beams are produced from a fundamental Gaussian mode using holograms [27], cylindrical lenses [28],spiral phase plates [29, 30], S-waveplates [31], and q-plates [32–35].

Material processing with a single nano- and pico-second OV pulse produced micro-needles [17, 18, 23–25] that exhibited spiral conical structures with the handedness of the optical vortex pulse imprinted on them. Their growth was controlled with the number of pulses. In contrast, micro-needle/nanopillar formation with a single femtosecond OV pulse remains ambiguous. Annular ablation craters with no features in the centre were produced by loosely focusing the OV pulse [14, 18]. However, tight focusing produced a nanopillar that disappeared when (a) the polarization was switched from radial to azimuthal, and (b) a second radially polarized pulse was incident on the sample [19]. In multi-pulse ablation, complex periodic surface patterns were fabricated using femtosecond OV beams with different spatial distributions of the state of polarization [16, 20–22]. However, the role of laser polarization remains unclear in nano-cone formation with a single laser OV pulse.

In this paper, we demonstrate polarization dependent nano-cone formation with a single femtosecond OV pulse with $\ell = \pm 1$. By manipulating the spatial profile of the laser beam, we show that irradiation of silicon with a single femtosecond Gaussian pulse formed a rim around the ablation crater while an OV pulse formed a nano-cone encircled by a rim, irrespective of laser polarization. We simulate the action of the laser pulse on fluid dynamics of the molten silicon and show that the radial inward (outward) motion of the molten silicon forms the nano-cone (rim). We demonstrate the nano-cone height to decrease at higher pulse energies for linear compared to that of circular polarization. This behaviour was attributed to an asymmetry in the radial inward fluid motion that arises from transient light-plasma interaction.

Linearly polarized light from a Ti:Sapphire laser (operating at 1 kHz repetition rate and producing 800 nm, 45 fs pulses) was transformed into left- or right-circularly polarized beam ($s = \pm 1$) by a quarter-wave plate (QWP). A q-plate with a topological charge of $q = 1/2$ produced OV beams with $\ell = \pm 1$ and inverted polarization ($s = \mp 1$) [33]. A linearly polarized OV beam ($s = 0$, $\ell = \pm 1$) was produced by a second QWP and a polarizer. Electrically detuning the q-plate generated Gaussian beams. A 0.25 NA (16×) aspheric objective focused the femtosecond pulse onto a p-type silicon surface [(100) orientation] mounted on a three-axis translation stage.

For a Gaussian beam, the focal spot size was measured to be 1.8 ± 0.1 μm using the knife-edge method. For an OV beam, the spot size, defined as the diameter of the maximum intensity, was measured to be 2.8 ± 0.2 μm compared to a theoretical value of 2.3 μm [36]. The ablated regions were characterized by a scanning electron microscope (SEM) with the electron beam perpendicular to the sample (zero tilt) and at an angle of 88° and by an atomic force microscope (AFM) in non-contact mode.

Figure 4.1 shows SEM images [(a) and (b)] and the corresponding 3D AFM profiles [(c) and (d)] of micro-structures on silicon induced by single, circularly polarized, femtosecond Gaussian and OV pulses (ℓ = -1, s = +1), respectively. The Gaussian pulse produced a rim with a uniform height of $\sim$ 50 nm around a $\sim$ 70 nm deep ablation crater. Besides the rim, OV pulse also produced a nano-cone in the middle of the ablation crater protruding $\sim$ 450 nm above the surface. Similar structures were observed for intrinsic and n-type silicon. The single shot ablation threshold of silicon, defined as the lowest energy at which

ablation features were visible under SEM, was determined to be 55 nJ (19 nJ) for an OV (Gaussian) beam corresponding to peak laser fluence of 0.41 J/cm^2 (0.37 J/cm^2), in good agreement with the published data [20, 37–39]. A small asymmetry in the rim shape was due to a slight misalignment of the beam through the q-plate.

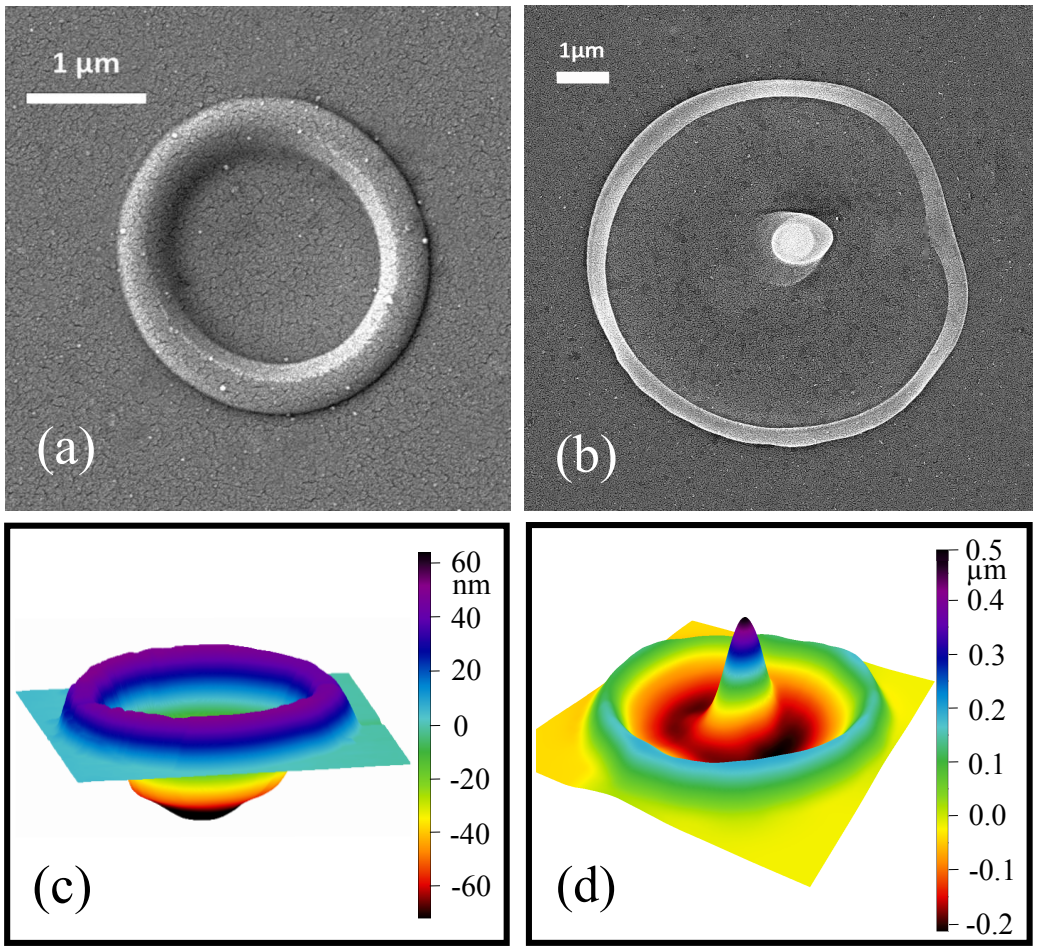

Figure 4.1: SEM (a, b) and AFM (c, d) images of surface topography induced by a single femtosecond laser pulse in p-type silicon [(100) orientation] with circularly polarized Gaussian and vortex beams (ℓ = -1, s = +1) with pulse energies of 150 nJ and 310 nJ, respectively.

Evolution of the ablation crater features with pulse energy for a single femtosecond vortex pulse is shown in Fig. 4.2. Four key observations can be made.

First, the nano-cone height was independent of the handedness of the twisted light ($\ell = \pm 1$) with spin ($s = \mp 1$), corresponding to a total angular momentum, $j = \ell + s = 0$. Formation of a nano-cone with a single femtosecond OV pulse differs from previous reports in three aspects. (i) Only pico- and nano-second pulses produced micro-needles [18], while femtosecond pulses produced annular ablation craters with no features in the centre. (ii) Ablation with a single twisted nanosecond OV pulse with $j = 0$ produced no

central protuberance [25]. It required overlapping of several twisted light pulses to produce a nanostructure. (iii) The tightly focused circularly polarized femtosecond vortex pulse ablated the material differently depending on the polarization handedness of light [40].

Second, the nano-cone height increased with pulse energy at two different rates: ~ 0.6 nm/nJ and 0.2 nm/nJ below and above 600 nJ, respectively, for left- and right-circular polarizations ($j = 0$).

Third, the nano-cone height increased at the same rate for linear ($j = +1$) and circular ($j = 0$) polarizations up to 600 nJ. Beyond this energy, the nano-cone height decreased for linear polarization at a rate of $\sim$1.3 nm/nJ (highlighted by an ellipse). This is discussed below in terms of an asymmetry in compressive forces that causes nano-cone formation.

Fourth, rim height and crater depth increased with pulse energy at the same rate for all three polarizations.

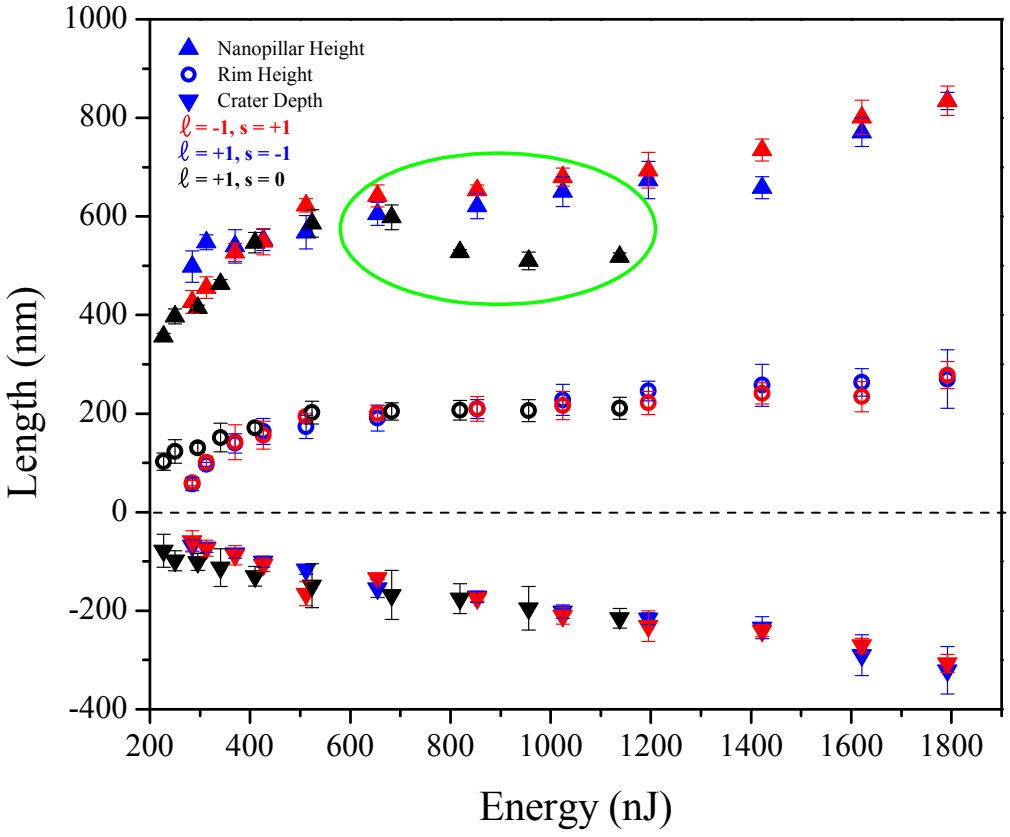

Figure 4.2: Nano-cone height ($\triangle$), rim height ($\bigcirc$) and crater depth ($\triangledown$) relative to the sample surface as a function of pulse energy for three different cases; (i) $\ell = -1$, $s = +1$ (red), (ii) $\ell = +1$, $s =$ -1 (blue), and (iii) $\ell = +1$, $s = 0$ (black). In all cases, a single femtosecond OV pulse irradiated the sample.

Figure 4.3 shows variation of the nano-cone width, measured at the surface, and the apex angle with pulse energy. The nano-cone width varied from 1.4 μm to 1.9 μm with

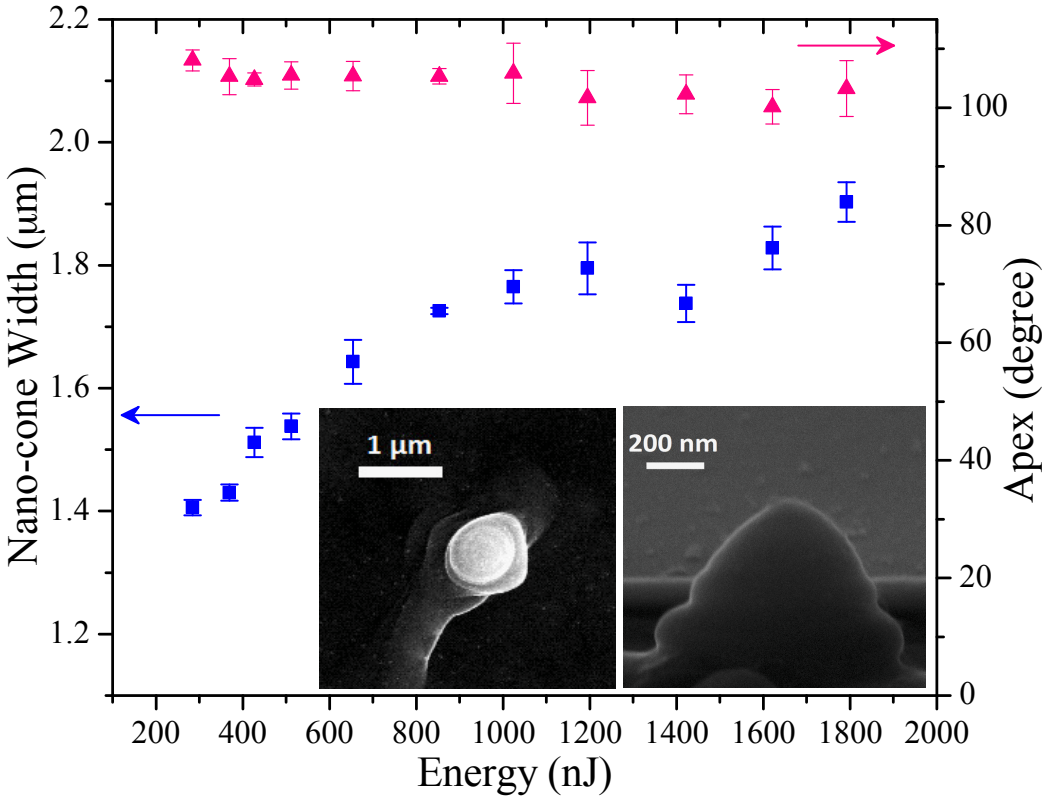

Figure 4.3: Nano-cone width (left axis) and apex angle (right axis) as a function of pulse energy for a single femtosecond OV pulse ($\ell = +1$, $s =$ -1). The insets show SEM images of a nano-cone at a pulse energy of 370 nJ; top view (left panel) and side view at a tilt angle of 88° (right panel).

two different rates 0.6 nm/nJ (0.18 nm/nJ) below (above) 700 nJ, similar to the height. However, the apex angle (measured with an AFM and SEM) remained nearly constant at 105°, decreasing marginally at higher energies. The radius of curvature of the nano-cone was about 70 nm. The insets show SEM images of the nano-cone at a pulse energy of 370 nJ. While the top view (left panel) suggests a spiral conical structure, it could not be confirmed by the side view (right panel) even when the handedness of the twisted light was changed. In contrast, spiral needles of several microns in length were produced with pico- and nano-second pulses [18, 24, 25]. This could be due to significantly lower height of the nano-cone and shorter duration of the OV pulse, thereby obscuring the effects of the twisted light.

The height of the nano-cone induced by the OV pulse of fixed energy increased with the number of laser pulses as shown in Fig. 4.4. However, the aspect ratio, defined as the ratio of the height of the nano-cone to its width, varied marginally from ~ 0.38 for a single pulse to ~ 0.45 for 5 pulses. This was in contrast to the narrowing of the micro-needle observed with nanosecond light pulses [25]. SEM images show that with increased number of laser pulses, more molten material was pushed to the outer rim forming nano droplets.

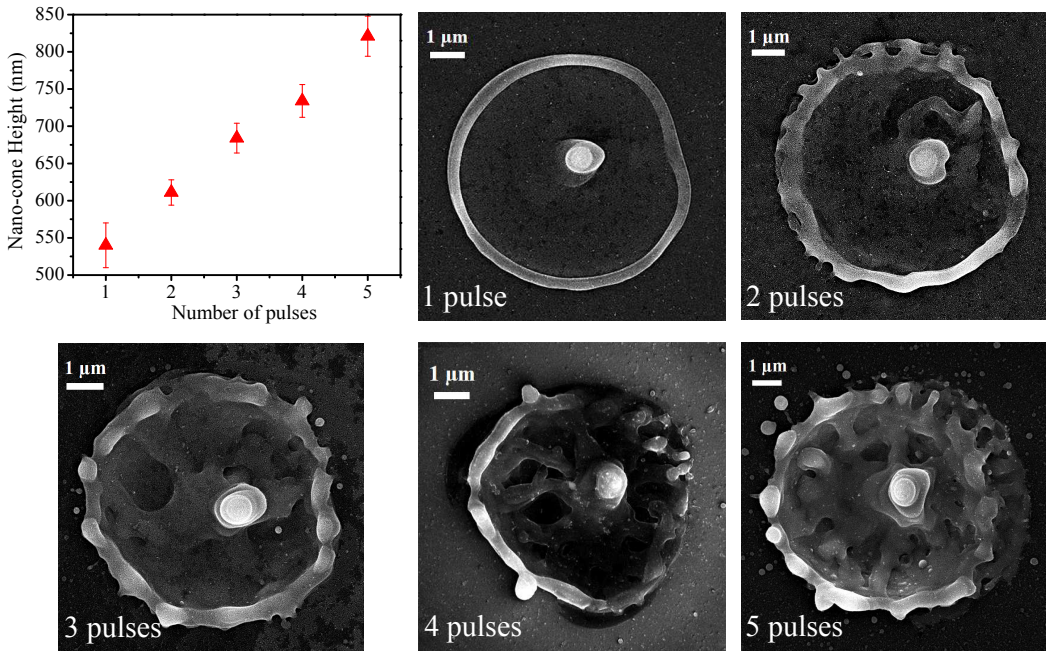

Figure 4.4: Nano-cone height for different number of laser pulses for a fixed energy of 310 nJ ($\ell = -1$, $s = +1$). Also shown are SEM images.

Also, the inside of the ablation crater developed ripples.

Polarization dependent rim formation on silicon irradiated by a single femtosecond Gaussian pulse has been recently observed [41–43] and discussed in terms of fluid dynamics [41] which can be extended to the vortex pulse. The annular intensity distribution of the OV beam is mapped onto the spatial profile of the free carriers generated by linear and two-photon absorption [Fig. 4.5(a)]. Picoseconds later, when energy of the free carriers is transferred to the lattice, the temperature distribution retains the shape of OV beam intensity distribution [Fig. 4.5(b)]. When melting occurs on nanoseconds, only a thin layer of molten silicon is formed, determined by the skin depth d_s. Thermocapillary [44–46] and/or hydrodynamic forces [47] displace the molten silicon radially outward to the periphery and also radially inward to the centre of the crater [Fig. 4.5(c)]. The outward motion leads to rim formation similar to a Gaussian beam. The inward motion leads to a compressive force that pushes the molten material away from the surface. Rapid expansion causes resolidification into a nano-cone [Fig. 4.5(d)]. The temporal evolution of the silicon micro-needle formation was recently captured with an ultra-high speed camera [18].

To gain further insight, we simulated the action of the short laser pulse on the fluid dynamics of the molten silicon. We solved the continuity and Navier-Stokes equations using the methodology of Schwarz-Selinger *et al.* [44] under the assumption of incompressibility, large viscosity, and steady-state flow. To simulate the effect of laser polarization with an asymmetric distribution, we have generalized the calculation to the full two-dimensional transverse coordinate (r and ϕ or x and y) and extended it to include Laguerre-Gaussian intensity profile. The boundary conditions are such that the fluid velocity must vanish at

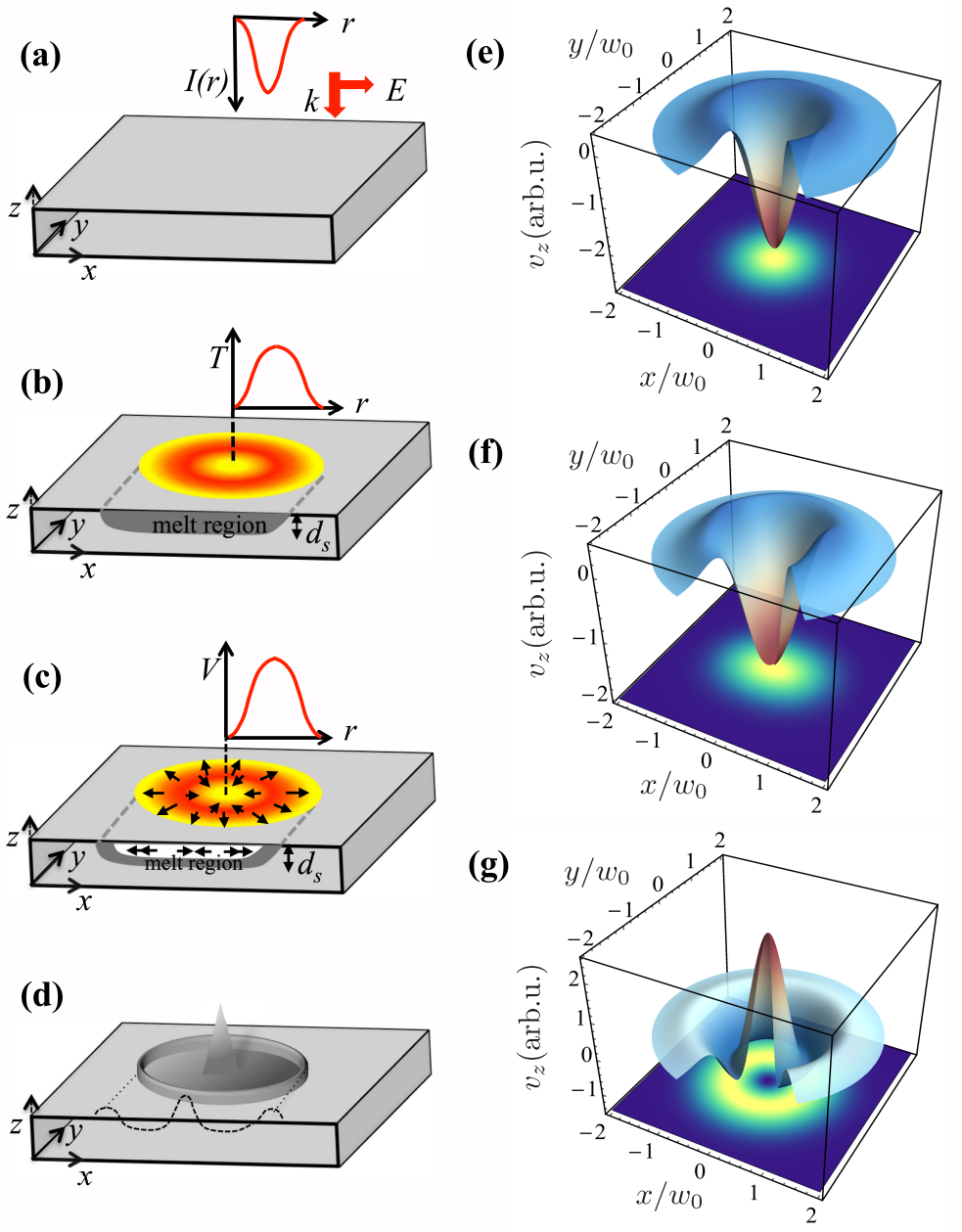

Figure 4.5: (a) - (d) Schematic showing rim and nano-cone formation with an OV beam at different stages of the interaction. (a) Intensity distribution of the incident pulse. k and E are propagation and polarization directions. (b) Spatial profile of the temperature distribution - d_s is the melt layer thickness. (c) Displacement of molten silicon indicated by arrows and melt layer velocity profile due to the exerted forces. (d) Nano-cone (rim) formation by radial inward (outward) motion of molten silicon. (e) - (g) Mass transport $v_z(r, \phi)$ for several temperature distributions (shown at the bottom) given by (e) symmetric Gaussian profile, (f) an asymmetric Gaussian profile and (g) a symmetric Laguerre-Gaussian profile with mode index of $\ell = 1$ and $p = 0$. The asymmetry in (f) was obtained by multiplying the Gaussian distribution by $(1 + y^2)$, where we consider the first order symmetric distortion.

the bottom of the molten material and that the fluid velocity at the surface is given in relation to the surface tension, i.e., $\mathbf{v} = 0$ at $z = -h$; $\eta\left(\partial_z v_r + \partial_r v_z\right) = \partial_r \alpha$ at $z = 0$; $\eta\left(\partial_z v_\phi + r^{-1}\partial_\phi v_z\right) = r^{-1}\partial_\phi \alpha$ at $z = 0$. Here, η is the dynamic viscosity of the fluid, α is the surface tension and r, ϕ, and z are the cylindrical coordinates.

Radial velocity and azimuthal velocity (v_r and v_ϕ) were obtained by solving the Navier-Stokes equation. Substituting them in the continuity equation and integrating with respect to z gives $v_z = (2\eta r)^{-1}\left(\partial_r\left(h^2\partial_r\alpha\right) + \partial_\phi\left(h^2\partial_\phi\alpha\right)\right)$. For the case in which the melt depth is independent of the transverse coordinates, r and ϕ, the above expression takes the simple form of, $v_z(r,\phi) = \frac{h^2}{2\eta}\nabla_\perp^2\alpha$, where $\nabla_\perp^2 := r^{-1}\,\partial_r\left(r\partial_r\right) + r^{-2}\,\partial_{\phi,\phi}$ is the transverse Laplacian operator. For simple materials, the surface tension may be given in terms of the temperature at the surface, where $\partial_T\alpha$ is often constant (independent of the temperature). Since the temperature distribution is proportional to the intensity profile of the incoming short pulse, i.e., $T(r,\phi) \propto I(r,\phi)$, the mass transport in the fluid can be approximated by $v_z(r,\phi) \propto \nabla_\perp^2 I$.

To calculate the mass transport for various intensity distributions of the laser pulse, we used Laguerre-Gaussian beams given by the following intensity profiles, $I(\rho) = A\,\rho^{2|\ell|}L_p^{|\ell|}\left(2\rho^2\right)\exp\left(-2\rho^2\right)$. Here, A is a constant that depends on the power of the laser pulse, $L_p^{|\ell|}(.)$ are the associated Laguerre polynomials, ℓ and p are the azimuthal and radial mode indices, respectively, $\rho = r/w_0$ and w_0 is the beam waist at the focus.

Figure 4.5(e) shows the mass transport for a Gaussian beam with the temperature distribution shown at the bottom. The longitudinal velocity, $v_z(r,\phi)$, is maximum at the centre of the interaction region pointing towards the thin layer of molten silicon. The resultant displacement causes the molten material to accumulate at the edges where $v_z(r,\phi)$ is pointing away from the silicon surface. This fluid motion leads to formation of a rim around the ablation crater.

When an asymmetry was introduced in the temperature distribution along a given direction, it is reflected in the mass transport giving rise to an asymmetric rim height and width as shown in Fig. 4.5(f). Such an asymmetry was observed for linearly polarized light, whereas it did not exist for circular polarization [41]. The polarization dependence was explained in terms of transient plasmonics [48, 49]. A dense free carrier plasma is created by the leading edge of an intense femtosecond pulse. The trailing edge of the pulse then interacts with the plasma giving rise to local field enhancement. The resultant asymmetry in the carrier distribution eventually translates into an asymmetric distribution of lattice temperature and hence thermocapillary/hydrodynamics forces. The field enhancement occurs along or perpendicular to the laser polarization depending on the plasma density [49].

For an OV beam, the annular intensity profile translates into a doughnut shaped temperature distribution as shown in Fig. 4.5(g). Where temperature is maximum, mass transport points towards the molten silicon. However, $v_z(r,\phi)$ is maximum at the centre, pointing away from the silicon surface. The resultant displacement causes molten silicon to move radially both outward and inwards forming the rim and nano-cone, respectively.

We now address the decrease in nano-cone height at higher pulse energies for the linearly polarized vortex pulse, shown in Fig. 4.2. Local field enhancement resulting from light-

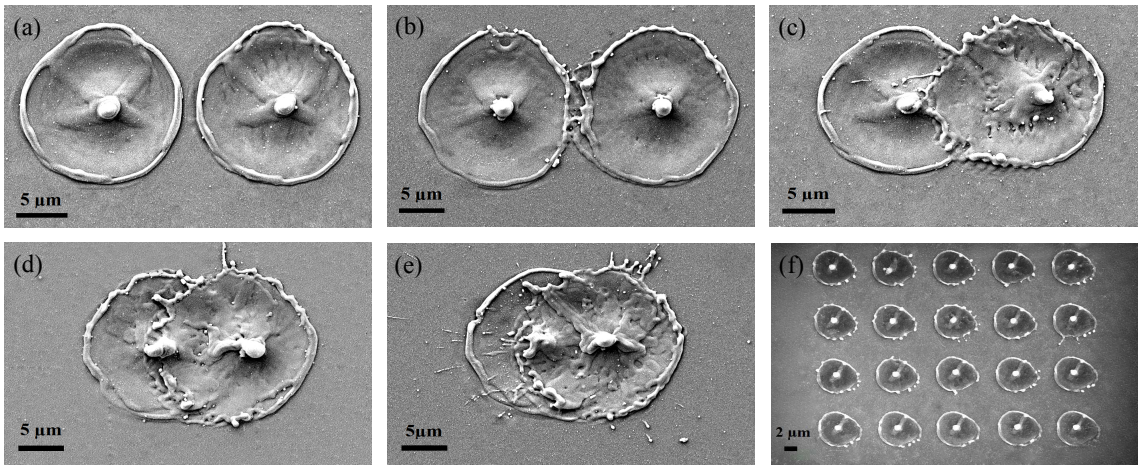

Figure 4.6: (a) - (e) SEM images of two overlapping structures with successive irradiation of silicon with single femtosecond OV pulse (ℓ = +1, s = -1) with a separation of 16 μm, 15 μm, 10 μm, 7 μm, and 5 μm, respectively. (f) SEM image of a 5×4 array of nano-cones. The pulse energy was 850 nJ.

plasma interaction leads to an asymmetry in the radial inward motion of the molten material. The resultant asymmetric compressive force causes the nano-cone height to be less. The local field enhancement *vis-a-vis* asymmetric compressive force becomes prominent at higher pulse energies. As a result, the height of the nano-cone with linear polarization deviates from that of a circularly polarized vortex pulse.

The role of fluid dynamics in the nano-cone formation is evident from SEM images of Fig. 4.6. Silicon was irradiated with a single vortex pulse at two different spots. At 16 μm separation [Fig. 4.6(a)], the ablation crater morphology was unaffected by the presence of the other. At 15 μm spacing, molten silicon from the second spot collided with the resolidified rim of the first spot deforming the rim at the point of contact [Fig. 4.6(b)]. When the two spots overlapped (10 μm separation), the nano-cones remained unaffected, but the rim of the first spot vanished in the overlap region [Fig. 4.6(c)]. When the spacing was reduced further, the molten material was propelled past the first nano-cone [Fig. 4.6(d)] and eventually disrupted it [Fig. 4.6(e)]. Intactness of the nano-cones even when the irradiated spots overlapped enables one to fabricate arrays of silicon nano-cones similar to those shown in Fig. 4.6(f).

To conclude, we demonstrated fabrication of a nano-cone on silicon with a single femtosecond OV pulse. Its formation was described in terms of fluid dynamics, and its polarization dependence was attributed to transient light-plasma interaction. Our results highlight key aspects of light-matter interaction. First, the fluid dynamics model suggests that any tightly focussed annular beam will produce a nano-cone. Tighter focusing by higher numerical aperture objectives can lead to higher compressive forces and can further increase the height of the nano-cone. Second, transient plasmonics influences the laser processed structures. Intense linearly polarized femtosecond light pulses distort the free-carrier density distribution due to local field effects that is imprinted on the subsequent

steps of the ablation/modification process [41,48,50]. Its effects can be minimized by using circularly polarized light.

One potential application of the laser fabricated nano-cone arrays in silicon is to enhance high harmonic radiation that has recently been demonstrated in bulk materials [51–54]. For example, an array of nano-antennas was used to show enhancement of plasmon assisted high harmonic generation from crystalline silicon substrate [55]. Also, nanostructured ZnO and silicon were used to demonstrate customized high-harmonic wave fields and to confine them to diffraction-limited spot sizes [56]. Structured light enables to not only alter the surface topography of a target material and possibly change its phase but also investigate the target by generating high harmonics. This all-optical technique can provide an opportunity to control and probe light-induced dynamical changes to material properties.

The authors acknowledge financial support from Natural Science and Engineering Research Council of Canada, Canada Research Chairs, Canadian Foundation for Innovation and Ontario Ministry of Economic Development and Innovation.

4.4 Nanocone Formation - Theory

In order to further understand and get insights into our experimental results, we simulate the action of the short laser pulse on the fluid dynamics of the molten material. This is done by considering the continuity equation and Navier-Stokes equation under the assumption of incompressibility, large viscosity, and steady-state flow, respectively given by

$$\begin{aligned} \nabla \cdot \mathbf{v} &= 0 && (4.3) \\ \nabla^2 \mathbf{v} &= 0. && (4.4) \end{aligned}$$

These equations are then solved given the boundary conditions that the fluid velocity must vanish at the bottom of the molten material and that the fluid velocity at the surface is given in relation to the surface tension, i.e.

$$\begin{aligned} \mathbf{v} &= 0, \quad z = -h && (4.5) \\ \eta \left(\frac{\partial v_r}{\partial z} + \frac{\partial v_z}{\partial r} \right) &= \frac{\partial \alpha}{\partial r}, \quad z = 0 && (4.6) \\ \eta \left(\frac{\partial v_\varphi}{\partial z} + \frac{1}{r} \frac{\partial v_z}{\partial \varphi} \right) &= \frac{1}{r} \frac{\partial \alpha}{\partial \varphi}, \quad z = 0, && (4.7) \end{aligned}$$

where η is the dynamic viscosity of the fluid, α is the surface tension, and r, φ and z are the cylindrical coordinates.

Let us start by solving Navier-Stokes equation under the assumption that transverse derivatives are much smaller than longitudinal derivatives, i.e. $\frac{\partial}{\partial z} >> \frac{\partial}{\partial r}$ and $\frac{\partial}{\partial z} >> \frac{\partial}{\partial \varphi}$. Hence we must then solve the following set of three equations,

$$\frac{\partial^2 v_r}{\partial z^2} = 0, \qquad \frac{\partial^2 v_\varphi}{\partial z^2} = 0, \qquad \frac{\partial^2 v_z}{\partial z^2} = 0. \tag{4.8}$$

Integrating the first two equations and using the boundary conditions, we obtain the following expression for v_r and v_φ,

$$\begin{aligned} v_r &= \frac{1}{\eta} \frac{\partial \alpha}{\partial r} (h + z) && (4.9) \\ v_\varphi &= \frac{1}{\eta} \left(\frac{1}{r} \frac{\partial \alpha}{\partial \varphi} \right) (h + z) && (4.10) \end{aligned}$$

We main now insert are solution for v_r and v_φ in the continuity equation to obtain an expression for v_z after integration with respect to z.

$$v_z = \frac{1}{2\eta}\left(\frac{1}{r}\frac{\partial}{\partial r}\left(h^2\frac{\partial\alpha}{\partial r}\right) + \frac{1}{r}\frac{\partial}{\partial\varphi}\left(h^2\frac{\partial\alpha}{\partial\varphi}\right)\right) \tag{4.11}$$

For the case where the melt depth is independent of the transverse coordinates, r and φ, the above expression takes the simple form of,

$$v_z(r,\varphi) = \frac{h^2}{2\eta}\nabla_\perp^2\alpha, \tag{4.12}$$

where $\nabla_\perp^2 := \frac{1}{r}\frac{\partial}{\partial r}\left(r\frac{\partial}{\partial r}\right) + \frac{1}{r^2}\frac{\partial^2}{\partial\varphi^2}$ is the transverse Laplacian operator. Finally, we must obtain an expression for the form of the surface tension in order to obtain the mass transport of the molten material, i.e. v_z, as shown in Fig. 4.7. For clean surfaces and simple materials, the surface tension may be given in terms of the temperature at the surface, where $\partial\alpha/\partial T$ is often independent of the temperature. Moreover, here the temperature distribution will be proportional to the intensity profile of the incoming short pulse, i.e. $T(r,\varphi) \propto I(r,\varphi)$. Finally, the mass transport in the fluid will be given by,

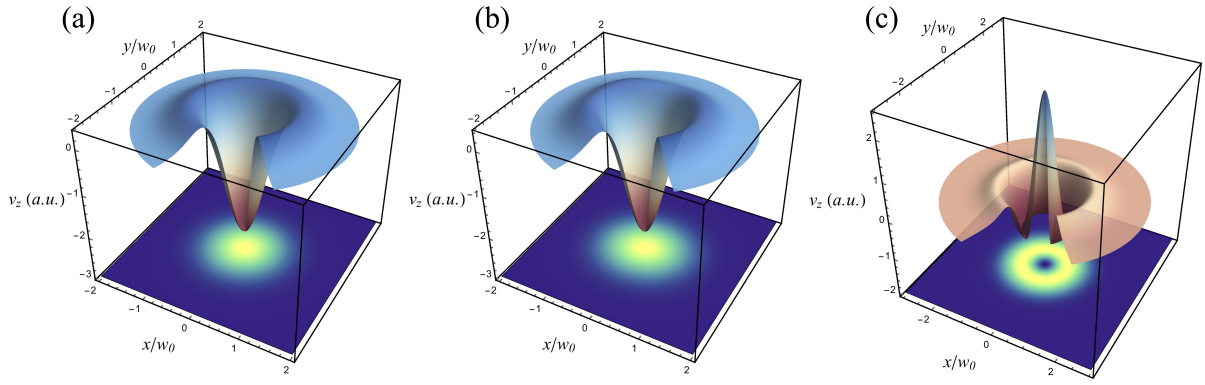

Figure 4.7: Mass transport ($v_z(r,\varphi)$) for several temperature distributions. The temperature distributions are given by an incident beam with a (a) symmetric Gaussian profile, (b) an asymmetric Gaussian profile and (c) a symmetric Laguerre-Gaussian profile with mode index of $\ell = 1$ and $p = 0$. In the case of (b), the asymmetry is given by multiplying the Gaussian distribution by $(1 + ay^2)$, where a is set to 0.4.

$$v_z(r,\varphi) \propto \nabla_\perp^2 I. \tag{4.13}$$

We may now calculate the mass transport for various intensity distributions for the laser pulse. To do so, we adopt the family of Laguerre-Gaussian beams given by the following intensity profiles,

$$I(r) = A\left(\frac{r}{w_0}\right)^{2|\ell|} L_p^{|\ell|}\left(2\left(\frac{r}{w_0}\right)^2\right) e^{-2\left(\frac{r}{w_0}\right)^2}, \tag{4.14}$$

where A is a constant that depends on the power of the laser pulse, ℓ and p are the azimuthal and radial mode indices, respectively, and w_0 is a beam parameter given by the beam waist at the focus.

Bibliography

[1] E. Fadeeva, S. Schlie, J. Koch, A. Ngezahayo, B.N. Chichkov, Phys. Status Solidi A, 206(6) 13481351 (2009).

[2] B. Raillard, L. Gouton, E. Ramos Moore, S. Grandthyll, F. Müller, F. Mücklich, Surf. Coat. Technol., 207, 102109 (2012).

[3] B.R. Tull, J.E. Carey, E. Mazur, J.P. McDonald, S.M. Yalisove, MRS Bull., 31, (08) 626633 (2006).

[4] F. korte, J. koch, B. N. chichkov, Appl. Phys. A 79, 879881 (2004).

[5] A. Ben-Yakar, A. Harkin, J. Ashmore, R. L Byer, and H. A. Stone, J. Phys. D: Appl. Phys., 40, 1447 (2007).

[6] V. N. Tokarev, and A. F. H. Kaplan, J. Phys. D: Appl. Phys., 32 152638 (1999).

[7] M. D. Perry, B. C. Stuart, P. S. Banks, M. D. Feit, V. Yanovsky, and A. M. Rubenchik, J. Appl. Phys. 85 6803 (1999).

[8] V. Garces-Chavez, D. McGloin, H. Melville, W. Sibbett, and K. Dholakia, Nature **419**, 145 (2002).

[9] V. G. Shvedov, A.V. Rode, Y.V. Izdebskaya, A. S. Desyatnikov, W. Krolikowski, and Y. S. Kivshar, Phys. Rev. Lett. **105**, 118103 (2010).

[10] M. Padgett, J. Courtial, and L. Allen, Phys. Today **57**, 35 (2004).

[11] M. Mazilu, D. Stevenson, F. Gunn-Moore, and K. Dholakia, Laser Photonics Rev. **4**, 529 (2010).

[12] S. W. Hell and J. Wichmann, Opt. Lett. **19**, 780 (1994).

[13] S.W. Hell, Nat. Methods **6**, 24 (2009).

[14] C. Hnatovsky, V. G. Shvedov, W. Krolikowski, and A.V. Rode, Opt. Lett. **35**, 3417 (2010).

[15] C. Hnatovsky, V. G. Shvedov, W. Krolikowski, and A.V. Rode, Phys. Rev. Lett. **106**, 123901 (2010).

[16] K. Lou, S.X. Qian, X. Wang, Y. Li, B. Gu, C. Tu, H. Wang, Opt. Express **20**, 120 (2012).

[17] F. Takahashi, S. Takizawa, H. Hidai, K. Miyamoto, R. Morita and T. Omatsu, Phys. Status Solidi A **213**, 1063 (2016).

[18] F. Takahashi, K. Miyamoto, H. Hidai, K. Yamane, R. Morita and T. Omatsu, Sci. Rep. **6**, 38545 (2016).

[19] R. Drevinskas, J. Zhang, M. Beresna, M. Gecevicius, A. G. Kazanskii, Y. P. Svirko and P. G. Kazansky, App. Phys. Lett. **108** 221107 (2016).

[20] J.J.J. Nivas, H. Shutong, K.K. Anoop, A. Rubano, R. Fittipaldi, A. Vecchione, D. Paparo, L. Marrucci, R. Bruzzese and S. Amoruso, Opt. Lett. **40**, 4611 (2015).

[21] K.K. Anoop, R. Fittipaldi, A. Rubano, X. Wang, D. Paparo, A. Vecchione, L. Marrucci, R. Bruzzese and S. Amoruso, J. App. Phys. **116**, 113102 (2014).

[22] J.J.J. Nivas, H. Shutong, A. Rubano, A. Vecchione, D. Paparo, L. Marrucci, R. Bruzzese and S. Amoruso, Sci. Rep. **7**, 42142 (2017).

[23] K. Toyoda, F. Takahashi, S. Takizawa, K. Miyamoto, R. Morita and T. Omatsu, Phys. Rev. Lett. **110**, 143603 (2013).

[24] K. Toyoda, K. Miyamoto, M. Aoki, R. Morita and T. Omatsu, Nano Lett. **12**, 3645 (2012).

[25] T. Omatsu. K. Chujo, K. Miyamoto, M. Okida, K. Nakamura, N. Aoki and R. Morita, Opt. Express. **18**, 17967 (2010).

[26] S. Syubaev, A. Zhizhchenko, A. Kuchmizhak, A. Porfirev, E. Pustovalov, O. Vitrik, Yu. Kulchin, S. Khonina and S. Kudryashov, Opt. Exp. **25**, 10214 (2017).

[27] V.Y. Bhazhenov, M.V. Vasnetsov and M.S. Soskin, JETP Lett. **52**, 429 (1990).

[28] L. Allen, N.W. Beijersbergen, R.J.C. Spreeuw and J.P. Woerdman, Phys. Rev. A **45**, 8185 (1992).

[29] M.W. Beijersbergen, R.P.C. Coerwinkel, M. Kristensen, and J.P. Woerdman, Opt. Commun. **112**, 321 (1994).

[30] K. Sueda, G. Miyaji, N. Miyanaga and M. Nakatsuka, Opt. Express **12**, 3548 (2004).

[31] M. Beresna, M. Gecevičius, P. G. Kazansky and T. Gertus, Appl. Phys. Lett. **98**, 201101 (2011).

[32] E. Karimi, B. Piccirillo, E. Nagali, L. Marrucci and E. Santamato, App. Phys. Lett. **94**, 231124 (2009).

[33] L. Marrucci, E. Karimi, S. Slussarenko, B. Piccirillo, E. Santamato, E. Nagali and F. Sciarrino, J. Opt. **13**, 064001 (2011).

[34] S. Slussarenko, A. Murauski, T. Du, V. Chigrinov, L. Marrucci and E. Santamato, Opt. Express. **19**, 4085 (2011).

[35] H. Larocque, J. Gagnon-Bischoff, F. Bouchard, R. Fickler, J. Upham, R. W. Boyd and E. Karimi, J. Opt. **18**, 124002 (2016).

[36] F. Bouchard, J. Harris, H. Mand, R.W. Boyd and E. Karimi, Optica **3**, 351 (2016).

[37] J. Bonse, S. Baudeach, J. Kruger, W. Kautek and M. Lenzner, Appl. Phys. A. **74**, 19 (2002).

[38] A. Borowiec, M. Mackenzie, G.C. Weatherly and H.K. Haugen, Appl. Phys. A **76**, 201 (2003).

[39] J. Bonse, K.-W. Brzezinka and A.J. Meixner, Appl. Surf. Sci. **221**, 215 (2004).

[40] C. Hnatovsky, V. G. Shvedov, N. Shostka, A. V. Rode, and W. Krolikowski, Opt. Lett. **37**, 226 (2012).

[41] H. Al Khazraji and V.R. Bhardwaj, App. Surf. Sci. **353**, 600 (2105).

[42] J. Zhang, R. Drevinskas, M. Beresna and P.G. Kazansky, App. Phys. Lett. **107**, 041114 (2015).

[43] X. Ji, L. Jiang, X. Li, W. Han, Y. Liu, Q. Huang and Y. Lu, Appl. Opt. bf 53, 6742 (2014).

[44] T. Schwarz-Selinger, D.G. Cahill, S.-C. Chen, S.-J. Moon and C.P. Grigoropoulos, Phys. Rev. B **64**, 155323 (2001).

[45] S.R. Vatsya and S.K. Nikumb, Phys. Rev. B **68**, 035410 (2003).

[46] Y. Lu, S. Theppakuttai and S.C. Chen, Appl. Phys. Lett. **82**, 4143 (2003).

[47] A. Ben-Yakar, A. Harkin, Jj. Ashmore, R. L. Byer and H. A. Stone, J. Phys. D: Appl. Phys. **40**, 1447 (2007).

[48] V. R. Bhardwaj, E. Simova , P. P. Rajeev, C. Hnatovsky , R. S. Taylor , D. M. Rayner and P. B. Corkum, Phys. Rev. Lett. **96**, 057404 (2006).

[49] P.P. Rajeev, M. Gertsvolf, C. Hnatovsky, E. Simova, R.S. Taylor, P.B. Corkum, D.M. Rayner and V.R. Bhardwaj, J. Phys. B **40**, S273 (2007).

[50] J-M. Guay, A. Villfranca, F. Baset, K. Popov, L. Ramunno and V.R. Bhardwaj, New J. Phys. **14**, 085010 (2012).

[51] S. Ghimire, A.D. DiChiara, E. Sistrunk, P. Agostini, L. F. DiMauro and D. A. Reis, Nat. Phys. **7**, 138 (2011).

[52] T. Luu, M. Garg, S. Y. Kruchinin, A. Moulet, M. T. Hassan and E. Goulielmakis, Nature **521**, 498 (2015).

[53] O. Schubert et al, Nat. Photon. **8**, 119 (2014).

[54] G. Vampa, T. J. Hammond, N. Thir, B. E. Schmidt, F. Lgar, D. D. Klug, and P. B. Corkum, e-print arXiv:1605.06345 (2016).

[55] G. Vampa, B. G. Ghamsari, S. Siadat Mousavi, T. J. Hammond, A. Olivieri, E. Lisicka-Skrek, A. Yu Naumov, D. M. Villeneuve, A. Staudte, P. Berini and P. B. Corkum, Nature Physics **DOI: 10.1038/NPHYS4087** (2017).

[56] M. Sivis, M. Taucer, K. Johnston, G. Vampa, A. Staudte, A. Naumov, D. M. Villeneuve, C. Ropers and P. B. Corkum - Submitted to Science.

Chapter 5

Ultra-high Resolution Material Manipulation

5.1 Introduction

Nanoscale spatial precision and control are essential to engineering material properties to develop smart materials and next generation nano-devices.

To achieve this goal, several nanostructuring techniques have been proposed and developed during the past few decades. Among them, those that employ light as a fascinating tool to directly fabricate and manipulate materials in sub-wavelength scale have recently raised an interest. For instance, holes, single nanoparticles, and self-organized periodic grating structures were fabricated via laser direct writing technique, for example, Laser-Induced Forward Transfer (LIFT) and Stimulated Emission Depletion (STED) lithography. Although exploiting these techniques enables one to fabricate structures with sizes below the diffraction limit of light, the degree of spatial control with light, i.e., positioning the individual structures with nanoscale spatial precision, remains a challenge. In this chapter, we present a technique that addresses this issue and offers precise control over the spatial resolution in material structuring. Before that, two of the most widely-used techniques (LIFT and STED lithography) to fabricate nanoscale features via direct laser writing method are briefly discussed.

Laser-Induced Forward Transfer (LIFT) is a direct-write technique that uses a Gaussian laser beam to perform nano-printing. It is referred to as "drop and place" technique where small volumes of materials are deposited in user-defined high resolution patterns.

In this method, the deposition material with a thickness of less than a few hundreds of nanometers is pre-coated on one side of a transparent donor. The substrate (receptor) is mounted at a distance (typically 2575 nm) from the donor, while the thin-film faces the substrate. A focused laser beam radiates the donor from the back. Absorption of the laser energy by the pre-coated material generates heat that eventually ablates the film from the donor. The thin film of material on a donor substrate is melted locally and lifted

off in the form of a droplet that becomes deposited onto a receiver substrate. A small gap separates the deposited droplets. The spatial resolution one could achieve in placing individual droplets is a few hundreds of nanometers. In this technique, by translating the source and receiving substrate or scanning and modulating the laser beam, 2D and 3D patterning are possible. The writing speeds are typically controlled by the laser repetition rate, computer-controlled translation stages and/or galvanometric scanning mirrors that provide the formation of high-resolution patterns.

There are several mechanisms involved in the LIFT process, depending on the laser intensity. At low intensities, intensities lower than the threshold intensity where the donor starts boiling ($I < I_{th}$), the molten film fragments are transferred to the receptor with a weak adhesion [1]. There are two possible causes for this particle removal. First, the generation of a vapor cavity between the donor and the donor's substrate exerts a force on the donor film. It causes a particle to be torn away from the donor. Second, thermal radial expansion caused by the laser heating leads to a radial compression force and subsequently a transversal tension normal to the donor-substrate surface. Once the force exceeds the adhesion threshold, the molten donor film is torn off. At higher intensities ($I_{th} < I < 5\, I_{th}$), the donor layer evaporates and then condenses at the receptor. Further enhancement of the laser intensity ($I > 5\ I_{th}$) causes the ions, atoms, and plasma implantation into the receptor.

Another key parameter that affects the morphology of the transferred material is the thickness of the donor layer. For example, at higher intensities in the evaporation intensity regime, when the donor's thickness is greater than its thermal diffusion length, the transferred material is spread into the receptor. This causes a low resolution in the printing process [2]. However, at lower intensities in the evaporation regime, when the donor lm has a thickness almost equal to its thermal diffusion length, the material is transferred to the receptor in the form of droplets. In this case, a printing resolution near the size of the laser pulse is achievable.

Apart from all the advantages, the LIFT technique is a pyrolytic process and cannot be used for the deposition of materials with crystallization temperature above room temperature [3]. Besides, this method has two main drawbacks: (1) a shock wave is generated at the surface of the film, which propagates in front of the flyer, reflects onto the receiver, and can destroy the flyer when crossing it [4], (2) a significant amount of debris is induced by the laser-matter interaction process, and they are also deposited onto the receiver; therefore, some additional strategies are required to prevent the generation of debris [5]. Other limitations of this method are uniformity, morphology, adhesion of the coatings to the substrate, impurities in the coating, ablation of the donor, and material implantation into the substrate. Apart from these, although nanoprinting with LIFT using a Gaussian beam enhances the resolution in the nanodroplet size, it cannot actively control their spatial position individually and with high precision.

Stimulated Emission Depletion (STED) lithography is a laser-material processing technique that employs the superposition of Gaussian and optical vortex beams and offers high resolution nanoprinting. In STED lithography, the Gaussian beam (typically femtosecond laser pulses of 780 nm) is used for multiphoton excitation of the photostarters

and the optical vortex beam (a 532 nm continuous wave laser) is used as a depletion beam. The vortex laser beam is overlapped with the excitation laser beam and depletes the previously excited photoinitiators. At the focus, the spatial shape of the vortex beam has a zero-intensity region at the location where the excitation beam has its maximum intensity [6].

The excitation laser excites photoinitiator molecules from the ground states to an excited (electronically and vibrationally) state via two-photon absorption. Most of the molecules will relax to an intermediate state from where they can fluoresce. The idea of STED is to bring the molecules from the intermediate state back to the ground state via stimulated emission induced by a second laser (depletion laser) of a different color. Increasing the depletion of laser power increases the number of photoresist molecules. These molecules are then forced into the non-polymerized state, except for the molecules located at zero depletion intensity region [7]. This method has been employed to fabricate nanometer-sized nanowires. For example, Gan *et al.* produced nanowires with the feature size (i. e., the line width) of 9 nm and two-line spatial resolution of 52 nm [8].

Using the STED technique in nanoprinting, however, has its own challenges. The greatest challenge is selecting a suitable material. This challenge could be recognized in two aspects. First, to fabricate smaller features and lower the resolution, specific materials need to be discovered. These materials should be rigid enough to resist the washing process and do not shrink. Second, only negative tone resists have been used in STED lithography so far; positive tone resists also needs to be tested. Indeed, finding a suitable photoinitiator is very difficult. Moreover, to efficiently deplete the molecules' excitation (transition) via stimulated emission, a considerable oscillator strength is required. Besides, a long excited-state lifetime is required for the interaction.

Apart from all the benefits, the degree of spatial control with light was restrictive. It was not feasible to position individual structures with nanoscale spatial precision. In other words, there have been no reports showing that this technique is capable of fabricating and spatially controlling single 3D structures. The limitations and challenges in these direct laser writing techniques motivated us to develop a more feasible method with high precision and fewer limitations in fabrication and resolution control.

The work reported in this chapter is my published paper that addresses how light can be employed to actively manipulate materials in 2D with nanoscale precision. We demonstrated a technique to fabricate individual nanocones in a complex pattern on the surface of silicon and control their position with nanometer resolution. The technique presented in this chapter exploits the unique properties of the structured light - phase and polarization singularities - that allow us to control the null intensity regions in the beam profile. Upon irradiation, the intensity distribution of the structured light is mapped onto the silicon surface and induces localized melting. Subsequent fluid dynamics, as mentioned in the previous chapter, leads to the formation of nanocones at the positions of null intensity regions. Varying the phase retardation of the two orthogonal polarization states of the structured light made us able to control their position.

5.2 Spatially controlled nano-structuring of silicon with femtosecond vortex pulses

Author Contribution

In the following, my paper published in Scientific Reports journal is presented. The published results come from experiments performed by M. G. Rahimian and A. Jain at Ultrafast Photonics Lab, University of Ottawa, ON, under the supervision of V. R. Bhardwaj. M. G. Rahimian, conducted the analysis of the results, performed the SEM and AFM measurements, and created the figures and graphs. A. Jain performed the calculations. H. Larocque fabricated the q-plate and assisted in producing vortex beams. P. B. Corkum, E. Karimi, and V. R. Bhardwaj designed the experiment and analyzed the data. All authors contributed to writing the manuscript.

Scientific Reports **10**, 12643 (2020)

Spatially controlled nano-structuring of silicon with femtosecond vortex pulses

M. G. Rahimian, A. Jain, H. Larocque, P. B. Corkum, E. Karimi, and V. R. Bhardwaj

Department of Physics, Advanced Research Complex, University of Ottawa, 25 Templeton Street, Ottawa, ON, K1N 6N5, Canada

Engineering material properties is key for development of smart materials and next generation nanodevices. This requires nanoscale spatial precision and control to fabricate structures/defects. Lithographic techniques are widely used for nanostructuring in which a geometric pattern on a mask is transferred to a resist by photons or charged particles and subsequently engraved on the substrate. However, direct maskless fabrication has only been possible with electron and ion beams. That is because light has an inherent disadvantage; the diffraction limit makes it difficult to interact with matter on dimensions smaller than the wavelength of light. Here we demonstrate spatially controlled formation of nanocones on a silicon surface with a positional precision of 50 nm using femtosecond laser ablation comprising a superposition of optical vector vortex and Gaussian beams. Such control and precision opens new opportunities for nano-printing of materials using techniques such as laser-induced forward transfer and in general broadens the scope of laser processing of materials.

Introduction

The fundamental limit to spatial resolution of any optical system is governed by diffraction and is approximately half the wavelength of light [9]. Diffraction also dictates how tightly a laser beam can be focused, which in turn determines the feature size one can achieve in laser ablation of materials. Therefore, shorter wavelengths (ultraviolet) are often used in combination with lithographic techniques to produce sub-wavelength features as small as 50 nm [10]. Driven primarily by the semiconductor industry, research efforts are ongoing to use coherent and non-coherent extreme ultraviolet light to produce features smaller than 10 nm to meet the ever increasing demand for miniaturization [11,12]. Concurrently, alternate methods are also being explored to overcome the diffraction limit of light that

does not involve the use of a photomask. These fall into two categories – near field and far field approaches.

Nanofabrication using near field approach exploits local field enhancement around a nanoparticle to confine light to sub-wavelength dimensions and thereby induce local deformations (melting or ablation) of the substrate. Large scale periodic array of nanoholes were fabricated by laser irradiation of a monolayer of microspheres [13] – a multistep process with no direct control on the position of nanostructures, analogous to lithographic techniques [14]. Alternately, controlled fabrication of individual nanostructures can be achieved using scanning probe microscope either directly [15] or by irradiating the tip with light [16].

Direct laser processing of materials is a far field approach that exploits the nonlinear nature of the light-matter interaction and localized energy deposition. Using ultrashort laser pulses, three-dimensional (3D) control was achieved in transparent materials [17, 18] and sub-wavelength structures were created with enhanced spatial precision in a cold ablation process due to negligible lateral heat transport to the surrounding material. Exploiting near threshold ablation, feature dimensions far below the diffraction limit were demonstrated [19, 20]. However, in such a threshold based material response, the ablation features were found not to be dependent on the nonlinear process responsible for light absorption but rather correspond to a one-to-one mapping of the beam profile at threshold intensity [21]. Nanoholes [22, 23], nanocones [24–27], nanodots [13] and self-organized periodic nano-ripple patterns [28–30] were also fabricated in different materials either by ablation or material modification using above threshold laser pulse energies.

Another non-contact direct laser-write technique that is widely used in nano-printing is Laser Induced Froward Transfer (LIFT) to "drop and place" small volumes of complex materials into user-defined, high-resolution patterns [31, 32]. A thin film of material on a donor substrate is melted locally by the laser beam and lifted off in the form of a droplet that gets deposited onto a receiver substrate separated by a small gap. The spatial resolution one could achieve in placing individual droplets is few hundreds of nanometers.

Although light induced nanostructures with feature sizes smaller than diffraction limit could be fabricated either by ablation or material modification [33], the degree of spatial control with light is restrictive. For example, it is not feasible to position individual structures with nanoscale precision. Only partial spatial control has been achieved with nano-ripples whose orientation and spacing was varied by changing the laser polarization and wavelength (λ) [29]. In this context, the present article addresses how light can be used to actively manipulate materials in two dimensions with a precision of $\sim \lambda/20$. It demonstrates positioning of ~ 0.1 μm^3 of the molten material in the form of a nanocone with 50 nm precision in an area of 40 μm^2 by manipulating the beam shape. The technique is extended to fabricate complex, unconventional structures involving multiple nanocones and control their relative positions with the same precision.

Apart from laser fabrication and spatial control of nanostructures, surpassing the diffraction barrier imposed by the wave nature of light is also critical in imaging/microscopy. It is accomplished by using the same (a) near field techniques that exploit the information contained in the evanescent wave [34, 35] or confine light using plasmonic nanostruc-

tures [36, 37], and (b) far field techniques that exploits the optical nonlinearity of the medium as in stimulated emission depletion microscopy [38].

Our approach to sub-wavelength precision in nano-fabrication is based on the coherent superposition of optical vector vortex beam (VVB) and a Gaussian beam [39]. VVBs are characterized by spatially variant linear polarization in the beam transverse plane. They may possess phase singularities in the transverse plane at which the field amplitude vanishes. VVBs can be expanded in terms of orbital angular momentum (OAM) carrying, i.e. twisted, beams. Twisted beam carry an OAM value of $\ell\hbar$ per photon, where $\hbar$ is the reduced Plank constant, and ℓ indicates the number of twists in the helical wavefront in one wavelength which its sign determines the chirality of the helix. We produce VVBs using a birefringent plate enclosing a patterned liquid crystal layer, known as a q-plate. The liquid crystals in the q-plate have an optic axis whose orientation depends on the azimuthal coordinate, thereby forming a pattern defined by a topological charge q consisting of either a full or a half-integer value. As light propagates in the q-plate, spin angular momentum associated with light polarization is coupled to photon OAM of $\ell = \pm 2q$. The conversion efficiency is determined by the q-plate's optical retardation, which can be controlled by an externally applied electric field.

Results

Our technique exploits two unique properties of VVBs. First, the annular intensity distribution of the VVB when focused is mapped onto the silicon surface causing melting of a thin layer, determined by the optical penetration depth of light. Thermo-capillary and/or hydrodynamic forces displace the molten silicon radially outward to the periphery and also radially inward to the centre of the crater. Compressive forces arising from radial inward motion of the molten material pushes it away from the surface. Rapid expansion causes re-solidification into a nanocone formed (Fig. 5.1a) at the centre where VVB has a zero intensity point [26]. Simultaneously, the radial outward motion of the molten material re-solidifies after reaching the cold boundary of the ablation region to form a rim. The height of the nanocone is $\sim$ 500 nm and increases with the increasing pulse energy while the rim height is only $\sim$ 100 nm [26]. Longer nanocones or nanoneedles have been produced with vortex beams using nanosecond and picosecond pulses on silicon [40] and metals [41]. They were shown to exhibit chirality and has been attributed to (a) mapping of the orbital angular momemtum of the beam on to the handedness of the nanoneedles [41], and/or (b) tailored chiral intensity distribution that also controls the handedness of nanoneedles [42]. In contrast, there was no clear signature of the chirality-control fabrication (by changing OAM value) of nanocones produced by femtosecond pulses.

Second, when a pure VVB is perturbed by adding coherently a tunable amount of a linearly polarized Gaussian beam, the central singularity either shifts or unfolds into multiple singularities depending on the topological charge. The shift can be precisely controlled by adjusting the applied external field to the q-plate. This action varies the optical retardation and thereby detunes the strength of the spin-to-orbital angular momentum coupling of light. A fraction of the input Gaussian beam co-propagates with a partly converted

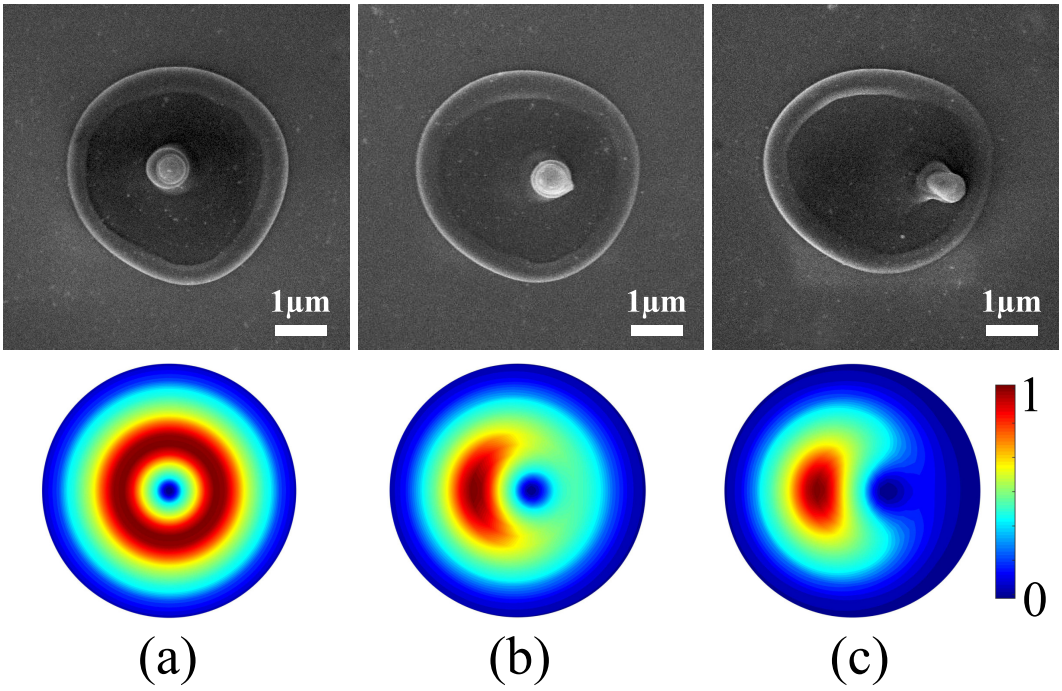

Figure 5.1: **Displacement of the nanocone and phase singularity with retardation.** Superposition of linearly polarized Gaussian beam with VV beam produced by a q-plate with topological charge of $q = +1/2$, having different weights (a) 0:100 (pure VV beam), (b) 10:90, and (c) 15:85. The top row shows SEM images of the nanocone position and the bottom row shows the corresponding intensity profile of the superposition beams. A single laser pulse with an energy of 280 nJ created the nanocone.

VVB. As a result, for q=1/2 or $\ell = \pm 1$, the position of the nanocone within the ablation region can be varied with nanometers precision (Fig. 5.1b, 5.1c). As the weight of the Gaussian beam increases, the position of the singularity shifts towards the outer region of the ablated region (also see Supplementary Fig. S2). For a pure VVB produced by q=1/2 plate, the output polarization was radial, azimuthal, or spiral [30] when the angle of the incident linear polarization with respect to the q-plate axis was 0°, 90°, or 45°, respectively.

The nanocone position can be controlled by moving the singularity anywhere in the transverse plane of the beam as shown in Fig. 5.2, for azimuthally polarized VVB. For a fixed optical retardation (relative weight of Gaussian beam to VVB), a half-wave plate (HWP) in front of the detuned q-plate rotates the input polarization with respect to the q-plate axis and changes the angular position of the singularity at the transverse plane rotating it in a circular arc. Radius of the circular arc depends on the optical retardation. Varying the applied electric field to the q-plate and rotating the incident linear polarization, the nanocone can be positioned anywhere in 2D space within the interaction region of ~ 40 μm^2 with a precision of 50 nm. Similar results were obtained for radial and spiral VVBs.

Figure 5.3 shows unfolding of the singularity when a pure VVB with a star-shaped polarization pattern [30] with $\ell = \pm 2$ (topological charge of $q = -1$) is perturbed by a Gaussian beam. The perturbation is achieved by electrically detuning the q-plate. In

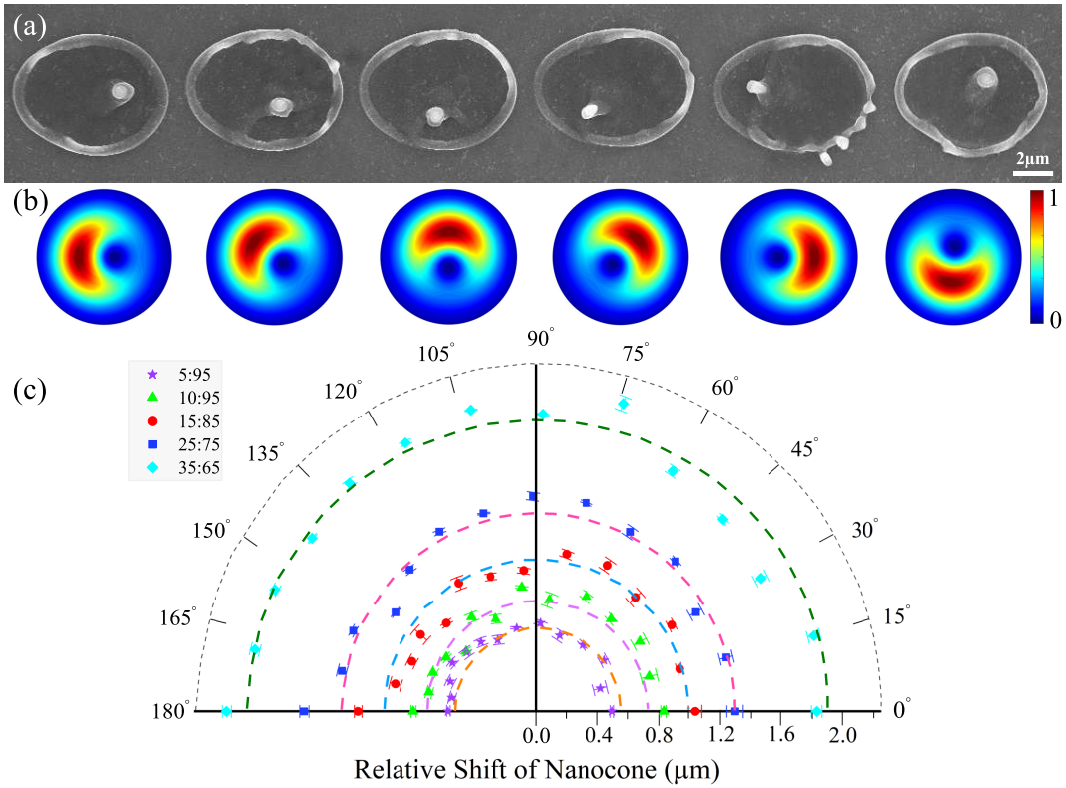

Figure 5.2: **Controlled positioning of the nanocone in 2D space.** (a) For a fixed relative weight (25:75) of Gaussian and VV beams produced by an electrically detuned q-plate with topological charge of q=+1/2, SEM images show the motion of the nanocone in a circular arc when an additional phase is added to the superimposed beams by rotating the polarization axis of the incident Gaussian beam with respect to the q-plate axis. A single laser pulse irradiated the sample with a pulse energy of 600 nJ. (b) The corresponding simulated intensity profiles. (c) Polar plot showing the measured relative shift of the nanocone with respect to its position for a pure VV beam as a function of the rotation angle of the HWP (relative phase of the linearly polarized Gaussian beam) for different optical retardations (different weights of Gaussian and VV beams). The dashed lines are the simulated nanocone position.

VVBs, the total field orientation is undefined along the beam axis and this polarization singularity is typically referred to as a V-point. A small perturbation to pure VVB causes the local polarization states to acquire a tiny ellipticity. The V-point no longer exists, instead two pairs of C-points appear where the orientation of the polarization ellipse is undefined. Unfolding of the polarization singularity also deforms the intensity pattern of the pure VVB giving rise to two null intensity points. The separation between these points can be controlled by varying the relative weight of Gaussian beam superimposed on the VVB and increases with the amount of Gaussian contribution. This results in the formation of two nanocones whose separation and relative orientation can be precisely controlled by detuning the q-plate and adding an extra phase to the superimposed beams (as in Fig. 5.2), respectively (see Supplementary Fig. S4).

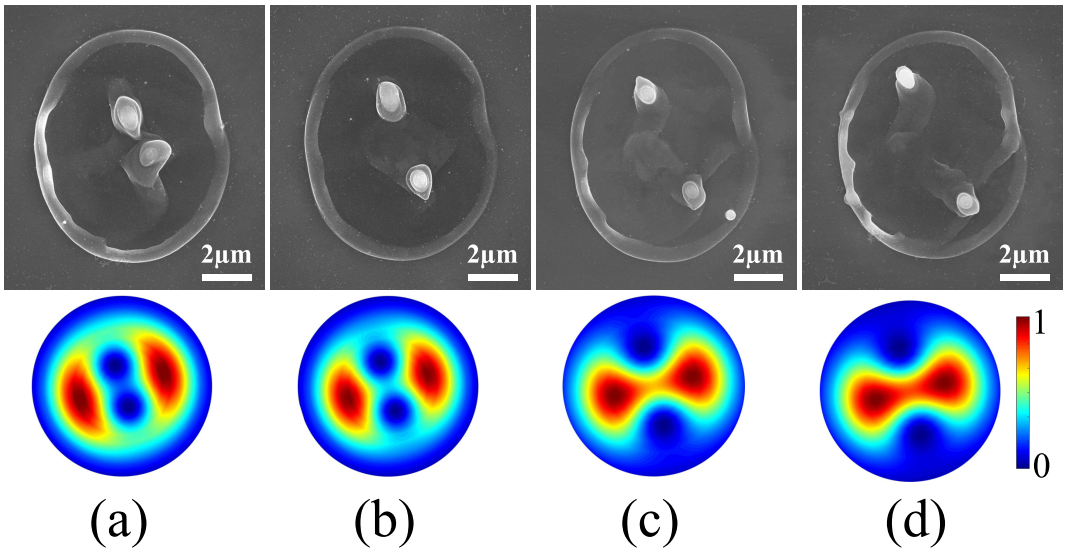

Figure 5.3: **Separation of nanocones with unfolding singularity.** Superposition of linearly polarized Gaussian and VV beams produced by a detuned q-plate, topological charge of $q = -1$, with different relative weights of (a) 10:90, (b) 15:85, (c) 20:80 (d) 25:75. Top panels shows the SEM images of two nano-cones generated by a single laser pulse with an energy of 310 nJ. The bottom panels show the corresponding intensity profiles. Separation between the singularities increases with increase in the Gaussian component.

Figure 5.4 shows how complex intensity patterns can be generated by superimposing different VVBs produced by a combination of two q-plates with topological charges of $q = -1$ and $q = 1/2$. A HWP between the $q = -1$ and a detuned $q = 1/2$ plates produces a superposition state $\alpha(e^{i2\phi}\mathbf{e}_R + e^{-i2\phi}\mathbf{e}_L) + \beta(e^{i\phi}\mathbf{e}_L + e^{-i\phi}\mathbf{e}_R)$, where α and β are given by the detuning parameter. The resultant intensity distribution displays three singularities around the central region where the intensity is also minimum (Fig. 5.4c). As a result 4 nanocones are formed (Fig. 5.4a). In the absence of the HWP the output corresponds to a superposition state defined by $\alpha(e^{i2\phi}\mathbf{e}_R + e^{-i2\phi}\mathbf{e}_L) + \beta(e^{i3\phi}\mathbf{e}_L + e^{-i3\phi}\mathbf{e}_R)$. The intensity pattern consists of 5 null points around the central null region (Fig. 5.4d). This should lead to 6 nanocones. However, any slight detuning of the $q = -1$ plate leads to splitting of the central singularity resulting in the formation of 7 nanocones (Fig. 5.4d) (see Supplementary Fig. S6).

Discussion

There are some similarities between our laser processing technique and stimulated emission depletion (STED) microscopy/ lithography in surpassing the diffraction barrier. Both use superpositions of Gaussian and non-Gaussian beams. In STED microscopy, a focused Gaussian beam that excites the fluorophores is superimposed with a beam having a doughnut intensity distribution that switches off the fluorophores except at its centre. In STED lithography the doughnut beam is used to inhibit photo-polymerization induced by the

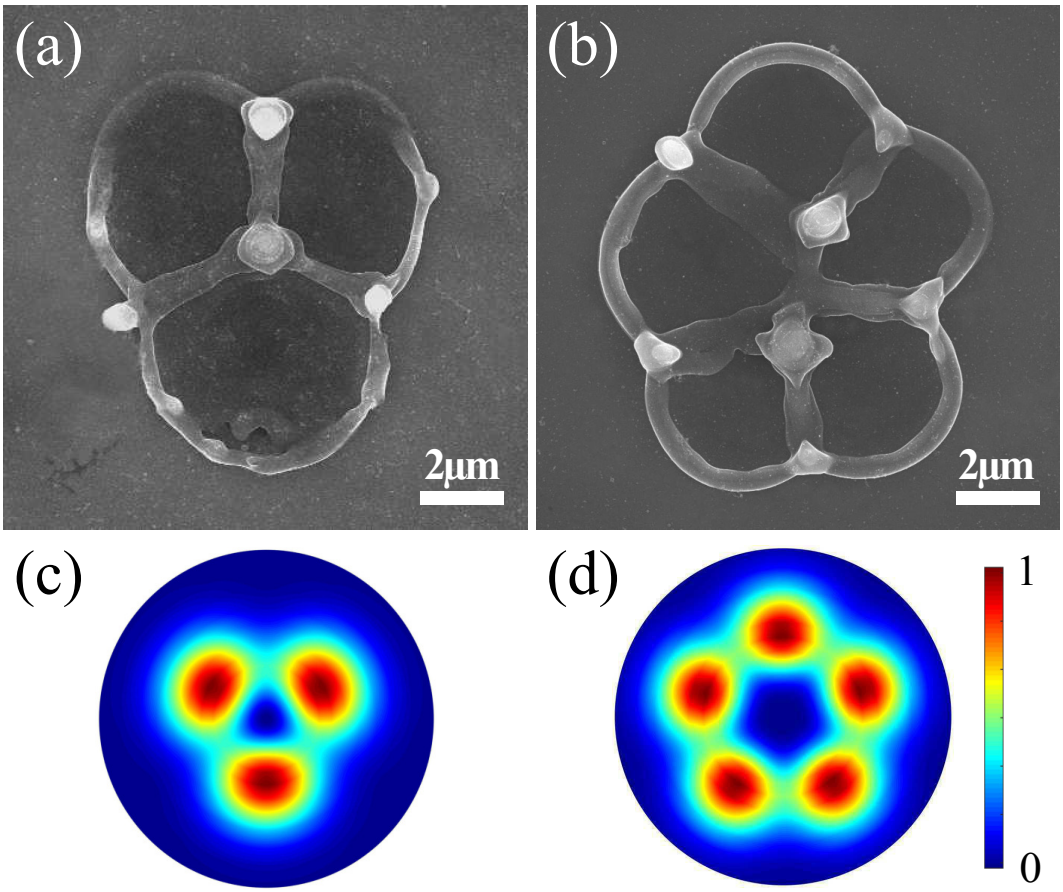

Figure 5.4: **Fabrication of complex nanostructures.** Mapping of complex intensity profiles generated by VVB produced by two q-plates with topological charge of $q = -1$, and $q = 1/2$. (a) A HWP between the $q = -1$ ($\ell = \pm 2$) plate and a detuned $q = 1/2$ ($\ell = \pm 1$) plate, and (b) without the HWP between the two q-plates. The corresponding calculated intensity profiles are shown in (c,d). Experimental patterns were produced by a single pulse with an energy of 700 nJ.

writing beam. However, the main drawback of STED lithography is the design and development of suitable photoresists [43]. In our method, varying the phase retardation between the VVB and Gaussian beam shifts the null intensity positions within the focal region enabling us to control the position of the nanocone.

However, the underlying physics is different between the two methods. In STED microscopy, the doughnut beam depletes the fluorescent state by stimulated emission in all molecules in the intense regions of the beam. The intensity of the doughnut beam determines (a) the probability of fluorescence switching that scales exponentially, and (b) the area to which fluorescence is confined that scales inversely thereby enhancing the spatial resolution. In our technique, VVB induces localized melting via multiphoton absorption and the subsequent fluid dynamics around the unmodified region of the material (due to null intensity region) displaces matter on nanoscale. The probability of such nonlinear interaction scales with n^{th} power of laser intensity, where n is the number of photons involved

in the multiphoton process. In silicon (band gap of 1.14 eV), the interaction of 800 nm light (photon energy of 1.55 eV) is dominated by single and two photon absorption. The intensity of the VVB determines the amount of the material displaced leading to nanocone formation whose height increases but the apex angle remains the same [26]. Therefore, the spatial resolution remains the same.

In our experiments, the spatial precision of $\sim$ 50 nm is due to loose focusing of the laser beam. The use of a high numerical aperture lens will reduce the size of the null intensity region and will lead to a smaller lateral extent and apex angle of the nanocone (see Supplementary Fig. S3). However, at very high numerical apertures the longitudinal component of the field can hinder the interference process and limit the spatial resolution. The spatial precision can be further improved to 10 nm by (a) using a highly stable power supply that can change the small voltage applied to the q-plate in 1 mV steps, and/or (b) changing the angle of the half-wave plate in front of the detuned q-plate in smaller steps of 0.1°. The laser pulse duration is not critical in our technique. In fact, longer durations were found to give rise to μm sized nano-needles likely due to larger melt volume [27].

The main limitation is that the nanocones can be efficiently created only on non-transparent materials where the melt layer is two dimensional. In transparent materials, light penetration into the medium leads to a 3D melt layer whose dynamics lead to surface swelling and ejection of the material instead of a well-defined nanocone. Also, the nanocones are always accompanied by an outer rim whose relative height can be minimized by laser parameters albeit with concomitant reduction in nanocone height [26]. Controlled fabrication of nanocones in semiconductors and metals can be used as field emission tips [44, 45], scanning probes, whispering gallery optical resonator [46], and for enhanced solar absorption in photovoltaics [47]. When implemented with LIFT, our technique provides the ability to control the deposited material with sub-wavelength precision in nano-printing of complex materials with applications ranging from microelectronics to bio-photonics.

Methods

Experiment

Femtosecond light pulses from a Ti:sapphire laser system (800 nm, 1 kHz, 45 fs, 2.5 mJ/pulse) were focused on a silicon surface with a 0.25 NA (16×) aspheric lens. The sample was mounted on three-axis translation stages with a resolution of 100 nm. The sample was irradiated with a single pulse selected by operating the laser in an external trigger mode. The incident pulse energies, varied using a half-wave plate (HWP) and a polarizer, were measured after the microscope objective taking into account the transmission and reflection losses of all the optics. The pulse duration before the microscope objective was 70 fs. The laser-ablated regions were characterized by a scanning electron microscope (SEM), with the electron beam incident normal to the sample surface and atomic force microscopy (AFM) in non-contact mode.

In our experiment, complex intensity profiles were generated using birefringent-based liquid crystal beam converters, called q-plates [48,49], with topological charges of $q = +1/2$ and -1. The optical retardation of the q-plates was changed by varying the voltage applied to them. At the optimal voltage, the q-plates converted linearly polarized Gaussian beams to optical VVBs composed of OAM states with $\ell = \pm 1$ and $\ell = \pm 2$, respectively [50]. Complex spatial intensity profiles were produced by varying the voltage applied on the q-plate. This process called voltage tuning of the q-plate results in varying the extent of coherent superposition of laser beam components. In other words, detuning the individual q-plate produced a superposition of partially converted VVBs with the incident Gaussian beam. A combination of different q-plates resulted in complex intensity profiles due to the superposition of VVBs. See Supplementary Fig. S1 for additional details.

Numerical

Intensity profiles of different order VVBs and their superposition states were simulated using the Laguerre Gaussian beam

$$U(r,\phi,z) = \frac{C_{\ell p}^{LG}}{w(z)}\left(\frac{r\sqrt{2}}{w(z)}\right)^{|\ell|} exp\left(\frac{-r^2}{w^2(z)}\right) L_p^{|\ell|}\left(\frac{2r^2}{w^2(z)}\right) exp\left(\frac{-ikr^2}{2R(z)} - i\ell\phi - ikz + i\Psi(z)\right), \tag{5.1}$$

where $p \geq 0$ is the radial index and ℓ is the azimuthal index. L_p^{ℓ} are the generalized Laguerre polynomials and $C_{\ell p}^{LG}$ is a normalization constant. $R(z)$ is the radius of curvature of the wavefront, $w(z)$ is the beam width and $\Psi(z)$ is the Gouy phase. r and z are the radial and axial distances. k is the wave number and $e^{i\ell\phi}$ is the phase factor containing the ℓ term.

Acknowledgements

A.J. thanks Sastri Indo-Canada foundation for fellowship. We acknowledge financial support from Natural Science and Engineering Research Council of Canada, Canadian Foundation for Innovation and Canada Research Chairs.

Author contributions

M.G.R. and A.J. contributed equally to the experimental work. M.G.R. analysed the data and prepared figures and graphs. A.J. performed the calculations. H. L. built the q-plate and assisted in producing vortex beams. P.B.C., E.K., and V.R.B. designed the experiment and analysed the data. All authors contributed to writing the manuscript.

Additional information

Correspondence and requests for materials should be addressed to Ravi Bhardwaj
Competing interests The authors declare no conflicts of interest.

5.3 Supplementary Material

5.3.1 Experimental Setup

A schematic of the experimental setup used to demonstrate spatially controlled formation of nanocones on silicon with femtosecond vortex pulses is shown in Fig. 5.5. Linearly polarized input pulses with a Gaussian spatial profile were converted to optical vortex pulses by employing q-plates with topological charges of q= +1/2 and -1. The resultant radial profile of the vector vortex (VV) pulse is similar to that of Hyper-Geometric Gaussian modes [51].

The q-plate is a slab of a birefringent material based on liquid crystal technology with uniform birefringent phase retardation (δ) and a transverse optical axis pattern with a topological charge of q [52]. The optical phase of the generated modes varies by $2\pi q$ when circling once the beam axis. The topological charge q is an integer or semi-integer, positive or negative value. A circular aperture after the q-plate filtered the central part of the beam resulting in a vortex beam with an annular spatial profile similar to that of Laguerre-Gauss modes.

Different polarization states with a variety of spatial intensity distributions were produced by (i) using a combination of different q-plates and wave plates, and (ii) varying the optical retardation of the q-plate, resulting in the superposition of pure vortex and Gaussian beams. The pulse energies of the emerging vortex beam with complex polarization and spatial structure were controlled by a combination of half wave plate (HWP) and polarizer. A glass plate (G) reflected a portion of the incident pulse on to a fast photodiode (PD) that was used for power calibration by operating it in the linear regime with the help of neutral density filters (ND).

An aspheric lens (16× with 0.25 NA, f = 11 mm, Newport) focused the vortex pulses on to a crystalline (100) p-type silicon mounted on a precision 3-axis (x, y, z) motion control system. The position of the laser focus relative to the sample's surface was determined accurately (±5 μm) by imaging the back-reflected light from the silicon surface. Glass plate directed the back-reflected light towards a charge-coupled-device (CCD) camera (MCE-B013-US, Mightex) after propagating through a focusing lens (Thorlabs, f = 100 mm, plano-convex lens). The Si surface morphology was analyzed using a field emission scanning electron microscope (Zeiss Gemini SEM 500) with both In-Lens detection mode (top-view images) and secondary electrons detection mode (sideview images) and a Park NX10 atomic force microscope in a non-contact mode.

The setup shown in Fig. 5.5 (a) produces a nanocone whose position can be shifted by changing the voltage applied on the q-plate with a topological charge of 1/2 (QP1). This corresponds to Fig. 1 in the main text. A half-wave plate in front of the QP1, as shown in Fig. 5.5 (b), enables to change the angular position of the nanocone. This corresponds to Fig. 2 in the main text. A q-plate with topological charge of -1, QP2, as shown in Fig. 5.5 (c) is used to produce two nanocones whose separation can be varied by changing the voltage applied on the QP2. This corresponds to Fig. 3 in the main text. The setup shown in Fig. 5.5 (d) produces three-petal shaped flower like structure with four nanocones,

corresponding to Fig. 4a in the main text. Removing the half-waveplate between QP2 and QP1, as shown in Fig. 5.5 (e), produces five-petal shaped flower like structure with 6 nanocones. This can be increased to 7 nanocones by detuning QP2, corresponding to Fig. 4b in the main text.

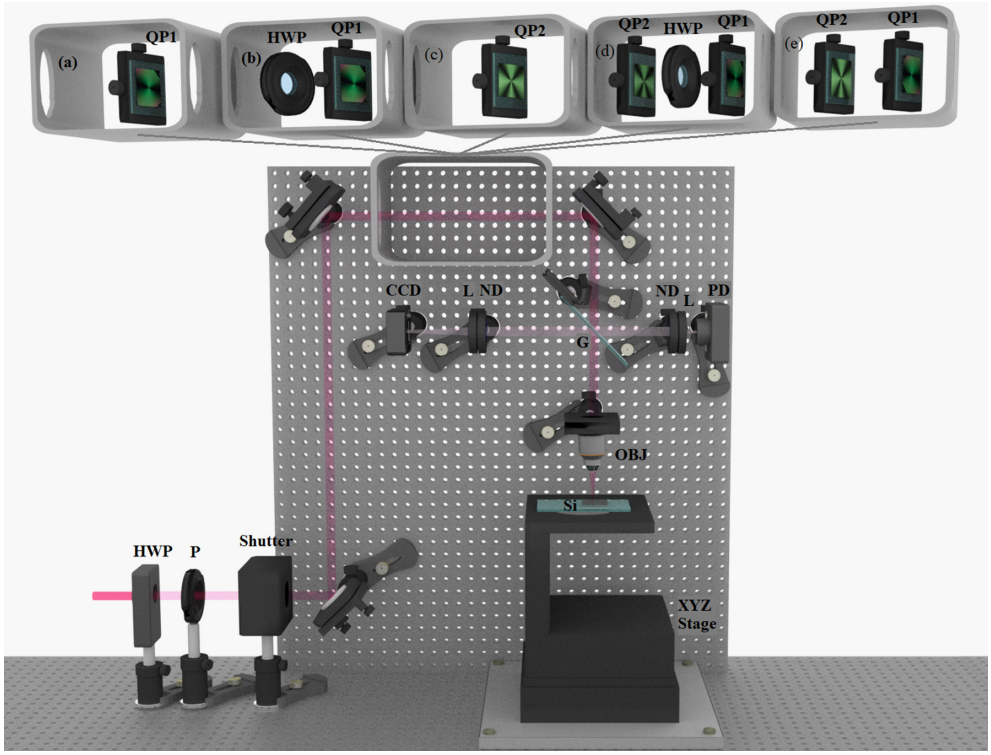

Figure 5.5: S1- The schematic shows the experimental setup. ND: neutral density filter, CCD: charge-coupled-device camera, G: glass plate, PD: photodiode, P: polarizer, L: Lens, OBJ: objective, QP1: q-plate with topological charge of 1/2, QP2: q-plate with topological charge of -1, HWP: Half-wave plate.

5.3.2 Optical Retardation Calibration with the Applied Voltage

A square-wave signal generator operating at 7 KHz and 4 KHz was used to adjust the driving voltages to the q= +1/2 and q = -1 plates, respectively. At optimal voltage of 2.97 V, both q-plates produced pure VV beams. Varying the voltage on the q-plates causes a change in the optical retardations (δ) enabling the tuning of the q-plates. When the q-plate is detuned, if the input Gaussain beam is circularly polarized, the resultant output beam will be a coherent superposition of two fundamental optical states; (i) the unconverted part of the input Gaussian beam with the same polarization as the input and (ii) the converted annular VV beam with opposite handedness to the input polarization with ℓ=$\pm$1(or $\pm$2). Invoking different input polarization states, optical retardation values, and/or different location of polarization optics within the setup produced a combination of converted and unconverted parts of the beam.

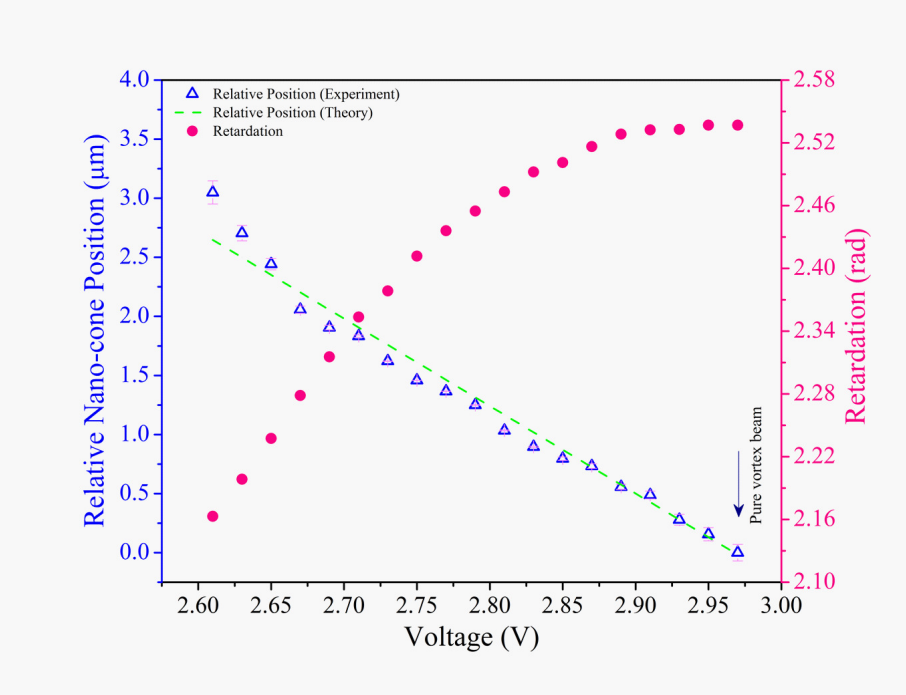

Figure 5.6: S2- The left ordinate in blue shows relative position of the nanocone as a function of voltage on the q-plate, measured with respect to its original location when a pure OAM beam irradiated the silicon surface. The green dashed line corresponds to the theoretical value demonstrating linear dependence. Right ordinate in pink demonstrates variation of optical retardation with applied voltage.

In a simple configuration, with only q=1/2 plate in the setup we were able to control the relative position of the nanocone with respect to its original location (produced by a pure vortex beam with ℓ=±1). For a fixed relative phase between the LG beam components, varying the optical retardation shifted the nanocone as shown in Fig. 5.6. This was achieved by detuning the voltage on the q-plate. As the relative weight of the Gaussian beam increased with respect to a pure VV beam (voltage decreased) the vortex and hence the nanocone position shifted linearly away from the center of the ablated region and moved towards the boundary (rim). The first data point corresponds to the nanocone's position when the composite beam is dominated by the Gaussian component while the last data point corresponds to a pure VV beam.

The following procedure illustrates how the optical retardation was calibrated with the voltage applied on the q-plate. Left-circular (L) polarized light was passed through the q=1/2 plate to achieve spin to orbital angular momentum conversion. After the q-plate, a quarter wave plate (QWP) whose optics axis is at 45° with respect to the q-plate and a polarizing beam-splitter (PBS) produced two output beams; a pure converted beam with a doughnut-shaped profile as a transmitted component, and an unconverted beam with a Gaussian profile as a reflected component. The transmitted component corresponds to the pure VV beam with right circular polarization (R, ℓ=1) while the reflected component corresponds to pure Gaussian beam with left circular polarization (L, ℓ=0).

For a total power of P_0, the powers of the coherently converted ($P_{R,1}$) and unconverted ($P_{L,0}$) components depend on the optical retardation as,

$$P_{R,1} = P_0\, sin^2\left(\frac{\delta}{2}\right)$$
$$P_{L,0} = P_0\, cos^2\left(\frac{\delta}{2}\right)$$

Varying the applied voltage to the q-plate and measuring the power of the two output beams of the PBS determined the optical retardation. The torque exerted on the liquid crystal molecules by the applied electric field is responsible for such dependency [53].

5.3.3 NA=0.25 Versus NA=0.55

Spatial precision of ∼50nm was achieved in placing the nanocone within the ablated region by focusing vortex pulses with a numerical aperture (NA) of 0.25, determined primarily by the dimensions of the nanocone tip. The spatial precision can be improved further by tighter focusing with a high NA lens. This creates a smaller null intensity region leading to a smaller/sharper nanocone as shown in Fig. 5.7 (a). The graph shows two nanocones with radii of curvature of 30 nm and 80 nm produced by aspheric lenses with NA=0.25 and NA=0.55, respectively. The results confirm that the radius of curvature of the nanocone tip decreases as the numerical aperture of the objective increases. Figure 5.7 (b) presents a side-view SEM image of a nanocone produced by a single vortex pulse with an energy of 400 nJ.

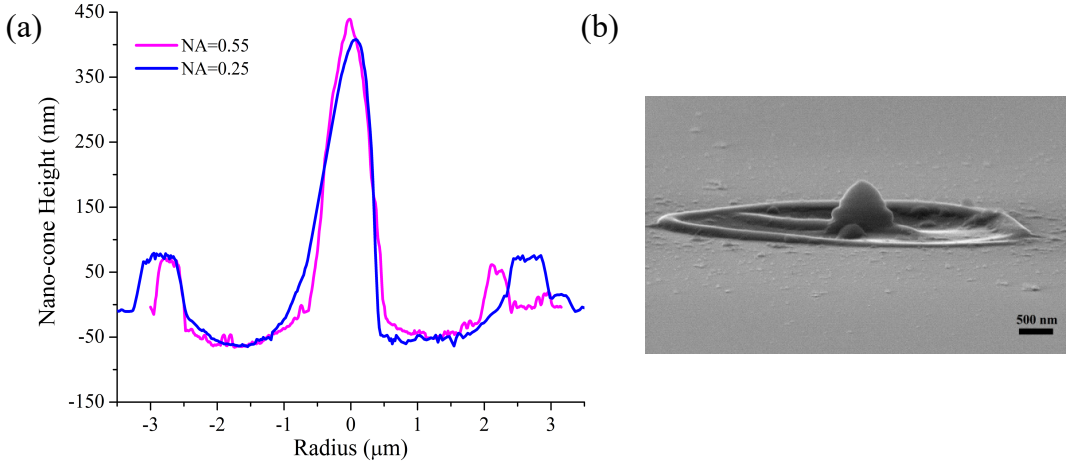

Figure 5.7: S3- (a) The AFM measurements for two nanocones produced by aspheric lenses with NA=0.25 and NA=0.55. The radii of curvature of 30 nm and 80 nm were achieved, respectively. (b) A side-view SEM image of a nanocone created by a 400 nJ vortex pulse.

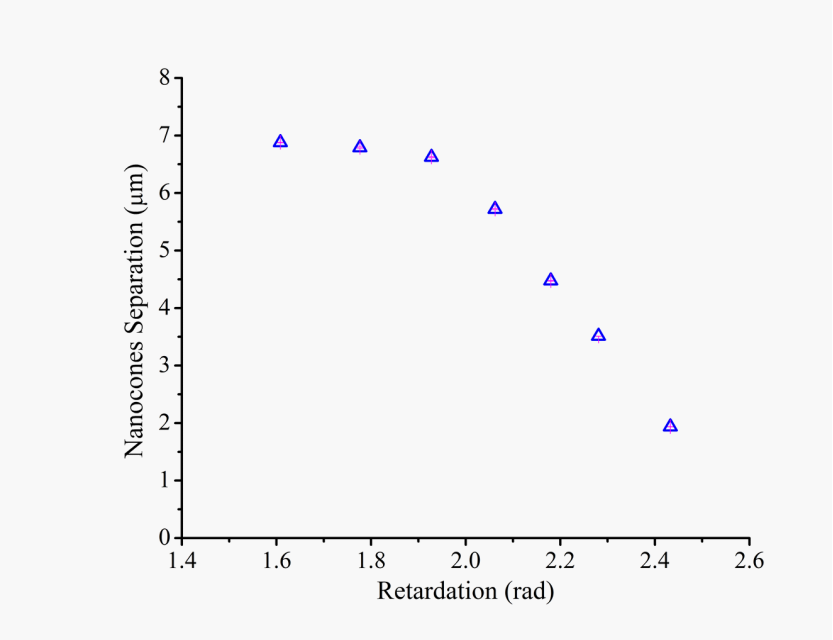

Figure 5.8: S4- Decrease in nanocones separation as the optical retardation of q=-1 plate is increased. For a tuned q-plate, only one nanocone exists at the center of the ablated region. When q-plate is detuned, optical retardation decreases leading to an increase in the weight of the Gaussian beam and the nanocones separation.

5.3.4 Nanocones Separation vs Optical Retardation

When a pure VV beam of ℓ=2 is perturbed, two nanocones are formed within the ablated region. Their separation can be precisely controlled by detuning the q-plate as shown in Fig. 5.8. In a detuned q-plate, Gaussian beam is superimposed on the VV beam. Such superposition results in decomposition of the vortex into two single-charged vortices (each dark spot with charge of ℓ=1). Varying the voltage on the q-plate changes the relative weights of the Gaussian and vortex components. In other words, the optical retardation hence the separation between the nanocones changes.

Figure 5.8 shows the nanocones separation decreases as the portion of the Gaussian beam decreases or the optical retardation increases. The orientation of the two nanocones can also be precisely controlled by varying the relative phase between the two components of the superimposed beams, as shown in Fig.2 of the main text. This can be achieved by rotating a HWP introduced before the q-plate.

5.3.5 Manipulating the Number and Position of the Nanocones

Optical retardation and topological charge of the q-plate play a crucial role in determining the number and the location of the nanocones. For a fixed topological charge, changing the optical retardation changes the relative weight of the optical states present in the coherent superposition leading to different asymmetric intensity distributions. For instance, a three-

petal flower intensity profile was produced by an experimental configuration consisting of a q-plate with topological charge of q=-1 followed by a HWP and a q-plate with topological charge of q=1/2. Varying the voltage applied on the second q=1/2 plate while the applied voltage on the first q=-1 plate was fixed for a maximum conversion ($\delta = \pi$), allowed us to set the intensity ratio and achieve several position-controlled nanocones. In this case, a superposition of two beams with ℓ=+1 and ℓ=-2 was generated which allowed to have an optical vortex of charge ℓ=+1 at the centre surrounded by three vortices of charge -1 arranged symmetrically and located at the same radial distance from the centre at the angles of $\pi/3$, π, and $5\pi/3$ [54]. As the relative amplitude of the ℓ=-2 component in the superimposed beam was decreased (increased), the peripheral vortices and hence the nanocones positions moved radially in (out), as shown in Fig. 5.9.

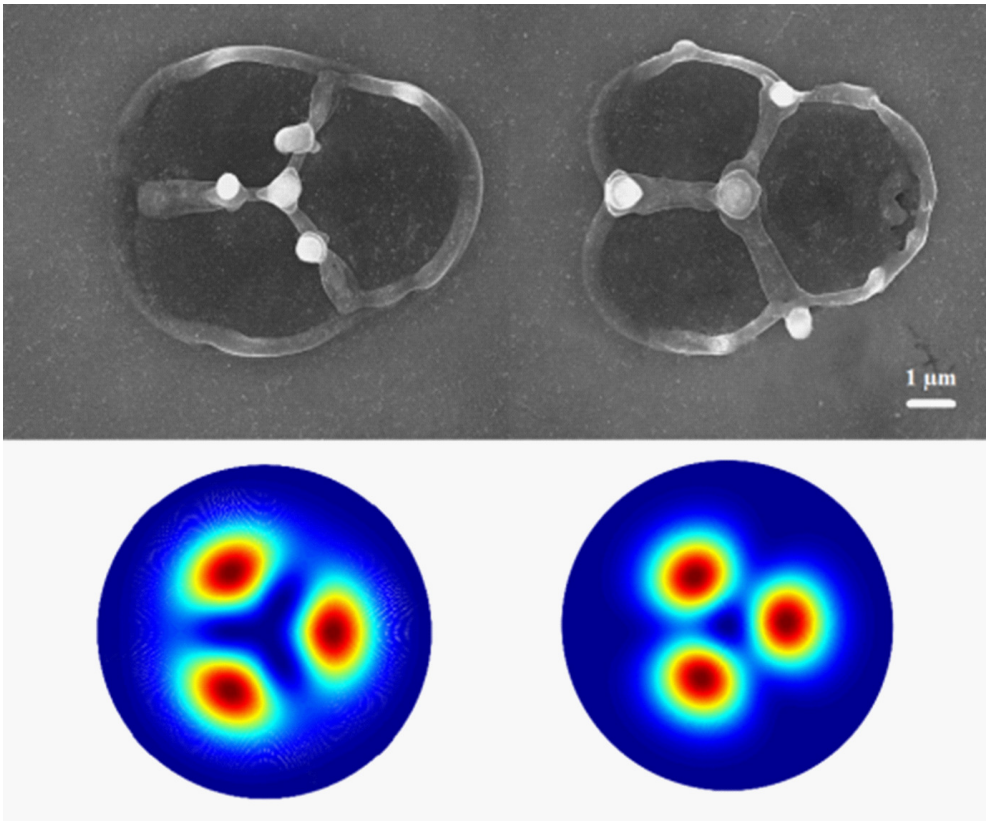

Figure 5.9: S5- (Top panel) the SEM images show the peripheral nanocones moving radially outward as the relative amplitude of the ℓ=-2 component in the superimposed beam increased. Three nanocones are located at the same radial distance from the centre at the angles of $\pi/3$, π, and $5\pi/3$. (Bottom panel) Simulation of intensity profiles corresponding to the SEM images.

We were also able to generate a five-petal flower intensity distribution by using a sequence of a HWP, a tuned q-plate with topological charge of q=-1, and a q=1/2 plate with an adjustable voltage. When the alignment is accurate, the vortex laser beam regenerated in this configuration produced a structure consisting of a single nanocone at the centre and five peripheral nanocones located at the same radial distance from the central cone,

as shown in Fig. S6 (a). A small detuning of the first q-plate with topological charge of q=-1 resulted in the central nanocone to split into two, as shown in Fig. 4b of the main text. The corresponding AFM image is shown in Fig. S6 (b). The nanocones height varies between 400 nm and 670 nm.

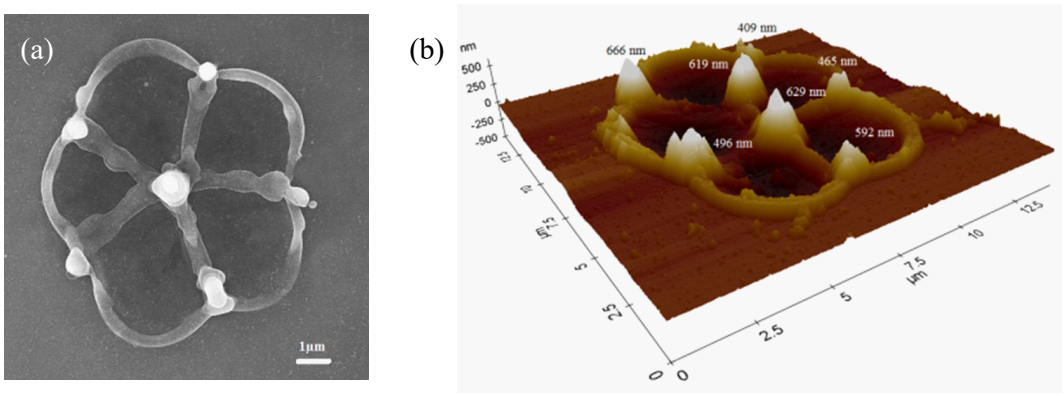

Figure 5.10: S6- (a) The SEM image shows a 5-petal flower-shaped structure produced by a tuned q=-1 and detuned q=1/2 plates. The structure consists of a single nanocone at the centre of the ablated region surrounded by 5 nanocones located at the same radial distance from the centre. (b) The AFM image of the 5-petal flower-shaped structure, shown in the Fig. 4b of the main text, with the central cone splitting into two due to detuning of the q=-1 plate. The heights of the nanocones vary from 400 nm to 670 nm.

Bibliography

[1] V. P. Veiko, E. A. Shakhno, V. N. Smirnov, A. M. Miaskovski, and G. D. Nikishin, "Laserinduced film deposition by LIFT: Physical mechanisms and applications", Laser and Particle Beams, 24, 203209 (2006).

[2] P. Serra and A. Piqué, "Laser-Induced Forward Transfer: Fundamentals and Applications", Adv. Mater. Technol., 4, 1800099 (2019).

[3] J. Lawrence, J. Pou, D.K.Y. Low, E. Toyserkani, "Advances in Laser Materials Processing-Technology, Research and Application", Woodhead Publishing, Pages 735-762 (2010).

[4] R. Fardel, M. Nagel, F. Nuesch, T. Lippert, A. Wokaun, "Laser-induced forward transfer of organic LED building blocks studied by timeresolved shadowgraphy", J. Phys. Chem. C, 114, 5617 (2010).

[5] Q. Li, D. Grojo, A. Alloncle, B. Chichkov, and P. Delaporte, "Digital laser micro- and nanoprinting", Nanophotonics, 8(1), 27 (2019).

[6] T. F. Scott, B. A. Kowalski, A. C. Sullivan, C. N. Bowman, R. R. McLeod, "Two-Color Single-Photon Photoinitiation and Photoinhibition for Subdiffraction Photolithography", Science, 324, 913917 (2009).

[7] P. Müller, R. Müller, L. Hammer, C. Barner-Kowollik, M. Wegener, E. Blasco, "STED-inspired Laser Lithography Based on Photoswitchable Spirothiopyran Moieties", Chem. Mater., 31, 1966 (2019).

[8] Z. Gan, Y. Cao, R. A. Evans, and M. Gu, "Three-dimensional deep sub-diffraction optical beam lithography with 9 nm feature size", Nat. Commun. 4, 2061 (2013).

[9] Abbe, E., "A contribution to the theory of the microscope and the nature of microscopic vision". Proc. Bristol Nat. Soc. 1, 20017261 (1874).

[10] Lin, B-J., "Immersion lithography and its impact on semiconductor manufacturing", J. of Micro/Nanolithography, MEMS, and MOEMS, **3** 377-395 (2004).

[11] Wagner, C. & Harned, N., "Lithography gets extreme", Nature Photonics, **4**, 24 (2010).

[12] "EUV lithography", Editor: Bakhsi, V., SPIE press, 2nd edition 2009

[13] Pereira, A., Grojo, D., Chaker, M., Delaporte, P., Guay, D. & Sentis, M., "Laser fabricated porous alumina membranes for the preparation of metal nanodot arrays" ,Small, **4**, 572 (2008).

[14] Ito, T. & Okazaki, S., "Pushing the limits of lithography", Nature, **406**, 1027 (2000).

[15] Xie, X. N., Chung, H. J., Sow, C. H. & Wee, A. T. S., "Nanoscale materials patterning and engineering by atomic force microscopy nanolithography", Materials Science and Engineering: R: Reports, **54**, 1-48 (2006).

[16] Jersch, J. & Dickmann, K., "Nanostructure fabrication using laser field enhancement in the near field of a scanning tunneling microscope tip", Appl. Phys. Lett. **68**, 868 (1996).

[17] Kawata, S., Sun, H-B., Tanaka, T. & Takada. K, "Finer features for functional microdevices", Nature, **412**, 697 (2001).

[18] Yanik, M. F., Cinar, H., Cinar, H. N., Chisholm, A. D., Jin, Y. & Ben-Yakar, A., "Functional regeneration after laser axotomy", Nature, **432**, 822 (2004).

[19] Joglekar, A. P., Liu, H-H., Meyhfer, E., Mourou, G. & Hunt, A. J., "Optics at critical intensity: Applications to nanomorphing", Proc. Natl. Acad. Sci., **101**, 5856 (2004).

[20] Juodkazis, S., Mizeikis, V., Seet, K. K., Miwa, M. & Misawa, H., "Two-photon lithography of nanorods in SU-8 photoresist", Nanotechnology, **16**, 846 (2005).

[21] Garcia-Lechuga, M., Utza, O., N. Sanner, N. & Grojo, D., "Evidencing the nonlinearity independence of resolution in femtosecond laser ablation", Opt. Lett. **45**, 952 (2020).

[22] Taylor, R. S., Hnatovsky, C., Simova, E., Rayner, D. M., Bhardwaj, V. R. & Corkum, P. B., "Femtosecond laser fabrication of nanostructures in silica glass", Opt. Lett. **28**, 1043-1045 (2003).

[23] Zhang, Q., Lin, H., Jia, B., Xu, L. & Gu, M., "Nanogratings and nanoholes fabricated by direct femtosecond laser writing in chalcogenide glasses", Opt. Express **18**, 6885-6890 (2010).

[24] Her, T-H., Finlay, R. J., Wu, C., Deliwala, S. & E. Mazur, "Microstructuring of silicon with femtosecond laser pulses", Appl. Phys. Lett. **73**, 1673 (1998).

[25] Nayak, B. K., Gupta, M. C. & Kolasinski, K. W., "Formation of nano-textured conical microstructures in titanium metal surface by femtosecond laser irradiation", Appl. Phys. A **90**, 39917402 (2008).

[26] Rahimian, M. G., Bouchard, F., Al-Khazraji, H., Karimi, E., Corkum, P. B. & Bhardwaj, V. R., "Polarization dependent nanostructuring of silicon with femtosecond vortex pulse", App. Phys.Lett., Photonics **2**, 086104 (2017).

[27] Toyoda, T., Miyamoto, K., Aoki, N., Morita, R. & Omatsu, T., "Using Optical Vortex To Control the Chirality of Twisted Metal Nanostructures", Nano Letters, **12**, 3645 (2012).

[28] Nivas, J. J. J., He, S., Rubano, A., Vecchione, A., Paparo, D., Marrucci, L., Bruzzese, R. & Amoruso, S., "Direct Femtosecond Laser Surface Structuring with Optical Vortex Beams Generated by a q-plate", Scientific Reports **5**, 17929 (2015).

[29] Bhardwaj, V. R., Simova, E., Rajeev, P. P., Hnatovsky, C., Taylor, R. S., Rayner, D. M. & Corkum, P. B., "Optically Produced Arrays of Planar Nanostructures inside Fused Silica", Phys. Rev. Lett. **96**, 057404 (2006).

[30] Alameer, M., Jain, A., Rahimian, M. G., Larocque, H., Corkum, P. B., Karimi, E. & Bhardwaj, V. R., "Mapping complex polarization states of light on a solid", Opt. Lett. **43** 5757 (2018).

[31] Serra, P. & Pique, A., "Laser-Induced Forward Transfer: Fundamentals and Applications", Adv.Mater. Technol., **4**, 1800099 (2019).

[32] Morales, M., Munoz-Martin, D., Marquez, A., Lauzurica, S. & Molpeceres, C., "Laser-Induced Forward Transfer Techniques and Applications", Advances in laser material processing, 2nd edition, Woodhead publishing, pages 339-379, (2018).

[33] Makarov, S. V., Zalogina, A. S., Tajik, M., Zuev, D. A., Rybin, M. V., Kuchmizhak, A. A., Juodkazis, S. & Kivshar, Y., "Light-Induced Tuning and Reconfiguration of Nanophotonic Structures", Laser Photonics Rev., **11**, 1700108 (2017).

[34] Betzig, E., Trautman, J. K., Harris, T. D., Weiner, J. S. & Kostelak, R. L., "Breaking the Diffraction Barrier: Optical Microscopy on a Nanometric Scale", Science, **251**, 1468-1470 (1991).

[35] Betzig, E. & Trautman, J.K., "Near-Field Optics: Microscopy, Spectroscopy, and Surface Modification Beyond the Diffraction Limit", Science,**257**,189-195 (1992).

[36] Gramotnev, D. K. & Bozhevolnyi, S. I., "Plasmonics beyond the diffraction limit", Nature Photonics, **4**, 831791 (2010).

[37] Schuller, J. A., Barnard, E. S., Cai, W., Jun, Y. C., White, J. S. & Brongersma, M. L., "Plasmonics for extreme light concentration and manipulation", Nature Materials ,**9**,19317204 (2010).

[38] Hell, S. W. & Wichmann, J., "Breaking the diffraction resolution limit by stimulated emission: stimulated emission depletion microscopy". Opt. Lett. 19, 78017782 (1994)

[39] D'Errico, A., Maffei, M., Piccirillo, B., de Lisio, C., Cardano, F. & Marrucci, L., "Topological features of vector vortex beams perturbed with uniformly polarized light", Scientific reports, **7**, 40195 (2017).

[40] Takahashi, F., Miyamoto, K., Hidai, H., Yamane, K., Morita, R. & Omatsu, T., "Picosecond optical vortex pulse illumination forms a monocrystalline silicon needle", Scientific Reports, **6**, 21738 (2016).

[41] Toyoda, K., Miyamoto, K., Aoki, N., Morita, R. & Omatsu,T., "Using Optical Vortex To Control the Chirality of Twisted Metal Nanostructures", Nano Lett. **12**, 3645 (2012).

[42] Syubaeva, S., Zhizhchenko, A., Vitrika, O., Porfirev, A., Fomchenkov, S., Khonina, S., Kudryashove, S., Kuchmizhak, A., "Chirality of laser-printed plasmonic nanoneedles tunable by tailoring spiral-shape pulses", Applied Surface Science, **470**, 526 (2019).

[43] Gan, Z., Cao, Y., Evans, R. A. & Gu, M., "Three-dimensional deep sub-diffraction optical beam lithography with 9nm feature size", Nature Comm, **4**, 2061 (2013).

[44] Kim, T., Kim, J-H., Son, S. J. & Seo, S-M., "Gold nanocones fabricated by nanotransfer printing and their application for field emission", Nanotechnology, **19**, (2008).

[45] Li, W., Zhou, J., Zhang, X-G., Xu, J., Xu, L., Zhao, W., Sun, P., Song, F., Wan, J. & Chen, K., "Field emission from a periodic amorphous silicon pillar array fabricated by modified nanosphere lithography", Nanotechnology, **19**, 1355308 (2008).

[46] Yang, Y. H., Zhang, Y., Wang, N. W., Wang, C. X., Li, B. J. & Yang, G. W., "ZnO nanocone: Application in fabrication of the smallest whispering gallery optical resonator", Nanoscale, **3** 59217597 (2011).

[47] Wang, B. & Leu, P. W., "Enhanced absorption in silicon nanocone arrays for photovoltaics", Nanotechnology, **23**, 194003 (2012).

[48] Marrucci, L., Manzo, C. & Paparo, D., "Optical spin-to-orbital angular momentum conversion in inhomogeneous anisotropic media", Phys. Rev. Lett. **96** 163905 (2006).

[49] Larocque, H., Gagnon-Bischoff, J., Bouchard, F., Fickler, R., Upham, J., Boyd, R. W. & Karimi, E., "Arbitrary optical wavefront shaping via spin-to-orbit coupling", J. Opt., **18**, 124002 (2016).

[50] Marrucci, L., Karimi, E., Slussarenko, S., Piccirillo, B., Santamato, E., Nagali, E. & Sciarrino, F., "Spin-to-orbital conversion of the angular momentum of light and its classical and quantum applications", J. Opt., **13** 064001 (2011).

[51] E. Karimi, B. Piccirillo, L. Marrucci, and E. Santamato, "Hypergeometric-Gaussian modes", Opt. Lett. 34, 1225 (2009).

[52] L.Marrucci, E. Karimi, S. Slussarenko, B. Piccirillo, E. Santamato, E. Nagali, and F. Sciarrino, "Spin-to-orbital conversion of the angular momentum of light and itsclassical and quantum applications", J. Opt. 13, 064001(2011).

[53] B. Piccirillo, V. D'Ambrosio, S. Slussarenko, L. Marrucci, and E. Santamato , "Photon spin-to-orbital angular momentum conversion via an electrically tunable q-plate", APPLIED PHYSICS LETTERS 97, 241104 (2010).

[54] S. Baumann, D. Kalb, L. MacMillan, E. Galvez, "Propagation dynamics of optical vortices due to Gouy phase" Opt. Express, 17, 98189827 (2009).

Chapter 6

Visualization of Complex Polarization States of Light

6.1 Introduction

It is known that there is a class of light beams characterized by a variable polarization direction along the azimuthal coordinate (φ). They are called vector vortex (VV) beams, also known as spirally polarized beams, that can be generated via several techniques, for instance, exploiting a q-plate. An important group of VV beams is those with cylindrical-symmetric polarization patterns, i. e., radial and azimuthal polarized beams that are made up of linear combinations of two helical waves with opposite topological charge $\ell = \pm 1$ and opposite polarizations ($s = \pm 1$, corresponding to the left and right circular polarization). In other words, a linear combination of two OAM eigenstates with eigenvalue $\pm\ell$ produces an arbitrary VV beam. Moreover, a linear combination of symmetric pairs of VV beams generates two-dimensional spaces of non-uniform polarization states known as "higher-order Poincaré spheres". Although there are some theoretical and experimental methods to determine these complex polarization states, they can not be easily characterized by polarizers and waveplates.

In recent years, there has been a rising interest in laser surface texturing using such beams with femtosecond pulse durations. This is because they can be easily achieved by tuning the q-plates. Doing this, one can produce vortex beams with various states of polarization (SoPs), and consequently, numerous spatially variant surface structures become a straightforward, single-step process. Moreover, there is a direct relationship between the morphology and orientation of the fabricated surface structures and the spatial intensity profile and SoP of the laser beam. Such a relation was our motivation to explore mapping the higher-order polarization states of light onto a solid surface to be able to directly visualize them without going through complex calculations and measurements to characterize them. In the following, a brief introduction to the Poincaré sphere and methods to calculate the polarization states is provided.

6.2 Poincaré Sphere and Stokes Parameters

A representation of the state of polarization of light was introduced in 1892 by Poincaré [1]. He showed that the polarization states of a beam of light could be represented by a point on the surface of a sphere, known as the Poincaré sphere, as shown in Fig. 6.1.

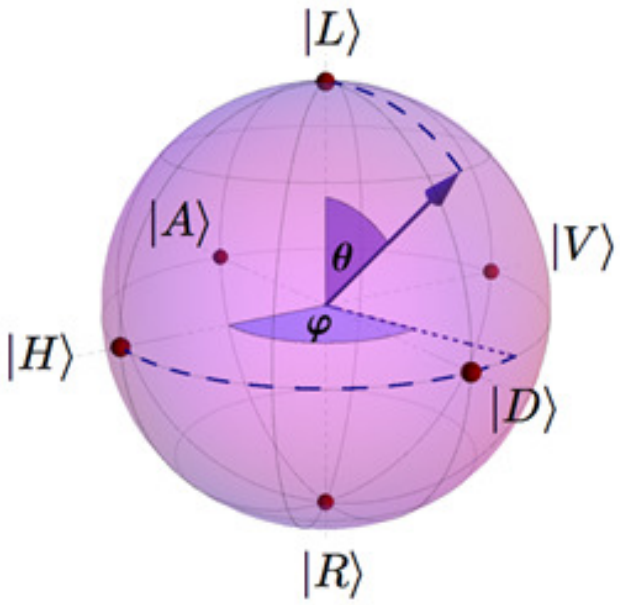

Figure 6.1: Poincaré sphere with three different polarization basis [2].

The poles of this sphere represent the circular polarizations whereas linear polarization states reside on the equator. Any state of polarization on the Poincaré sphere can be represented by specifying two angles, θ and χ:

$$|\psi\rangle = cos(\frac{\theta}{2})\,|L\rangle + sin(\frac{\theta}{2})e^{i\varphi}\,|R\rangle \tag{6.1}$$

where $|L\rangle$ and $|R\rangle$ denote the left- and right circular polarization states, respectively. The special polarizations are given by the following angles; Left circular polarization (L): θ=0, Right circular polarization (R): θ=π and φ=0, Horizontal polarization (H): θ=$\pi/2$ and φ=0, Vertical polarization (V): θ=$\pi/2$ and φ=π, Diagonal polarization (D): θ=$\pi/2$ and φ=$\pi/2$, Antidiagonal polarization (A): θ=$\pi/2$ and φ=$3\pi/2$. Any other combinations represent the elliptical polarization. We can extend the concept of the Poincaré sphere to include points within the sphere as well. In this case, the center of the sphere is associated with a completely unpolarized state, whereas other points within the interior of the sphere represent states that are partially polarized, and finally, points on the surface of the sphere represent pure polarized states.

6.2.1 Stoke's Parameters

The Poincaré sphere is equivalent to all of the fundamental ways to describe polarization. The Stokes parameters can be described as the Cartesian coordinates in which the Poincaré sphere is originated. The state of polarization that is complex Jones vectors are mapped on the surface of the Poincaré sphere through the Stokes parameters [3]. Another method of describing the polarization of an electromagnetic field is through specifying a set of numbers (namely four) known as Stoke's parameters. This method is similar to describing a two dimensional observable in quantum mechanics by expanding in terms of the spin 1/2 Pauli matrices and the Identity operator. The Stoke's parameters for two-dimensional states are given by:

$$\begin{aligned} I_D + I_A &= 1 \\ S_0 &\equiv I_L + I_R = I_H + I_V \\ S_1 &\equiv I_H - I_V, S_2 \equiv I_D - I_A, S_3 \equiv I_L + I_R \end{aligned} \tag{6.2}$$

Here I_i is the modulus square amplitude (intensity) of the polarization component i. The subscript D, A, L, R, H, and V indicate the diagonal, anti-diagonal, left circular, right circular, horizontal, and vertical polarization states, respectively. For a completely polarized light one can show that:

$$S_0^2 = S_1^2 + S_2^2 + S_3^2 \tag{6.3}$$

Sometimes it is more convenient to work with the dimensionless reduced Stokes parameters defined as:

$$s_1 \equiv \frac{S_1}{S_0}, \quad s_2 \equiv \frac{S_2}{S_0}, \quad s_3 \equiv \frac{S_3}{S_0} \tag{6.4}$$

6.3 Higher Order Poincaré Sphere and Stokes Parameters

Though extremely useful, the state of polarization representation by the Poincaré sphere has its shortcomings. First of all, it can only represent the simplest solutions to Maxwell's equations in the form of fundamental homogeneous wave planes. However, there are problems in which the solutions of Maxwell's equations are even more complicated, such as laser cavity resonators and fiber optical waveguides [4]. In these cases, higher-order solutions to Maxwell's equations admit spatially inhomogeneous states of polarization, typically in cylindrically symmetric systems. Most importantly, vectorial vortex beams (known as spirally polarized beams) [5] such as radial and azimuthally polarized cylindrical vector beams cannot be properly described by the ordinary Poincaré sphere. In this case, higher-order Poincaré spheres representation can be used [6]. As we will see later, light possesses a

spin angular momentum per photon of $s\hbar$ where s=+1 for left circular polarization and s=-1 for left circular polarization. Moreover, light can carry orbital angular momentum, which is quantized by values of $\ell\hbar$ (ℓ=0,±1,±2,$\cdots$ is the topological charge). This quantity is associated with the helical wavefront (otherwise known as the optical vortex) by the azimuthal phase factor $e^{i\ell\varphi}$. Moreover, in the paraxial regime, light has two degrees of freedom, spin and orbital angular momentum, become additive resulting in the total angular momentum given by $(\ell + s)\hbar$. The state of polarization of vector vortex beams is a linear combination of orthogonal circular polarization and optical vortices with opposite topological charges. Consider a monochromatic beam in the paraxial approximation, if the plane of polarization is the XY plane, then its angular momentum state can be represented by $|\pi,\ell\rangle = c_L^\ell\,|L,\ell\rangle + c_R^\ell\,|R,\ell\rangle$ where $|L,\ell\rangle = \frac{1}{\sqrt{2}}(\hat{x}+i\hat{y})e^{-i\ell\varphi}$ and $|R,\ell\rangle = \frac{1}{\sqrt{2}}(\hat{x}-i\hat{y})e^{i\ell\varphi}$ are the left and right circular polarization states of topological charges of -ℓ and +ℓ respectively. The related normalized higher order Stokes parameters are given by [6]

$$\begin{aligned}
S_0^\ell &= |\langle R,\ell|\pi,\ell\rangle|^2 + |\langle L,\ell|\pi,\ell\rangle|^2 = |c_R^\ell|^2 + |c_L^2|^2,\\
S_1^\ell &= 2Re\left(\langle R,\ell|\pi,\ell\rangle^*\langle L,\ell|\pi,\ell\rangle\right) = 2|c_R^\ell||c_L^\ell|cos\phi,\\
S_2^\ell &= 2Im\left(\langle R,\ell|\pi,\ell\rangle^*\langle L,\ell|\pi,\ell\rangle\right) = 2|c_R^\ell||c_L^\ell|sin\phi,\\
S_3^\ell &= |\langle L,\ell|\pi,\ell\rangle|^2 - |\langle R,\ell|\pi,\ell\rangle|^2 = |c_L^\ell|^2 + |c_R^2|^2,
\end{aligned} \tag{6.5}$$

In the relations above, ϕ is the relative phase given by Arg(c_L^ℓ)-Arg(c_R^ℓ). The higher-order Poincaré sphere is constructed using S_1^ℓ, S_2^ℓ, and S_3^ℓ as the spheres Cartesian coordinates with $S_0^"\ell$ the unit radius from the origin and the spheres spherical angles (2θ;2φ) given by: 2θ=tan^{-1} (S_2^ℓ/S_1^ℓ) and 2φ=sin^{-1}(S_3^ℓ/S_0^ℓ) [6]. The sphere then describes a higher order vector vortex state of polarization at each point (2θ;2φ) on the surface. The poles of the sphere represent circularly polarized optical vortices, and the equator represents a vector vortex state of polarization that is linearly polarized everywhere. Points between the poles and the equator represent elliptically polarized vector vortex polarizations. The higher-order Poincaré sphere reduces to the standard Poincaré sphere for ℓ=0. For nonzero topological charges, the optical vortex and circular polarization handedness of each pole can be either the same or opposite, and thus in higher-order basis, two spheres must be described. In the figure below, two spheres representing ℓ=1 and ℓ=-1 are shown

Finally, we mention that in order to describe the full state of polarization of light, one must perform a full state quantum tomography in order to determine the density matrix. Practically this is done via using optical elements such as half-wave plates, quarter-wave plates, and polarizing beam splitters, which provide an experimental method to measure the Stokes parameters which are used for the full tomography [7].

6.4 Polarization Tomography

Based on what was mentioned earlier on the Poincaré Sphere and Stokes's parameters, there is an experimental technique used to reconstruct the polarization state of a beam

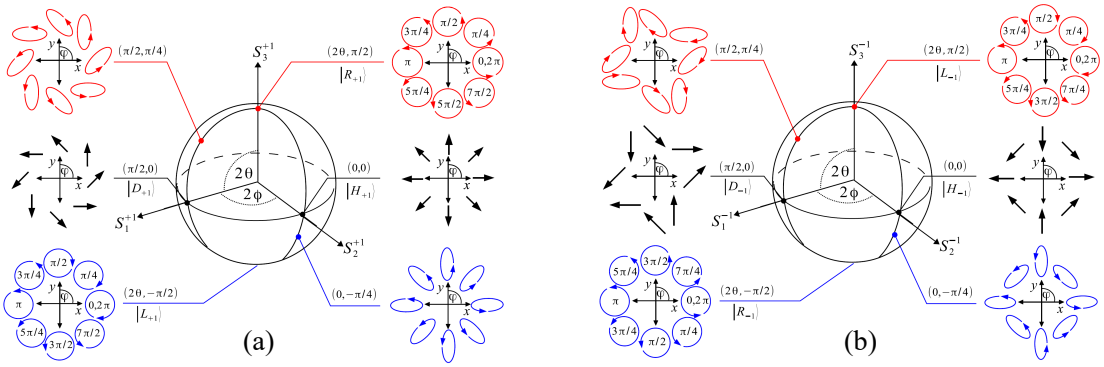

Figure 6.2: Higher order Poincaré spheres with three different polarization basis [6].

of light. The purpose of polarization tomography is to achieve this goal by performing light intensity measurements on different bases. In practice, the process of polarization tomography can be realized by performing a set of projective measurements on the light beam. With a simple setup, as shown in Fig. 6.3 and the aid of a CCD camera, one can register the intensities of light, which are projected along the three different bases discussed earlier. The outcomes of the projected measurements lead to 6 values I_L (recorded intensity of left circular light), I_R (recorded intensity of right circular light), I_H (recorded intensity of horizontally polarized light), I_V (recorded intensity of vertically polarized light), I_D (recorded intensity of diagonally polarized light), and I_A (recorded intensity of anti-diagonally polarized light). With these values at hand, the four Stoke's parameters are evaluated as

$$\begin{aligned} S_0 &= I_L + I_R \\ S_1 &= I_H + I_V \\ S_2 &= I_A + I_D \\ S_3 &= I_L - I_R \end{aligned} \tag{6.6}$$

In suitable units, these intensities are the module squares of the field amplitudes: $I_L = |E_L|^2$, $I_R = |E_R|^2$, $I_H = |E_H|^2$, $I_V = |E_V|^2$, $I_D = |E_D|^2$, and $I_A = |E_A|^2$. Equipped with the set S_0, S_1, S_2, S_3, one can determine the state of polarization of light. The process is as follows. As we saw earlier, any given polarization can be represented by a unique point on the surface of the Poincaré sphere. Thus, in order to reconstruct a particular polarization state, it suffices to specify two angles; the polar angle (θ and the azimuthal angle φ).

$$|\pi\rangle = cos(\theta/2)\,|\mathrm{L}\rangle + sin(\theta/2)e^{i\varphi}\,|R\rangle \tag{6.7}$$

These angles are related to the two angles χ and ψ, since the Poincaré sphere is also the parametrisation of the three Stoke's parameters, S_1, S_2 and S_3 in spherical coordinates

$$\begin{aligned}\theta &= \frac{\pi}{2} - 2\chi \\ \varphi &= 2\psi\end{aligned} \tag{6.8}$$

The Stoke's parameters which describe the polarization state of a beam of light, are given in terms of the total beam intensity, I, degree of polarization, p, and the shape parameters (χ and ψ) of the polarization ellipse:

$$\begin{aligned}S_0 &= 1 \\ S_1 &= I\ p\ cos(2\psi)cos(2\chi) \\ S_2 &= I\ p\ sin(2\psi)cos(2\chi) \\ S_3 &= I\ p\ sin(2\chi)\end{aligned} \tag{6.9}$$

The degree of polarization, p, can take any value between 0 and 1, where 0 is related to completely unpolarized light, and 1 is related to fully polarized electromagnetic radiation. Since we use the Poincaré sphere representation, we can normalize the total intensity of the beam, I, to 1. We also restrict ourselves to points on the surface of the Poincaré sphere, thereby looking only at fully polarized light, p=1. Thus, we have

$$\begin{aligned}S_0 &= 1 \\ S_1 &= cos(2\psi)cos(2\chi) = sin(\theta)cos(\varphi) \\ S_2 &= sin(2\psi)cos(2\chi) = sin(\theta)sin(\varphi) \\ S_3 &= sin(2\chi) = cos(\theta)\end{aligned} \tag{6.10}$$

With a little algebra one finds the two angles θ and φ, in terms of the measured intensities along the three axes of the Poincaré sphere as

$$\begin{aligned}\theta = \frac{\pi}{2} - 2\chi &= \frac{\pi}{2} - tan^{-1}\left[\frac{S_3}{\sqrt{S_1^2 + S_2^2}}\right] \\ &= \frac{\pi}{2} - tan^{-1}\left[\frac{I_L - I_R}{\sqrt{(I_H - I_V)^2 + (I_A - I_D)^2}}\right] \\ \varphi = 2\psi &= tan^{-1}\left(\frac{S_2}{S_1}\right) = tan^{-1}\left[\frac{I_A - I_D}{I_H - I_V}\right]\end{aligned} \tag{6.11}$$

We thus reconstruct the desired state of polarization as

$$\begin{aligned}|\pi\rangle = &cos\left(\frac{1}{2}\left\{\frac{\pi}{2} - tan^{-1}\left[\frac{I_L - I_R}{\sqrt{(I_H - I_V)^2 + (I_A - I_D)^2}}\right]\right\}\right)|L\rangle \\ &+ sin\left(\frac{1}{2}\left\{\frac{\pi}{2} - tan^{-1}\left[\frac{I_L - I_R}{\sqrt{(I_H - I_V)^2 + (I_A - I_D)^2}}\right]\right\}\right)e^{i(tan^{-1}\left[\frac{I_A - I_D}{I_H - I_V}\right])}|R\rangle\end{aligned} \tag{6.12}$$

Figure 6.3, shows a simple experimental setup to measure the intensities along with the horizontal and vertical polarization directions. Experimentally, this can be done by using a quarter-wave plate, a half-wave plate, and a polarizing beam splitter. The role of wave plates is to perform unitary operations. In other words, they act as rotations about an axis lying in the plane of a great circle of the Poincaré sphere. In general, a waveplate with an optics axis oriented at an angle θ with respect to the horizontal direction induces a rotation on the Poincaré sphere about an axis 2θ from the horizontal, in the linear plane (the equatorial disk of the Poincaré sphere). The amount of rotation depends on the waveplate's retardance. For a half-wave plate, it is π, and for a quarter-wave plate, it is equivalent to $\pi/2$. A $\pi/2$ rotation of a point on the Poincaré sphere (a given polarization) about a linear axis directly below it will rotate that state into a linear polarization. This state will be rotated to the equator of the Poincaré sphere. The quarter-wave plate rotates the projection state into the linear polarization plane (the equator of the Poincar sphere). The half-wave plate rotates this linear state to horizontal. The PBS transmits the projection state ($|H\rangle$) and reflects its orthogonal complement ($|V\rangle$), which can then both be measured. Now by rotating the axis of the half-wave plate by 22.5°, the linear state will be rotated into diagonal. Thus, the intensities along the diagonal and anti diagonal polarization can be measured. Finally, by removing the half-wave plate and replacing it with another quarter-wave plate with an axis orthogonal to the first quarter-wave plate, one can measure the intensities in the circular bases, and thus, the tomography is completed.

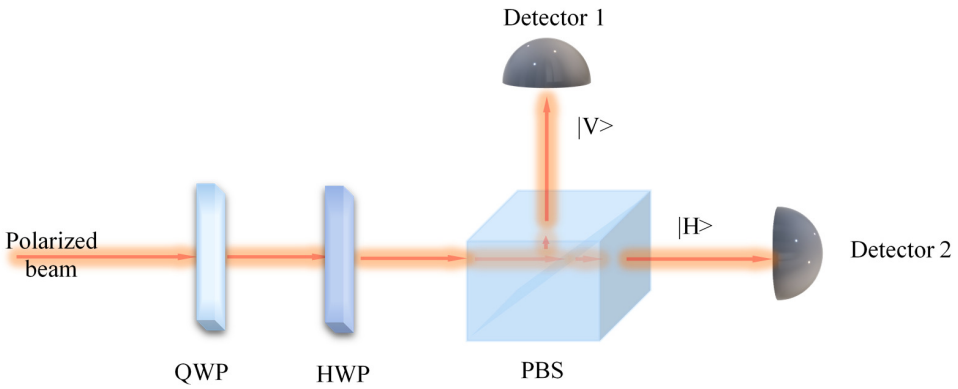

Figure 6.3: An experimental setup to determine the state of polarization.

In the following, for the first time, we present a direct way to visualize these higher-order polarization states by direct fs-laser surface structuring. These VV beams were generated by varying the birefringence optical retardation, δ, of a q-plate. By irradiating multiple pulses on the diamond sample, we could fabricate ripple structures in very complex patterns, whose orientations were an exact map of the polarization states. The technique employed in our experiment can be extended to other materials.

6.5 Mechanism of Ripple Formation

The creation of nano-ripples is the result of localized ionization and laser-plasma interaction in the multiple pulse regime, and can be discussed in three steps: (1) nanoplasma formation, (2) growth of the nanoplasma into nanoplanes, and (3) self-organization of the nanoplanes.

Nanoplasma Formation: When the first tightly focused fs laser pulse irradiates, it ionizes the material via multiphoton ionization in random spots. Local defects such as color centers and impurities are responsible for the locally seeded multiphoton ionization. In these defect points, electrons or holes are trapped and can be ionized more easily due to their reduced ionization potential [8]. Next laser pulses ionize the same spots more preferentially due to the pulse-to-pulse memory effect in the nonlinear ionization [9]. Due to this effect, the local changes induced by the first laser pulse remain in the material and promote the interaction of subsequent pulses irradiating the same areas. Therefore, instead of a uniform plasma, a single pulse in the focal volume can generate preferentially localized ionization resulting in hot ionized spots. Over several laser shots, random ionized spots can evolve into random localized nanoplasmas with spherical shapes.

The growth of the generated nanoplasmas is further affected by the local electric field enhancement around them.

Local Field Enhancement: An external electric field (e. g., a laser beam) causes electrons to behave as dipoles and oscillate back and forth as the electric field oscillates. Depending on the electron density in the material, the oscillations alter the field distributions around the dipoles along the laser electric field or perpendicular to it. By considering the nanoplasma as a spheroid, the electric field enhancement takes place either at the poles or the equator, depending on the plasma density or the electric permittivity. Note that for a spherical nanoplasma, permittivity is determined by $\varepsilon_p = \varepsilon_r + i\varepsilon_i$, where $\varepsilon_r = 1 - N_e/N_{cr}$, N_e is the electron density and N_{cr} is the critical density (where the plasma frequency and the laser frequency are equal).

When the electron density is higher than the critical density (overcritical nanoplasmas), the spherical nanoplasmas behave like metallic nanoparticles in a dielectric target, and thus permittivity becomes a negative quantity with an absolute value greater than one ($\varepsilon \ll -2$).

In this case, the boundary conditions at an interface, defined by Maxwell's equations, require the electric field to be continuous parallel to the interface, and discontinuous perpendicular to it. This means that electric fields inside a metal vanish and electric fields parallel to the interface become equal. It also implies that fields perpendicular to the interface constructively interfere with the dipole radiation causing a field enhancement at the poles of the nanoplasma while the electric field around the equator is suppressed, i.e., $E_{pole} > E_{equator}$, as shown in Fig. 6.4. Since the polar axis of the spherical nanoplasma is along the laser electric field or the laser polarization direction, overcritical nanoplasmas grow along with the laser polarization.

The local field distribution for a sphere at a point on the polar axis and in the equatorial plane are given by

$$E_{pole} = \frac{3\varepsilon\, E}{\varepsilon + 2}$$
$$E_{equator} = \frac{3\, E}{\varepsilon + 2}$$

where $\varepsilon = \frac{\varepsilon_{plasma}}{\varepsilon_{dielectric}}$ is the relative permittivity, and E is the laser electric field.
The local field distribution around a spherical nanoplasma in a dielectric medium is shown in Fig. 6.4.

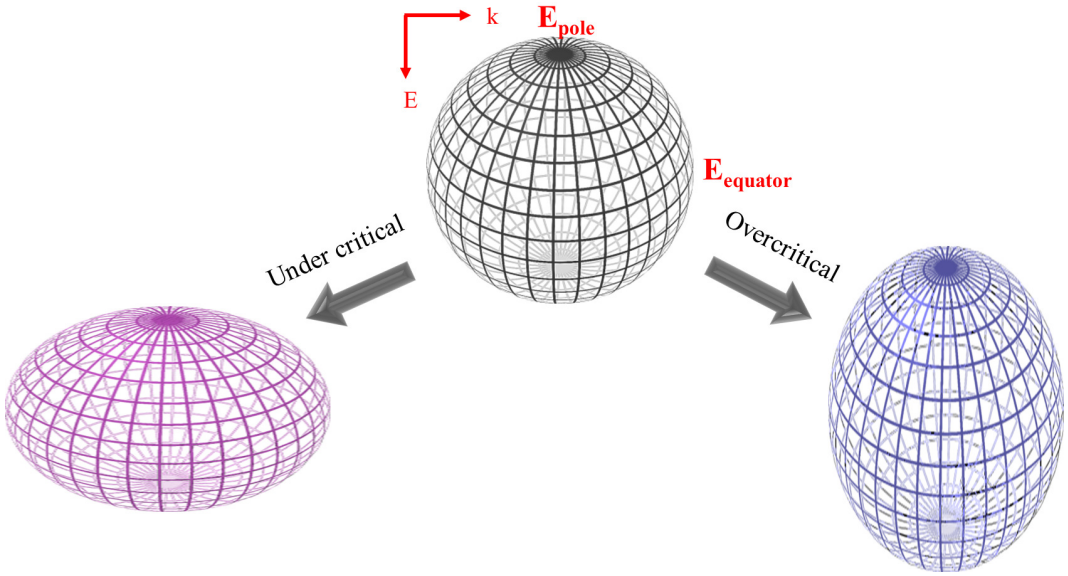

Figure 6.4: Schematic shows how spherical nano-plasma becomes a nano-plane due to the local field enhancement. E is the electric field of the laser beam, k shows the propagation direction of the beam, $E_{equator}=\frac{3\,E}{\varepsilon+2}$ represents the local fields at the equator of the spherical nanoplasma, and $E_{pole}=\frac{3\,\varepsilon\,E}{\varepsilon+2}$ is the local fields at the poles. The relative permittivity is denoted by ε. In the case of overcritical plasma ($\varepsilon > 1$), i. e., when the plasma density is larger than the critical density, field enhancement occurs at the poles that cause the spherical nanoplasma becomes elongated parallel to the laser polarization. However, for undercritical plasma ($0 < \varepsilon < 1$), elongation takes place perpendicular to the laser polarization direction.

In contrast, when the electron density is lower than the critical density (undercritical plasma, $0 < \varepsilon < 1$), dipoles oscillate with a frequency less than the laser frequency and they are out-of-phase with the laser field. The out-of-phase dipole radiation destructively interferes with the laser field, suppressing the field everywhere except in the equatorial plane perpendicular to the electric field. In other words, the perpendicular component of the electric field outside the nanoplasma is enhanced, resulting in $E_{equator} > E_{pole}$. In this case, the electric field inside the plasma is also enhanced and is equal to $E_{equator}$.

Therefore, in contrast to the overcritical case, for an underdense (undercritical) plasma, the field enhancement occurs perpendicular to the laser polarization, which means the nanoplasmas are elongated perpendicular to the laser polarization. Such an undercritical plasma formation has been previously shown when fs laser pulses were focused inside fused silica [10]. In fact, when the focus is inside a bulk, as the pulse propagates through the focus, pulses with intensities above the threshold are absorbed which causes a pulse modification in time and spatial distribution. Therefore, once the pulse reaches the focus, it is trimmed to a flat top intensity. This laser pulse depletion effect is known as the "lawn-mower" effect, because similar to grass clipping, the laser pulse intensity is clamped along with the focus [11]. This effect is due to high order non-linear absorption which is dominant in high band gap transparent materials. This intensity clamping effect, self-limits the modification of the material. In fact, in fs-laser transparent dielectric modification, high intensities required for multiphoton ionization and energy absorption can be reached. However, these intensities cannot exceed the threshold for the self-focusing effect. Further increase in the laser power increases the volume for multiphoton absorption without changing the deposited energy density significantly.

In contrast, in the ablation experiments, when the focus is on the surface of the target (e. g., CVD diamond in my experiment), the plasma density is higher than that inside the material. Therefore, overcritical plasma density is achieved, and nanoplasmas elongate parallel to the laser electric field. Over irradiation of many laser pulses, the spherical nanoplasmas deform into spheroids and grow more creating randomly-placed nanoplanes parallel to the polarization directions.

Self-Organization: As mentioned earlier, the final step in nano-ripple formation is the self-organization of the nano-planes. This process could be attributed to the quasi-metallic properties of the nanoplanes. As the nanoplanes grow, due to their transient nature, they can become quasi-metallic and subsequently influence the light propagation [8]. In a single nanoplane, light can excite surface plasmon polaritons (SPPs), the transverse magnetic waves (TM) with field distributions that are maximum at the interface and decay exponentially outwards [12]. This metallic behavior forces the electric field to propagate in the same way as in a planar metallic waveguide. Therefore, only specific modes will be allowed, and the field distributions at individual nanoplanes have to satisfy the boundary conditions. Due to these conditions, the TE_0 mode is not allowed, while TM_0 can exist and has a uniform field distribution with electric and magnetic fields transverse to the direction of propagation. The next lowest order modes, TE_1 (field maximum in between the metal plates) and TM_1 (field maxima at the plates with a phase flip), can propagate when the waveguide spacing d satisfies the condition $\lambda/2n \leqslant d < \lambda$, where n is the refractive index of the material and λ is the wavelength of the incident light. However, since the SPPs are transverse magnetic waves (TM) in nature, TM waveguide modes are expected [8]. The wave vector of the SPP wave on a metal-dielectric interface is given by [13]

$$k_s = k \sqrt{\frac{\varepsilon_d \, \varepsilon_p}{\varepsilon_d + \varepsilon_p}}$$

where $k = 2\pi/\lambda$ is the wavevector of the incident laser beam, ε_d and ε_p are the permittivity of the dielectric and plasma, respectively.

These surface waves can be excited only if the real part of ε_p is smaller than $-n^2$ and phase-matching condition for k_s and k is satisfied. The first condition implies that the plasma density is greater than the critical density, where $|\varepsilon_p| \gg 1$ and the SPP wavelength is $\lambda_s \approx \lambda/\sqrt{\varepsilon_d}$ ($k_s = n\,k$). The phase matching condition requires that k_s matches half of the Bragg wavevector of the surface structure period (d) [14, 15], therefore,

$$k_s = \frac{2\,\pi}{\lambda_s} = \frac{\pi}{d} \quad \Rightarrow \quad d = \frac{\lambda_s}{2}$$

Since $\lambda_s \approx \lambda/\sqrt{\varepsilon_d} \approx \lambda/n$, the nanoplane are placed at $d = \lambda/2\,n$.

Thus the growth of the nanoplanes will be favored if they support modes whose field distributions reinforce their own growth and are placed in specific positions (d). Other planes do not grow any further [8]. Therefore, in the final step, among all the possible SPPs existing on the plasma surface the smallest period exists that leads to a self-organization phenomenon. To sum up, since the light only reinforces those nanoplanes that are exactly at half of the light wavelength, over the irradiation of many pulses, ordering the nanoplanes evolves from a random distribution of nanoplasmas to planes with the spacing of $\lambda/2n$ imprinted on the surface.

Important note 1: Polarization ellipses defining the SoP in each location of the beam can be well-approximated by small segments whose orientation indicates the dominant local component of the polarization. These segments represent snapshots of the polarization vectors. However, one must notice that they do not have a well-defined direction as their polarization directions are constantly changing .

Important note 2: The laser spot produced with a circularly polarized beam shows no ripple structure. The reason comes from the fact that in a circularly polarized beam, the direction of the polarization vectors varies over time.

6.6 Mapping Complex Polarization States of Light on a Solid

Author Contribution

The published results come from experiments performed by M. Alameer, A. Jain, and M. G. Rahimian at Ultrafast Photonics lab, University of Ottawa, ON, under supervision of V. R. Bhardwaj. M. Alameer, A. Jain, and M. G. Rahimian conducted the analysis of the results, M. Alameer performed the SEM and AFM measurements. A. Alameer and M. G. Rahimian prepared the figures and graph. A. Jain performed the calculations. H. Larocque fabricated the q-plate and assisted in producing vortex beams. P. B. Corkum, E. Karimi, and V. R. Bhardwaj designed the experiment and analysed the data. All authors contributed to writing the manuscript.

Optics Letters, Vol. 43, No. 23, December 2018

Mapping Complex Polarization States of Light on a Solid

M. Alameer, A. Jain, M. G. Rahimian, H. Larocque, P. B. Corkum, E. Karimi, and V. R. Bhardwaj

Department of Physics, Advanced Research Complex, University of Ottawa, 25 Templeton Street, Ottawa, ON, K1N 6N5, Canada

Polarization states of light, represented by different points on a Poincaré sphere, can be readily analyzed for a Gaussian beam by a combination of wave plates and polarizers. However, this method cannot be extended to higher-order Poincaré spheres and complex polarization patterns produced by coherent superpositions of vector vortex (VV) beams. We demonstrate the visualization of complex polarization patterns by imprinting them onto a solid surface in the form of periodic nano-gratings oriented parallel to the local structure of the electric field of light. We design unconventional surface structures by controlling the superposition of VV beams. Our method is of potential interest to the production of sub-wavelength nano-structures.

https://doi.org/10.1364/OL.43.005757

Introduction

Light-matter interactions are governed by the polarization state of light. In solids, the spatial periodic surface structures induced by the Gaussian laser beams are strongly correlated with the laser polarization [16, 17]. In the domain of attosecond technology, laser polarization influences the generation of higher-order harmonics of the fundamental laser beam, both in solid and gas phases, by manipulating the trajectories of the ionized electrons [18, 19]. In circular dichroism [20, 21], the differential absorption of light by chiral molecules (liquid or gas phase) also depends on the polarization state of light. Light-matter interactions involving non-Gaussian intensity profiles such as optical vector vortex (VV) [22] beams with complex states of polarization (SoPs) have recently been investigated due to their potential applications. For example, first-order VV beams such as tightly focused radially polarized beams were used in particle acceleration [23], spectroscopy [24], optical trapping, and manipulation [25]. In general, a thorough knowledge of SoPs, therefore, will enable us to properly understand the light-matter interaction process.

Pure SoPs of light can be represented by points on the surface of a Poincaré Sphere [26]. For a Gaussian beam, all the points on the equator of the sphere represent linear

polarizations while the poles represent the handedness of circular polarization. Other points on the sphere represent elliptically polarized light. SoPs of light represented by such a zero-order Poincaré sphere can be readily analyzed by a combination of wave plates and polarizers. Extending this technique to characterize higher-order Poincaré spheres requires measuring the four Stokes parameters related to the intensities of six different zero-order polarization states using a spatially resolved detector. Using polarization tomography, the output polarization state can be reconstructed from the measured spatially dependent intensity profiles [27]. However, direct visualization of the higher-order Poincaré spheres is not feasible.

To visualize a polarization pattern, light has to interact with a medium that allows the pattern to be spatially resolved. In recent years, laser structuring of materials has been used to characterize the SoPs of Gaussian (linear) and first-order vortex beams (radial and azimuthal) [28, 29]. Periodic grating-like structures were induced by the laser within the ablation craters, as well as in the bulk of solids [16, 17]. Primarily, patterns were observed to be oriented parallel [30] (perpendicular [31, 32]) to the laser polarization on the surface (inside the bulk) of the material, although both orientations have also been reported on the surface [29, 33]. However, SoPs of higher-order VV beams and complex polarization patterns produced by coherent superpositions of such vector beams have not been experimentally realized.

In this Letter, we demonstrate the direct visualization of the SoPs of higher-order VV beams and extend it to complex asymmetrical SoPs arising from coherent superpositions of different order vortex beams. We permanently imprint the major axis of complex polarization ellipse distributions on a transparent medium (diamond), through nonlinear light-matter interaction. The resultant self-organized periodic nano-structures (ripples), formed upon irradiation with multiple laser pulses, are oriented parallel to the laser polarization axis, thereby accurately replicating the complex local polarization pattern. We show that the ripple spacing is $\sim 170 \pm 25$ nm and is almost independent of the incident pulse energy, the number of laser pulses, and polarization of light.

In our experiment, different SoPs were generated using beam converters based on birefringent liquid crystal devices called q-plates [34, 35] with topological charges of $q = +1/2$ and -1. The q-plates were tuned by varying the applied voltage to change its optical retardation. At the optimal voltage, the q-plates converted linearly polarized Gaussian beams to optical VV beams composed of orbital angular momentum (OAM) states with $\ell = \pm 1$ and $\ell = \pm 2$, respectively [36]. Detuning the individual q-plate produced a superposition of partially converted VV beams with the incident Gaussian beam. A combination of different q-plates resulted in complex asymmetric SoPs due to the superposition of VV beams.

Ultrashort light pulses from a Ti:sapphire laser system (800 nm, 1 kHz, 45 fs, 2.5 mJ/pulse) were focused on a diamond surface (3 3 0.3 mm) with a 0.25 NA microscope objective. The sample was mounted on three-axis translation stages with a resolution of 100 nm. The incident pulse energies were measured after the microscope objective, thereby taking into account the transmission and reflection losses of all the optics. Pulse energies were varied from $\sim$ 200 - 700 nJ by using a half-wave plate (HWP) and a polarizer.

The pulse duration before the microscope objective was 70 fs. The laser-ablated regions were characterized by a scanning electron microscope (SEM). The periodicity of the nano-structures was analyzed using 2D fast Fourier transforms.

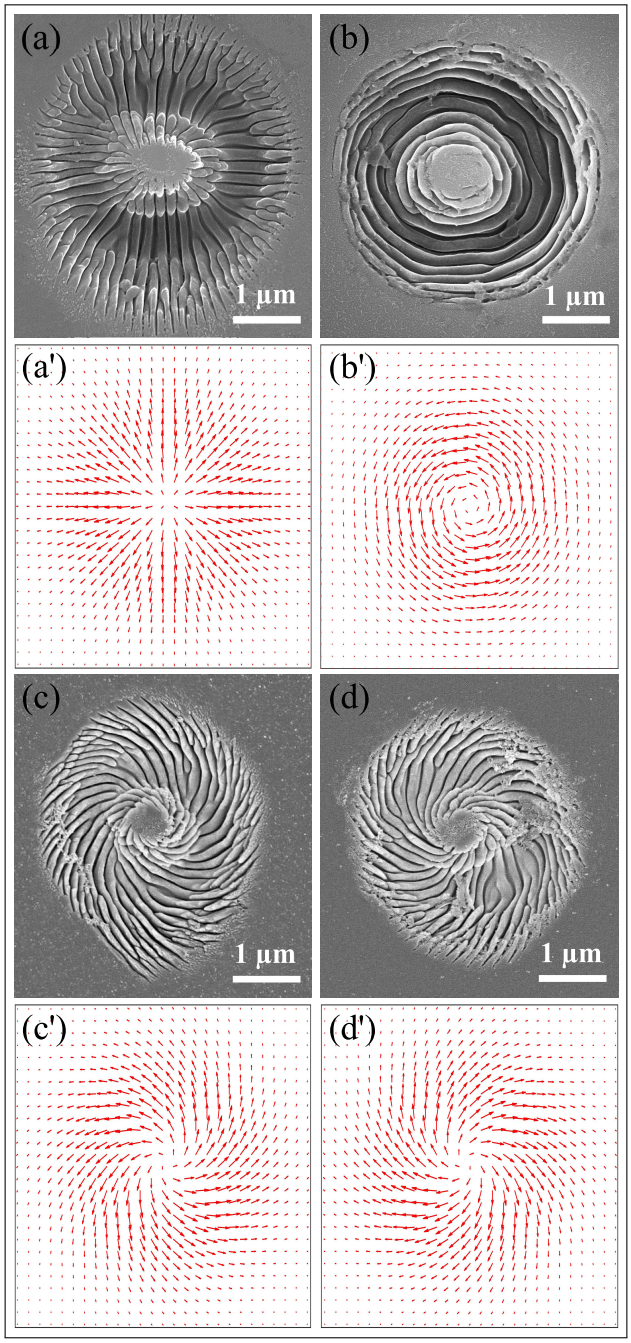

Figure 6.5: SEM images showing the mapping of the laser polarization patterns onto the diamond surface in the form of periodic nano-structures. 100 pulses irradiated the sample with an energy of 280 nJ for (a) radial, (b) azimuthal, (c) counter-clockwise spiral, and (d) clockwise spiral polarizations states of a first-order VV beam. a'-d' are the corresponding expected polarization patterns.

Figure 6.5 shows periodic nano-structures produced with radial, azimuthal, and spiral/sink polarizations. These structures were produced by irradiating the diamond surface with 100 laser pulses of energy 280 nJ. Different SoPs were generated by rotating the angle of the incident linear polarization with respect to the q-plate (topological charge = +1/2) axis, θ, using a HWP. Radial, azimuthal and spiral/sink polarizations were obtained for θ = 0°, 90°, ± 45°. SEM images reveal an interesting aspect of the interaction: the emergent ripple pattern is a complete map of the polarization and intensity profile of the VV beams. It accurately reflects the local structure of the electric field, as shown by theoretically simulated polarization patterns in Fig. 6.5. At low pulse energies, the intensity null at the center of the beam profile results in an unmodified region. However, when using higher pulse energies and a larger number of pulses, the periodic structures extend slightly into the central unablated region.

The periodic structures are oriented parallel to the laser polarization axis and conform with the nano-plasmonic model [37]. The model is based on local field enhancements that arise when the trailing edge of the laser pulse interacts with the plasma generated by the leading edge of the same laser pulse. Inhomogeneous ionization within the focal volume results in randomly formed nano-plasmas that grow into nano-planes with successive laser irradiation. Nano-planes grow along the electric field direction whenever the plasma density is above the critical density. Periodic structures develop over many laser shots, as the growing nano-planes affect the propagation of incident light. From the random distribution, the only planes that are enhanced are the ones that support the propagating modes whose field distributions reinforce their own growth. The periodic structures in the ablated region are spaced by ∼170 ±25 nm corresponding to $\lambda/2n$, where $n = 2.4$ is the refractive index of the medium, and λ is the free-space wavelength of the laser beam.

SoPs of different order VV beams and their superposition states were simulated using the Laguerre Gaussian beam

$$U(r,\phi,z) = \frac{C_{\ell p}^{LG}}{w(z)}\left(\frac{r\sqrt[2]{2}}{w(z)}\right)^{|\ell|} exp\left(\frac{-r^2}{w^2(z)}\right) L_p^{|\ell|}\left(\frac{2r^2}{w^2(z)}\right)\times$$
$$exp\left(\frac{-ikr^2}{2R(z)} - i\ell\phi - ikz + i\psi(z)\right).$$

where, $p \geq 0$ is the radial index, and ℓ is the azimuthal index. L_p^ℓ are the generalized Laguerre polynomials, and $C_{\ell p}^{LG}$ is a normalization constant. $R(z)$ is the radius of curvature of the wavefront, $w(z)$ is the beam width, and $\psi(z)$ is the Gouy phase. r, ϕ, z are cylindrical coordinates, and k is the wave number.

By decomposing the SoP of the incident light on the q-plate into left ($\mathbf{e}_\mathrm{L}$) and right ($\mathbf{e}_\mathrm{R}$) circular polarizations, the polarization state after the q-plate is given by

$$\mathbf{E}_\mathrm{out} = \cos\frac{\delta}{2}\begin{pmatrix}\mathbf{e}_\mathrm{L}\\ \mathbf{e}_\mathrm{R}\end{pmatrix} + i\sin\frac{\delta}{2}\begin{pmatrix}\mathbf{e}_\mathrm{R}e^{+2i(q\varphi+\alpha_0)}\\ \mathbf{e}_\mathrm{L}e^{-2i(q\varphi+\alpha_0)}\end{pmatrix}$$

where, φ is the azimuthal angle in the beam transverse plane, δ is the optical retardation, and α_0 specifies the initial molecular orientation of the liquid crystals with respect to a reference axis. A tuned q-plate, i.e. $\delta = \pi$, produces a pure OAM carrying beam with $\ell = \pm 2q$ when exposed to a circularly polarized light. When $\delta \neq \pi$, the q-plate produces a coherent superposition of the incident beam with OAM value of ℓ and a converted beam with an OAM value of $\ell = \pm 2q$ whose relative weights are determined by the parameter δ. The arrows in simulated SOPs indicate local SoP and the intensity distribution.

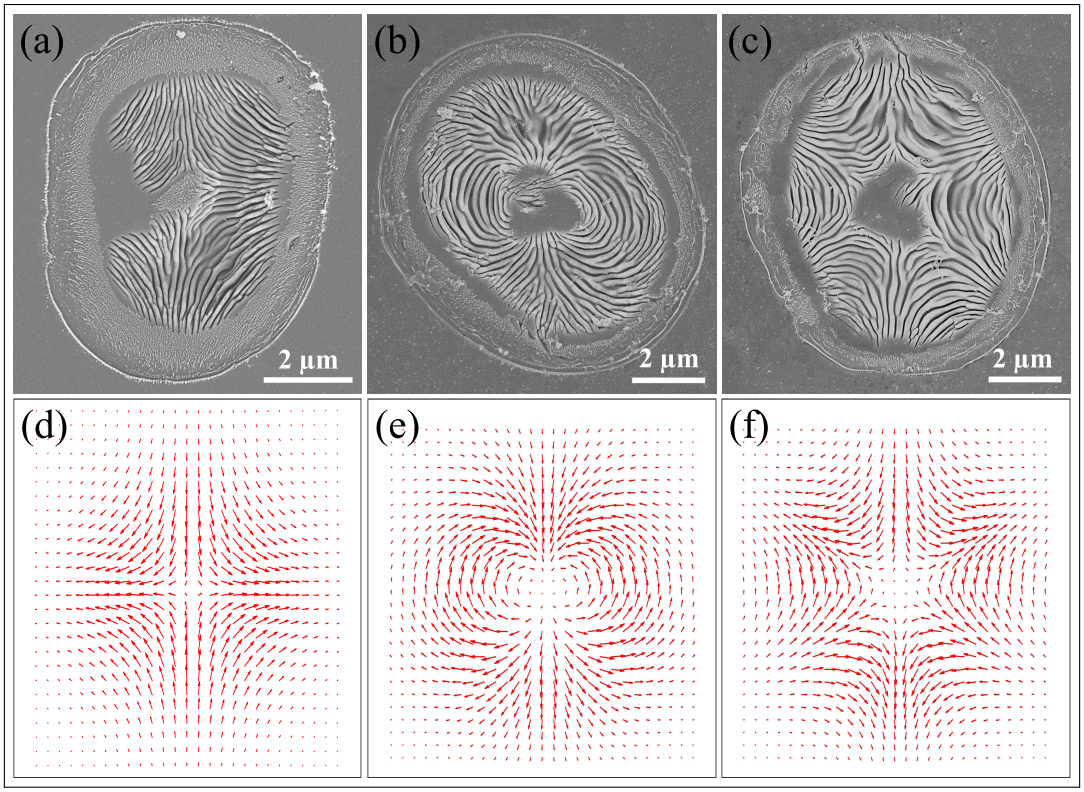

Figure 6.6: SEM images of periodic structures formed by q-plates with topological charges of (a) $q = -1/2$, (b) $q = +1$ and (c) $q = -1$. The corresponding expected polarization patterns are presented in the lower panels (d)-(f). 100 pulses irradiated the sample with a pulse energy of 310 nJ.

Figure 6.6 shows the mapping of complex polarization patterns formed by VV beams. The first beam [Fig.6.6(a)] was produced with a q-plate defined by a topological charge of $q = +1/2$ followed by a HWP. The resulting polarization pattern is equivalent to the one produced by a q-plate with a topological charge of $q = -1/2$. The second and third VV beams were produced by a q-plate with a topological charge of $q = -1$ [Fig. 6.6(c)] followed by a HWP [Fig. 6.6(b)]. Due to an asymmetry in the intensity profile of the beam, there are some regions where the nano-ripples merge to form wider structures.

Periodic nano-structures arising from differently weighted superpositions of Gaussian and VV beams with topological charge of $q = +1/2$ are shown in Fig. 6.7. Coherent superpositions were obtained by detuning the q-plate, such that a partly converted vortex beam co-propagates with the incident linearly polarized Gaussian beam. The superposition

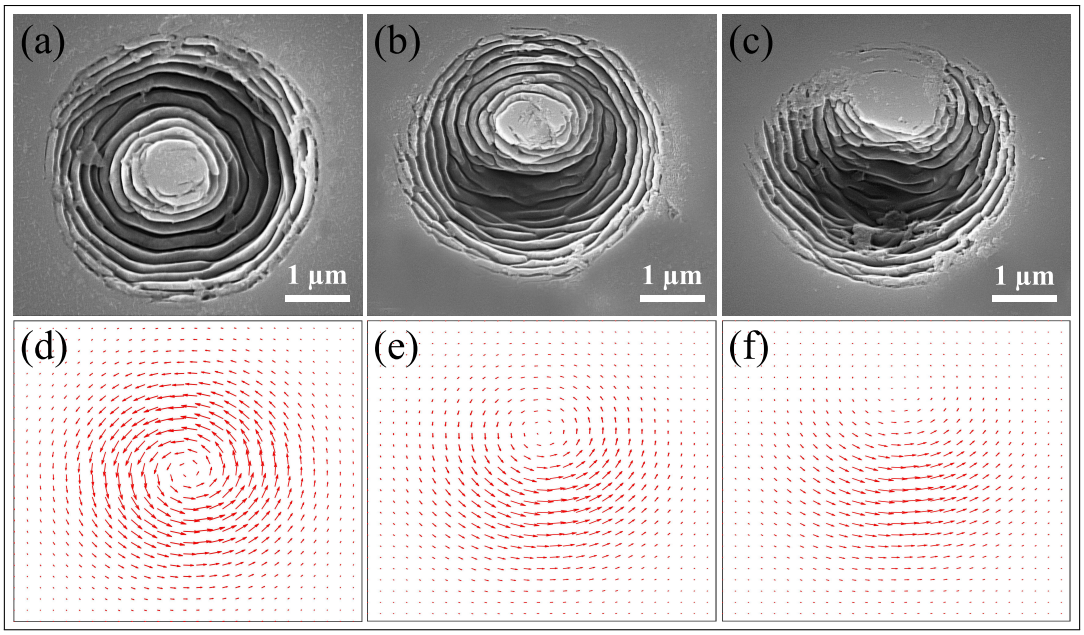

Figure 6.7: Superpositions of a linearly polarized Gaussian beam with a VV beam produced by a q-plate with a topological charge of $q = +1/2$ of differing weights (a) 0:100 (pure VV beam), (b) 30:70, and (c) 45:55. A shift in the position of the singularity with an increasing ratio of the Gaussian component agrees with the expected results in the bottom row. 100 pulses irradiated the sample with a pulse energy of 280 nJ.

of the two beams causes a shift in the null intensity region. The position of the singularity in the intensity profile and, hence, that of the unmodified area within the ablated region shifts from the center with the relative weight between the two beams. As the portion of the Gaussian beam is increased from 30% to 45% by correspondingly modifying the voltage applied to the q-plate, the position of the singularity shifts more towards the outer region of the ablated area, producing a crescent-shaped structure. However, the topological nature of the electric field structure is still preserved.

Complex nano-structures produced by superpositions of VV beams with a topological charge of $q = -1$ [Fig. 6.6(c)] and a Gaussian beam are shown in Fig. 6.8. The singularity (null intensity region) is split and mapped into two distinct regions. This is due to destructive interference in the central vertical region, as the incident linear polarization of the Gaussian beam is out-of-phase with respect to the VV beam [as shown by arrows in Fig. 6.6(f)]. The nano-structure orientation is still primarily dictated by the polarization of the VV beam. The spacing between the two null regions increases from 1.21 to 1.95 μm by varying the relative weight of the Gaussian beam superimposed on the VV beam.

Figure 6.9 demonstrates the unique capability of producing distinct nano-structured regions within the ablated area by using superpositions of VV beams and polarization selection. Figure 6.9(a) shows periodic nano-structures localized to three regions with distinct orientations. This three petal flower-like structure was obtained by placing a HWP between the $q = -1$ ($\ell = \pm 2$) and the detuned $q = 1/2$ ($\ell = \pm 1$) plates. The HWP reverses the handedness of the polarization ellipse forming the VV beam. After the

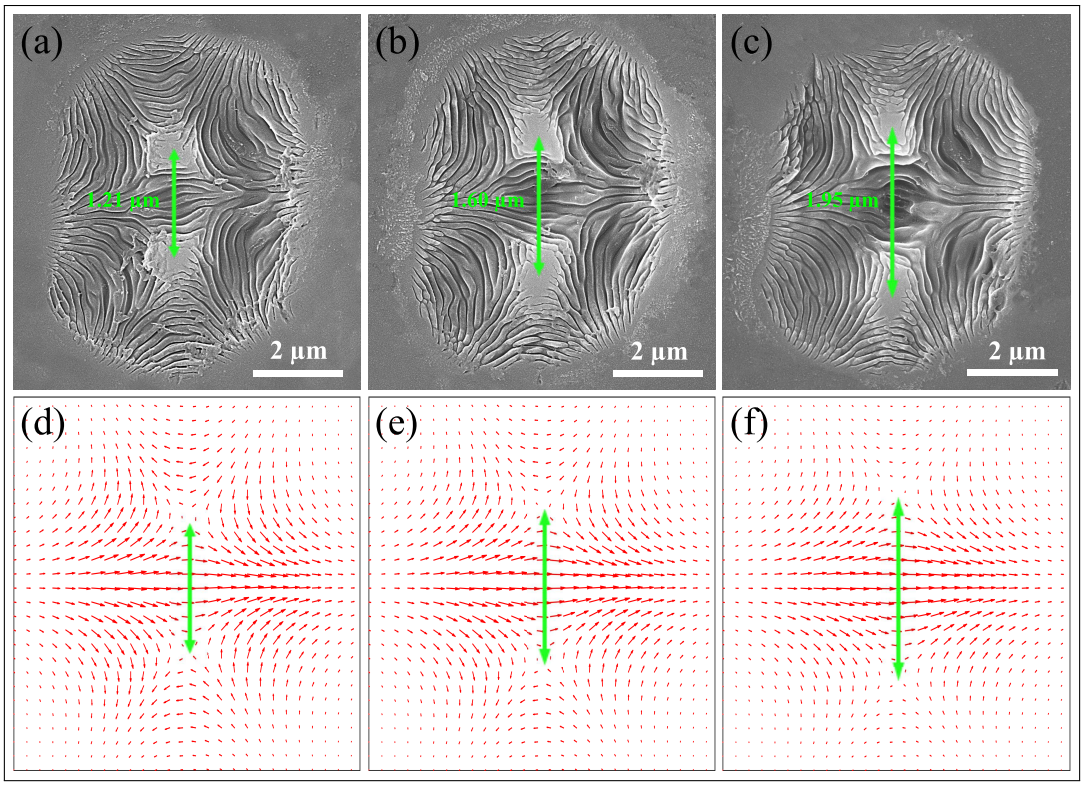

Figure 6.8: Superpositions of linearly polarized Gaussian and VV beams produced by a detuned q-plate with a topological charge of $q = -1$ for relative weights of (a), (d) 20:80; (b), (e) 30:70; and (c), (f) 40:60. The top panel shows the SEM images of the nano-structures generated by 50 pulses with an energy of 600 nJ. The bottom panel shows the corresponding polarization patterns. The length of the green arrows indicates the separation between the singularities.

HWP, the beam incident on the detuned $q = +1/2$ plate, defined by $e^{i2\varphi}\mathbf{e}_\mathrm{R} + e^{-i2\varphi}\mathbf{e}_\mathrm{L}$, undergoes a conversion resulting in $\alpha(e^{i2\varphi}\mathbf{e}_\mathrm{R} + e^{-i2\varphi}\mathbf{e}_\mathrm{L}) + \beta(e^{i\varphi}\mathbf{e}_\mathrm{L} + e^{-i\varphi}\mathbf{e}_\mathrm{R})$ state, which can be interpreted as a coherent superposition of two VV beams.

A four-petal flower-like structure shown in Fig. 6.9(b) was obtained by placing a polarizer after the $q = -1$ plate. The polarizer introduces diagonal nodes in the intensity profile of the VV beam as in Fig. 6.6(c) and 6.6(f) or Fig. 6.6(b) and 6.6(e). The orientation of periodic nano-structures in each of the four regions is identical and determined by the axis of the polarizer. Figure 6.9(c) shows structures obtained by using the same configuration as in Fig. 6.9(a) without the HWP. The output now corresponds to a superposition state defined by $\alpha(e^{i2\varphi}\mathbf{e}_\mathrm{L} + e^{-i2\varphi}\mathbf{e}_\mathrm{R}) + \beta(e^{i3\varphi}\mathbf{e}_\mathrm{R} + e^{-i3\varphi}\mathbf{e}_\mathrm{L})$. The result is a five-petal flower-like structure in which the orientation of nano-structures in each of the five localized regions is different.

Figure 6.10 shows the periodicity of the nano-ripples as a function of the pulse energy [Fig. 6.10(a)] and the number of laser pulses [Fig. 6.10(b)]. Fast Fourier transforms were used to calculate the periodicity of the ripples. While the orientation of the nano-ripples is controlled by the local electric field structure, their spacing seems to have negligible

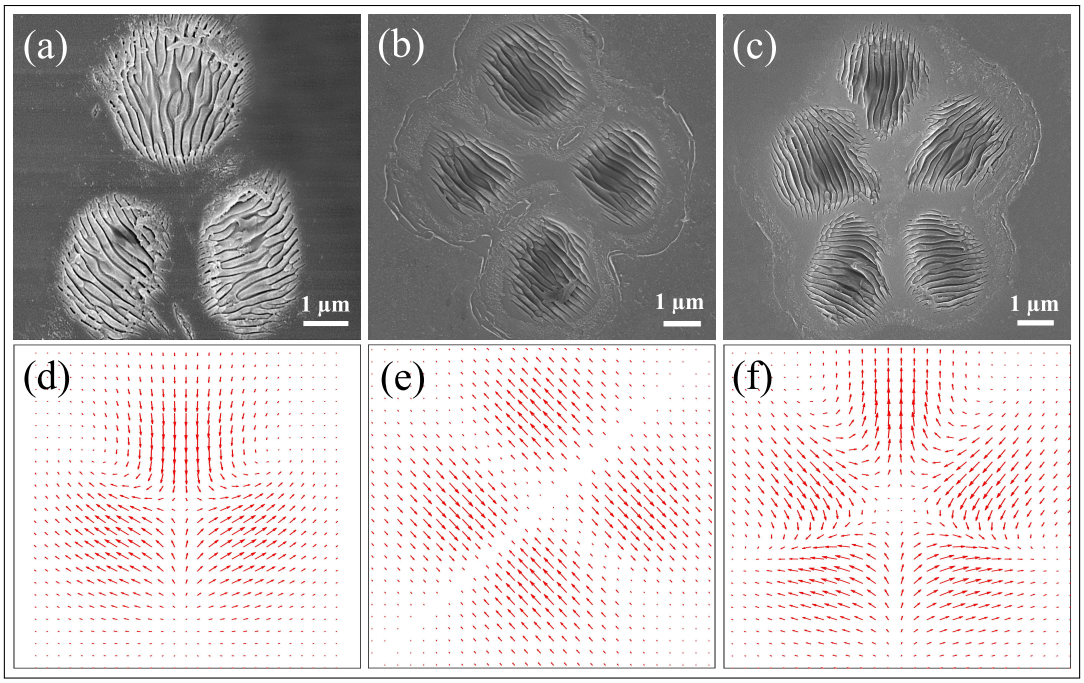

Figure 6.9: Mapping of polarization patterns generated by VV beams produced by a combination of (a) q-plates with topological charges of $q = -1$, $q = 1/2$, and a HWP in between (b) a q-plate with a topological charge of $q = -1$ and polarizer (c) q-plates with topological charges of $q = -1$ and $q = 1/2$. All patterns were produced with 50 pulses and an energy of 700 nJ. The bottom panels (e)-(f) show the expected polarization patterns.

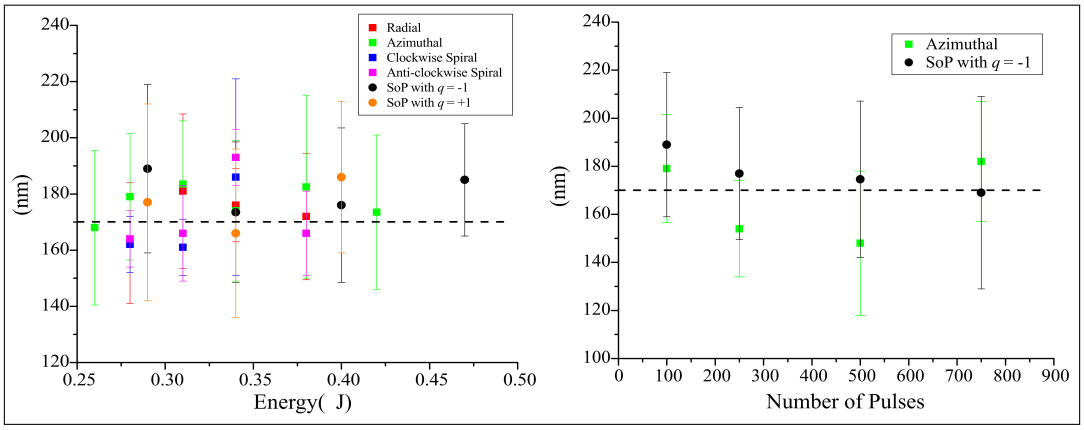

Figure 6.10: Periodicity of nano-ripples as a function of (a) pulse energy and (b) number of laser pulses for SoPs corresponding to first- and second-order VV beams ($q = \pm 1/2$ and $q = \pm 1$), respectively. The dashed line represents the $\lambda/2n$ value in both graphs.

dependence on laser parameters such as pulse energy and number of pulses. The average spacing is $\sim 170 \pm 25$ nm corresponding to $\lambda/2n$, in accordance with the predictions of the nano-plasmonic model [16, 17].

To conclude, we demonstrate direct visualization of local electric field structure in the

form of periodic nano-ripples by accurately mapping complex polarization patterns of VV beams onto a sample surface. Superpositions of different order VV beams enabled the controlled fabrication of unconventional, asymmetric surface structures. Configurations discussed in Fig. 6.9 enabled the fabrication of multiple localized regions of periodic structures in a small area of $< 50\ \mu m^2$. Further confinement of these regions is possible by focusing the laser beam with a higher numerical aperture objective. In general, the number of such localized regions within the focal area of the laser increases with the order of the VV beams being superimposed. Each localized region will exhibit different degrees of birefringence owing to different orientations of the periodic nano-structures within the region. Therefore, our findings have potential technological significance.

FUNDING. Natural Sciences and Engineering Research Council of Canada (NSERC); Canada Research Chairs; Canadian Foundation for Innovation; Ontario Ministry of Economic Development and Innovation.

Bibliography

[1] H. Poincaré, "Theorie mathematique de la lumiere", vol. 2, G. Carre, Paris, 275 (1892).

[2] F. Cardano, "Engineering spin and orbital angular momentum interactions in a light beam: Quantum and classical application", PhD Thesis (2015).

[3] M. Born and E. Wolf, Principles of Optics (Cambridge University Press, Cambridge, England, 1999, 7th ed.

[4] R. H. Jordan and D. G. Hall, Opt. Lett. 19, 427 (1994)

[5] F. Gori, J. Opt. Soc. Am. A 18, 1612 (2001), Q. Zhan, Adv. Opt. Photon. 1, 1 (2009).

[6] Giovanni Milione, H. I. Sztul, D. A. Nolan, and R. R. Alfano1, PRL 107, 053601 (2011)

[7] J. Söderholm et al 2012 New J. Phys. 14 115014.

[8] P. P. Rajeev, M. Gertsvolf, C. Hnatovsky, E. Simova, R. S. Taylor, P. B. Corkum, D. M. Rayner, and V. R. Bhardwaj, "Transient nanoplasmonics inside dielectrics", J. Phys. B: At. Mol. Opt. Phys., 40 S273 (2007).

[9] P. P. Rajeev, M. Gertsvolf, E. Simova, C. Hnatovsky, R. S. Taylor, V. R. Bhardwaj, D. M. Rayner, and P. B. Corkum, "Memory in Nonlinear Ionization of Transparent Solids", Phys. Rev. Lett. 97 253001 (2006).

[10] V. R. Bhardwaj, E. Simova, P. P. Rajeev, C. Hnatovsky, R. S. Taylor, D. M. Rayner, and P. B. Corkum, "Optically Produced Arrays of Planar Nanostructures inside Fused Silica", PRL 96, 057404 (2006).

[11] D. M. Rayner, A. Naumov, and P. B. Corkum, "Ultrashort pulse nonlinear optical absorption in transparent media", Opt. Exp., vol. 13, pp. 3208 (2005).

[12] H. Raether, "Surface Plasmons", Berlin: Springer (1988).

[13] M. Born, E. Wolf, "Principles of Optics: Electromagnetic Theory of Propagation, Interference and Diffraction of Light", 7th ed. Cambridge: Cambridge University Press (2002).

[14] W. L. Barnes, A. Dereux, T. W. Ebbesen, "Surface plasmon subwavelength optics", Nature, 424, 824 (2003).

[15] K. Miyazaki, G. Miyaji, "Nanograting formation through surface plasmon fields induced by femtosecond laser pulses", J. Appl. Phys., 114, 153108 (2013).

[16] V. R. Bhardwaj, E. Simova, P. P. Rajeev, C. Hnatovsky, R. S. Taylor, D. M. Rayner, and P. B. Corkum, Phys. Rev. Lett. 96, 057404 (2006).

[17] Y. Shimotsuma, P. G. Kazansky, J. Qiu, and K. Hirao, Phys. Rev. Lett. 91, 247405 (2003).

[18] P. B. Corkum and F. Krausz, Nat. Phys. 3, 381 (2007).

[19] G. Vampa, T. J. Hammond, N. Thiré, B. E. Schmidt, F. Légaré, C. R. McDonald, T. Brabec, and P. B. Corkum, Nat. Phys. 522, 462 (2015).

[20] K. Nakanishi, N. Berova, and R. Wood, Circular Dichroism: Principles and Applications (John Wiley & Sons, 1994).

[21] C. Lux, M. Wollenhaupt, T. Bolze, Q. Liang, J. Köhler, C. Sarpe, and T. Baumert, Angew. Chem. (Int. Ed.) 51, 5001 (2012).

[22] L. Allen, M. W. Beijersbergen, R. J. C. Spreeuw, and J. P. Woerdman, Phys. Rev. A 45, 8185 (1992).

[23] V. Marceau, C. Varin, and M. Piché, Opt. Lett. 38, 821 (2013).

[24] R. Dorn, S. Quabis, and G. Leuchs, Phys. Rev. Lett. 91, 233901 (2003).

[25] B. J. Roxworthy and K. C. T. Jr., New J. Phys. 12, 073012 (2010).

[26] H. Poincaré, Théorie mathématique de la lumière (Gauthiers-Villars, 1892), Vol. 2, p. 318.

[27] F. Cardano, E. Karimi, S. Slussarenko, L. Marrucci, C. de Lisio, and E. Santamato, Appl. Opt. 51, C1 (2012).

[28] C. Hnatovsky, V. Shvedov, W. Krolikowski, and A. Rode, Phys. Rev. Lett. 106, 123901 (2011).

[29] J. J. Nivas, F. Cardano, Z. Song, A. Rubano, R. Fittipaldi, A. Vecchione, D. Paparo, L. M. R. Bruzzese, and S. Amoruso, Sci. Rep. 7, 42142 (2017).

[30] J. Bonse, J. Krüger, S. Höhm, and A. Rosenfeld, J. Laser Appl. 24, 042006 (2012).

[31] Y. Jin, O. J. Allegre, W. Perrie, K. Abrams, J. Ouyang, E. Fearon, S. P. Edwardson, and G. Dearden, Opt. Express 21, 25333 (2013).

[32] K. K. Anoop, A. Rubano, R. Fittipaldi, X. Wang, D. Paparo, A. Vecchione, L. Marrucci, R. Bruzzese, and S. Amoruso, Appl. Phys. Lett. 104, 241604 (2014).

[33] E. M. Hsu, N. A. Mailman, G. A. Botton, and H. K. Haugen, Appl. Phys. A 103, 185 (2011).

[34] L.Marrucci, C.Manzo, and D. Paparo, Phys. Rev. Lett. 96, 163905 (2006).

[35] H. Larocque, J. G. Bischoff, F. Bouchard, R. Fickler, J. Upham, R. Boyd, and E. Karimi, J. Opt. 18, 124002 (2016).

[36] L. Marrucci, E. Karimi, S. Slussarenko, B. Piccirillo, E. Santamato, E. Nagali, and F. Sciarrino, J. Opt. 13, 064001 (2011).

[37] V. R. Bhardwaj, P. P. Rajeev, P. B. Corkum, and D. M. Rayner, J. Phys. B 39, S397 (2006).

Chapter 7

Helical Dichroism in Solids

7.1 Introduction

Interaction of intense light with matter has been extensively studied over the years and led to significant progress towards understanding the mechanisms involved in the interaction process. Until recently, most studies on light-matter interactions, involved using light pulses with a Gaussian intensity profile interacting with atomic [1] or molecular gases [2], transparent liquids [3], and solids [4].

Since the generation of beams carrying OAM, there has been a growing interest in research on the topic of twisted light-matter interaction. As mentioned in previous chapters, OAM beams possess a vortex phase of $e^{i\ell\varphi}$ with a topological charge of ℓ, a doughnut-shaped intensity profile with a vortex size determined by the term r^{ℓ}, and a helical wavefront. Due to such unique characteristics, one may anticipate observing new phenomena beyond the standard ionization, absorption, scattering, and propagation.

However, how the OAM of light beams interacts with matter is not clear. For example, one of the main questions in the context of the interaction of twisted light with atoms is the possibility of OAM exchange between the twisted light and the internal atomic states, which lead to a transition between the energy levels. In a dipole-allowed transition, the atoms engage with the optical field strength. It is well-established that atomic dipole transitions between atomic states that differ by $\pm\hbar$ can be engaged with a circularly polarized Gaussian beam that provides the angular momentum of $\pm\hbar$. In a quadrupole- and octupole-transition, atoms are driven by an oscillating field gradient, and the field's second derivative (or its curvature), respectively. A legit question that arises is whether OAM can provide additional atomic transitions, e.g., multipole transitions where more than a single unit of angular momentum per photon is exchanged.

Answering such questions has led the research in this field to cover many areas such as interaction with mesoscopic particles in optical tweezers [5], interaction with atoms and molecules [6] with introducing new quantum selection rules concerning the OAM of light, and interaction with Bose-Einstein condensates [7].

New studies revealed the influence of OAM when structured light interacts with single particles such as atoms, molecules, or quantum dots. For example, for molecular and atomic systems, it has been shown that the OAM of a photon can be transferred to the internal degrees of freedom of electron configurations if atomic transitions are driven by higher order contributions other than the electric dipole moment (E1). More interestingly, it is now known that, due to the presence of strong field gradients, atoms located near the zero intensity region of the twisted light beam can experience higher order multipole transitions leading to the new selection rules. These studies expand our knowledge in many areas. However, they have not predicted any particular phenomena where structured light interacts with solid-state systems.

This was my main motive to investigate the role of OAM and SAM in material response when an optical vortex beam is focused inside a transparent material. The resultant phenomenon is presented in this chapter. My studies show a discrimination in the nonlinear absorption of transparent bulk dielectric when it interacts with structured femtosecond light with opposite helicity in its phase front.

Nonetheless, the interaction of vortex beams with solids has not been fully understood so far, and there is still an ongoing debate on the significance of the OAM and the physical mechanisms involved in this interaction.

Before going through our experimental results, I present a couple of the breakthrough theoretical and experimental findings that motivated and directed us to explore any possible differential response of bulk materials to the OAM of light. These findings reveal the role of OAM when vortex beams interact with atoms, ions, and molecules.

7.2 OAM Beam Interaction with Matter

The interactions of light and matter are of fundamental interest and the additional degree of freedom offered by OAM of light in addition to SAM has inspired basic science as well as applications. There have been several studies that revealed that this newborn degree of freedom could strongly modify the fundamental processes of light-matter interactions, e. g., absorption or emission.

One of the most prominent questions in this field was the validity of the dipole transition approximation, where the bound electron in atoms or solids has a wave function much smaller than the wavelength of light. For a long time, it was believed that this point-like wave function experiences a uniform electric field that makes the higher multipolar effects too small to be considered. Further investigations on this matter led to introducing new fundamental modifications in the processes involved in the structured light-matter interaction. For instance, new selection rules came into consideration when an OAM beam interacted with atoms. Generally, selection rules describe the allowed or forbidden transitions of a system from one quantum state to another. For instance, selection rules for electric dipole transitions are as follows,

$$\begin{cases} |L| \leq 1 \\ \Delta M \in \{0, 1, -1\} \\ Parity\ changes \\ Transition\ 0 \rightarrow 0\ is\ forbidden \end{cases} \tag{7.1}$$

where ΔL and ΔM are the change of the total orbital angular momentum and the projection of the orbital angular momentum on the z-axis, respectively, and ± 1 comes from the spin.

However, it has been shown that by taking OAM into account, electron transitions that are usually allowed can be made forbidden while electron transitions that are usually forbidden may become allowed [8]. Due to these modifications, the possibility of higher-order electromagnetically driven transitions such as quadrupolar transition and octupole transition have been shown to be possible. The selection rules for electric quadrupole transitions are:

$$\begin{cases} |L| \leq 2 \\ \Delta M \in \{0, 1, -1, 2, -2\} \\ Parity\ is\ conserved \\ Transition\ 0 \rightarrow 0\ and\ \frac{1}{2} \rightarrow \frac{1}{2}\ are\ forbidden \end{cases} \tag{7.2}$$

Among all the higher order transitions, quadrupole transitions seems more exciting as they can occur even when there is no light intensity, but with the presence of a strong field gradient [9].

In the following, two novel studies that have explored the role of photon's OAM and higher order transitions when structured light interacts with atoms and ions, are presented.

7.2.1 Interaction with Atoms and Ions

In the case of atoms, the distinction between the allowed transitions can be understood by symmetry and parity. It is expressed in the form of selection rules that indicate the possible changes of the atom's angular momentum while it interacts with a photon.

In general, atomic transitions can occur if the overlap between the atomic wave function of the initial (ψ_i) and final state (ψ_f) matches the multipole structure of the optical field [10]. The coupling strength of a dipole transition is determined by $\int d^3r \psi_i^* \mu \psi_f$ and similar expressions for the higher-order terms, where μ is the transition dipole moment. When the integrand has odd parity, the transition is forbidden. Therefore, the symmetry of the OAM beam is anticipated to play a crucial role in determining the coupling strengths. It has been shown that, in the dipole approximation, the OAM of light couples to the atom's centre of mass motion without affecting its internal degrees of freedom [11, 12] while in quadrupole and higher-order transitions the electronic levels of an atom can be affected.

There are several interesiting studies in this context, for example:

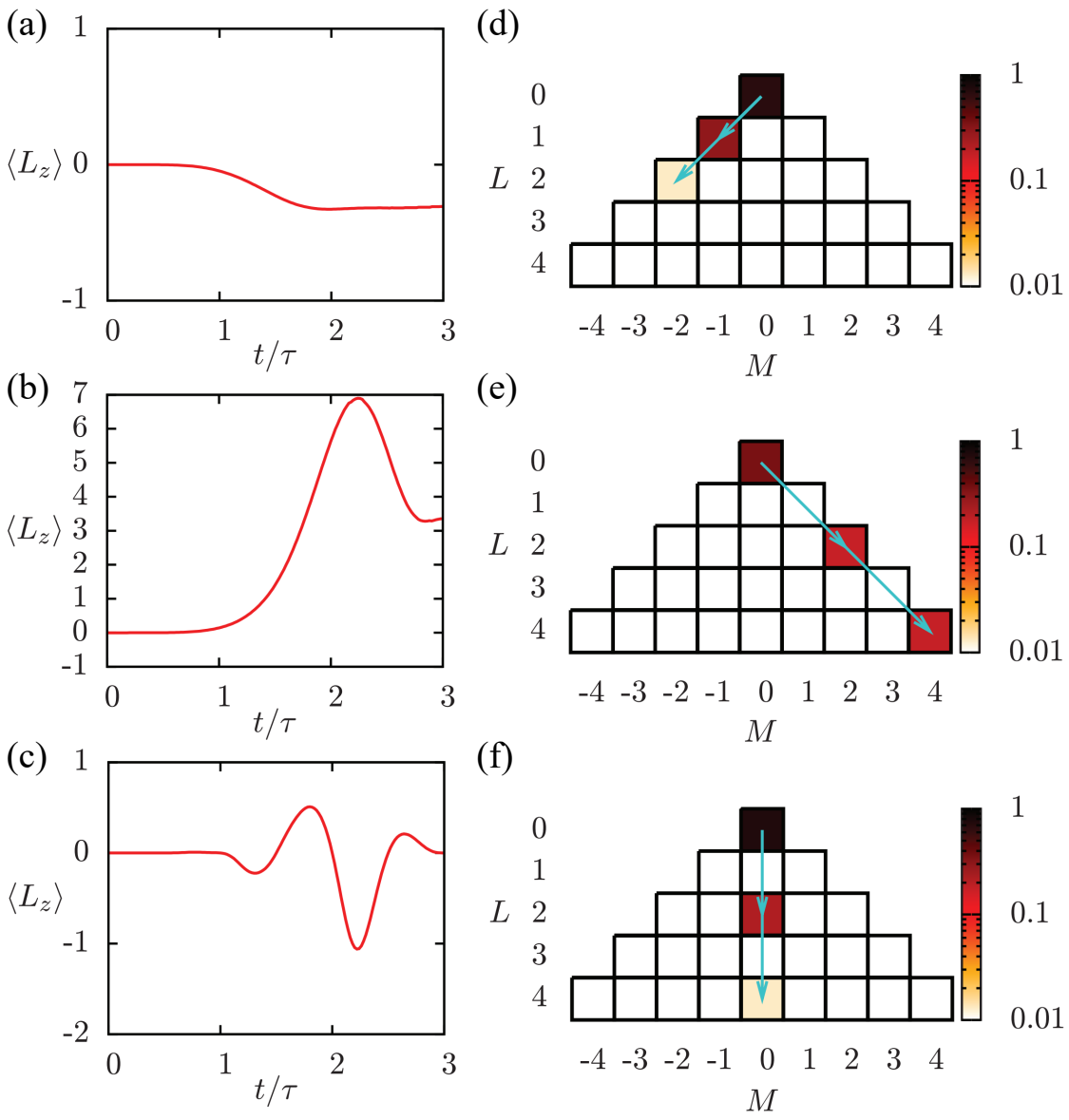

Figure 7.1: Angular momentum exchange and the allowed transitions between spherical harmonics when atoms interact with ligth: (top panel) right circularly polarized Gaussian beam, (middle panel) left circulary polarized OAM beam, and (bottom panel) right circularly polarized OAM beam [13]. (a)-(c) Show the temporal evolution of the expected value of the angular momentum along the z-axis, $\langle L_z \rangle$. (d)-(f) Demonstrate the most excited spherical harmonics where arrows correspond to the transitions that are allowed by the selection rules.

- Picon *et al.* [13] investigated the interaction of ultrashort light pulse carrying both OAM and spin with a hydrogen atom. They showed that such interactions induce a modification in the standard dipolar selection rules. Therefore, they predicted an OAM exchange from the incident photons to the ejected electrons during a photoion-

ization process. For a Hamiltonian in the form of $H = H_0 + H_1 + H_2$, where H_0 is the free hydrogen Hamiltonian, and $H_1 \equiv -q(\mathbf{p}\cdot\mathbf{A} + \mathbf{A}\cdot\mathbf{p})/2m$ (q:electron charge, $\mathbf{p}$:linear momentum operator, $\mathbf{A}$: vector potential) and $H_2 \equiv q^2\mathbf{A}^2/2m$ (m: electron mass) are the interaction parts, they proposed "modified selection rules" in the following forms:

$$\begin{cases} |\Delta L| \leq |\ell| + 1 \leq L_i + L_f\,, & \Delta M = \pm\ (\ell + s)\ , & \Delta L + \ell \quad is\ odd \\ |\Delta L| \leq 2|\ell| \leq L_i + L_f\,, & \Delta M = \pm\ 2\ell\ , & \Delta L \quad is\ even \end{cases} \tag{7.3}$$

These are also known as the absorption and emission selection rules associated with H_1 and H_2, respectivley. In these relations ℓ is the topological charge of the OAM pulse, $s = \pm 1$ is its circular polarization state. $\Delta L \equiv L_f - L_i$ and $\Delta M \equiv M_f - M_i$ represent a change between the initial and final values of the quantum number of the orbital angular momentum and magnetic quantum number, respectively. Doing so, they showed the possibility of more than one unit of $\hbar$ exchange in angular momentum along the propagation direction of the pulse that satisfies the selection rule of $\Delta M = \ell + s$.

Figure 7.1 demonstrates the results presented by Picon *et al.* [13]. It shows that (i) at the end of the pulse, the electron has $\langle L_z \rangle$ = - 0.3, 3.35, and 0 in arbitrary units corresponding to the right circular polarization Gaussian pulse, left circularly, and right circularly polarized OAM pulse, respectively, (ii) a right circularly polarized Gaussian pulse mostly excites spherical harmonics of Y_1^{-1} while an OAM pulse (with ℓ=+1) with right and left circular polarizatin can excite states obeying $M = 0$ (as $\ell + s = 0$) and $\Delta M = \Delta L = \ell + s = 2$, respectively.

- Schmiegelow *et al.* [14] observed modified selection rules that show the role of OAM when structured light interacted with laser-cooled $^{40}Ca^{+}$ ion placed in the beam centre. They have shown that when the ion is exposed to the optical field that is in resonance with the quadrupole transition, the internal state of the ion undergoes coherent oscillations between the ground and excited states. The interaction strength was quantified by measuring the Rabi frequency (Ω) of those oscillations. They reported that under such circumstances, an atom could absorb two quanta of angular momentum from the optical field, both orbital and spin angular momentum.

7.2.2 Interaction with Molecules

In general, the mechanisms behind the chiral discrimination in optical processes rely on the coupling between the electric dipole (E1) and either the magnetic dipole (M1) or the electric quadrupole (E2) transition moments [15]. The origin of such interactions can be explained in terms of the overall parity symmetry [16]. Since the electric dipole moments have odd spatial parity and the magnetic dipole and the electric quadrupole have even parity, the E1-M1 and E1-E2 interference terms change their sign under spatial inversion resulting in a difference for left- and right-handed forms of any chiral molecule.

In the following, some studies that discuss how dichroism-like effects appear with twisted fields are briefly reviewed.

Before opening the discussion, it is noteworthy that similar to the spin angular momentum (circular polarization state), the OAM can take positive and negative values. However, while SAM is characterized by only two values ($s = \pm 1$), OAM can possess any integer value. Therefore, when the question comes to dichroism-like effects defined and/or achieved by the orbital angular momentum, some people define two distinct classes: the parallel class (ℓ and s have the same signs) and the anti-parallel class (ℓ and s have opposite signs [17].

One way to study the role of vortex beams in chiroptical effects is to start discussing interactions of such beams with a molecule in the ground state absorbing a photon from a single mode LG beam. Such interactions can be formulated by the interaction Hamiltonian in the multipolar form [15], known as Power-Zienau-Wooley (PZW) Hamiltonian. It considers the sum of the Hamiltonians for the molecule, radiation, and the mutual interaction between them

$$H^{mult} = H^{mult}_{mol} + H^{mult}_{rad} + H^{mult}_{int} \tag{7.4}$$

$$H^{mult}_{int} = \sum_{\xi} \left[-\varepsilon_0^{-1} \boldsymbol{\mu}(\xi) \cdot \mathbf{d}^{\perp}(\mathbf{R}_\xi) - \varepsilon_0^{-1} Q_{ij}(\xi) \nabla_j d_i^{\perp}(\mathbf{R}_\xi) - \cdots - \mathbf{m}(\xi) \cdot \mathbf{b}(\mathbf{R}_\xi) - \cdots \right] \tag{7.5}$$

where for a molecule ξ positioned at $\mathbf{R}_\xi$, $\boldsymbol{\mu}$ is the transition electric dipole (E1) moment operator, $\mathbf{d}^{\perp}(\mathbf{R}_\xi)$ is the electric field, $\mathbf{Q}$ is the transition electric-quadrupole (E2) operator, $\mathbf{m}$ is the transition magnetic-dipole (M1) moment operator, and $\mathbf{b}(\mathbf{R}_\xi)$ is the magnetic field. In equation 7.5, the first term is the electric dipole coupling E1 for the molecule ξ, the second term represents the E2 coupling, and the final term is the magnetic dipole interaction (M1).

It has been shown that considering the paraxial approximation in cylindrical coordinates, leads to Laguerre-Gaussian modes, which are the most common modes for generating and describing OAM beams. The electric displacement and magnetic field expansions can be described as [18]:

$$\mathbf{d}^{\perp}(\mathbf{r}) = i \sum_{k,\eta,\ell,p} \left(\frac{\hbar c k \varepsilon_0}{2V} \right)^2 \left[\mathbf{e}^{(\eta)}_{\ell,p}(\mathbf{k}) a^{(\eta)}_{\ell,p}(\mathbf{k}) f_{\ell,p}(r) e^{(ikz + i\ell\varphi)} - \bar{\mathbf{e}}^{(\eta)}_{\ell,p}(\mathbf{k}) a^{\dagger(\eta)}_{\ell,p}(\mathbf{k}) \bar{f}_{\ell,p}(r) e^{-(ikz + i\ell\varphi)} \right] \tag{7.6}$$

$$\mathbf{b}(\mathbf{r}) = i \sum_{k,\eta,\ell,p} \left(\frac{\hbar k}{2\varepsilon_0 c V} \right)^2 \left[\mathbf{b}^{(\eta)}_{\ell,p}(\mathbf{k}) a^{(\eta)}_{\ell,p}(\mathbf{k}) f_{\ell,p}(r) e^{(ikz + i\ell\varphi)} - \bar{\mathbf{b}}^{(\eta)}_{\ell,p}(\mathbf{k}) a^{\dagger(\eta)}_{\ell,p}(\mathbf{k}) \bar{f}_{\ell,p}(r) e^{-(ikz + i\ell\varphi)} \right] \tag{7.7}$$

where V is the quantization volume, $a_{\ell,p}^{(\eta)}$ and $a_{\ell,p}^{\dagger(\eta)}$ are the annihilation and creation operators, respectively, for a photon of mode $(\mathbf{k}, \eta, \ell, p)$ in which $\mathbf{k}$, η, ℓ, and p are the wavevector, polarization label, topological charge, and radial order of LG beam, respectively, and $f_{\ell,p}(r)$ is the radial distribution function of the LG beam, represented by

$$f_{\ell,p}(r) = \frac{C_p^{|\ell|}}{w_0}\left[\frac{\sqrt{2}r}{w_0}\right]^{|\ell|} e^{\left(-r^2/w_0^2\right)} L_p^{|\ell|}\left(\frac{2r^2}{w_0^2}\right) \tag{7.8}$$

here, $C_p^{|\ell|}$ is a normalization constant, w_0 is the beam waist, and $L_p^{|\ell|}$ is the generalized Laguerre polynomial of order p. By looking at the above equations, one can see that there could be a chiral discrimination associated with the sign of OAM at the coupling between E1 and E2 terms. There have been several studies concentrated on single-photon absorption which utilized the perturbation theory to demonstrate such discriminations. Those studies consider a molecule in a ground state ($|g\rangle = |E_g\rangle\,|n\,(\mathbf{k}, \eta, \ell, p)\rangle$) that absorbs a radiation and will be excited to a final state ($|f\rangle = |E_f\rangle\,|n\,(\mathbf{k}, \eta, \ell, p)\rangle$), therefore, the matrix elements of the transition can be presented as [19]

$$\begin{aligned} M_{fg} &= \langle f\,|H_{int}|\,g\rangle \\ &= -\langle E_f\,|\mu_i|\,E_g\rangle\,\langle (n-1)\,|d_i^{\perp}(\mathbf{r})|\,n\rangle - \langle E_f\,|Q_{ij}|\,E_g\rangle\,\langle (n-1)\,|\nabla_j d_i^{\perp}(\mathbf{r})|\,n\rangle \\ &\quad - \langle E_f\,|m_i|\,E_g\rangle\,\langle (n-1)\,|b_i(\mathbf{r})|\,n\rangle \end{aligned} \tag{7.9}$$

where $|n\rangle$ is the radiation state. Substituting equations 7.6, 7.7, and 7.8 into the equation 7.9 and implementing the $\nabla_j d_i^{\perp}$ in cylindrical coordinates which has the form of

$$\begin{aligned} \nabla_j d_i^{\perp} &\approx \nabla_j f_{\ell,p}(r) e^{(ikz+i\ell\varphi)} \\ &= f_{\ell,p}(r)\partial_r \hat{r}_j e^{(ikz+i\ell\varphi)} + f_{\ell,p}(r)\frac{1}{r}\partial_\varphi \hat{\varphi}_j e^{(ikz+i\ell\varphi)} + f_{\ell,p}(r)\partial_z e^{(ikz+i\ell\varphi)} \\ &= \hat{r}_j \partial_r f_{\ell,p}(r) e^{(ikz+i\ell\varphi)} + f_{\ell,p}(r)\frac{1}{r}\left(i\ell\hat{\varphi}_j - \hat{r}_j\right) e^{(ikz+i\ell\varphi)} + f_{\ell,p}(r) ik\hat{z}_j e^{(ikz+i\ell\varphi)} \end{aligned} \tag{7.10}$$

results in the matrix elements to take the form of [19]

$$\begin{aligned} M_{fg} &= -i\left(\frac{n\hbar\omega}{2\varepsilon_0 V}\right)^{1/2} f_{\ell,p}(r) \\ &\quad \times \left[e_i \mu_i^{fg} + \frac{1}{c} b_i m_i^{fg} + e_i Q_{ij}^{fg}\left(\hat{r}_j \frac{1}{f_{\ell,p}(r)}\frac{\partial f_{\ell,p}(r)}{\partial r} + \frac{1}{r}(i\ell\hat{\varphi}_j - \hat{r}_j) + ik\hat{z}_j\right)\right] e^{(ikz+i\ell\varphi)} \end{aligned} \tag{7.11}$$

The equation above shows a dependency on both the magnitude and the sign of ℓ, in the phase factor and the fourth term in the square bracket, respectively. It is a result of

the quadrupole moment transition, E2. The importance of the sign of ℓ is more significant than its magnitude because the dependency on ℓ in the phase factor will disappear when calculating the modulus square of the matrix element to find the absorption rate ($\left|e^{i\ell\varphi}\right|^2 = 1$). Using Fermi's golden rule, the absorption rate, Γ can be found as [18]

$$\begin{aligned}\Gamma &= \frac{2\pi}{\hbar}\rho_f \left|M_{fg}(\xi)\right|^2 \\ &= \frac{2\pi}{\hbar}\rho_f f_{\ell,p}^2(r)\left|\underbrace{e_i\mu_i^{fg}}_{E1} + \underbrace{\frac{1}{c}b_i m_i^{fg}}_{M1} + \underbrace{e_i Q_{ij}^{fg}\left(\hat{r}_j\frac{1}{f_{\ell,p}(r)}\frac{\partial f_{\ell,p}(r)}{\partial r} + \frac{1}{r}(i\ell\hat{\varphi}_j - \hat{r}_j) + ik\hat{z}_j\right)}_{E2}\right|^2\end{aligned} \tag{7.12}$$

where ρ_f is the density of final states and is related to the radiant energy density per unit frequency interval and consequently to the irradiance per unit frequency interval given by

$$\rho_f = \frac{I(\omega)V}{2\pi n\hbar^2\omega c} \tag{7.13}$$

Equation 7.12 indicates that if only E1 and M1 terms in 7.12 were considered [20], there would be no dependency on the handedness of the vortex beam(sign of ℓ). By considering E2 terms, the absorption rate consists of several coupling terms: E1E1, M1M1, E1M1, E1E2, M1E2, and E2E2. The E1E1 and M1M1 terms do not have any ℓ-dependency that causes no discrimination in the single-photon absorption rate in the dipole approximation. On the other hand, the term E1M1 shows discrimination, but it leads to circular dichroism (CD). The rest of the terms which involve the E2 interaction (E1E2, M1E2, and E2E2) exhibit a discrimination with regards to the sign of ℓ.

By removing the terms with no dependency on the sign of ℓ and substituting 7.13 into 7.12, one can rewrite the absorption rate as [19]

$$\Gamma' = \frac{I(\omega)N}{2c\hbar^2\varepsilon_0}f_{\ell,p}^2(r)e_i\bar{e}_k\left|\mu_i^{fg} + \frac{1}{r}Q_{i,j}^{fg}(i\ell\hat{\varphi}_j - \hat{r}_j)\right|^2 \tag{7.14}$$

where $\bar{e}_k$ in the complex conjugate of e_k and N is the total number of molecules in the system. Eliminating the terms that do not contain ℓ, one can rewrite the modulus square as [19]

$$\begin{aligned}&\left|\mu_i^{fg} + \frac{1}{r}Q_{i,j}^{fg}(i\ell\hat{\varphi}_j - \hat{r}_j)\right|^2 \approx \\ &i\ell(r^{-1}\hat{\varphi}_j\mu_k^{fg}Q_{ij}^{fg} - r^{-1}\hat{\varphi}_l\mu_i^{fg}Q_{kl}^{fg} + r^{-2}\hat{r}_j\hat{\varphi}_l Q_{ij}^{fg}Q_{kl}^{fg} - r^{-2}\hat{\varphi}_j\hat{r}_l Q_{ij}^{fg}Q_{kl}^{fg})\end{aligned} \tag{7.15}$$

which clearly states that the absorption rate depends on the sign of ℓ.

Multipole Moments	Spatial Parity
E1, E1M1, E1E2	-1
M1, E2, E1E1, M1M1, M1E2, E2E2	+1

Table 7.1: Spatial parity of multipole transition moments and their products [21].

By looking into the spatial parity of these terms (as summarized in table 7.1), one gains a good intuition on the role that each term plays in the interaction between the vortex beam and molecules, either chiral or achiral. Based on the parity point of view, one can study the absorption rate within two different categories;

- An interaction with chiral material
- An interaction with achiral material

As seen in table 7.1, in the case of single photon absorption, replacing a chiral molecule with its enantiomer (non-centrosymmetric molecules and in general for chiral species), E1E2 terms experience a sign change. In contrast, the contribution of the M1E2 and E2E2 terms in a chiroptical effect depends only on the radiation. Therefore, these terms are considered to be necessary when the handedness of the polarization and topological charge interact with an achiral material to produce discriminatory effects.

7.2.3 OAM Beams Interact with Chiral Materials

As mentioned above, when a vortex beam interacts with chiral molecules, E1E2 terms cause discriminatory effects. Focusing only on these terms simplifies the rate equation 7.14 as

$$\Gamma'_{E1E2} = i\ell \frac{I(\omega)N}{2c\hbar^2\varepsilon_0} \frac{f^2_{\ell,p}(r)}{r} e_i \bar{e}_k \hat{\varphi}_j \left(\mu^{fg}_k Q^{fg}_{ij} - \mu^{fg}_i Q^{fg}_{kj}\right) \tag{7.16}$$

Since both μ^{fg} and Q^{fg} are real quantities, this equation indicates that in order to observe a non-zero real absorption rate, one needs to apply a beam with circular polarization (with complex polarization vector). Therefore, a beam needs to possess both OAM and SAM to engage the vortex handedness in the chiroptical interactions with chiral molecules. Due to this similarity to the standard circular dichroism, such an optical process is also known as "circular-vortex dichroism (CVD)" [19]. However, Brullot *et al.* [22] has shown that a discriminatory effect, known as "helical dichroism", can be produced invoking linearly polarized OAM beam when it interacts with the plasmonic nanoparticle aggregates, which was attributed to the chiral electric quadrupole contributions.

To investigate the effects of OAM and circular polarization, following relations [16] can be applied

Transformation	Sign Variation in $\Gamma'(\ell)$
$(\sigma, \ell) \rightarrow (-\sigma, -\ell)$	No change
$(\sigma, \ell) \rightarrow (-\sigma, \ell)$	Change
$(\sigma, \ell) \rightarrow (\sigma, -\ell)$	Change

Table 7.2: Sign variation of the absorption rate, for a given molecular handedness, under different transformations [18].

$$\begin{aligned} e_i^L e_k^{-L} &= \frac{1}{2}\left[(\delta_{ik} - \hat{k}_i\hat{k}_k) - i\varepsilon_{ikm}\hat{k}_m\right] \\ e_i^R e_k^{-R} &= \frac{1}{2}\left[(\delta_{ik} - \hat{k}_i\hat{k}_k) + i\varepsilon_{ikm}\hat{k}_m\right] \end{aligned} \tag{7.17}$$

Therefore, equation 7.16 will be simplified as

$$\begin{aligned} \Gamma'^{L}_{E1E2}(\ell) &= \ell\frac{I(\omega)N}{4c\hbar^2\varepsilon_0}\frac{f^2_{\ell,p}(r)}{r}\varepsilon_{ikm}\hat{k}_m\hat{\varphi}_j\left(\mu_k^{fg}Q_{ij}^{fg} - \mu_i^{fg}Q_{kj}^{fg}\right) \\ \Gamma'^{R}_{E1E2}(\ell) &= -\ell\frac{I(\omega)N}{4c\hbar^2\varepsilon_0}\frac{f^2_{\ell,p}(r)}{r}\varepsilon_{ikm}\hat{k}_m\hat{\varphi}_j\left(\mu_k^{fg}Q_{ij}^{fg} - \mu_i^{fg}Q_{kj}^{fg}\right) \end{aligned} \tag{7.18}$$

These relations can be further simplified as

$$\Gamma'^{L/R}_{E1E2}(\ell) = \sigma\ell\frac{F(r)}{r}\varepsilon_{ikm}\hat{k}_m\hat{\phi}_j\mu_k Q_{ij} \tag{7.19}$$

where $\sigma = \pm 1$ represent left circular polarization (L) and right circular polarization (R), and $F(r) = I(\omega)f^2_{\ell,p}(r)/2c\hbar^2\varepsilon_0$ is a constant.

Performing these calculations, Forbes *et al.* [18] showed that in the case of an interaction between OAM beams and chiral molecules, a product of both angular momenta (SAM and OAM) as well as molecular handedness are crucial and need to be considered. Equation 7.19 reveals the CVD differential to be linearly dependent on the three aspects of handedness: (1) left- and right-handed circular polarization (σ), (2) sign of the topological charge (ℓ), and (3) molecular chirality. This means when the beam possesses no OAM, any ℓ dependency vanishes, and one can see only the standard circular dichroism. The material response in terms of the sign of the absorption rate, is summarized in the table 7.2.

Forbes *et al.* proved that, although the CVD effect in one-photon absorption is non-zero for oriented systems of molecules, it vanishes for randomly oriented molecules. More details can be found in [19].

7.2.4 OAM Beams Interacting with Achiral Material

In recent years, there has also been an interest in possible chiroptical effects observed when light interacts with achiral material. Several experiments presented the observation of circular dichroism using twisted light in the non-chiral atomic matter and nanostructures [23, 24].

As was shown in previous sections, E1E2 terms have no contribution to chiroptical effects in isotropic chiral or achiral media. Therefore, the E2E2 term is the one that needs to be considered. However, the magnitude of any possible effects induced by these terms is lower than that produced by the E1E2 terms in chiral media. These E2E2 contributions in the absorption rate, as proposed in [18] are

$$\begin{aligned} \Gamma'_{E2E2} &= F(r) e_i \bar{e}_k Q_{ij} A_j \bar{A}_l, and \\ A &= \left[\hat{r} \frac{1}{f_{\ell,p}(r)} \partial_r f_{\ell,p}(r) + \frac{1}{r}(i\ell\hat{\phi} - \hat{r}) + ik\hat{z} \right] \end{aligned} \tag{7.20}$$

Extracting relevant terms from 7.20, one can realize a similar discriminatory single-photon absorption upon irradiation of twisted photons in achiral molecules,

$$\Gamma'^{(L/R)}_{E2E2}(\ell) = \sigma\ell \frac{F(r)}{2r} \varepsilon_{ikm} \hat{k}_m Q_{ij} Q_{kl} (\hat{\phi}_j \hat{r}_l - \hat{\phi}_l \hat{r}_j) \left[\partial_r ln f_{\ell,p}(r) - \frac{1}{r} \right] \tag{7.21}$$

This relation proves that for a given polarization handedness, the absorption rate behaves differently for a right-handed and left-handed twisted light and vice versa. However, this effect is shown to be zero when it is averaged over the whole cross-section of the structured beam. It was shown to exist only in 2D materials.

After reviewing a couple of the most significant discoveries revealing the role of OAM in atomic and molecular transitions, I present our experimental findings that demonstrate the effect of OAM in the nonlinear absorption of transparent dielectric materials.

7.2.5 Interaction with Bulk

Transmission-based Measurements of Nonlinear Absorption
Gaussian beam

Nonlinear absorption is one of the main mechanisms involved in the interaction of intense ultrashort laser pulses with wide bandgap materials. One method to analyze the nonlinear absorption is to monitor the transmission of the incident pulse that is focused inside the material [25, 26]. In this method, two photodetectors simultaneously measure the incident and the transmitted pulse energies. The transmission measured on a shot-to-shot basis shows a gradual decrease after a certain threshold in the laser energy, where the nonlinear absorption starts playing a role. Below the threshold, the transmission of a single pulse

incident on a fresh spot remains unaffected as the pulse energy increases. However, after the threshold energy, absorption inside the material increases dramatically and then saturates. Therefore, above the threshold, any further increase in the pulse energy causes a continuous drop in the transmission data. This indicates that by monitoring the pulse energy at which the transmission data starts to drop, one can determine the nonlinear absorption threshold energy in glass for single pulse irradiation, as shown in Fig.7.2.

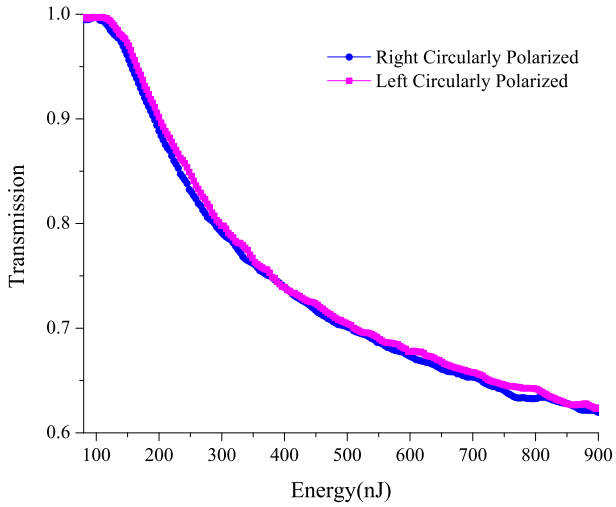

Figure 7.2: Transmission of femtosecond Gaussian pulses as a function of laser pulse energy. The transmission data show the nonlinear absorption inside borosilicate glass.

This threshold energy depends on the material bandgap and laser parameters such as wavelength and pulse duration. For most glasses with a bandgap in the range of 4-10 eV, the threshold intensity was found to be in the range of $15{\times}10^{13} W/cm^2$ [25] which is lower than the self-focusing or any other damage threshold. Up until now, this method has been used to study several phenomena such as memory in nonlinear ionization of the material [26], induced by laser beams with a Gaussian intensity profile.

We found this experimental technique suitable to observe the role of OAM in the nonlinear absorption when an optical vortex interacts with bulk materials.

7.2.6 Experimental Studies on Chiroptical Effects Driven by OAM in Bulk

In this section, we studied the interaction of tightly focused low power fs-laser vortex pulses with three different transparent materials. The vortex pulses possess both SAM and OAM. Our experimental findings demonstrate a helical dichroism phenomenon when an OAM beam with opposite topological charges passes through the bulk. The transmission of the circularly polarized OAM beam shows a discriminatory effect sensitive to the sign and magnitude of the OAM.

Experimental Setup

Our experimental setup, shown in Fig.7.3, was built to allow transmission measurements through dielectric materials, such as borosilicate glass, fused silica, and quartz. We controlled several critical experimental parameters, including pulse duration, energy, and repetition rate. In our experiment, 800 nm femtosecond Gaussian beams produced by Ti:Sapphire laser (operating at 1 kHz, producing 45 fs) were converted to vortex beams carrying OAM $\ell = \pm 1$ and $\ell = \pm 2$ by electrically tunable q-plates with topological charges of $q = +1/2$ and $q = -1$, respectively. The OAM beam was focused into: (a) 1 mm thick borosilicate glass plate, (b) 2 mm thick fused silica, and (c) quartz with the thickness of 750 μm mounted on an XYZ motorized translation stage, using an aspheric lens with a numerical aperture of 0.25 NA (16×, 11.0 mm effective focal length, 8.0 mm working distance). The beam focus was located 650 μm, 1.2 mm, and 450 μm inside the borosilicate, fused silica, and quartz, respectively, to avoid aberrations. Due to the tight focusing and reaching the high intensities inside the samples, any surface effects were eliminated, and a fully three-dimensional interaction was guaranteed. We actually used low F# to keep the peak power below the critical power (e.g., P_c of fused silica=2.6 MW). Doing so, we were able to eliminate nonlinear effects such as self-focusing or self-phase modulation on the beam propagation, while we reached the required intensities for the material breakdown. Also, we minimized the spherical aberration effect by focusing the light close to the sample's surface. The incident pulse energy at the sample was precisely controlled by a half-wave plate (HWP)-polarizing beam splitter (PBS) combination. Different polarization states and handedness of the OAM beam were produced by tuning the fast axes of a quarter-wave plate (QWP) and a half-wave plate (HWP).

The transmitted light was then collected by a 0.55 NA (20×, 8.0 effective focal length, 5.9 mm working distance) aspheric lens. It was attached to a XYZ positioning stage that enabled us to control the lens position carefully. Using a higher NA lens to collect the transmitted light ensures that the beam is completely collected, even if it is scattered or defocused by the plasma formed by the ionization. In order to monitor both the incoming and the transmitted light, we utilized two avalanche photodiodes (PD1 and PD2, APD120A2, Thorlabs). Figure 7.3 shows a schematic of our experimental setup. While samples were moved at a constant speed, the transmission spectrum was measured on a shot-to-shot basis so that each time the laser beam hits a fresh spot. The laser was operating in the gated mode, using a computer-controlled data acquisition system, as described in chapter 4, section 2.4. The signal was acquired independently for every laser shot. The transmitted signal was then normalized to the incident light signal so that any fluctuations in the pulse energy were to be considered.

Results

Before going through the experimental results, we address several issues regarding the beam refraction. It is known that along the propagation direction, the laser beam experiences dispersion, nonlinear refraction, beam focusing, and plasma refraction. Here, in our experiment, we assume that the laser propagation remains unchanged (except for

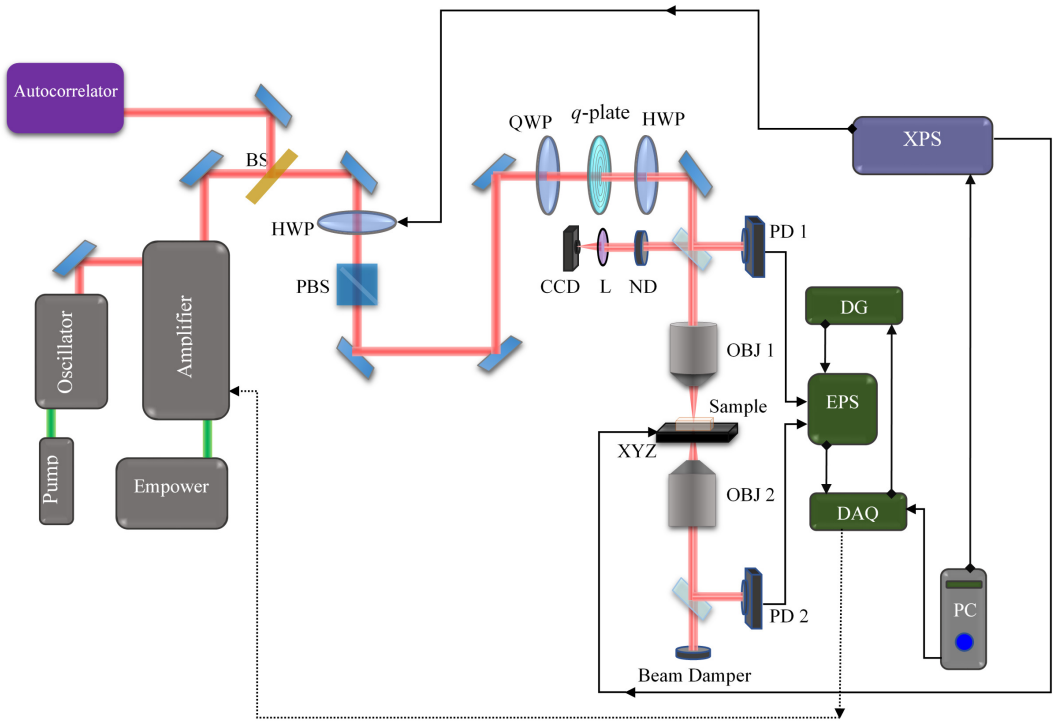

Figure 7.3: Schematic of the transmission measurement experiment. BS: beam splitter, HWP: half wave plate, PBS: polarizer, QWP: quarter wave plate, CCD: camera, L: lens, ND: neutral density filter, OBJ: aspheric objective lens, PD: photodiode, XYZ: translation stages, DG: delay generator, DAQ: data acquisition card, and EPS: electronic pulse stretcher, and XPS: motion controller. The ellipticity (ε) of the circularly polarized OAM beam was measured in three different places in the beam path: after the set of wave plats, right before the first objective, and right after the first objective. In all cases, it was measured to be above %92.

clamping) for a wide range of input pulse energies. For example, pulse broadening due to dispersion in fused silica (β_2=36 fs^{2}mm^{-1}) is negligible for 30 nm pulse bandwidth and $\sim 20\mu$m interaction length, comparable to our experimental conditions.

We also kept the pulse energy range below the breakdown threshold, which means the pulse power was kept below the critical power for self-focusing (e.g., in fused silica, P_c is approximately 2.6 MW). For very high pulse energies, the peak power is clamped inside the material due to pulse depletion long before the focal region. As a result, we can neglect the impact of all low order nonlinear effects such as Kerr effects and Raman scattering [27] on the beam propagation. Moreover, as mentioned earlier, by keeping the focal point close to the surface of the sample, we minimized the spherical aberration effect.

We also precisely calibrated all the wave plates used in our experiments because any poor alignment induces an angle- and depth-dependent ellipticity at the focus that modulates multi-photon ionization via the effective intensity [28]. Besides, we measured the ellipticity of the beam for both left- and right- circular polarization, in three different parts

of the setup: after the wave plates, before and after the lens. They were all above %92. Figure 7.4 shows the nonlinear transmission of femtosecond vortex pulses as a function of laser pulse energy in three different transparent materials (a) borosilicate, (b) fused silica, and (c) quartz. The transmission spectra were measured on a shot-by-shot basis while the pulse energy was increased from 100 nJ to 600 nJ in small increments. The graphs demonstrate that once the ionization is initiated, the transmission drops monotonically from unity (at low pulse energies). In other words, this point defines an ionization threshold, where the nonlinear absorption takes place. Beyond this threshold point, the transmission is reduced with an increase in pulse energy

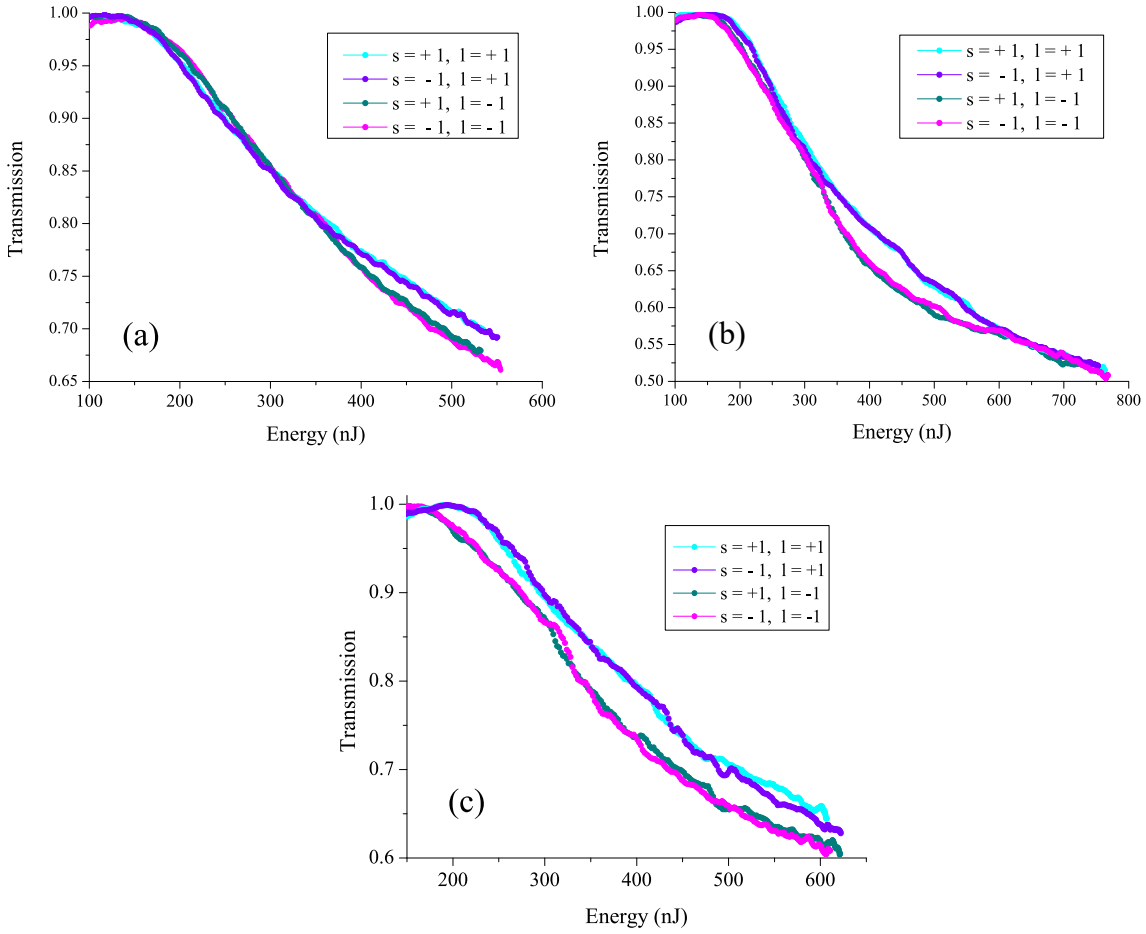

Figure 7.4: Helical dichroism produced by circularly polarized OAM beam carrying ℓ=$\pm$1 in (a) Borosilicate glass plate, (b) Quartz, and (c) Fused silica. Left circular polarization and right circular polarization are represented by $s+$ and $s-$, respectively.

Transmission curves were obtained for vortex beams carrying four different combinations of spin and orbital angular momentum: (1) left circular polarization ($s = +1$) having left-handed twist($\ell = +1$), (2) left circular polarization ($s = +1$) having right-handed twist ($\ell = -1$), (3) right circular polarization ($s = -1$) having left-handed twist ($\ell = +1$), and (4) right circular polarization ($s = -1$) having right-handed twist ($\ell = -1$). The transmitted spectra for left- and right-circular polarization states show an overlap when

the wavefront of the incident pulses twist in the same directions, in other words, when they have topological charges with the same sign, as shown in Fig. 7.4. In contrast, the transmission curves show a significant gap when pulses with similar polarization states endowed with OAMs of opposite sign. This behavior illustrates the main characteristics of helical dichroism that we observed in our experimental studies. The differences are observed only in the nonlinear regime. Below the ionization threshold (linear regime), absorption remains the same for beams with OAM of different helicities.

We further improved our findings by increasing the number of twists in the beam's wavefront by increasing the magnitude of the topological charge (ℓ). To do so, we inserted a q-plate with a topological charge of q=-1 to produce an OAM beam with ℓ=$\pm$2. The resultant graphs are presented in Fig. 7.5. As illustrated, a behavior similar to the one that was observed in the case of ℓ=$\pm$1 was detected. These graphs explicitly show a slightly larger gap, as compared to the case of ℓ=$\pm$1. Such an effect was observed in all three materials used in our experiments.

To obtain more insight into this context, we plotted a graph illustrating the ratio of the transmission for pulses with the same polarization state, the same OAM value, and opposite helicity. This was performed for both $\ell = \pm 1$ and $\ell = \pm 2$. The ratios were taken in all points having the same energies. For each energy value, we took the corresponding data from L+ (left-circular polarization and OAM value of ℓ=+1) and L- (left-circular polarization and OAM value of ℓ=-1). Then, we calculated the ratio L+/L- and plotted it against energy for different bulk materials, as shown in Fig. 7.6. Each material shows a unique profile, however, the overall behavior of all three materials is similar.

For ℓ=$\pm$1, as the incident pulse energy increases from 50 nJ to 500 nJ, the ratio curves show a gradual increase. For ℓ=$\pm$2, we conducted the measurements for energies up to 1000 nJ. For borosilicate glass and fused silica, there appears to be a peak in the ratio curves and then a decline. However, quartz shows a saturation-like pattern. This difference can also be realized in Fig. 7.5 where the discriminatory effect (gap) shown in the graphs starts vanishing for fused silica and borosilicate, but remains almost intact for quartz.

Another key point is that for the case of ℓ=$\pm$1, fused silica has the highest values for both ratio curves (L+/L- and R+/R-), as shown in Fig. 7.6. The next highest values were achieved for quartz, and borosilicate glass showed the lowest values. This pattern could be attributed to the bandgap of these materials, and hence to the strength of the multi-photon absorption. The bandgap of these materials are, 9.0 eV [29], 6.3 eV [30], and 4.28 eV [31] for fused silica, quartz, and borosilicate glass, respectively.

To conclude,

- Our experimental results highlighted that phase-structured light possessing orbital angular momentum (OAM) could cause considerable effects when interacting with matter.
- This study proposed the presence of helical dichroism in bulk materials, sensitive to both magnitude and sign of the twist (ℓ) in the OAM beam. This effect was shown in terms of the absorption of twisted photons by molecules inside the bulk of material.

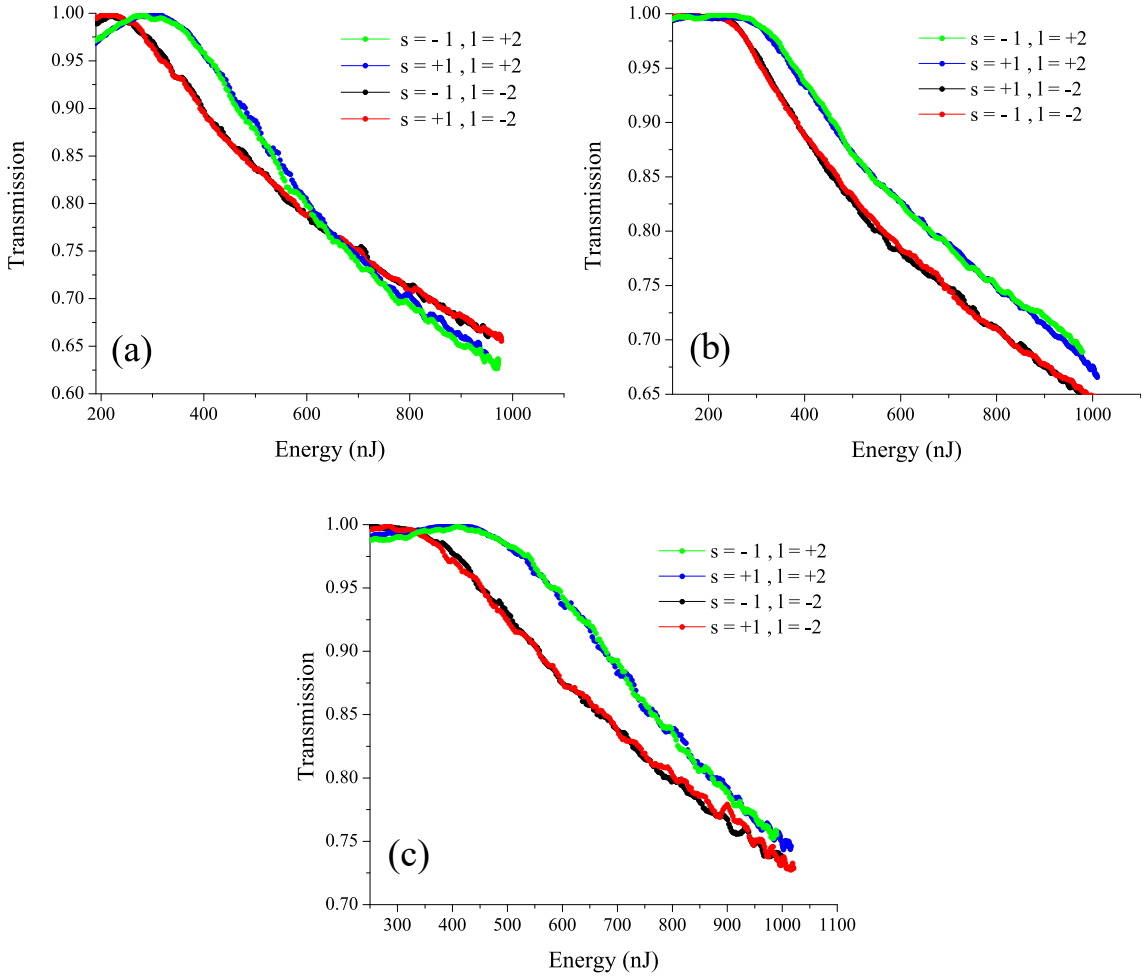

Figure 7.5: Helical dichroism produced by circularly polarized OAM beam possessing $\ell = \pm 2$ in (a) Borosilicate glass plate, (b) Quartz, and (c) Fused silica. Left circular polarization and right circular polarization are represented by $s+$ and s-, respectively.

- Our findings suggest that in order to realize helical dichroism caused by orbital angular momentum, there is no limitation in material selection. In other words, it can be observed even in ordinary materials such as fused silica and borosilicate glass.

The interaction of the OAM beam with bulk material is not fully understood yet, and the fundamental origin of observation of helical dichroism and the shape of the curves remains to be elucidated. However, as mentioned earlier, there have been plenty of works showing that the interaction of OAM beams with single particles differs significantly compared to a plane wave beam due to dipole-forbidden transitions, specially quadrupole transition moments [17, 32–35]. This explanation, alongside further investigations, may open new ways to confirm and explain our results. At this point, we postulate that the efficiency of the electric quadrupolar transition plays a crucial role in this context, and its influences increase by increasing the ℓ value.

Our study can be used in the future for further research in this direction and provides

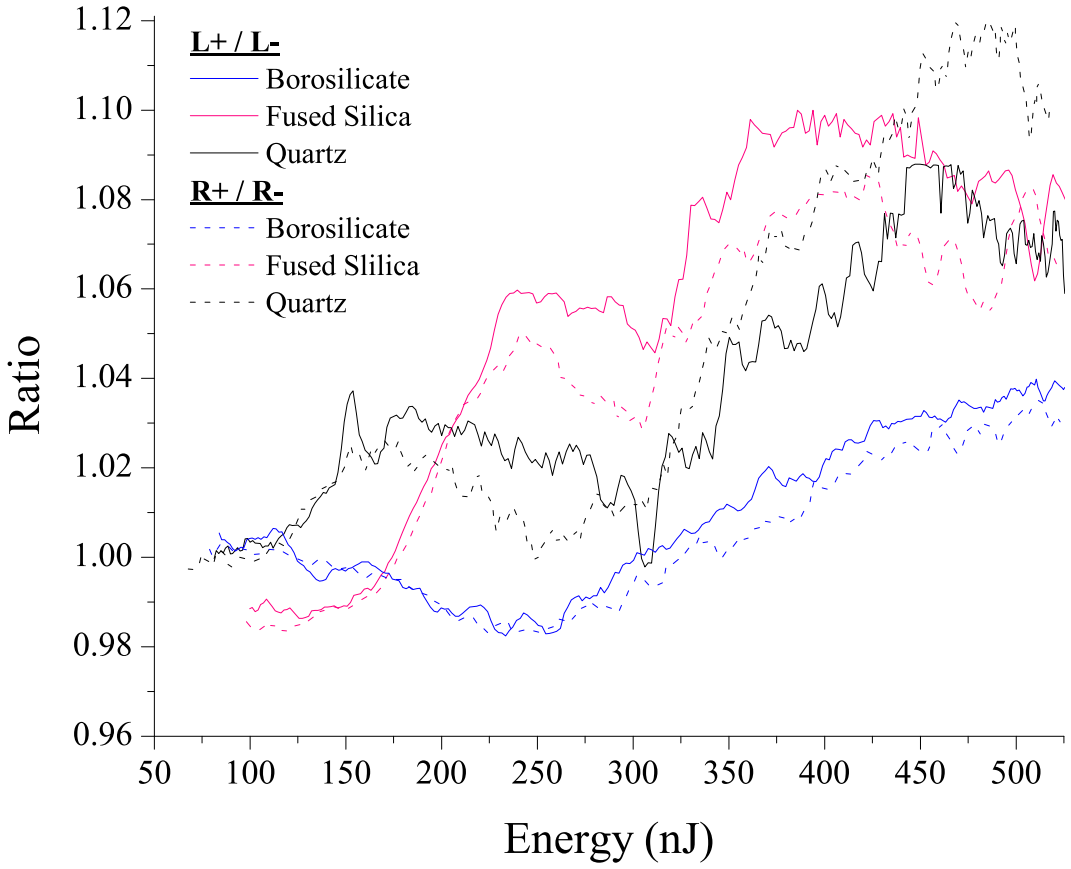

Figure 7.6: The ratio of L+/L- and R+/R- are plotted as a function of femtosecond vortex pulse energy. L (R) represents the left (right) circularly polarized beam, + represents the OAM value of +1, and - represents the OAM value of -1.

a deeper insight into the field of structured light-matter interactions and the significant role of orbital angular momentum. For instance, it could help scientists who are working to investigate the brain's functions as it allows for the optimization of the optical brain imaging by targeting different areas of the brain, as it has already begun [36].

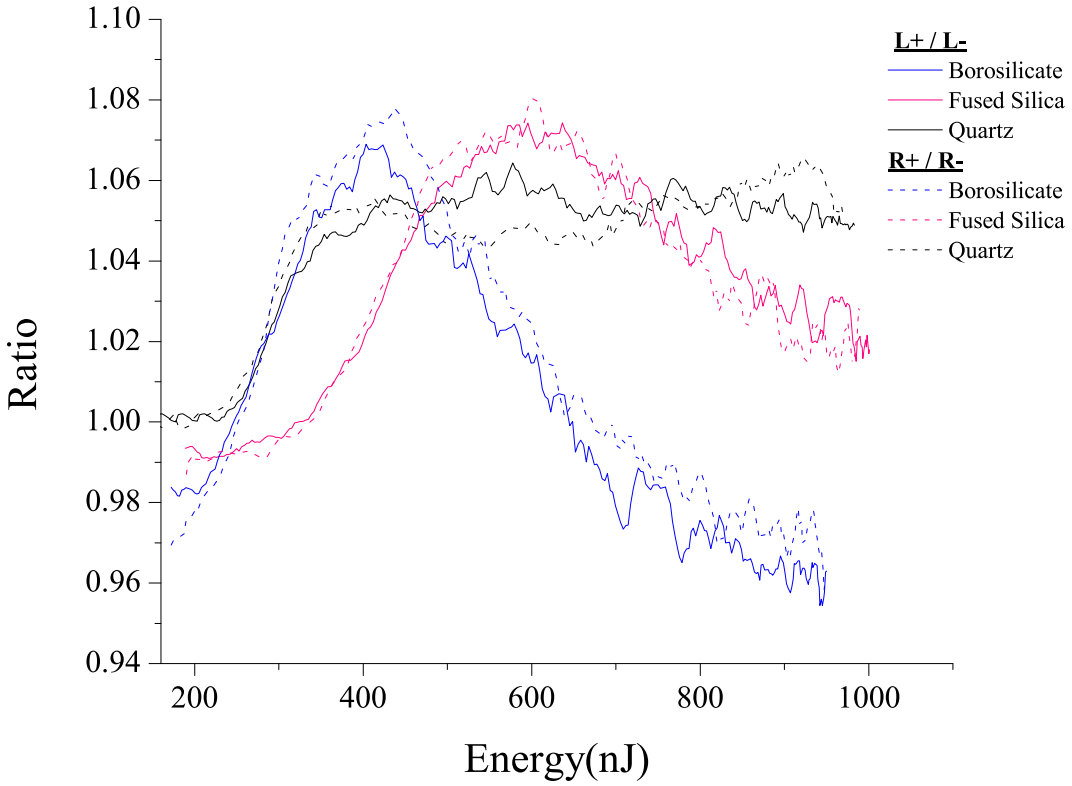

Figure 7.7: The ratio of R+/R- plotted as a function of OAM pulse energy. R+ represents the right circularly polarized OAM beam carrying ℓ=+1 and R- represents the right circularly polarized OAM beam possesses ℓ=-1.

Bibliography

[1] B. Walker, B. Sheehy, L. F. DiMauro, P. Agostini, K. J. Schafer, and K. C. Kulander, "Precision Measurement of Strong Field Double Ionization of Helium", Phys. Rev. Lett. 73, 1227 (1994).

[2] S. M. Hankin, D. M. Villeneuve, P. B. Corkum, and D. M. Rayner, "Nonlinear Ionization of Organic Molecules in High Intensity Laser Fields", Phys. Rev. Lett. 84, 5082 (2000).

[3] C. Pépin, D. Houde, H. Remita, T. Goulet, and J. P. JayGerin, "Evidence for resonance-enhanced multiphoton ionization of liquid water using 2 eV laser light: Variation of hydrated electron absorbance with femtosecond pulse intensity", Phys. Rev. Lett. 69, 3389 (1992).

[4] B. C. Stuart, M. D. Feit, A. M. Rubenchik, B. W. Shore, and M. D. Perry, "Laser-Induced Damage in Dielectrics with Nanosecond to Subpicosecond Pulses", Phys. Rev. Lett. 74, 2248 (1995).

[5] M. E. J. Friese, T. A. Nieminen, N. R. Heckenberg, and H. Rubinsztein-Dunlop, "Optical alignment and spinning of laser-trapped microscopic particles", Nature 394, 348350 (1998)

[6] L. C. Dávila Romero, D. L. Andrews, and M. Babiker, "A quantum electrodynamics framework for the nonlinear optics of twisted beams", J. Opt. B: Quantum Semiclass. Opt. 4 S66 (2002).

[7] M. F. Andersen, C. Ryu, P. Cladé, V. Natarajan, A. Vaziri, K. Helmerson, and W. D. Phillips, "Quantized Rotation of Atoms from Photons with Orbital Angular Momentum", Phys. Rev. Lett. 97, 170406 (2006).

[8] J. D. Joannopoulos, P. R. Villeneuve, and S. Fan, "Photonic crystals: putting a new twist on light", Nature 386, 143149 (1997).

[9] A. Mundt, A. Kreuter, C. Russo, C. Becher, D. Leibfried, J. Eschner, F. Schmidt-Kaler, R. Blatt, "Coherent coupling of a single $^{+}Ca^{40}$ ion to a high-finesse optical cavity", Appl. Phys. B 76, 117124 (2003).

[10] S. Franke-Arnold, "Optical angular momentum and atoms", Phil. Trans. R. Soc. A, 375, 20150435 (2017).

[11] S. J. van Enk, G. Nienhuis, "Commutation rules and eigenvalues of spin and orbital angular momentum of radiation fields", J. Mod. Opt. 41, 963977 (1994).

[12] S. M. Lloyd, M. Babiker, J. Yuan, "Interaction of electron vortices and optical vortices with matter and processes of orbital angular momentum exchange", Phys. Rev. A 86, 023816 (2012).

[13] A. Picón, A. Benseny, J. Mompart, J. R. Vázquez de Aldana, L. Plaja, G. F. Calvo, L. Roso, "Transferring orbital and spin angular momenta of light to atoms". New J. Phys., 12, 083053, (2010).

[14] C. T. Schmiegelow, J. Schulz, H. Kaufmann, T. Ruster, U. G. Poschinger, and F. Schmidt-Kaler, "Transfer of optical orbital angular momentum to a bound electron", NATURE COMMUNICATIONS, 7:12998 (2016).

[15] K. A. Forbes, D. L. Andrews, "The angular momentum of twisted light in anisotropic media: chiroptical interactions in chiral and achiral materials", Proc. SPIE 10672, 1067210 (2018);

[16] D. P. Craig and T. Thirunamachandran, "Molecular Quantum Electrodynamics: An Introduction to Radiation-Molecule Interactions", Academic Press, London (1984).

[17] G. F. Quinteiro, D. E. Reiter, and T. Kuhn, "Formulation of the twisted-light matter interaction at the phase singularity: the twisted-light gauge", Phys. Rev. A 91, 033808 (2015).

[18] K. A. Forbes and D. L. Andrews, "Spin-orbit interactions and chiroptical effects engaging orbital angular momentum of twisted light in chiral and achiral media", PHYSICAL REVIEW A 99, 023837 (2019)

[19] K. A. Forbes and D. L. Andrews, "Optical orbital angular momentum: twisted light and chirality", Optics Letters, Vol. 43, No. 3 (2018).

[20] D. L. Andrews, L. C. D*á*vila Romero, and M. Babiker, "On optical vortex interactions with chiral matter", Optics Communications 237, 133139 (2004).

[21] K. A. Forbes, D. L. Andrews, "Chiroptical interactions between twisted light and chiral media", Proc. of SPIE Vol. 10549 1054915-5 (2018)

[22] W. Brullot, M. K. Vanbel, T. Swusten, and T. Verbiest, "Resolving enantiomers using the optical angular momentum of twisted light", Sci. Adv. 2, e1501349 (2016).

[23] X. Zambrana-Puyalto, X. Vidal, and G. Molina-Terriza, "Angular momentum-induced circular dichroism in non-chiral nanostructures", Nat. Commun. 5, 4922 (2014).

[24] A. Afanasev, C. E. Carlson, and M. Solyanik, "Circular Dichroism of Twisted Photons in the Non-Chiral Atomic Matter," J. Opt. 19, 105401 (2017).

[25] C. B. Schaffer, A. Brodeur, and E. Mazur, "Laser-induced breakdown and damage in bulk transparent materials induced by tightly focused femtosecond laser pulses", Measurement Science and Technology,12(11), 1784 (2001).

[26] P. P. Rajeev, M. Gertsvolf, E. Simova, C. Hnatovsky, R. S. Taylor, V. R. Bhardwaj, "Memory in Nonlinear Ionization of Transparent Solids", PRL 97, 253001 (2006).

[27] R. W. Boyd, "Nonlinear Optics", Academic Press, 1992.

[28] M. Gertsvolf, H. Jean-Ruel, P. P. Rajeev, D. D. Klug, D. M. Rayner, and P. B. Corkum, "Orientation-Dependent Multiphoton Ionization in Wide Band Gap Crystals", PRL, 101, 243001 (2008).

[29] L. Sudrie, A. Couairon, M. Franco, B. Lamouroux, B. Prade, S. Tzortzakis, and A. Mysyrowicz, "Femtosecond Laser-Induced Damage and Filamentary Propagation in Fused Silica", Phys. Rev. Lett. 89, 186601 (2002).

[30] E. Calabrese, "Electronic energy-band structure of n quartz", Phys. Rev. B, 18 NO 6 (1978)

[31] D. J. Little, M. Ams and M. J. Withford, "Influence of bandgap and polarization on photo-ionization: guidelines for ultrafast laser inscription", Optical Materials Express, Vol. 1, Issue 4, pp. 670-677(2011).

[32] G. F. Quinteiro, F. Schmidt-Kaler, and C. T. chmiegelow, "Twisted lightion interaction: the role of longitudinal fields", Phys. Rev. Lett. 119, 253203 (2017).

[33] K. Köksal, and F. Koç, "The effect of twisted light on the ring-shaped molecules: the manipulation of the photoinduced current and the magnetic moment by transferring spin and orbital angular momentum of high frequency light", Comput. Theor. Chem. 1099, 203208 (2017).

[34] M. Babiker, C. Bennett, D. Andrews, and L. D. Romero, "Orbital angular momentum exchange in the interaction of twisted light with molecules", Phys. Rev. Lett. 89, 143601 (2002).

[35] J. R. Zurita-Sánchez, and L. Novotny, "Multipolar interband absorption in a semiconductor quantum dot. I. electric quadrupole enhancement", J. Opt. Soc. Am. B 19, 13551362 (2002).

[36] S. Mamani, L. Shi1, T. Ahmed, R. Karnik, A. Rodriguez-Contreras, D. Nolan, R. Alfano, "Transmission of classically entangled beams through mouse brain tissue", J. Biophotonics (2018).

Chapter 8

Conclusions and Future Works

The results presented in this thesis are on study of the interaction of femtosecond structured light with matter. This research is divided into two main categories. The first one is exploiting the unique properties of the structured light (phase singularities and complex polarization states) to fabricate surface micro- and nano-structures with an ability to manipulate material with an ultra-high spatial resolution. The second is a fundamental investigation of the possible role of orbital angular momentum, carried by the structured light, in relation with chiroptical effects within bulk materials.

Nanostructuring experiments were carried out by mapping the spatial distribution and polarization state of the optical vortex pulse on crystalline silicon (100) and diamond which was fabricated by chemical vapor deposition (CVD) synthesis process, respectively. The silicon surface exhibited the formation of a single nanocone surrounded by a rim as well as several nanocones located in complex patterns under irradiation of a single optical vortex pulse. In the multiple-pulse regime, however, we fabricated polarization-sensitive ripple structures on the diamond surface. Our findings in this context are summarized in the following.

In **chapter 4** , having known that the fluid dynamics plays a crucial role in light-matter interaction, we took advantage of the doughnut-shaped intensity profile of optical vortex beams to fabricate single nanocone features on a silicon surface. Single individual nanocones and an array of well-placed nanocones are shown to be fabricated in a feasible, single-step process. This is in contrast to the other well-known fabrication techniques, such as lithography that involve several preparation steps, including deposition, cleaning, etching, characterization, in addition to being very expensive. Our findings show that the pulse energy and the number of pulses irradiated on silicon are the crucial parameters affecting the properties of a fabricated nanocone. The major highlights of this work are:

- First time demonstration of nanocone formation with a single femtosecond optical vortex pulse.
- First time demonstration of polarization dependent nanocone formation. Fundamentally, our results highlight the role of transient plasmonics. They show how an

asymmetry in the free carrier density generated by the femtosecond pulse is preserved through the fluid dynamics resulting in asymmetric compressive forces that inhibit the height of the nanocone for linear polarization. The asymmetry vanishes for circular polarization resulting in higher nanocones.

- The nanocone height increases with the number of laser pulses while the aspect ratio remains unchanged. Also, the apex angle is independent of the pulse energy and the number of pulses.

- Overlapping of laser focus does not destroy the nanocones, allowing fabrication of an array of closely spaced nanocones that can be used in several applications.

Further work could be done by attempting to increase the height of such conical structures by irradiating a single nanosecond vortex pulse. This all-optical technique can be effectively practical not only to structure the target material and possibly change its phase but also to investigate the target by generating high harmonics via fabrication of a large array of conical nanostructures similar to those reported in this thesis. This provides an opportunity to control and probe light-induced carrier dynamics and dynamical phase changes in a target. Moreover, nanostructured materials provide the basis for a new generation of high-harmonic devices in the solid-state with the possibility of manipulating spatial distribution, intensity, and phase of high-harmonic emission (this emerging field bridges attosecond science with nanophotonics).

The degree of spatial control with light is restrictive. Therefore, it is not feasible to position individual structures with nanoscale precision, except in laser-induced forward transfer that has a resolution of hundreds of nanometers. Even in nano-ripple structures, whose orientations and spacings can be varied by changing the laser polarization and wavelength, only partial spatial control has been achieved. In this context, in **chapter 5** , we address how light can be used to actively manipulate materials in two dimensions with a precision of $\lambda/20$. By manipulating the beam shape, positioning of $\sim 0.1\ \mu\text{m}^3$ of the molten material in the form of a nanocone with 50 nm precision within an area of 40 μm^2 was possible. This technique is extended to fabricate complex, unconventional structures involving multiple nanocones and control their relative positions with the same precision. Here are the main highlights of our work:

- The nanocone on the silicon surface could be actively positioned anywhere within the focal volume by manipulating the singularity of the structured light beam. This manipulation was achieved by (a) rotating the polarization of the input Gaussian beam with respect to the q-plate axis (used to generate the structured light), and (b) introducing phase retardation in the q-plate.

- About 0.1 μm^3 of the molten silicon in the form of a nanocone (height $\sim$ 500 nm, tip size $\sim$ 70 nm, and a base of $\sim$ 850 nm) can be moved with 50 nm precision in an area of 40 μm^2. The wavelength of the light used in our experiment was 800 nm. Therefore, the spatial resolution is approximately 8 times smaller than what is predicted by the diffraction limit.

- The spatial resolution can be further improved to 10 nm by exploiting (a) highly stable power supply that can change the induced phase retardation in fine steps, and/or (b) rotating the input polarization angle in small steps.
- This technique suggests the fabrication of complex, unconventional structures involving multiple nanocones as well as controlling their relative positions with the same precision.
- Our technique is analogous to stimulated emission depletion (STED) microscopy/ lithography that is used to overcome the diffraction limit in imaging/ nanostructuring. STED microscopy (lithography) uses a Gaussian beam to turn on the fluorescence (photo-polymerization) in molecules within the focal volume and a doughnut-shaped beam to turn off the emission (inhibit polymerization) except in the central region. In contrast, the nanocone can be actively positioned anywhere within the focal region in our technique. The main drawback of STED lithography is the development of suitable photoresists, whereas our technique can be implemented to structure semiconductors, metals, and to some extent dielectrics.

Controlled fabrication of nanostructures in a single-step, precise technique can broaden the scope of laser processing of solids and have potential applications in present-day silicon photovoltaics, light-emitting devices, and sensors. To further improve this approach and its potential application, one can combine it with the LIFT technique (laser-induced forward transfer). Our technique proposes an ability to control the deposited material with nanometer precision in nano-printing of complex materials with applications ranging from microelectronics to bio-photonics.

In **chapter 6** , we address the characterization of complex polarization states of light, represented by points on a Poincaré sphere. The standard approach involves measuring the four Stokes parameters. Extending this technique to characterize higher-order Poincaré sphere requires polarization tomography, where the output polarization state is reconstructed from the measured spatially dependent intensity profiles of six different zero-order polarization states. The novelty of our method lies in the direct visualization of higher-order Poincaré spheres, i.e., complex polarization states, by imprinting complex polarization patterns into a solid surface in the form of laser-induced periodic nanogratings oriented parallel to the local structure of the electric field of light.

In this chapter, we demonstrate that this technique can be extended to (a) any higher-order Poincaré spheres, (b) complex polarization states produced by a coherent superposition of different vector vortex beams, and (c) various material surfaces. Our method could have potential applications to produce complex sub-wavelength nanostructures. Multiple localized regions of periodic nanostructures can be fabricated, each exhibiting different degrees of birefringence owing to different orientations of the periodic nanostructures within the laser modified region. Another significant aspect of this technique is that these complex structures are fabricated in a single-step process, known as direct laser writing. This is very fast and achieved with no need for an expensive and bulky vacuum system in comparison to other techniques such as lithography. Therefore, our findings have several potential technological significances. To name a few, these periodic structures can be employed:

- as diffraction gratings, since their periodicity is equal to or less than the wavelength of light.
- as an effective tool to create interference patterns and study polarization-selective transmission.
- as a nanograting-based 5-D optical data storage that corresponds to XYZ coordinates, the direction of its slow axis, and retardance. In fact, the birefringence of such gratings is described by retardance and slow axis direction that can be independently controlled by adjusting the intensity and the polarization state of the incident laser beam. This property adds two more dimensions than conventional structure-based storage devices.

The second part of my work, **chapter 7** , was focused on experimentally investigating the nonlinear nature of the interaction between an OAM beam and bulk materials. The experiments were carried out on borosilicate, fused silica, and quartz. We demonstrate that the transmission spectrum of a circularly polarized OAM beam passing through a bulk of material shows a discriminatory effect sensitive to the sign and magnitude of the OAM.

In recent years, fundamental studies on OAM beam interaction with matter has captured the attention of the scientific community. For instance, very recently, it has been demonstrated that when electrons and molecules (either chiral or achiral) interact with the OAM beam, having the same OAM value but opposite helicity, they behave differently. However, all efforts in this field were limited to single particles, and there have been no reported studies to investigate a similar behavior in bulk material. Our results, for the first time, showed that transparent dielectric materials exhibit helical dichroism and respond to a circularly polarized optical vortex with discrimination that is sensitive to the sign and magnitude of the OAM carried by the beam. In other words, OAM can produce a chiroptical effect in the bulk material. However, there is no well-understood mechanism behind such a phenomenon. To fully verify the mechanism, a potential method could be carrying out experiments with varying values of ℓ, and then plotting the absorption results for $\Gamma^{(L)} - \Gamma^{(R)}$ versus ℓ. Therefore, one can probe the locally differential absorption while considering the differences in intensity distribution associated with various radial distribution functions $f_{\ell,p}(r)$. Such experiments would appear to necessitate resolving the extent of absorption at different locations within the beam profile.